DRAKKAR Project

Variability of the subpolar Atlantic and the Southern Ocean : Local processes and Interactions with the Global Ocean.

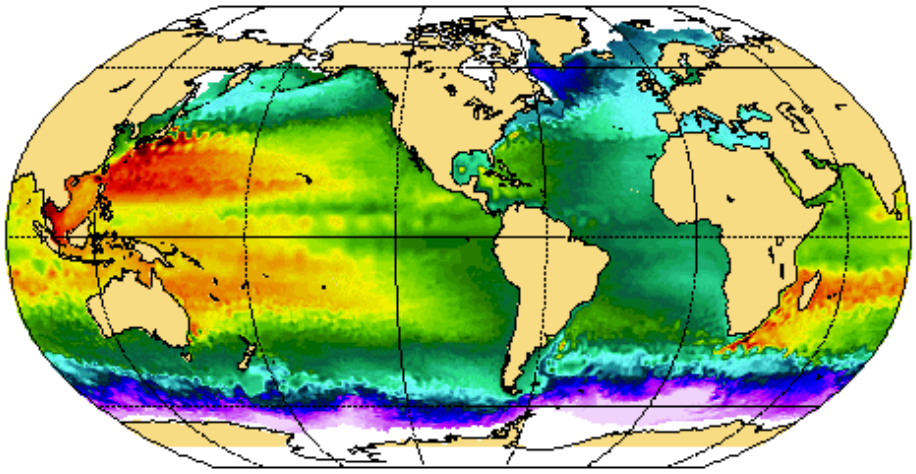

Report of Activity 2005-2006
LEGI, LPO, LOCEAN
With contributions from MERCATOR-Océan, LSCE and LEGOS

Décembre 2006

Rapport LEGI-DRA-4-12-2006
Equipe MEOM, Laboratoire des Ecoulements Géophysiques et Industriels, BP53, 38041 Grenoble Cedex 9

Contact: *bernard.barnier@hmg.inpg.fr*

Table of Content

1. Scientific Objectives and Modelling Approach

1.1. Scientific objectives

The primary concern of DRAKKAR is related to the circulation and the day-to-decade variability in the North Atlantic Ocean, as driven by the atmospheric forcing, by interactions between processes of different scales, by exchanges between basins and regional circulation features of the North Atlantic (including the Nordic Seas), and by the influence of the world ocean circulation (including the Arctic). New scientific objectives have emerged in the past two years relative to the variability of the Southern Ocean. DRAKKAR is also concerned by the role of the changing ocean circulation in ecosystem dynamics, and in climate through the transport of heat and freshwater and the uptake of atmospheric CO2.

1.2. Modelling approach

The scientific approach of the teams participating in DRAKKAR mainly relies upon numerical simulations. Therefore, the project has built a hierarchy of embedded model configurations, based on the NEMO code (http://www.lodyc.jussieu.fr/NEMO/), able to provide continued and systematic development and assessment of the ocean model components used in ecosystem, carbon cycle, and climate studies as well as in regional and operational oceanographic applications. The various DRAKKAR configurations will be run for multiple decades to provide a relevant, four-dimensional description of the atmospherically driven world ocean circulation and variability over the last 50 years. This description will allow (in the limits of model accuracy) to study the regional impacts of the global oceanic variability during this period, and to identify remote interactions between the North Atlantic and the World Ocean. It is also expected to contribute to the interpretation of the changes noticed in past and future ocean observations.

2. Project organisation

2.1. Drakkar concept

During the last decade, the DRAKKAR participating scientists fostered co-operative scientific activities within the Mast3 European project DYNAMO (Dynamics of North Atlantic Models), and between their national projects, CLIPPER in France and FLAME (Family of Linked Atlantic models) in Germany. The expertise gained through projects such as these also helped to build their capability to make significant contributions to a variety of modelling needs. However, the challenge of developing realistic ocean models required for the diverse range of applications can only be met by an effective integration and co-ordination of the activities and complementary expertise of every member of the group. This fact yielded the DRAKKAR concept. The project is organised with an international project-team comprising research groups in France, Germany, and Russia, and associated scientists who cooperate with the project.

2.2. Drakkar project-team

Scientists participating to the Drakkar project-team are from 8 different laboratories; LEGI in Grenoble, LPO in Brest, LOCEAN in Paris, MERCATOR-Ocean in Toulouse, LSCE in Orsay, IFM-Geomar in Kiel, and Shirshov Institute of Oceanography (SIO) in Moscow. The project-team conducts the project activities. It has the charge to define details of the model configurations, to implement and to validate their various components. This team also defines

model experiments to run, co-ordinates their execution by the participating groups, and organises the sharing of model results.

2.3. Associate Scientists

The DRAKKAR project team promotes collaboration with Associate Scientists conducting researches complementary to the DRAKKAR objectives to enhance the scientific value of model developments, simulation outputs and to foster multidisciplinary studies. Associate scientists may also get DRAKKAR model configurations to carry out their own simulations. In that case, it is important that when possible, they co-ordinate their simulations with those carried-out with the project-team. An objective of DRAKKAR is to gather a community of competences and means to improve global eddy-permitting to eddy resolving models. Collaborating partners are thus expected to contribute to model refinement, in particular by additional, complementary sensitivity experiments. This includes the participation in experiments dedicated to the coordinated development. Associate scientists using DRAKKAR model configurations must commit themselves to not give model configurations to other groups. The DRAKKAR project team wants to control the distribution configurations to avoid their distribution on the grapevine.

2.4. Cooperation with scientists outside the project

The DRAKKAR team is generally favourable to share model outputs and configurations with scientists outside the project. In case the scientific objectives of outside scientists overlap those of the project-team, a cooperation should be sought that favours complementarity of studies. Note that the group has no means dedicated to service outside the group, and technical support to transfer DRAKKAR configurations will be limited. Scientists using Drakkar model configurations must commit themselves to not give them to a third party. Major funding of DRAKKAR project comes from the MERCATOR consortium, and model configurations have been (and will continue to be) developed jointly with MERCATOR. Consequently, the team will not give model configurations to groups involved in activities directly related to operational or commercial oceanography. These groups will have to address such request directly to the MERCATOR consortium. Finally, it should be noted that DRAKKAR model configurations are not included in the NEMO distribution, but are using it. NEMO is freely available and is distributed by LOCEAN. Users of DRAKKAR configurations, as all NEMO users, must register at LOCEAN.

3. DRAKKAR model configurations

The various configuration of the ocean/sea-ice NEMO numerical model are schematically presented in the figure below. Advances in model performances achieved during the development of this hierarchy of configurations are described in a series of papers published or submitted (Barnier et al.,2006, Le Sommer et al., 2006, Penduff et al., 2006), and several reports (http://www.ifremer.fr/lpo/drakkar/).

a) Global Configurations

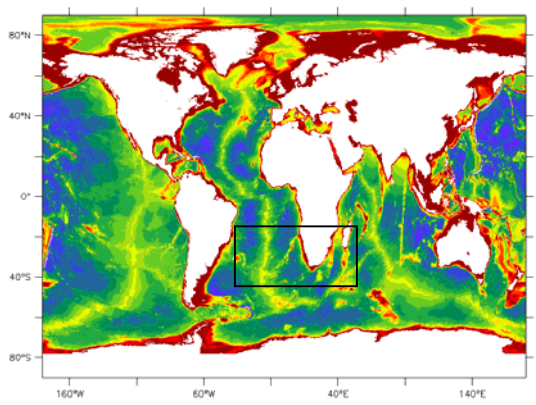

ORCA2: Global, coarse ~2° resolution, non eddy permitting configuration with sea-ice, 182×140×31 grid pts, time step 9400 s. Operated at LOCEAN, IFM, and LEGI

ORCA05: Global, 1/2° resolution, non eddy permitting configuration with sea-ice, 722×511×46 grid pts, time step 2160 s. Developed in 2004. Operated at LOCEAN, IFM, and LEGI

ORCA025: Global, 1/4° resolution, eddy permitting with sea ice, 1442×1021×46 grid pts, time step 1440 s. Developed in 2005, Operated at LEGI, IFM-Geomar and MERCATOR-Ocean. IFM-Geomar is implementing a 1/12° AGRIF refinement in the region of the Agulhas Retroflection region.

b) North-Atlantic/Nordic-Seas configurations (80°N – 30°S) driven at open boundaries by the global configurations

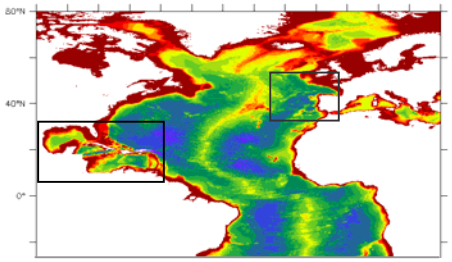

NATL4: 1/4° resolution, eddy permitting, with sea-ice. Open boundaries, 486×529×46 grid pts, time step 2400. Developed in 2004, it has the possibility of AGRIF grid refinement. Operated at LPO and LEGI.

AMEN: AGRIF refinement in NATL4 in the north east Atlantic: 1/12° resolution, eddy resolving. AMEN has 383x397x64 grid pts, time step 720s. Developed in 2006. Operated at LPO.

NATL12: 1/12° resolution, eddy resolving, with sea-ice. Open boundaries, 1615×1576×64 grid pts, time step 720s. Developed in 2006. Operated at LPO and MERCATOR-Ocean.

AGRIFMEX: NATL3 (similar to NATL4 at 1/3° resolution, inherited from CLIPPER) with AGRIF refinement in the Caribbean/Gulf-of-Mexico (CARIB15): 1/15° resolution, eddy resolving. NATL3 has 358x361x43 grid pts, time step 1800 s. CARIB15 has 604x399x43 grid pts, time step 600 s. Developed in 2006. Operated at CICESE and LEGI.

c) Southern Ocean configurations (30°S – 80°S) driven at open boundaries by the global configurations

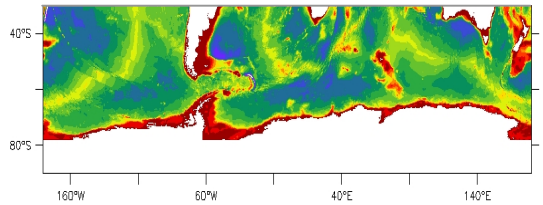

PERIANT05: 1/2° resolution, non eddy permitting, with sea-ice. Open boundary at 30°S, 722×202×46 grid pts, time step 2400 s . Developed in 2006. Operated at LEGI.

PERIANT025: 1/4° resolution, eddy permitting, with sea-ice. Open boundary at 30°S, 1442×402×46 grid pts, time step 1440 s. Developed in 2007. Operated at LEGI.

d) Indonesian throughflow configuration (15°N-15°S) driven at open boundaries by the global configurations

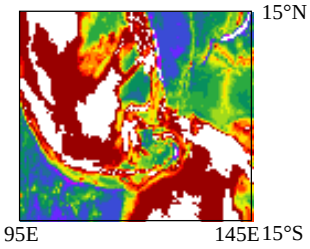

ITF025: 1/4° resolution, eddy permitting from 15°S-15°N and 95°E-145°E. Four open boundaries driven by ORCA025. 204×210×46 grid pts, time step 2400 s. Developed in 2006. Operated at LOCEAN.

Figure 1: DRAKKAR Hierarchy of Model Configurations.

4. DRAKKAR Project: Report of Activity 2006

We present here a summary of research activities carried out in 2005 and 2006 by the DRAKKAR French Team (LEGI, LPO, LOCEAN and LSCE). A section of this report in written in French, because it is a paper submitted to the IDRIS newsletter, the news letter of the French National Computer Centre where all calculations presented here were performed. This paper present a 47 year long experiment (1958-2004) carried out with the 1/4° global configuration ORCA025-G70.

The report is organized as follows. The first part presents our efforts to improve the model configurations, numerical schemes, and forcing fields. The second part describes the long experiments with the 1/2° model and the 1/4° global model, and ongoing analysis. The third part presents the studies of the Southern Ocean, and the fourth our regional configurations. Finally, studies realized in collaboration with associated teams are summarized in the last section.

4.1. Improvement of DRAKKAR model configurations

4.1.1. Parameterisations

Experiments have been carried out in order to fix or reduce several identified deficiencies of the ORCA025 configuration in order to prepare the 50 year long inter-annual experiments. Four issues were addressed: The summer mixed layer, the freshwater runoff of the Amazon River, the overflows at major sills and straits, and the geometry of the strait of Torrés.

Mixed layer. The summer mixed layer was generally too shallow in model configurations based on NEMO. A modified *TKE* scheme (Madec, 2006) which accounts for *(i)* the effect of surface waves, *(ii)* an enhanced vertical penetration of the turbulent kinetic energy (*tke*), and *(iii)* includes a parameterisation of the effect of the Langmuir Cells on the vertical mixing have been tested in ORCA025. In this series of tests ORCA025 is run from rest during 4 years, driven by the CORE normal year atmospheric forcing. Results from two experiments are presented here: run G42 with standard *TKE* scheme, and run G43b with the modified *TKE* scheme in which the *tke* penetration is 7.5% of the wind energy. The mixed layer depth (*mld*) climatology of de Boyer Montégut et al. (2004) is used to measure the impact of the new *TKE* scheme. The primary effect expected from the new *TKE* parameterisation is to increase the summer mixed layer depth, which is usually too shallow with respect to the climatology. In our calculations of the *mld*, we use the same temperature criterion as in the climatology (a 0.2°C temperature change).

In the Southern ocean, the climatology indicates summer *mld* values of 60-100 m. (Fig 1a). With values of 40 m (Fig. 1b) the standard run (G42) significantly underestimate the *mld*. The run with the modified *TKE* (Fig. 1c) with a *mld* in the range 80-120 m is much closer to observations. In the northern hemisphere (no figure shown), the North-East Pacific is a region where the new *TKE* makes a noticeable difference. Climatology shows a wide band where *mld* is 40 m stretching from Bering Strait to California. The standard run G42 does not reproduce this feature with a *mld* which rarely exceeds 20 m. On the contrary, with the modified *TKE* scheme the model reproduces well the shape and amplitude of this feature. Similar result is observed in the North Atlantic, the new *TKE* scheme producing again a deeper summer *mld* than in the standard case. These improvements are found to be robust for every summer month in both hemispheres. However, we observed that the model *mld* produced by the modified *TKE* scheme often exceeded the observed values, suggesting that using a penetrating fraction of *tke* of 7.5% is slightly too strong. But setting the corresponding parameter to 0% (run G43a) produced too shallow *mld* as in the standard case. Our conclusion is that the new *TKE* scheme performs better

than the standard one, in particular in the Southern Ocean and we recommend to use a value of 5% for the fr_emin parameter which sets the vertical *eke* penetration.

a) Climatological Mixed Layer Depth in January - de Boyer Montégut - 2004

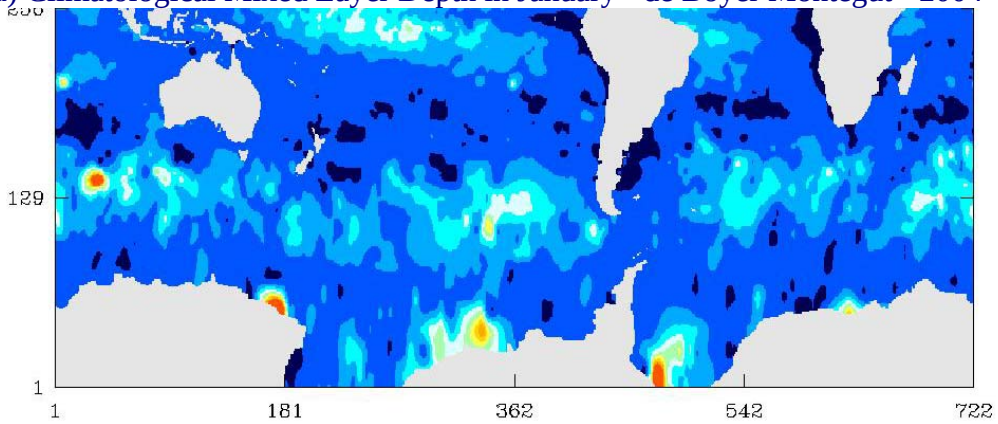

b) Mixed Layer Depth in January - Experiment G42 - Standard *TKE* Scheme

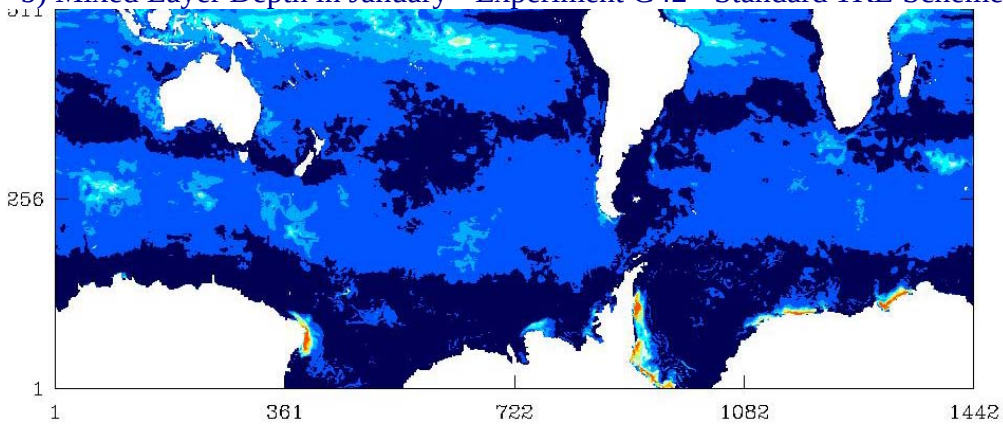

c) Mixed Layer Depth in January - Experiment G43b - Modified *TKE* Scheme

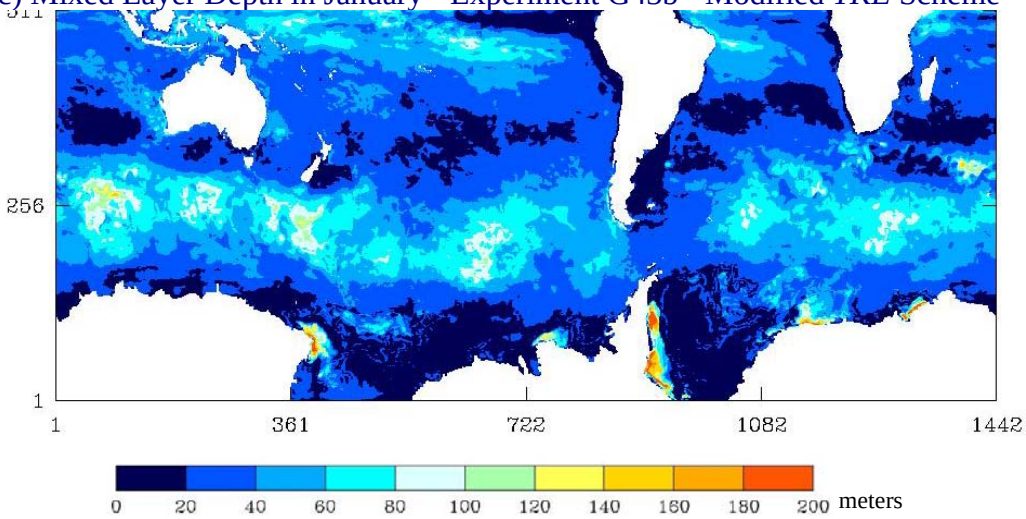

Figure 1: Summer mixed layer (January) in the Southern hemisphere from a) estimate from climatological hydrographic data by de Boyer Montégut (2004), b) by the model ORCA025 with the standard TKE vertical mixing scheme, and c) by the model ORCA025 with the new TKE vertical mixing scheme.

Amazone river runoff : the strong runoff of the Amazon river was found not to spread out enough off shore the river outlet, generating an unrealistic, very fresh coastal current along the Brazil-Guyana Coast, feeding the Caribbean Sea with too fresh upper waters. An analysis of this particular case have been realized and modification of the runoff distribution at the outlet have been proposed (run G45b).

Overflow parametrization : All DRAKKAR simulations carried out in 2005 showed deficiencies in the representation of deep water overflows, which occur mainly between the Norvegian Sea and the North Atlantic (Denmark Strait and Faroes Bank Channel, hereafter respectively named DS and FBC), the Mediteranean Sea and the Atlantic (Gibraltar Strait, hereafter GIB) and between the Red Sea and the Gulf of Aden (Bab-el-Mandeb strait, herafter BEM). Sensitivity experiments have been carried out first with the idealised DOME configuration, then with the NATL4 configuration (for a fine tuning in DS, FBC and GI), to find modifications of the bottom topography, and for fine tuning of locally enhanced bottom friction and parameters of the diffusive and advective bottom boundary layer (BBL).

First, the numerical code of the advective BBL has been modified to run with the Partial Step topography. Second, a series of tests with the idealised DOME configuration demonstrated that increasing bottom friction was significantly contributing to bring overflow waters at greater (and more realistic) depths. However, tests with NATL4 demonstrated that this effect was much more limited in a realistic configuration.

Third a modification of the topography of the sills which would optimise the effect of the advective BBL has been searched. Using the DOME configuration, we demonstrated that the advective BBL is the most efficient on the first topographic step. The DOME configuration is a 1200 km long, and 300 km wide, east-west channel (Figure 2a). It is shallow to the north and deep to the south, depth increasing linearly from north to south. The flow is linearly stratified. A flow of water which density is the bottom density is injected at 600 m depth in a narrow north-south channel at the north-east corner. The topographic slope in this narrow channel has one of the profiles shown in Fig. 2b. The dense water flows down-slope and westward, and tends to form a vein of dense fluid at some depth. A passive tracer of concentration one is injected in the dense water at the entrance of the narrow channel. The tracer concentration at the near bottom level is taken as the dense water overflow.

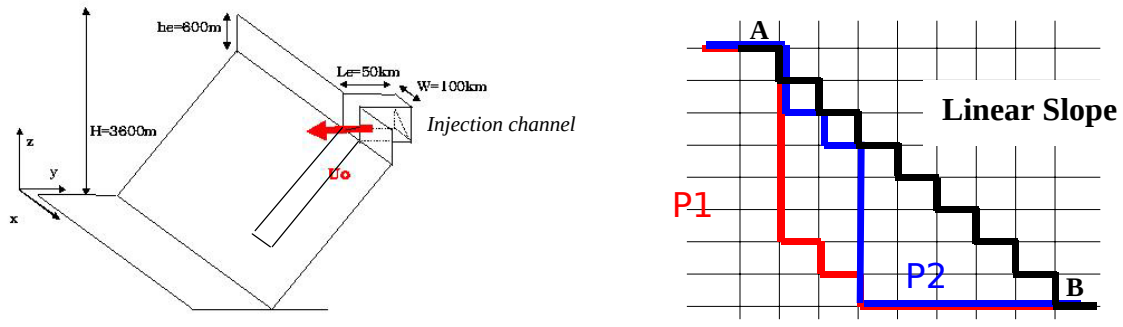

a) b)

Figure 2: Schematic representation of a) the DOME configuration and b) the various topographic profiles tested for the injection channel in the DOME configuration. The cliff profile is P in red. A (and B) are the top (and the bottom) of the dense water injection channel. The study aims to quantify the impact the different profiles have on the descent of dense water (i. e. passive tracer).

Among the 3 different topographic profiles shown in Figure 2, the profile which has the greater topographic jump (profile P1, the *cliff* profile thereafter) is the one insuring the highest concentration of a passive tracer from A to B, but only when associated to the advective BBL (Fig. 3).

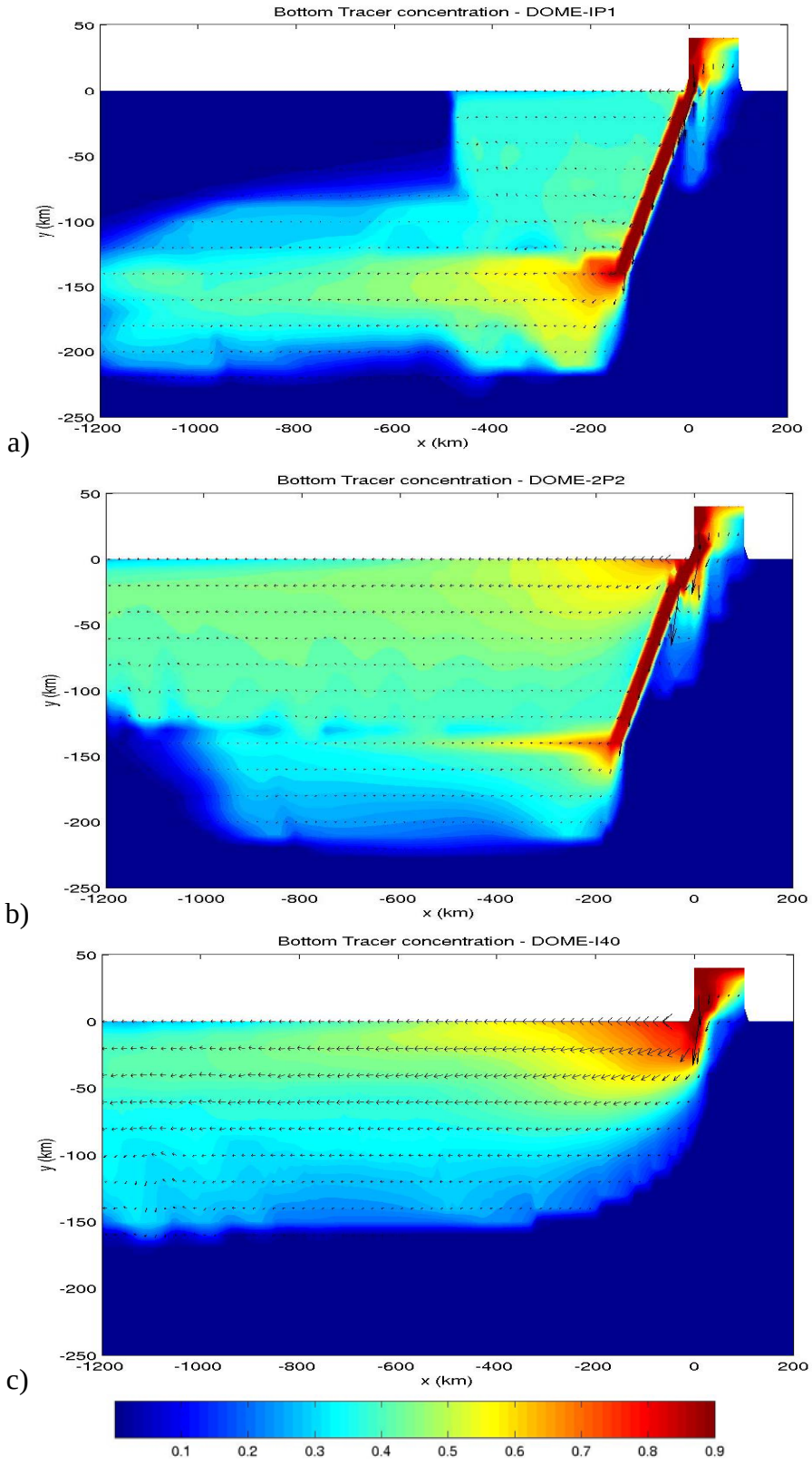

Figure 3: Concentration of passive tracer(colours) near the bottom after 60 days in 3 different DOME runs with advective BBL, a) with the "cliff" profile P1, b) with profile P2 and c) with the linear profile. It is the cliff profile P1 associated with the advective BBL which has the highest concentration of tracer at the exit of the channel at y = -140 km. The other profile P2 has a lesser tracer concentration at depth and shows a strong leakage at the upper part of the channel. With a linear slope, no dense fluid is found at the depth corresponding at y = - 140 km. Arrows show current velocity.

The modification of ORCA025 bottom topography at DS, FBC, GIB and BEM has been inspired by the above DOME results. The bathymetry of those straits have been modified such that the greatest topographic jump occurs at the first grid point after the sill (Figure 4 for the Denmark strait). The results are very positive regarding the depth reached by the overflow waters. However, this solution was found to under-mix the Mediterranean outflow waters which where much to warm and salty. Relaxation to climatological values was thus implemented at the outlet of the sill for the ORCA025-G70 experiment (1958-2007). After viewing the results of run G70 (see below), the good behaviour at GIB suggest that a similar relaxation should also be used at BEM.

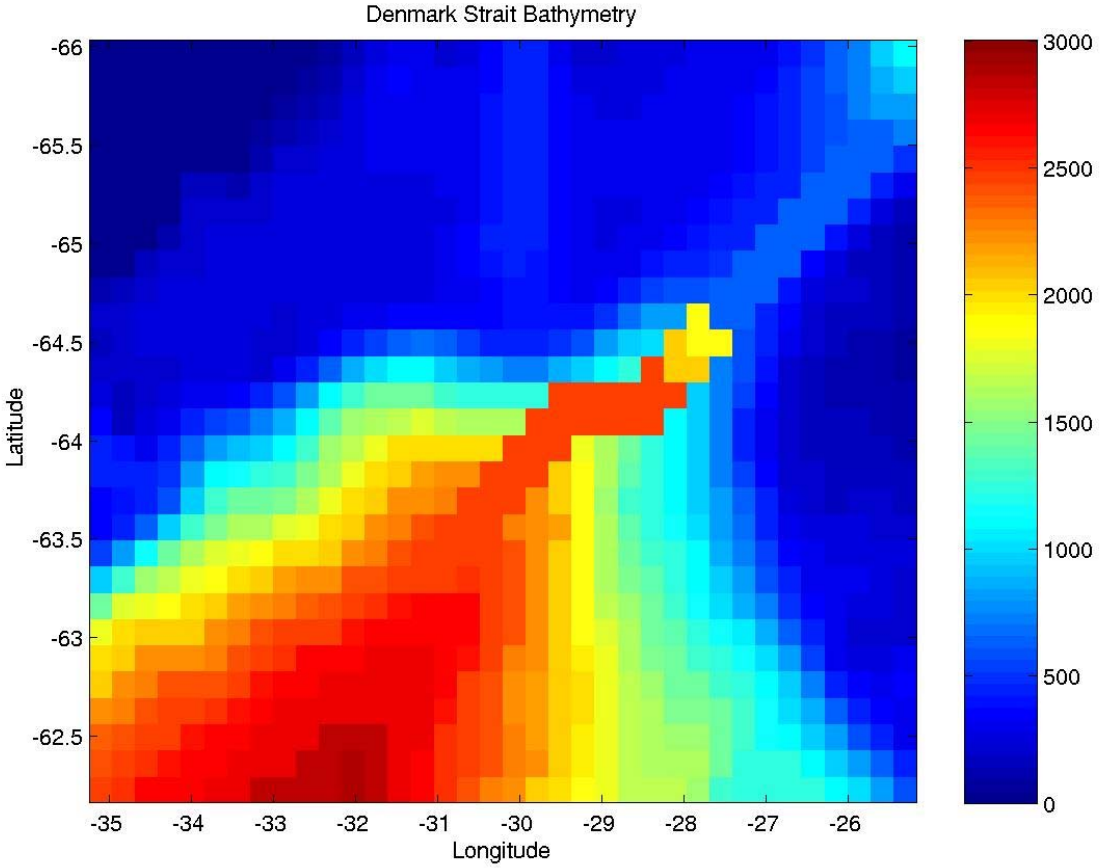

Figure 4: Denmark Strait bottom topography (in meters) in ORCA025-G70. The channel connecting the Nordic Seas to the North Atlantic is characterised by a jump at the sill from nearly 600 m to 1800 m (the yellow colour at 64.5°N,27.6°W).

Opening Torrés Strait : The tuning of the bathymetry in the Indonesian through-flow area first led to the closing of the Torrés Strait, in order to reduce the water transport through it. This drastic solution was not fully satisfactory because of the lack of diffusive transport between the Pacific Ocean and the Arafura Sea is questionable. We decided to open the strait, including 2 small islands to mimic the effect of very shallow areas, and using locally enhanced bottom friction (factor of 50) in order to slow down the flow as much as possible. This solution proved to be rather satisfactory (runs G44, G45 and G45b).

Definition of sea-ice model parameters: We used the 1/2° southern ocean configuration PERIANT05 to tune the sea-ice parameters in the Antarctic. The accretion parameter for sea-ice proved to be crucial regarding ice thickness. Parameters values used in the run ORCA025-G70 are issued from these experiments (Molines et bal., 2006).

4.1.2. Momentum advection

A series of simulations with the NATL4 configuration have been carried out to understand the influence of momentum advection schemes on mean currents and current-topography interactions. It was found that near-bottom grid-scale velocity irregularities play a major role. The first DRAKKAR global simulations at 1/4° have shown that the use of an enstrophy-and-energy-conserving momentum advection scheme substantially reduces widespread biases of mean currents at the surface (Barnier et al., 2006) and at depth (Penduff et al., 2006). We have investigated the origin of these improvements (Lesommer et al., 2006). A series of sensitivity simulations with different momentum advection schemes is performed with the North Atlantic 1/4° DRAKKAR model NATL4. Three second order momentum advection schemes conserving respectively enstrophy (*ens*), energy (*efx*) and both quantities (*een*) are tested and their impact on the model solution are compared. The mean kinetic energy vertical profile is found to change within up to 10% depending on the chosen scheme. This sensitivity is maximum in bottom layers. The analysis of the vorticity tendency due to horizontal momentum advection reveals that the three schemes differ mostly in bottom layers indeed. The average magnitude of this term is enhanced with scheme *efx* and reduced with scheme *een*. These differences are found to be consistent with the instantaneous tendency of each scheme. In addition, we show that these differences are related to the irregularity (i.e. non-smoothness of the gradients) of the velocity field, which is enhanced in bottom layers. We conclude that the model solution is crucially dependent on the ability of the momentum advection scheme to handle under-resolved flows close to the bottom topography. This work emphasizes the critical influence of current-topography interactions in eddy-active regions on mean current features such as the position of the North-Atlantic current, the Gulf Stream separation, ot the Zapila Anticyclone in the Argentine basin.

4.1.3. Atmospheric forcing: Definition of DFS3

A series of studies have been conducted to produce a forcing function which correct the major biases and drifts noticed in run ORC05-G50. The only equivalent forcing data set available is the ECMWF reanalysis ERA40. Radiative fluxes (downward short wave and long wave) from ERA40 show a strong trend over the whole period (Brodeau et al., 2006), and they were discarded. We decided to retain CORE radiation which is a satellite product (ISCCP). We compared the turbulent fluxes of CORE and ERA40. The basic variables (wind speed, air temperature and air humidity) are rather different between data sets (Figure 5 and Figure 6). CORE winds are always stronger, and are suspected to be too strong since they are also stronger than ERS satellite winds.

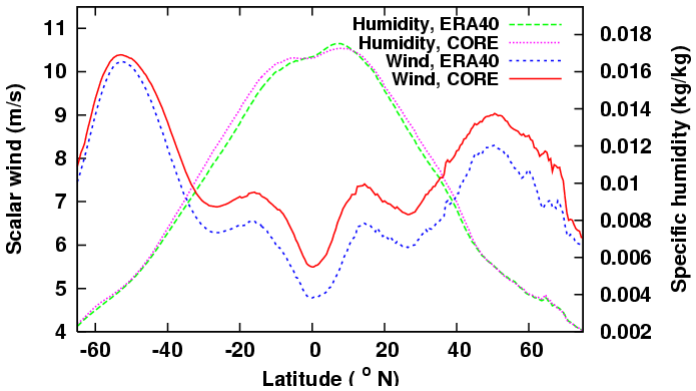

Figure 5: Latitudinal distribution of the zonally averaged 10m wind speed and 10m air humidity in ERA40 and CORE data sets. The 1958-2000 mean is plotted. CORE wind is significantly greater. Air is ERA40 is generally dryer than in CORE excepted in the 0°N-10°N equatorial band.

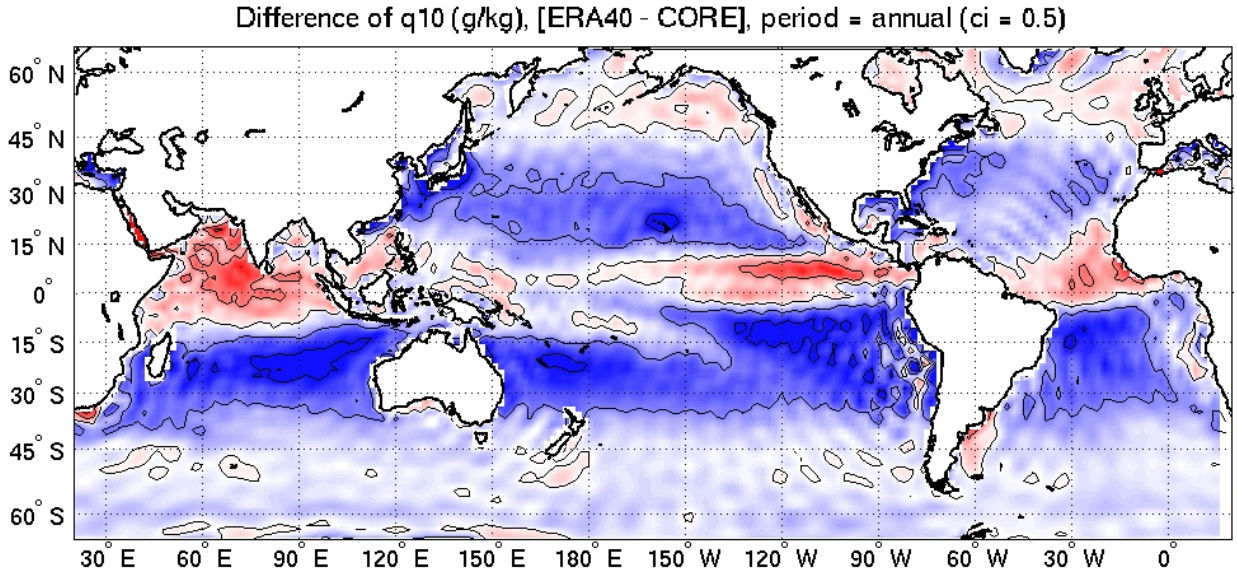

Figure 6: Mean difference in 10m air humidity between ERA40 and CORE. This difference is calculated over the period 1958-2000. Positive (negative) values in red (blue) areas indicate moister (dryer) air in ERA40. We expect a significant reduction of the latent heat flux in the tropics with ERA40 due to weaker winds and moister air. Stronger evaporation is expected in subtropical gyres and the ACC, significantly dryer in ERA40, which amplitude might be however limited by weaker wind speed. Note that the "wiggles" are introduced by CORE, ERA40 fields being significantly more regular. Contour interval is 0.5 g/kg.

Air is dryer in ERA40 excepted in the band 0°N-10°N. Regarding air temperature (Figure 7), EA40 is warmer between 30°S-30°N, and in north-eastern Pacific and Atlantic Oceans. At subpolar latitudes in the northern hemisphere (no figure shown), air in ERA40 is slightly warmer than in CORE (about 0.5°C), but is significantly colder in winter (1 to 3°C in the Labrador Sea for example). Thus we expect more active deep convection in the North Atlantic with this data set. In the Artic (Figure 8), ERA40 temperature is higher (by 2°C o 3°C) in all seasons. Interannual variability is very consistent between both data sets over the whole 1958-2001 period.

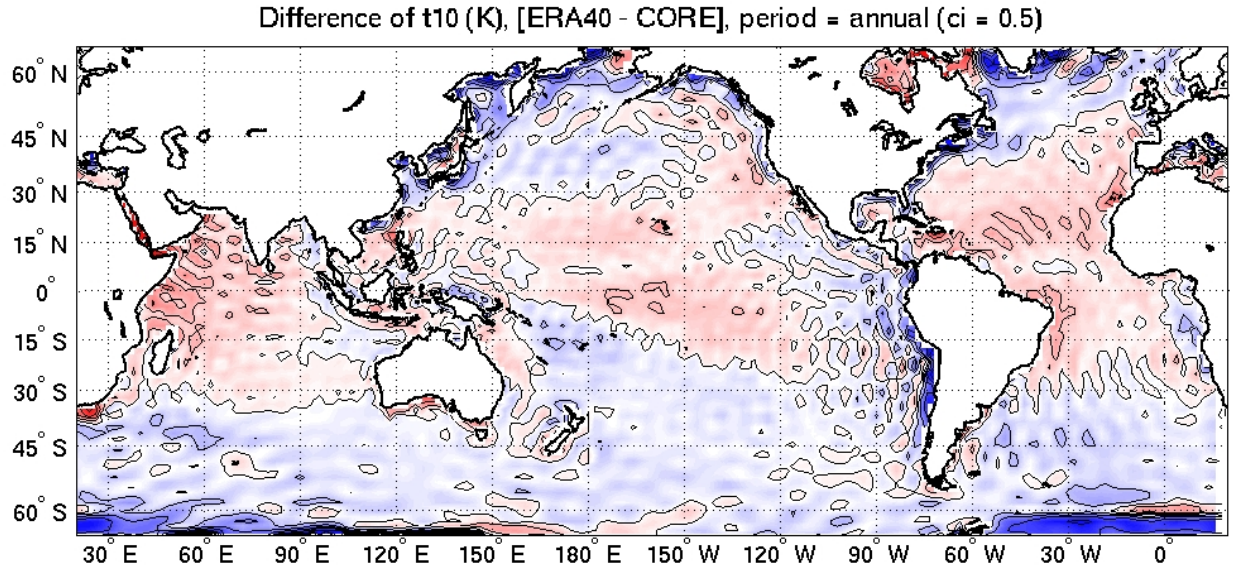

Figure 7: Mean difference in 10m air temperature between ERA40 and CORE. This difference is calculated over the period 1958-2000. Positive (negative) values in red (blue) areas indicate warmer (colder) air in ERA40. Note that the "wiggles" are introduced by CORE, ERA40 fields being significantly more regular. Contour interval is 0.5°C.

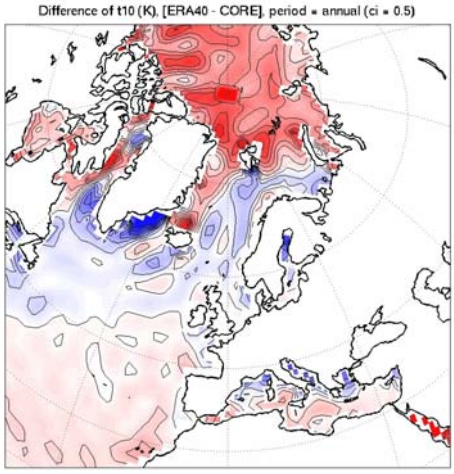

Figure 8: Difference in 10m air temperature between ERA and CORE in the Arctic. Positive (negative values) in red (blue) indicate warmer (colder) air in ERA40. Contour interval is 0.5°C. In area covered by sea-ice, air in ERA40 is significantly warmer, suggesting that ice thickness might be less in a run driven by this data set.

Our analysis of the freshening of the surface ocean in run ORCA05-G50 identified precipitation as an important contributor at mid and high latitudes in the northern hemisphere. We decided to apply a correction to the CORE precipitation between 30°S to the North Pole. CORE precipitation are derived from the GXGXS precipitation data set (Fig. 9), but a correction was applied which increased the amount of rainfall over the ocean by 0.3 to 0.5 mm/day in zonal average (Fig. 10). The reader is invited to see Large and Yeager (2004) for the justification of the correction. Analysis of simulation G50 suggests that the correction is reasonable except beyond 30°N, so we decided to use the standard GXGXS precipitation field between 90°N and 30°N and to keep the CORE values from 30°N to 80°S (Figure 10). This blended data set is referred to as DPS3 (Drakkar Precipitation Set #3).

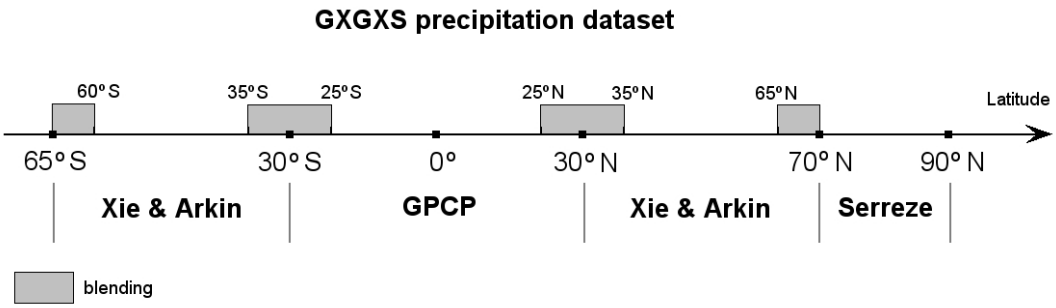

Figure 9: GXGXS precipitation data set: it is a blending of various precipitation estimates, which largely rely on satellite estimates. The study of Béranger et al. (2006) identified Xie&Arkin (also named CMAP) and GPCP estimates as the most reliable estimates among 20 different global precipitation fields to drive an ocean model.

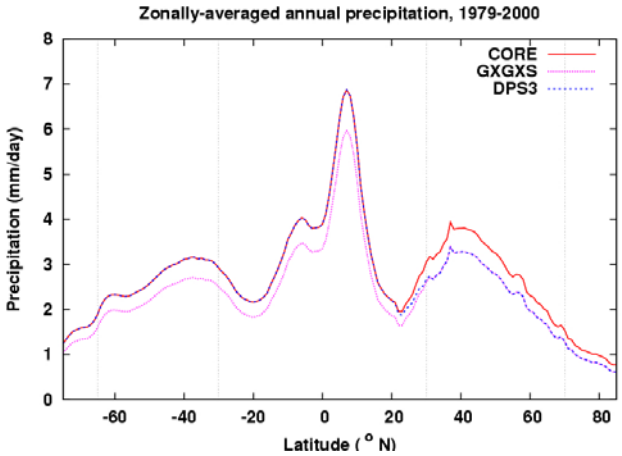

Figure 10: Latitudinal distribution of zonally averaged precipitation in the CORE and GXGXS data set. DPS3 (DRAKKAR Precipitation Set #3), retained for the hybrid DRAKKAR Forcing Set #3 is a blend of GXGXS from 90°N to 30°N and CORE from 30°N to 80°S.

DRAKKAR Forcing Set #3 (DFS3): From the above analysis, we defined a new set of atmospheric forcing variables, referred to as DFS3. It comprises :

- daily downward shortwave and lonwave radiation from CORE (ISCCP satellite product)
- PS3 monthly precipitation (CORE corrected by GXGXS northward beyond 30°N)
- 6 hourly wind vector (10 m), air temperature (10 m), air humidity (10 m) from ERA40 between 1958 and 2001, and from ECMWF operational analysis from 2002 to 2004.
- a correction for the katabatic winds in Antarctica (see below)
- monthly climatology of river runoff (from MERCATOR-Ocean operational center).

A series of experiments using DRAKKAR global configurations at 2° and 1/2° and have been used to evaluate DFS3, and confirmed that this forcing set produces more intense convection at high latitude, reduces significantly the freshening of the upper ocean and produces a stronger overturning. DFS3 was retained for the next DRAKKAR 50 year global experiment at 1/4° resolution, run ORCA025-G70.

4.2. Long simulations of the global variability

4.2.1. Run ORCA05-G50 : a 56 year long simulation from 1949 to 2004

This run is the first interannual experiment of the 1/2° global DRAKKAR configuration ORCA05 driven by the CORE forcing set (Large et Yeager, 2004) with 6 hourly forcing for turbulent fluxes. Although the interannual CORE forcing starts in 1958, the run was spun-up in 1949 because transient tracers begin to enter the ocean in the early 1950s. Therefore, the run starts January 1st 1949. CFC is started after 1 year (i.e. 01/01/1950), and Bomb-C14 after 6

years (01/01/1955). From 1949 to 1958, the model is driven with the forcing of year 1958 made periodic and repeated cyclically. Then from 01/01/1959 to the end of 2004, the interannual forcing is used. This run departs from the previous DRAKKAR runs (G0x to G4x series) in many aspects. It has the following characteristics:

- modified *TKE* scheme, with a 5% penetrating fraction of *tke* as recommended from our sensitivity studies
- open Torrés Strait with enhanced bottom friction (x50) and 2 islands in the strait
- modified bathymetry at the various straits, (overflow regions adapted to help BBL work)
- new runoffs provided by Mercator (Romain Bourdallé Badie, Nov. 2005)
- modified Sea-ice parameters (different from standard values)
- initial state for sea-ice deduced from January of the year 10 of run G45b
- enhanced SSS restoring in the Red Sea
- restoring to climatological SSS with a time scale of 36 days, except under sea-ice where no relaxation is applied, as in the standard DRAKKAR runs.

To follow the evolution on a year to year basis of the main characteristics of the model solution, an original monitoring system of the model integration has been developed. It produces times-series of relevant model variables like temperature and salinity drifts, MOC at given latitudes, depth averaged transport through major straits (Fig. 11), overflows at DS, FBC, GIB, etc., and many other indexes.

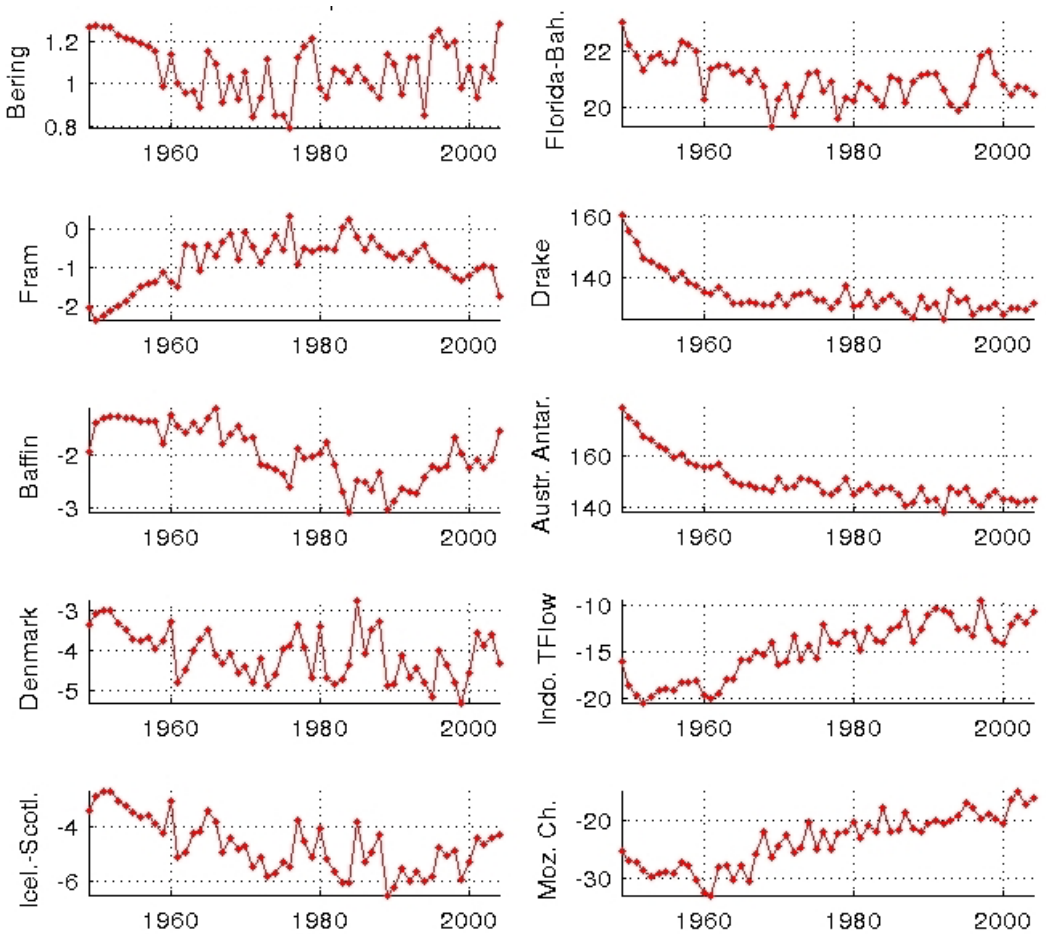

Figure 11: Run ORCA05-G50: Monitoring of the annual mean depth integrated transport (in Sv) across 10 major straits.

The analysis of the variability simulated by this experiment is presently on going and is compared to observations. Already, it has been established that the model simulates rather well the variability of the SST in the equatorial Pacific and El-Nino events (Fig. 12 & Fig. 13).

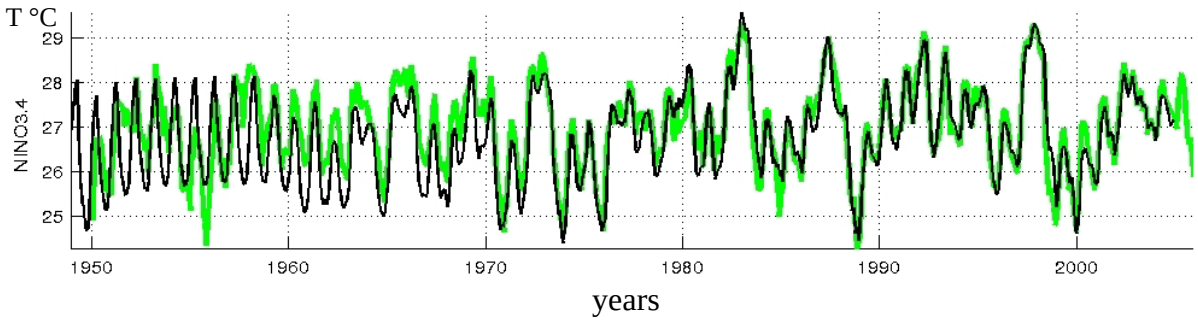

Figure 12. SST evolution in zone Nino3.4 (central equatorial Pacific) between 1949 and 2004 as simulated by ORCA05-G50 (CORE forcing). The black line is the model and the green line the observation. Passed the spin-up phase (1949-1958) when the model is driven by a repeated periodic annual forcing, one notices the remarkably good agreement between simulated and observed SST (correlation is 0.95 and bias less than 0.22°C).

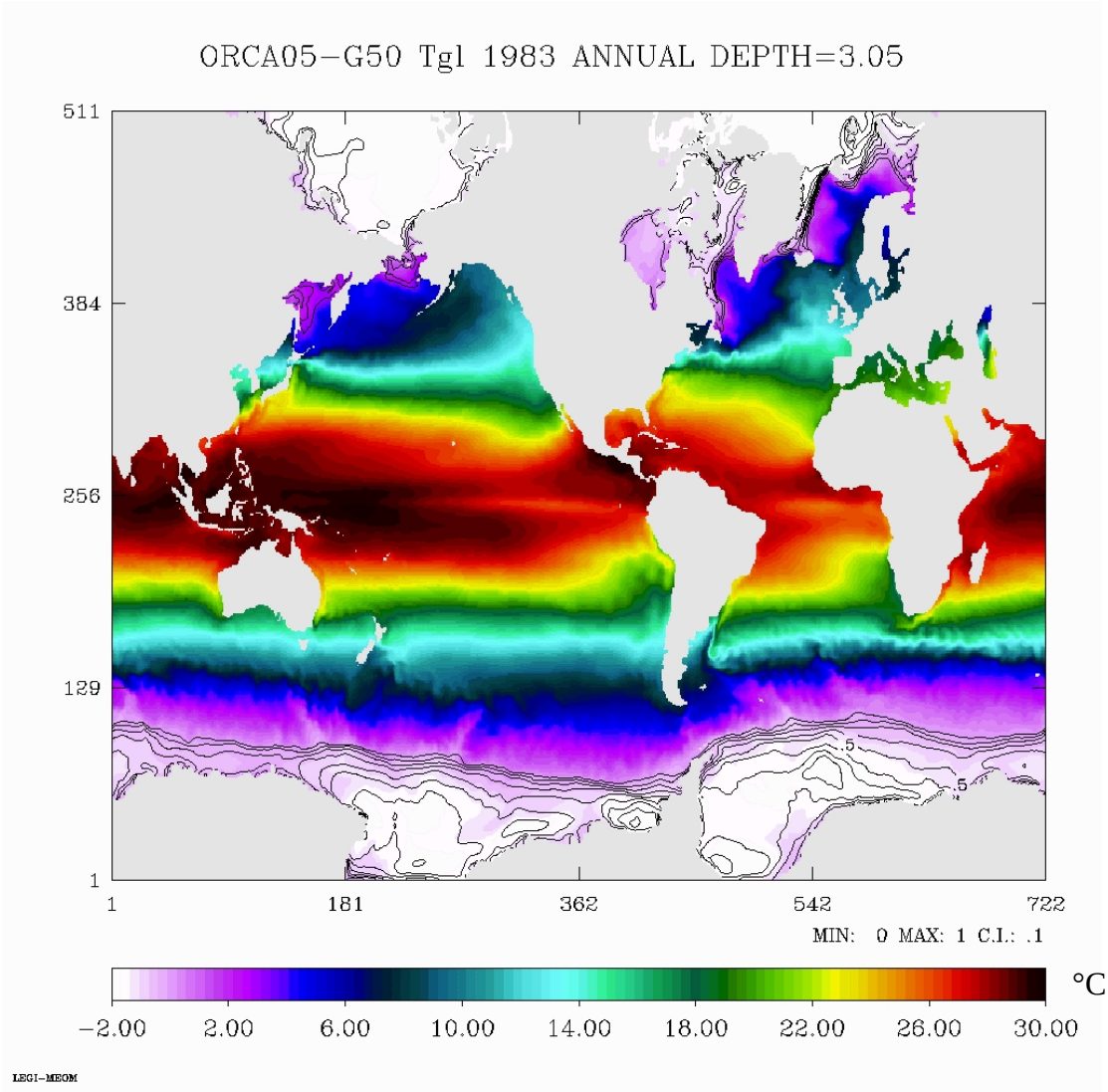

Figure 13: Annual mean SST (°C in colour) and sea-ice thickness (contour lines in meters) in 1983 (year of a strong El-Nino). Notice the warm water along Central America.

However, this experiment being the first interannual experiment using the CORE forcing, our priority was to investigate the amplitude of the meridional circulation and model drifts in order to identify flaws in the forcing which could be improved for the next simulations to come. This analysis shows a strong rise of the global sea level (Fig . 14a) going with a global freshening of the ocean at high latitudes, principally in its upper layers (Fig 14b). Deep convection in the Nordic Seas and the Labrador Sea is generally weak, and the amplitude of the Meridional Overturning Cell (MOC) is below 12 Sv in annual mean. We also noticed a progressive decrease of the overflow waters from the GIN Seas which density shifted from σ_0 = 27.8 to σ_0 = 27.6 (Fig. 14c).

The major reason for this is an excess of freshwater in the CORE forcing at high latitudes. The results motivated the construction of an hybrid atmospheric forcing combining satellite, CORE and ERA40 variables, the DRAKKAR Forcing Set # (DFS3), described in the next section.

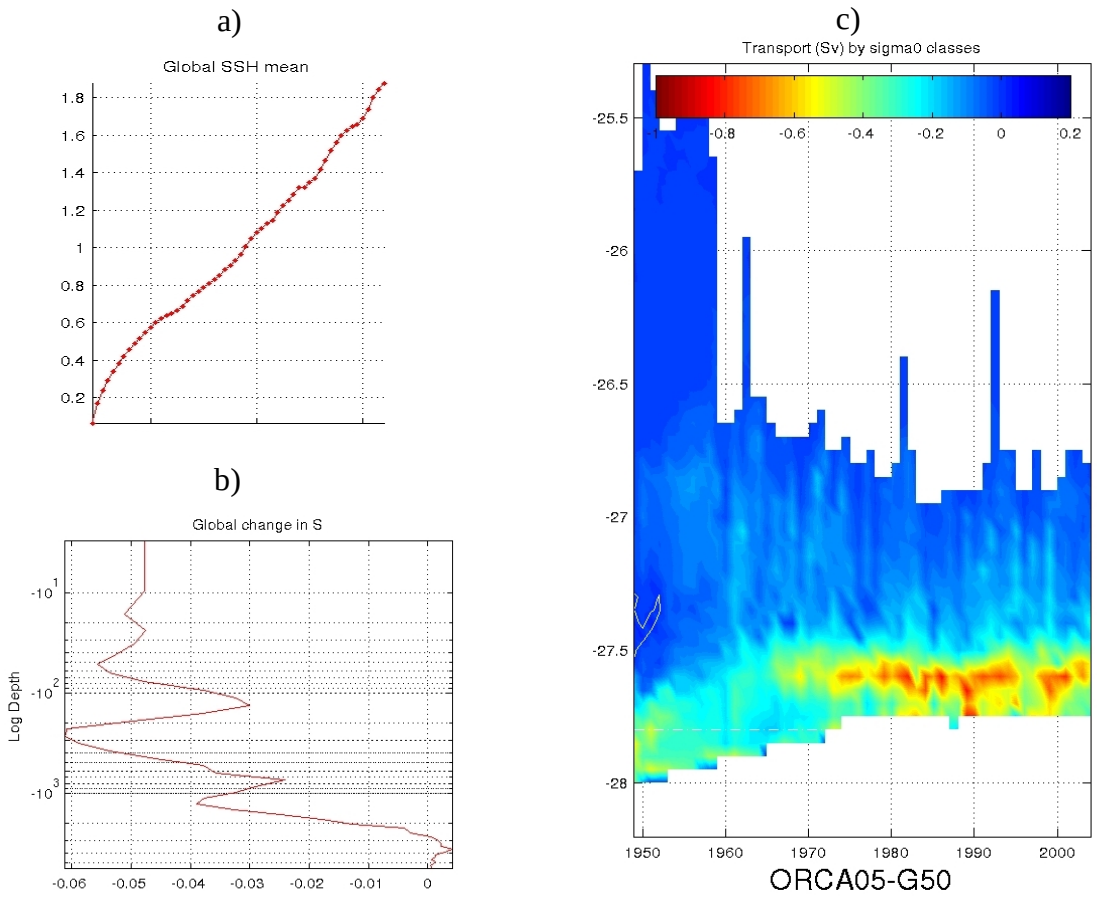

Figure148. Monitoring of ORCA05-G50. a) Evolution of the global mean sea level. The increase is 1.9 meters over 56 years. b) Horizontally averaged Salinity: difference between initial conditions and 2004 as a function of depth. Waters above 3000 m have freshened during the run, especially in the top 100 meters. c) Volume transport (in Sv) by density classes (σ_0) across Denmark Strait (negative values indicate a flow from the GIN Seas into the Atlantic). As time integration proceeds, the density of overflow water decreases. In 1972, overflow waters are always lighter than 27.8 (the white dashed line). In 1974, most overflow waters have a density of 27.6, but significant interannual variability is noticeable.

4.2.2. ORCA025-G70: a 47 year long simulation from 1958 to 2004

This run is the first interannual experiment carried out with the 1/4° global DRAKKAR configuration ORCA025. It is driven by the DFS3 forcing described above, which differs from the CORE forcing used previously by the use of ERA40 6 hourly variables in the calculation of the turbulent fluxes, a reduction of precipitation north of 30°N and a correction for the katabatic winds in Antarctica. Differently to the previous run ORCA05-G50, we applied a relaxation to SSS climatology under sea-ice. The model starts from rest on January 1st 1958, with initial conditions from Levitus (1994) climatology for T,S. CFC and BombC14 calculation is started after one year of spin-up on January 1st 1959 with as initial condition the concentration from run ORCA05-G50 at this date. Details about the set-up of this experiment are given in a report by Molines et al. (2006). The run is presently in year 2003. Most flaws noticed in the previous run have been significantly corrected. The *ssh* trend, as well as the tri-dimensional T and S trends, has been considerably reduced, deep convection is strong in winter in the GIN and Labrador Seas, and the maximum amplitude of the MOC remains around 16/17 Sv during the duration of the experiment. We also notice the good depth of the Mediterranean water outflow, thanks to the use of a local relaxation, and the persistence of overflow waters denser than σ_0 = 27.8 in Denmark Strait and the Faroe Channel (Figure 15).
A overview of this simulation will be published (in French, Molines et al., 2006) in the next newsletter of the IDRIS computational centre where all model calculations mentioned in this report have been performed. The content of this newsletter is attached at the end of this report.

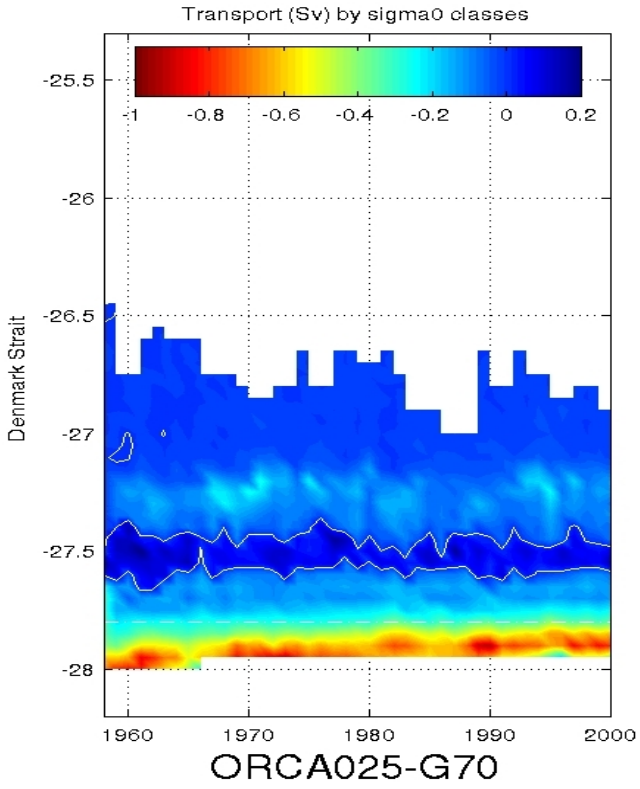

Figure 15. Monitoring of ORCA025-G70. Volume transport (in Sv) by density classes (σ_0) across Denmark Strait (negative values indicate a flow from the GIN Seas into the Atlantic). As time integration proceeds, the density of overflow waters slightly decreases, but remains denser than 27.8 (the white dashed line). Significant inter-annual variability is noticeable in the amplitude of the overflow.

The ERA40 reanalysis stops in early 2002. The first part of the ORCA025-G70 has been carried out until the end of 2001, and we have switched to a new forcing set for years 2002-2004. The CORE radiative fluxes and precipitations are still used through the end of 2004. The other forcing variables are taken from the ECMWF operational analysis (ECMWF hereafter) provided through a partnership with MERCATOR-Ocean. We have verified a good continuity of the wind, and to a lesser degree air temperature between the two datasets. On the other hand, the air humidity differs considerably between ERA40 and ECMWF, operational analysis producing

significantly dryer air (0.3 g/kg) in the 20°N-20°S latitude band. We have reasons to believe that the ECMWF humidity is more realistic (ERA40 is known to be biased high), so we have applied no correction. Users of the ORCA025-G70 experiments are warned that this discontinuity in the forcing may results in spurious interannual variability between 2001 and 2002 in the tropics.

4.2.3. Analysis of model simulations with regard to observations

Runs ORCA05-G50 and ORCA025-G70 are presently being analysed. An important effort is carried out at LEGI (T. Penuff and M. Juza) to confront these model results to observations over the same period. Tools have been developed which permit to collocate model output with observation of the ENACT/ENSEMBLES (including CTDs, TAO moorings, XBTs and ARGO data) and AVISO data bases. This permit to carry out collocated model/observation comparisons with advanced statistical methods. This activity is just starting, and an example is shown below (Fig. 16).

a) 1/4° run ORCA025-G70

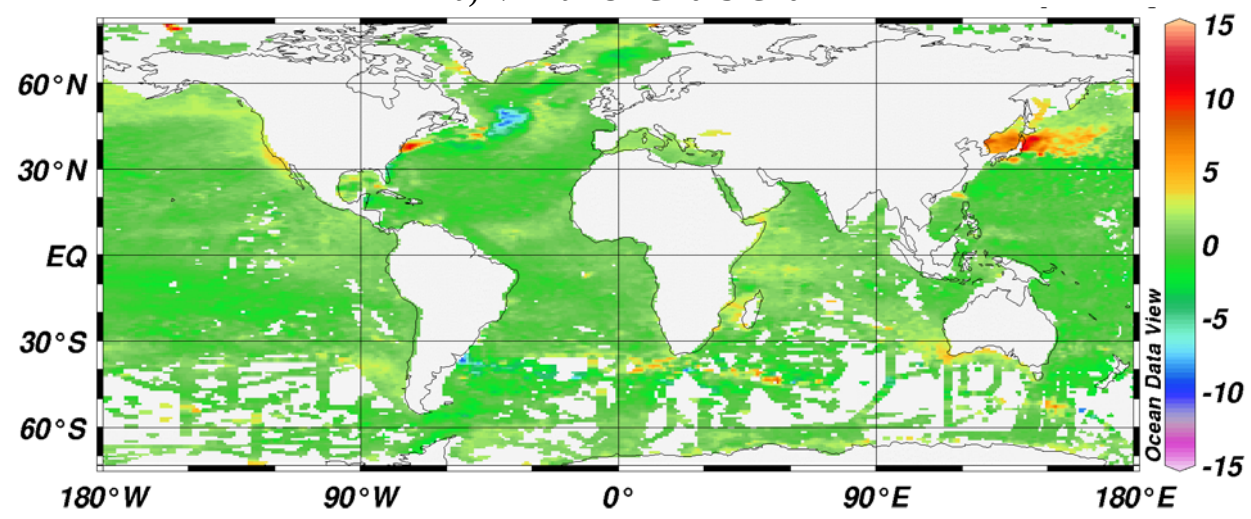

b) 1/2° run ORCA05-G50

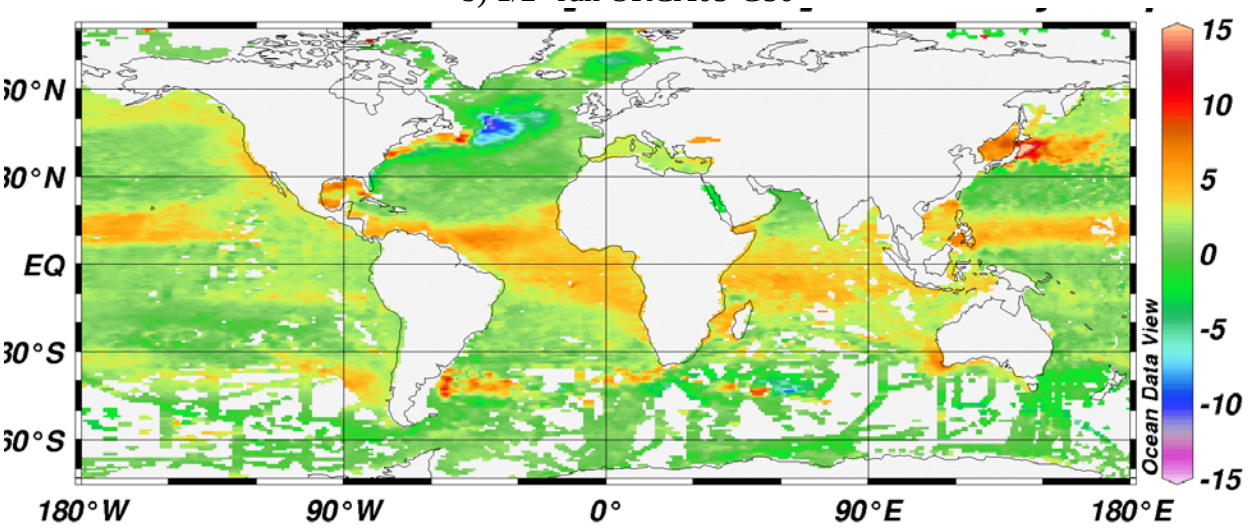

Figure 16: Difference in ocean heat content integrated from 50 m to 450 m between collocated model and hydrography during the period 1980-1995. a) The model is the 1/4° ORCA025-G70 experiments, and b) the model is the 1/2° ORCA05-G50 experiment. Despite significant biases remaining in the Kuroshivo and the Gulf Stream/NAC regions, the integrated heat content is significantly closer to observations in the 1/4° simulation.

4.3 Dynamics of the Southern Ocean

Our studies in the Southern ocean have started at the beginning of 2005 with the PhD of Pierre Mathiot, in collaboration between LEGI and LGGE, with the objective of studying the effect of the katabatic winds on the formation of sea-ice and water masses. A second project, started in 2005 in collaboration Australian colleagues, is aimed at understanding better the dynamics of the Antarctic circumpolar current and the variability of water mass formation in the Southern ocean. The latter was also the central theme of the project presented by Julien le Sommer at CNRS in 2006 (Julien is now CNRS scientist at LEGI, currently on leave at the University of New South Wales).

4.3.1. Correction for Katabatic Winds

It has been shown that in the Antarctic, ERA40 has katabatic winds of small amplitude (Mathiot, 2005). A dowscaling of ERA40 winds has been performed by H. Gallée (LGGE) with a regional model of the Antarctic atmosphere (MAR model) over a 10 year period (1980-1989). The comparison of ERA40 and MAR winds at the coast around the continent showed that MAR winds have greater amplitude. A correction factor, define by the mean slope of the scatter plot of Fig. 17a, has been applied to correct ERA40 winds near the coast (Fig. 17b, the details of the correction method is not given here, PhD thesis of P. Mathiot).

Several 10 year long simulations were carried out with the 1/2° Southern Ocean DRAKKAR configuration with both corrected and uncorrected ERA40 winds. They show (Fig.18) that the correction of katabatic winds increases the amplitude and extent of coastal polynia (thinner sea-ice) and that colder and saltier waters are produced around Antarctica, which T,S properties compare better with observations.

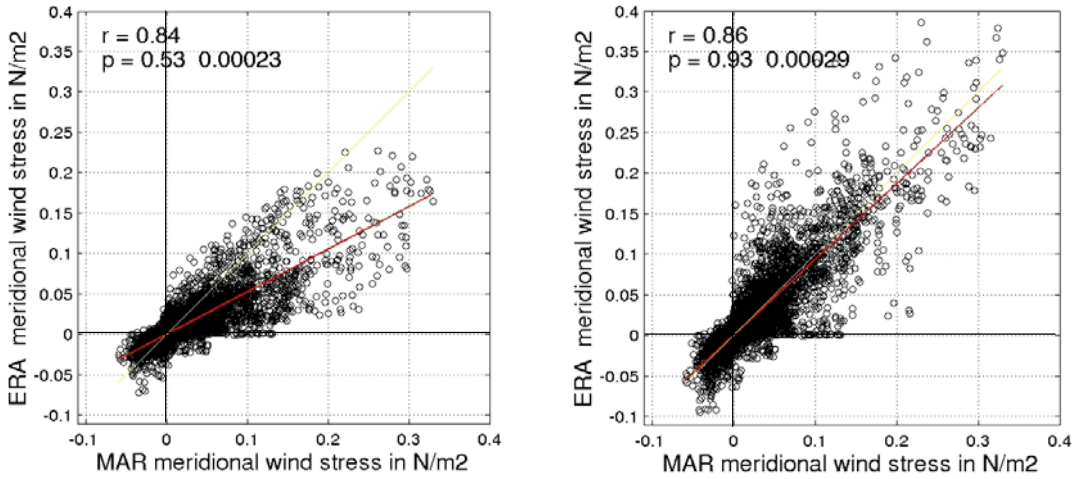

a) b)

Figure 17: Scatter plots comparing the meridional wind component of MAR and ERA40 at the coast around the Antarctic continent (the comparison of the zonal component, not shown, gives very similar results). a) The raw fields are compared. Correlation (r = 0.84) is rather good, indicating good consistency of wind direction between data sets. In term of amplitude, ERA40 winds are generally weaker, by almost a factor of 2 in average. b) Comparison after correction of ERA40 winds. Correlation (r = 0.86) is slightly increased, and the amplitude bias is now less than 10%.

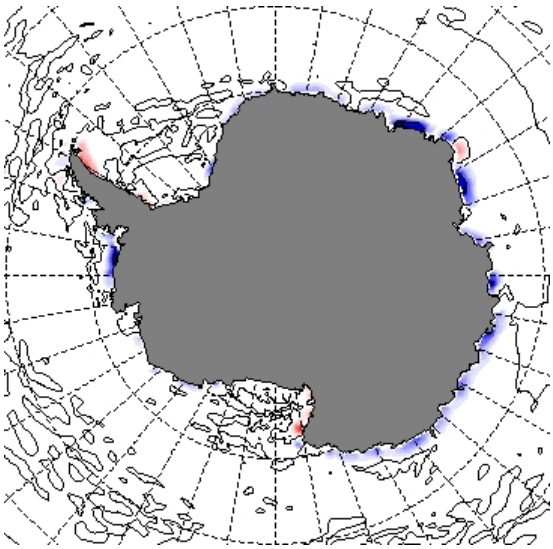

Figure 18: Difference in the time mean zonal wind stress between corrected ERA40 and uncorrected ERA40. Blue areas indicate strong eastward winds. The picture is obtained with the meridional component indicate stronger northward wind in theses areas in corrected ERA40. These regions are regions of known katabatic winds. The correction vanishes offshore over about a 100 km.

4.3.2. Antarctic circumpolar ocean dynamics

This work is based on the global 1/4° DRAKKAR model and has been initiated during a 4 month stay of A.M. Treguier in Australia from october 2005 to march 2006. It is a collaboration with M. England (University of New South Wales, Sydney) and S. Rintoul (CSIRO, Hobart), financed by a PAI (FAST-DEST program) and the ARC (Australian research council).

The Antarctic circumpolar current (ACC) which flows around Antarctica without encountering continental barriers, is the prominent feature of the Southern Ocean. Due to its geometry, the ACC has often been compared with the atmospheric jet stream and studied in a "zonal mean" framework. The ACC path is strongly influenced by continental masses, however. This is shown in Fig.19 where the ACC extension is indicated by black contours (time-mean barotropic streamlines). Ivchenko et al (1996) were the first to study the ACC dynamics following streamlines, and they showed that zonal means underestimate the contribution of transient eddies to the dynamics. All recent theories of the ACC are based on an analysis following streamlines (for example, Marshall et Radko, 2003). Those theories are based on a simplified density equation: the purpose of our work is to assess the validity of those simplifications in the ORCA025 model. One key contribution to the density balance is the atmospheric forcing (Fig 19a). In the model the ACC gains buoyancy (average negative flux in Fig.19) because the freshwater input dominates the cooling contribution. There is a large cooling region in the south west pacific that coincides with deep surface mixed layers (Fig.19b).

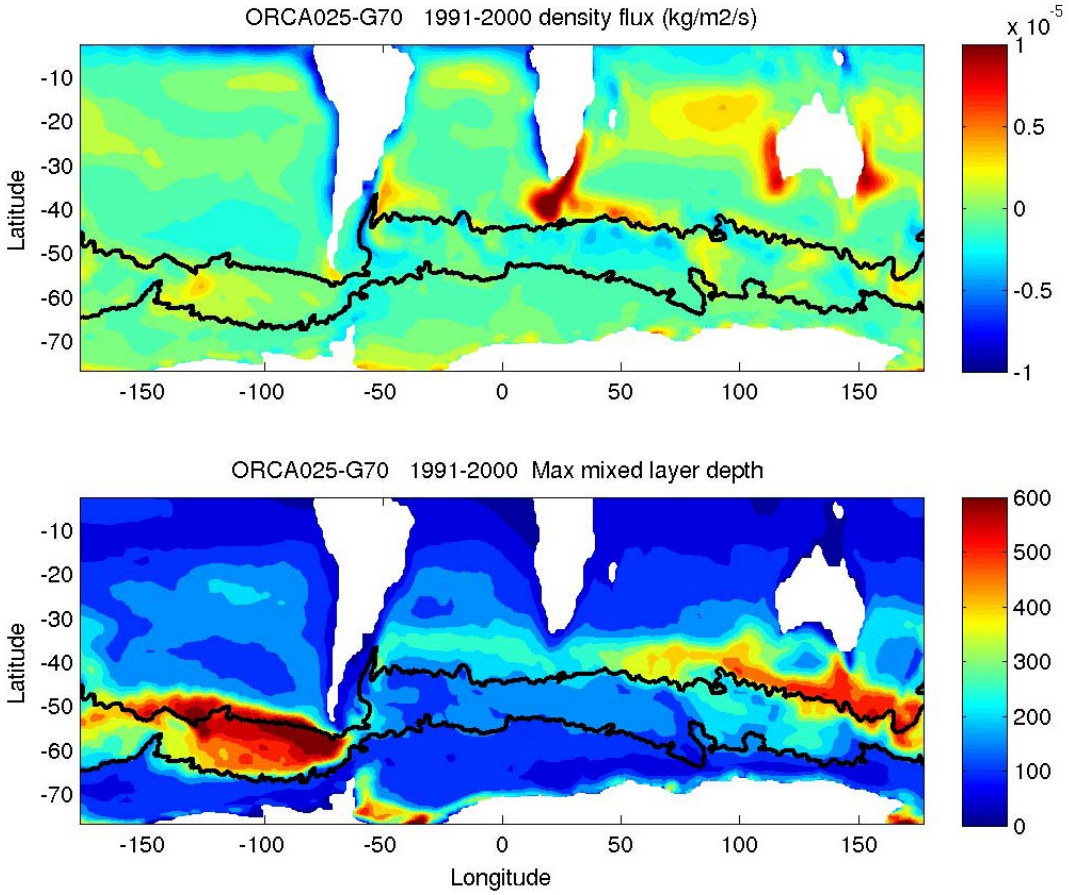

Figure 19: Density surface flux (top) and maximal mixed layer depth (bottom) for the global 1/4° DRAKKAR model, years 1991 to 2000. The ACC is defined by the two black contours (baroitropic streamfunction lines going through Drake Passage).

Just considering the streamline geometry suggests a more complex equilibrium than assumed by theories. All streamlines "climb" onto continental slopes like the Falklands or the Kerguelen islands, and all cross regions of deep mixed layers. It is thus impossible to define (in the streamline-averaged sense) a range of depths situated below the mixed layer and above topographic influences and where a compensation between mesoscale transient fluxes and the Ekman flux could apply. We provide pictures of the streamline-averaged ACC (Fig20): neither alongstream velocity nor velocity variance show multiple fronts, that are prominent features of sections at any longitude. This happens because streamlines get together in various choke points like Drake passage and therefore continuous, distinct fronts can only be defined in individual basins, not in the circumpolar average. This work continues with the consideration of the density balance and eddy fluxes.

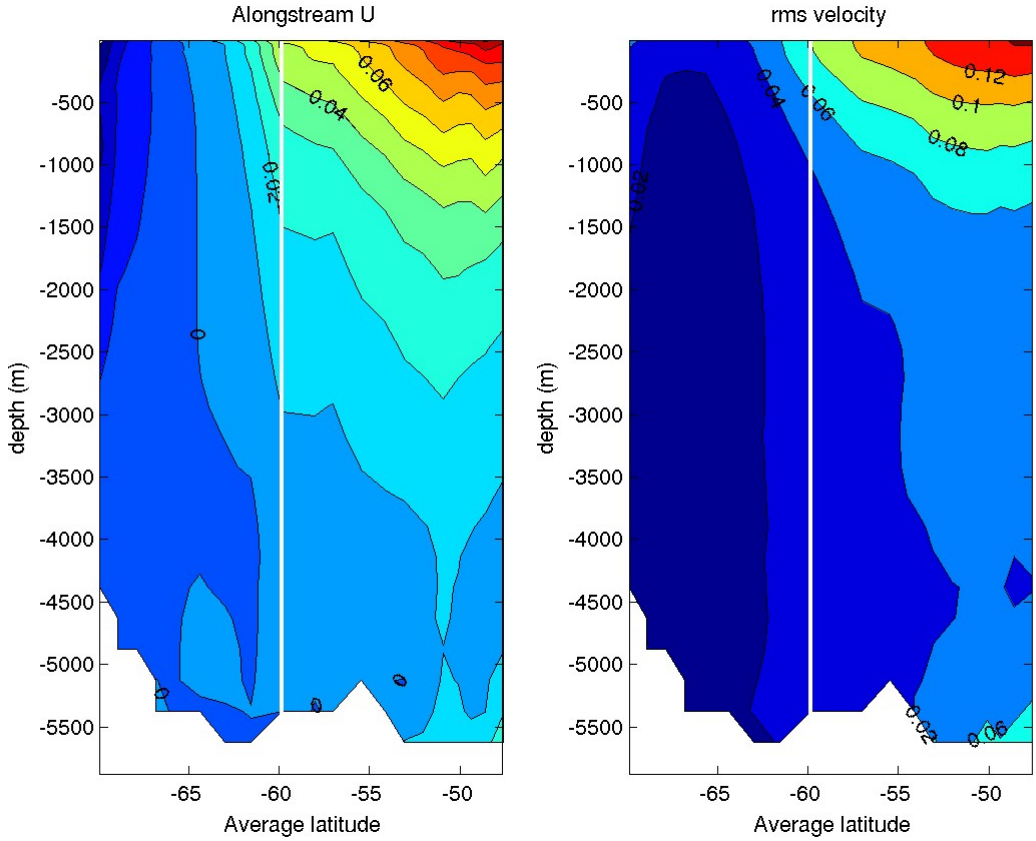

Figure 20: Circumpolar average of alongstream velocity profile (left) and rms velocity (right). The coordinate is the average latitude of each streamline. The white line is the southernmost streamline of the ACC. The picture has been extended southwards to sample all the southern ocean, by linearly interpolating between the southern extension of the ACC and the coastline.

Another collaboration has been developed with Gary Froyland, school of mathematics, at the university of New South Wales. This project, financed by ARC (Australian research council) with the participation of A.M. Treguier and J. Le Sommer, aims at characterizing fronts and mixing with original mathematical methods. A paper using the global 1/4° DRAKKAR model has been submitted (Froyland et al, 2006).

References:

Froyland G., K Padberg, M. H. England, A. M. Treguier, 2006: Detection of coherent oceanic structures via transfer operators, submitted to phys. rev. letter.

Ivchenko, V.O., K. Richards and D. P. Stevens, 1996: The dynamics of the Antarctic circumpolar current. J. Phys. Oceanogr., 26, 753-774.

Marshall, J. and T. Radko (2003) Residual mean solutions for the Antarctic Circumpolar Current and its associated overturning circulation. J Phys. Oceanogr. 33 (11): 2341-2354

4.4. Regional model configurations

Many scientific objectives of the DRAKKAR project require regional configurations. The first regional configuration to be set up was NATL4, covering the North Atlantic and Nordic seas (Theetten, 2004). So far this configuration has been implemented with closed boundaries. It has been used for extensive tests that are not detailed in the present report: for example tests of

forcing fields (report by F. Nicolas, 2005) or effects of topography and parameterizations on the overflows (report by R. Almar, 2005). NATL4 has been used for modelling the isotopic composition of Neodymium, in collaboration with scientists at LEGOS and LSCE (section 4.4.1). It has been adapted to support AGRIF zooms (development of the AMEN configuration, section 4.4.2).
Two other regional configurations, with open boundaries, are being used within the DRAKKAR team. The first one is ITF025, a 1/4° local model of the Indonesian throughflow (PhD of A. Koch Larrouy, LOCEAN, section 4.4.3) and the second one is a 1/12° model of the Gulf of Guinea (PhD of C. Guiavarch, LPO, section 4.4.4).

4.4.1. AMEN configuration (Atlantic Mode water in Embedded model using Nemo/agrif)

This work is aimed at the study of the formation and subduction of subpolar mode water (SPMW), and especially the influence of mesoscale turbulence and direct atmospheric forcing. The properties of subtropical mode waters are correlated with the atmospheric North Atlantic Oscillation (NAO); we want to find out whether similar correlations exist with the properties of SPMW. The numerical model complements studies based on observations of ARGO floats and OVIDE hydrography (Thierry et al, 2006).
The AMEN model configuration is based on NATL4, with a grid refinement between the North Atlantic current and the Azores front, between 0°W and the mid-Atlantic ridge. The grid refinement is based on the new parallel version of the AGRIF code implemented in NEMO (L. Debreu, J.M. Molines). A lot of preliminary work has been necessary in 2005 and early 2006 to validate this new code and to ensure its portability on different machines.

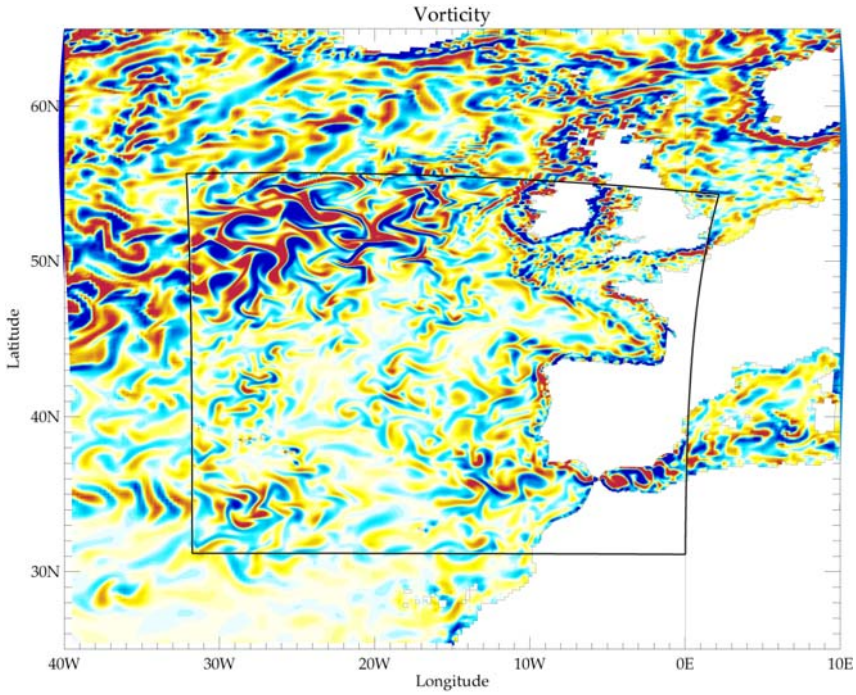

Figure 21: Snapshot of the upper ocean relative vorticity field in the AMEN configuration, featuring the 1/4° NATL4 with a grid refinement at 1/12° with AGRIF in the intergyre zone (marked by the square box).

For an accurate representation of mode waters and flow-topography interaction we use a refined vertical grid (64 levels instead of 46 in previous DRAKKAR configurations). This grid has been designed in concertation with colleagues at the National OCeanography Centre in Southampton; it is very similar to the grid curently used in the OCCAM model. The bathymetry and the runoff

data are extracted from the NATL12 1/12° configuration of MERCATOR-ocean, which covers the same domain as NATL4. The preparation of bathymetry and initial conditions requires special care to ensure compatibility of the refined region with the rest of the domain. This is performed by a software package called "nesting tools" developed by L. Debreu et al. As the first users of this package we have contributed to its development. The AMEN configuration is running on 64 processors of the IBM zahir at IDRIS; a few years of experiment and a validation will be performed before the end of 2006.

4.4.2. Simulation of the isotopic composition of Neodymium.

Drakkar was not leader in this study, but A.M. Treguier contributed to the simulations. This is an example of cooperation with associated scientists. (S. Peronne, T. Arsouze, A.M. Treguier, C. Jeandel, F. Lacan, JC Dutay).

The oceanic water masses differ by their temperatures, salinity, but also a number of geochemical tracers characterized by their weak concentrations and their ability to quantify oceanic processes (mixing, scavenging rates etc…). Among these tracers, the Nd isotopic composition (hereafter ε_{Nd}) is a (quasi) conservative tracer of water mass mixing in the ocean interior, far from any lithogenic inputs. It has been recently established that exchange of Nd at the oceanic margins could be the dominant process controlling both its concentration and isotopic composition distributions in the ocean. This has been confirmed using the low resolution global ORCA2 model (Arsouze et al., 2006). However, the currents flowing on the ocean margins are not correctly represented in ORCA2, especially in the North Atlantic ocean. The North Atlantic is of particular interest since *i)* it is the area of deep water formation and *ii)* these deep waters are characterized by the most negative ε_{Nd} values of the world ocean, which are used as “imprint” of the present and past thermohaline circulation. It is therefore essential to understand how these water masses acquire their ε_{Nd} signature.

During a 5-month internship at LPO-Brest, Simon Peronne has used the method of Arsouze et al (2006) to calculate the distribution of ε_{Nd} in the DRAKKAR model configuration NATL4. This method is based on a very simple model of the modification of ε_{Nd} by interaction at the ocean margins, without a complete modelling of the neodymium concentration itself (this would require a full carbon cycle model). First, two 20-years "on-line" experiments have been run. Longer experiments being required to equilibrate the concentration, we have used the dynamical fields of one of these experiments to perform a 150 years "offline" simulation. The new version of TOP (the tracer component of NEMO) has been used, and we have found necessary to modify the input/output strategy to run efficiently on 54 processors of the Zahir machine at IDRIS.

Simulated ε_{Nd} distributions have been compared to the present-day data base, vertical profiles, and the results of the low resolution model ORCA2. The eddy permitting model generally provides improved results, when a high enough exchange rate of ε_{Nd} is imposed in the deep ocean. Deficiencies of the simulated distribution in the Nordic Seas and the subpolar gyre are explained by errors in the input function on the margins of the Iceland-Scotland Ridge and south of Iceland. The model does not account for all the complexity of the ε_{Nd} profiles observed downstream of Denmark Strait and in the Labrador Sea. This is partly due to the representation of the deep western boundary currents, still marginally resolved in this eddy-permitting model.

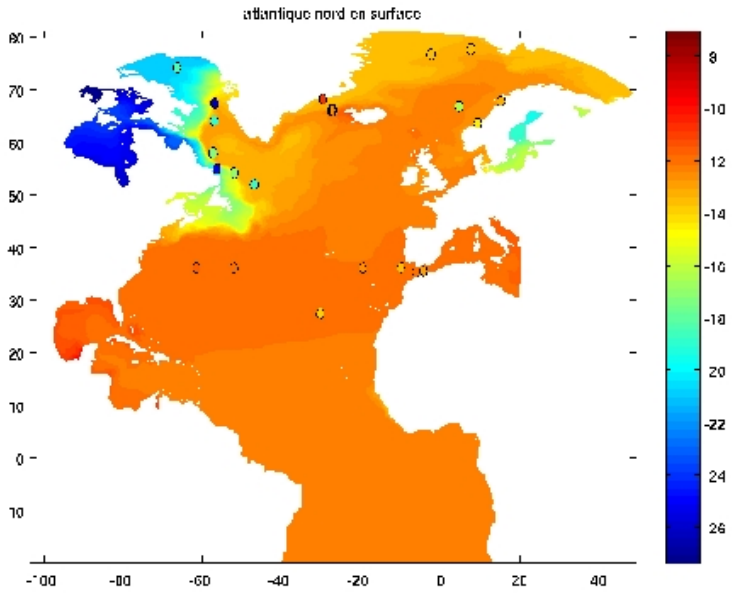

Figure 22: Neodymium isotopic composition ε_{Nd} (it is a dimensionless number), after a 150 year offline experiment with the NATL4 model. The field is mapped at the surface, and compared with recent observations indicated by circles. The model reproduces low values in the Labrador current, and the ε_{Nd} in the subtropical gyre is much more realistic than with the ORCA2 model.

4.4.3. Water mass transformations in the Indonesian throughflow

This study is the topic of the PhD of Ariane Koch-Larrouy, working with Gurvan Madec at LOCEAN, Paris. The first aim was to examine the influence of mixing parameterizations and especially tidal mixing on the properties of the water masses that cross the Indonesian Throughflow. A regional configuration with open boundaries (ITF025) has been set up in order to be able to run a large number of sensitivity studies. The configuration is extracted from the global DRAKKAR configuration and uses the same grid. It is forced at the boundaries by outputs of ORCA025, with slight modifications of the temperature and salinity of some input water masses. Preliminary studies have shown the need for adjustments of the bathymetry (figure...) that have led to considerable improvements of the circulation. The total transport of the throughflow has not changed, but the repartition of the flow across the different passages has become much more realistic.

Even after those improvements, the ITF025 configuration failed to reproduce the intense mixing that is observed in the region. The incoming warm Pacific waters undergo strong transformations that have been attributed to internal tides that are confined within this semi-enclosed area. A specific parameterization has been built to mimic this process. The power converted from barotropic tides into baroclinic tides is constrained by tidal model results while the vertical dependency of energy dissipation is inferred from a 2D internal tide generation model. The model is significantly improved in most of the Indonesian basins, which suggests that the spatial distribution of the eddy diffusivity is adequately prescribed by the new parameterization. These results are described in a paper submitted to Geophysical Research Letters (Koch Larrouy et al, 2006).

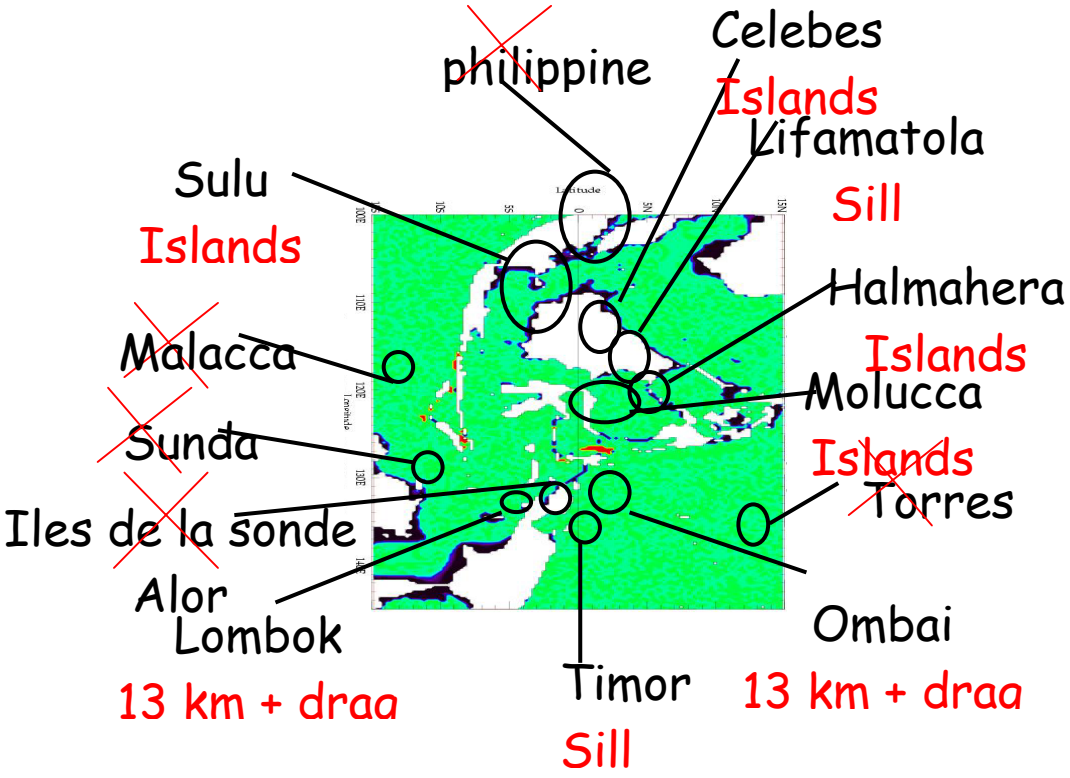

Figure 23: Schematics of the adjustments made to the grid and topography of the global 1/4° model in the ITF region. Some passages have been closed (red cross), islands have been restored, sill depths have been adjusted, the grid width and lateral friction drag have been modified in some places.

4.4.4. Modelling biweekly oscillations in the Gulf of Guinea

This study is the topic of the PhD of Catherine Guivarc'h, supervised by A.M. Treguier and A. Vangriesheim at LPO. The aim is to understand the origin of biweekly current oscillations that have been observed on the continental slope off Angola at 1300m depth (Vangriesheim et al, 2005). We have found that a high resolution model (1/12° grid and 70m thick layers near the bottom) greatly improves the representation of the currents trapped to the topography. The GUINEA model configuration is forced at the boundaries by another regional configuration, NATL4; this allows us to use the same forcing for both the large scale and the local model and to generate daily boundary data. The main result of the study is that 95% of the biweekly energy found at the observation site is due to equatorial yanai waves that propagate eastward to the African coast and then south. The Yanai waves are forced by equatorial winds. The map of rms velocity at 1160m (Figure) represents well this phenomenon, and underlines the large assymetry between the amount of energy propagating north and south along the coast. This effect is mainly due to the coastline geometry. Two publications are in preparation.

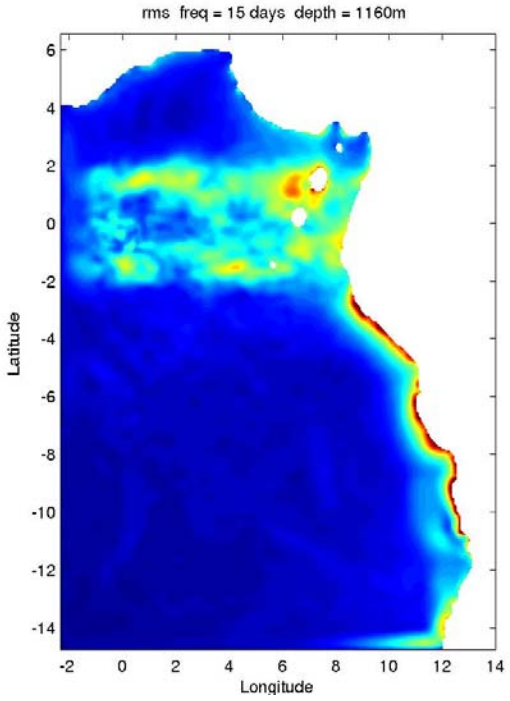

Figure 24: rms velocity for periods close to 15 days in the GUINEA model at 1160m depth. The energy near the equator is due to Yanai waves. The energy concentrates along the coast as the waves propagate south as coastal trapped waves (similar to coastal Kelvin waves).

reference:

Vangriesheim A., A.M. Treguier, and G. Andre, 2005: Biweekly current oscillations on the continental slope of the Gulf of Guinea. Deep Sea Res., 52,11, 2168-2183.

4.5. Studies carried out with Associate Scientists

We present here the abstract of several studies carried out in a close cooperation between Associated Scientists and the DRAKKAR project.

4.5.1. Transient Tracers

Off line calculations of the global ocean distributions of CFC-11, CO2 and Δ14C using ORCA2 and ORCA05 outputs have been performed at LSCE (Lachkar, Orr) to ask what role do eddies play in ocean uptake, storage, and meridional transport of transient tracers. We made global anthropogenic transient tracer simulations in non-eddying (2°cosϕ×2°, ORCA2) and eddying (1/2°cosϕ×1/2°, ORCA05) versions of the ocean general circulation model OPA9. We focus on the Southern Ocean where tracer air-sea fluxes are largest. Eddies have little effect on global and regional bomb $\Delta^{14}C$ uptake and storage. Yet for anthropogenic CO_2 and CFC-11, increased eddy activity reduces southern extra-tropical uptake by 28% and 25% respectively. There is a similar decrease in corresponding inventories, which provides better agreement with observations. With higher resolution, eddies strengthen upper ocean vertical stratification and reduce excessive ventilation of intermediate waters by 20% between 60°S and 40°S. By weakening the Residual Circulation, i.e., the sum of Eulerian mean flow and the opposed eddy-induced flow, eddies reduce the supply of tracer-impoverished deep waters to the surface near the Antarctic divergence, thus reducing the air-sea tracer flux. Consequently, inventories for both CFC-11 and anthropogenic CO_2 decrease because their mixed layer concentrations in that region equilibrate with the atmosphere on relatively short time scales (15 days and 6 months, respectively); conversely, the slow air-sea equilibration of bomb $\Delta^{14}C$ of 6 years, gives surface waters little time to exchange with the atmosphere before they are subducted.

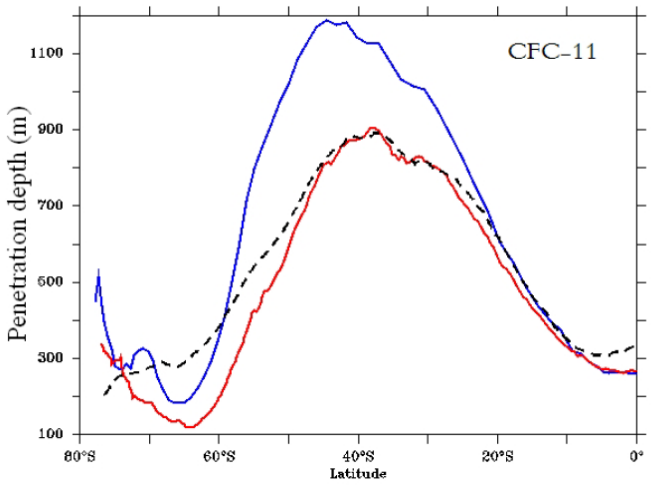

Figure 25: Zonal mean of CFC-11 penetration depth (in m) as observed (black dashes, GLODAP) and as simulated by the eddying (red) and the non-eddying (blue) model over the Southern Hemisphere. The penetration depth of a tracer is defined as the tracer inventory divided by its surface concentration (after Lackhar et al., 2006).

4.5.2. Ensemble study of the vertical transmission of atmospheric induced temperature anomalies

DRAKKAR was not leading this study carried out by M. Lucas and N. Ayoub during their stay at LEGI. Interaction with the DRAKKAR team has been very strong, in Brest and Grenoble, around the NATL4 configuration, and the interpretation of the results. This is an example of a good cooperation with associated scientists.

The penetration of atmospheric forcing into the ocean is a fundamental issue in physical oceanography and climate research. In this study, we use a ensemble method with fifty 7-months (September to March) primitive equation ¼° integrations to investigate the processes that control the vertical transmission of the atmospheric signal into the ocean, focusing principally on its impact on the upper oceanic temperature field. The ensemble is generated by perturbing the wind, atmospheric temperature and incoming solar radiation of the ERA40 reanalysis. Each perturbation consist of a random combination of the first twenty EOFs of the difference between the ERA40 and NCEP/CORE reanalysis data sets. The ensemble standard deviation of various interfacial and oceanic quantities is then examined in the upper 200 metres of 3 distinct regions of the North Atlantic: the Gulf stream, the equatorial band and the North east Atlantic. These show that even a very small perturbation can lead to significant changes in the ocean properties and that regions of oceanic mesoscale activity are the most sensitive. The transmission is driven by the vertical diffusivity and the eddy activity. The role of subsurface currents is also crucial in carrying the eddy signal away from the regions of mesoscale activity. Finally, the decorrelation time scale of the mesoscale activity is critical in determining the amplitude of the oceanic response.

4.5.3. Agrifmex

To develop and validate the MPI version of the new AGRIF grid refinement package, an application has been made (PhD of J. Jouano) in cooperation with CICESE at Ensenada in Mexico (J. Sheinbaum, J. Candela). The NATL3 configuration inherited from CLIPPER (similar to NATL4 but extending only to 70°N and with a resolution of 1/3°) is used. The configuration has been updated to NEMO. A grid refinement to 1/15° using the new MPI version of AGRIF is applied to the Caribbean Sea and the Gulf of Mexico (CARIB15, Fig. 26). This configuration is referred to as AGRIFMEX.

The objective is to identify the main source of the Caribbean Eddies: are they the continuity of the North Brazil Current eddies after they pass through the lesser Antilles, or are they locally generated by Baroclinic instability. This study requires both a high resolution in the Caribbean Sea to resolve instability processes, and a correct representation of the remote forcing by the tropical Atlantic ocean. The grid refinement approach in an Atlantic model configuration thus appear quite well suited. The AGRIFMEX configuration was first implemented at the IDRIS computer centre, then on the PC cluster of CICESE. Results from model simulation show that the relevant dynamical processes are well simulated by the model (Fig. 26), and suggest that the local baroclinic instability is a major driver of the Caribbean Eddies (Fig. 27).

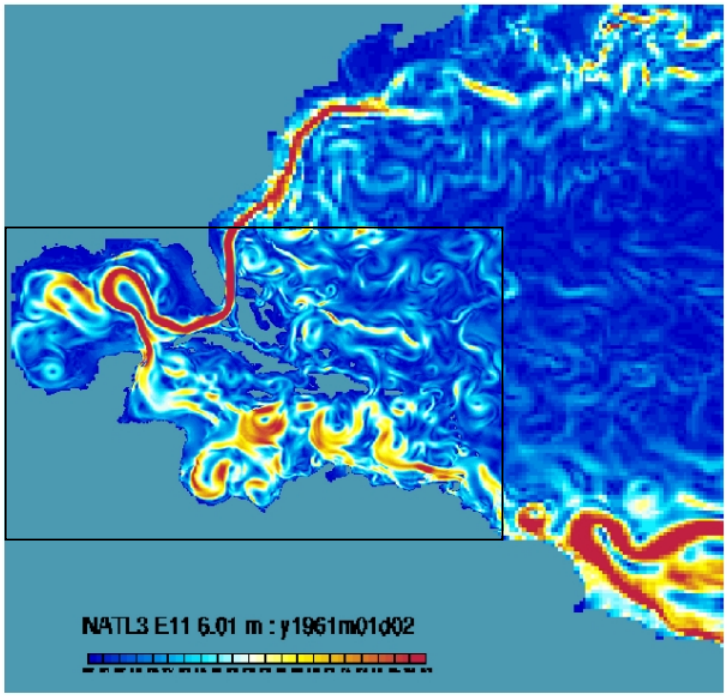

Figure 26. Snapshot of current velocity in the AGRIFEX configuration (yellow colour indicate velocities of 40 cm/s, and red colour velocity of 70 cm/s or higher). The area refined to 1/15° is the black rectangle. Outside, the resolution is 1/3°, a resolution which allows the generation of NBC eddies. Large eddies can be seen in the Caribbean Sea.

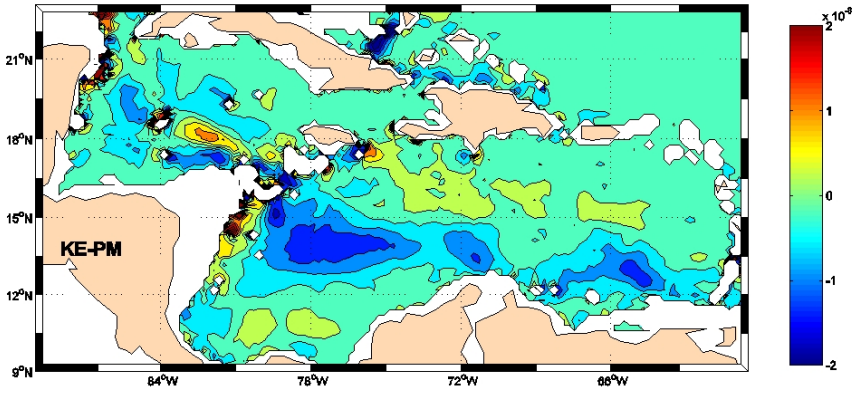

Fig. 27: Rate of baroclinic energy conversion (i.e. transfer between mean potential energy (mpe) and eddy kinetic energy (eke) between 80 m and 280 m). Negative values indicate that baroclinic instability extract eddy energy from the mean stratification. This term being dominant in the energy balance, suggests that the local instability plays a major role in the growth of the Caribbean Eddies.

5. DRAKKAR Publications in 2006

Peer Review Journals

Barnier B., G. Madec, T. Penduff, J.-M. Molines, A.-M. Treguier, J. Le Sommer, A. Beckmann, A. Biastoch, C. Böning, J. Dengg, C. Derval, E. Durand, S. Gulev, E. Remy, C. Talandier, S. Theetten, M. Maltrud, J. McClean, and B. De Cuevas, 2006: Impact of partial steps and momentum advection schemes in a global ocean circulation model at eddy permitting resolution. Ocean Dynamics, Vol 4, DOI 10.1007/s10236-006-0082-1.

Béranger K., B. Barnier, S. Gulev and M. Crépon, 2006 : Comparing twenty years of precipitation estimates from different sources over the world ocean. Ocean Dynamics, Vol. 56-2, 104-138, DOI: 10.1007/s10236-006-0065-2 2006.

Gulev S.K., Barnier B., Molines J.-M., and Penduff T., 2006: Impact of spatial resolution on simulated surface water mass transformation in the Atlantic. Ocean Modelling, submitted.

Koch-Larrouy A., G. Madec, P. Bouruet-Aubertot, T. Gerkema, L. Bessières, and R. Molcard, 2006: On the transformation of Pacific Water into Indonesian ThroughFlow Water by internal tidal mixing, submitted to *Geophysical Research Letters*.

Lachkar Z., J. C. Orr, J.-C. Dutay, and P. Delecluse, 2006: Effects of mesoscale eddies on global ocean distributions of CFC-11, CO2 and Δ14C. *Ocean Sciences*, in révision.

Le Sommer J, Penduff T, Madec G (2006) How momentum advection schemes affect current-topography interactions in the DRAKKAR 1/4-degree z-coordinate model. Submitted to Ocean Modelling;

Lucas M., N. Ayoub, B. Barnier, T. Penduff, and P. de Mey, 2006: Vertical transmission of the atmospheric induced temperature anomaly: an ensemble study. To be submitted to Ocean Modelling.

Penduff T., J. Le Sommer, B. Barnier, A-M. Treguier,, J-M. Molines, and G. Madec, 2006: Depth-dependant effects of momentum advection, sidewall boundary conditions, and partial steps topography in 1/4° global ocean simulations, To be submitted to Ocean Modelling.

Newsletters and Proceedings

Ayoub N., M. Lucas, B. Barnier, T. Penduff, G. Valladeau, and P. De Mey, 2006: A study of model errors in surface layers due to uncertainties in the atmospheric forcing fields, *Lettre trimestrielle Mercator* No 22, Juillet 2006, p 29-38.

Barnier B., Brodeau L., et Penduff T.: Ocean Surface Forcing and Surface Fields. *Lettre trimestrielle Mercator* No 22, Juillet 2006, p 4-7.

Molines J.M., A.M. Treguier, B. Barnier, L. Brodeau, J. Le Sommer, G. Madec, T. Penduff, S. Theetten, Y. Drillet, C. Talandier, J. Orr, Z. Lachkar Le modèle DRAKKAR de la variabilité océanique globale, 1958-2004. à paraître dans la Lettre de l'IDRIS, Novembre 2006.

Penduff T., 2006: DRAKKAR : modélisation à haute résolution de la variabilité océanique au cours des 50 dernières années. DRAKKAR : high-resolution modeling of ocean variability over the last 50 years, *Lettre PIGB-PMRC, No19*, Mai 2006, p 15-21.

Brodeau L., T. Penduff, and B. Barnier, 2006: Sensitivity of DRAKKAR global simulations to two existing and a hybrid atmospheric forcing functions. *Proceedings of the Radar Satellite Altimetry Colloquium*, March 13-17, Venice, Italy;

Penduff T., B. Barnier, A-M. Treguier, and P-Y. Le Traon, 2006: Synergy between ocean observations and numerical simulations: CLIPPER heritage and DRAKKAR perspectives, *Proceedings of the Radar Satellite Altimetry Colloquium*, March 13-17, Venice, Italy

Communications at international colloquiums

Barnier B., 2006: Impact of partial steps and momentum advection schemes in a global ocean circulation model at eddy permitting resolution, *MERSEA Annual Science Meeting*, March 6-7, London.

Barnier B., 2006: Recent progresses in modelling the ocean general circulation at eddy permitting resolution, *Radar Satellite Altimetry Colloquium*, March 13-17, Venice, Italy.

Brodeau L., T. Penduff, B. Barnier, A.M. Treguier, S. Gulev, and J.M. Molines, 2006: Combining satellite products and reanalysed atmospheric variables to build long-term forcing for global ocean/sea-ice simulations, *Geophysical Research Abstracts, Vol. 8*, 07880, *2006* EGU General Assembly 2006, Vienna, 2-7 avril.

Lachkar Z., J.C. Orr, J.C. Dutay and P. Delecluse, 2006: Effect of ocean mesoscale eddies on global

distributions of CFC-11, C-14, and CO2, Geophysical Research Abstracts, Vol. 8, 06717, 2006, EGU General Assembly 2006, Vienna, 2-7 avril.
Le Sommer J., T. Penduff, G. Madec, S. Theetten and B. Barnier, 2006: What does vertical velocity tell about the behavior of numerical schemes? *Geophysical Research Abstracts, Vol. 8, 09532, 2006*, EGU General Assembly 2006, Vienna, 2-7 avril.
Mathiot P., B. Barnier, H. Gallée, J.M. Molines and T. Penduff, 2006: On the role of katabatic winds in the formation of Antarctic Bottom Waters, *Geophysical Research Abstracts, Vol. 8, 07356, 2006*, EGU General Assembly 2006, Vienna, 2-7 avril.
Peronne S., A.M. Treguier, T. Arsouze, JC Dutay, F. Lacan,C. Jeandel, 2006: Modelling the oceanic Nd isotropic composition with a North Atlantic eddy permitting model. Abstract, AGU meeting, november 2006.
Penduff T., L. Brodeau, M. Juza, and B. Barnier, 2006: Hybridizing satellite products and reanalyzed atmospheric fields for the forcing of long-term ocean/sea-ice DRAKKAR simulations, OST/ST meeting *M*arch 17, Venice, Italy.

Project reports

Peronne S., 2006: Simulation numérique du Néodyme dans l'Atlantique Nord. Rapport de stage de fin d'étude, ISITV, Université du Sud Toulon Var, La Garde Cedex, 110 pp.
Bourdallé-Badie R., and A. M. Treguier, 2006: A climatology of Runoff for the global ocean-ice model ORCA025. Mercator Ocean Reference: MOO-RP-425-365-MER, 28 pp.
Molines J. M., B. Barnier, T. Penduff, L. Brodeau, A.M. Treguier, S. Theetten, and G. Madec, 2006: Definition of gtlobal ½° experiment with CORE interannual forcing, ORCA05-G50. *LEGI internal report*, 27 pp.
Molines J. M., B. Barnier, T. Penduff, L. Brodeau, A.M. Treguier, S. Theetten, and G. Madec, 2006: Definition of a 45 years interannual experiment ORCA025-G70. *LEGI internal report*, 34 pp.
Treguier A.M., J.M. Molines, G. Madec, 2006: Meridional circulation and transports in ORCA025 climatological experiments. *Report LPO-06-02*, 23 pp.

6. Personnel

Ayoub Nadia	CR CNRS	LEGI/LEGOS	30%
Barnier Bernard	DR CNRS	LEGI	90%
Madec Gurvan	DR CNRS	LODYC	15%
Orr James	DR CNRS	LSCE	30%
Penduff Thierry	CR CNRS	LEGI	90%
Thierry Virginie	Chercheur IFREMER	LPO	50%
Treguier Anne Marie	DR CNRS	LPO	90%
Wirth Achim	CR CNRS	LEGI	20%
Collaborateurs techniques			
Brasseur Josiane	Secrétariat	LEGI	40%
Molines Jean Marc	IR1 CNRS	LEGI	80%
Theetten Sébastien	IE CNRS	LPO	90%
Postdoctorants et ingénieurs contractuels			
Le Sommer Julien	PostDoc UE	LEGI	100%
Juza Mélanie	Ingénieur CNES/INSU	LEGI	100%
Marc Lucas	PostDoc SHOM	LPO	100%
Etudiants en thèse			
Brodeau Laurent	Thèse	LEGI	100%
Guiavarc'h Catherine	Thèse	LPO	30%
Hervieux Gaëlle	Thèse	LEGI	100%
Koch-Larrouy Ariane	Thèse	LOCEAN	100%
Lackhar Zouhair	Thèse	LSCE	50%
Mathiot Pierre	Thèse	LEGI/LGGE	100%
Etudiants stagiaires			
Lecointre Albanne	DEA	LEGI	100%

Acknowledgements

Support to DRAKKAR comes from various grants and programs listed hereafter. French national programs GMMC, LEFE, and PICS 2475 from Institut National des Sciences de l'Univers (INSU) and Centre National de la Recherche Scientifique(CNRS). European integrated project MERSEA. Support from CNES and marché EPSHOM-UBO 02.87.024.00.470.29.25 are acknowledged. Computations presented in this study were performed at Institut du Développement et des Ressources en Informatique Scientifique (IDRIS).

Liste of Annexes

ANNEX 1 : Le modèle DRAKKAR de la variabilité océanique globale, 1958-2004. To appear in IFRIS Newsletter.

ANNEX 2: Synergy between ocean observations and numerical simulations: Clipper heritage and Drakkar perspectives. Proceeding of Symposium on 15 years of Progress in Radar Altimetry. Venice, 13-18, March 2006.

ANNEX 3 : DRAKKAR, modélisation à haute résolution de la variabilité océanique au cours des 50 dernières années. Lettre du PIGB N°19, May 2006.

ANNEX 4 : Impact of partial steps and momentum advection schemes in a global ocean circulation model at eddy permitting resolution. Ocean Dynamics, November 2006.

ANNEX 5: Ocean surface forcing and surface fields. Mercator News Letter, July 2006.

ANNEX 6: A study of model errors in surface layers due to uncertainties in the atmospheric forcing fields Mercator News Letter, July 2006.

ANNEX 7: Sensitivity of DRAKKAR global simulations to two existing and a hybrid atmospheric forcing functions. Proceeding of Symposium on 15 years of Progress in Radar Altimetry Venice, 13-18 Mars 2006.

ANNEX 8: Comparing 20 years of precipitation estimates from different sources over the world ocean. Ocean Dynamics, April 2006.

TECHNICAL ANNEX 1: A Climatology of Runoff for the global ocean-ice model ORCA025. Mercator-Ocean Technical note, August 2006.

TECHNICAL ANNEX 2: Definition of the global 1/2° experiment with CORE interannual forcing ORCA05-G50. LEGI Technical note, November 2006.

TECHNICAL ANNEX 3: Definition of the interannual experiment ORCA025-G70 1958-2004. LEGI Technical note, November 2006.

ANNEX 1

Le modèle DRAKKAR de la variabilité océanique globale, 1958-2004

Article à paraître dans la lettre de l'IDRIS

Novembre 2006

Le modèle DRAKKAR de la variabilité océanique globale, 1958-2004[1]

J.M. Molines[1], A.M. Treguier[2], B. Barnier[1], L. Brodeau[1], J. Le Sommer[1], G. Madec[3], T. Penduff[1], S. Theetten[2], Y. Drillet[4], C. Talandier[3], J. Orr[5], Z. Lachkar[5]

[1]LEGI Grenoble, [2] LPO Brest, [3]LOCEAN Paris, [4]MERCATOR-océan Toulouse, [5]LSCE Saclay

Introduction

Par sa capacité calorifique mille fois supérieure à celle de l'atmosphère, l'océan joue un rôle fondamental dans l'évolution lente du climat de notre planète. Notre compréhension de la variabilité de l'océan reste cependant limitée par le manque d'observations historiques. Toutefois, une grande partie de la variabilité océanique est forcée par l'atmosphère : les vents génèrent des courants, l'évaporation et la pluie modifient la salinité de l'eau de mer, et les flux de chaleur air-mer agissent sur la température. Comme la densité dépend de la température et de la salinité, ces flux atmosphériques génèrent aussi des courants, appelés "circulation thermohaline". Or, l'observation de l'atmosphère bénéficie d'un réseau de mesures depuis les années cinquante. L'état de l'atmosphère sur les 40 à 50 dernières années a pu être restitué grâce aux "réanalyses atmosphériques", par exemple celle, ERA 40, du Centre Européen de Prévision à Moyen Terme (ECMWF, 2002). Il est donc possible, avec un modèle numérique d'océan, de simuler la variabilité des dernières décennies forcée par l'atmosphère. Tel est le but du projet inter-laboratoires DRAKKAR, mené conjointement par des équipes CNRS de Grenoble, Paris, Brest et une équipe du groupement d'intérêt public MERCATOR-Océan à Toulouse, en association avec des partenaires Européens.

Lorsque l'on considère le spectre en fréquence des mouvements de l'océan, on constate que les courants les plus énergétiques sont associés à ce qu'on appelle la "turbulence d'échelle moyenne". Il s'agit de méandres et de tourbillons de 20 à 200 km de diamètre et d'échelle temporelle de l'ordre du mois. Ce sont les analogues océaniques des fameuses "perturbations" atmosphériques, qui font la météo de tous les jours. On n'imaginerait pas un modèle d'atmosphère incapable de représenter l'anticyclone des Açores : c'est pourtant la situation des modèles d'océan dits "de climat", comme la plupart de ceux utilisés pour prédire l'effet de l'augmentation des gaz à effet de serre. Ces modèles d'océan à maille grossière (100km) ne résolvent pas les tourbillons et les fronts, dont on sait pourtant qu'ils jouent un rôle essentiel dans la variabilité du "temps" de l'océan. L'originalité du projet DRAKKAR est d'utiliser un modèle d'océan à haute résolution, capable de représenter (du moins en partie) la turbulence d'échelle moyenne, et d'appliquer ce modèle à des expériences numériques d'intérêt climatique (c'est à dire globales et de plusieurs décennies). Les exigences combinées d'une maille fine, d'un modèle d'océan global et d'une simulation de plus de 40 ans dont le pas de temps n'est que d'une fraction d'heure, résultent en des besoins considérables en calcul. Nous avons pu réaliser notre première expérience en juillet-août 2006 sur la machine Zahir de l'IDRIS. Nous en présentons ici quelques résultats préliminaires.

Le modèle d'océan ORCA025

Le modèle de circulation océanique et de glace de mer ORCA025 est basé sur le système NEMO (Nucleus for European Modelling of the Ocean, www.lodyc.jussieu.fr/NEMO), qui comprend la version la plus récente du code de circulation océanique OPA9.0 du laboratoire LOCEAN à Paris (Madec, 2006), et le code de glace de mer LIM développé à l'université de Louvain la Neuve (Fichefet et al., 1997). Le code d'océan résout les équations de la mécanique des fluides

[1] Article soumis pour publication dans le lettre de l'IDRIS

(équations de Navier-Stockes) avec des approximations appropriées à l'océan (hydrostatique et Boussinesq). La discrétisation des équations utilise une méthode similaire à celle des volumes finis, et un algorithme original est utilisé pour filtrer les ondes de surface et la houle (Roullet et Madec, 2000). L'écriture du code en fortran 90 et les efforts d'optimisation en calcul vectoriel et parallèle font que NEMO est au niveau des meilleurs codes d'océan sur le plan international. Il est très largement utilisé en Europe et son développement est actuellement l'objet d'un consortium Européen. La configuration globale ORCA025 couvre l'océan mondial; la singularité du pôle Nord (qui, contrairement au pôle Sud, se trouve dans l'océan) nécessite un traitement spécial (Madec et Imbart, 1996). La grille d'ORCA025 est donc tripolaire, et elle est aussi isotrope horizontalement ce qui est indispensable à une bonne simulation de la turbulence océanique. Pour la configuration ORCA025, la résolution nominale est de 1/4°, soit une maille de 28 km à l'équateur devenant plus fine avec la latitude jusqu'à être voisine de 10 km dans l'océan Arctique et le long du continent Antarctique. Avec 46 niveaux verticaux pour représenter la stratification et le relief du fond de l'océan, le modèle comporte en tout $1442 \times 1021 \times 46 \approx 7\ 10^7$ points de grille. Le raffinement des régions polaires est crucial pour la simulation du climat, car la dynamique y prévalant est fortement contrainte par les fines échelles des passages profonds et des seuils topographiques permettant les échanges entre les différents bassins.

Le code NEMO est parallélisé selon une décomposition de domaines classiques avec MPI (Guyon et al. 1999). Le domaine de calcul est réparti sur 186 processeurs de la machine Zahir (Fig. 1). Le pas de temps est de 1440 secondes. Le forçage du modèle se fait à partir de variables atmosphériques (vent, température de l'air, humidité, flux radiatifs, précipitation et apports des fleuves) et les flux sont calculés par les formules aérodynamiques globales proposées par Large and Yeager (2004).

La simulation ORCA025-G70

Les données atmosphériques nécessaires au forçage du modèle sont disponibles à partir de 1958. Pour la modélisation des traceurs transitoires (voir dernière section de cet article) il était nécessaire de débuter au plus tard en 1950 : nous avons donc réalisé une première simulation de 8 ans avec un forçage répété de l'année 1958 pour initialiser les traceurs. L'expérience portant sur les années 1958 à 2004 a commencé fin juillet 2006 et s'est terminée début septembre, une production pratiquement sans interruption sur la machine zahir de l'IDRIS (l'été étant une période favorable à la réalisation de grosses expériences). Le coût total de l'expérience est de 179000 heures CPU. Afin d'étudier la méso-échelle il est nécessaire d'archiver les résultats fréquemment (tous les 5 jours) ce qui représente une très grande quantité de données (environ une dizaine de Téra octets). Les modèles d'océan nécessitent un bon équilibre entre la puissance de calcul disponible et la facilité de stockage, ce qui a toujours été un point fort de l'IDRIS.

L'une des grandes difficultés de la modélisation océanique "forcée" consiste à équilibrer les flux atmosphériques. Les incertitudes sur la température de l'air, l'humidité, les vents, les pluies et les flux air-mer sont telles que lorsqu'on calcule l'intégrale des flux de chaleur et d'eau douce sur le globe on trouve souvent un déséquilibre énorme qui conduit à une dérive inacceptable du modèle d'océan. De nombreuses expériences de sensibilité nous ont été nécessaires pour arriver à un équilibrage satisfaisant des flux d'eau douce dans ORCA025-G70. Ces tests nous ont conduits à choisir un forçage mixte combinant certaines variables de la réanalyse ERA40 (vent, température et humidité atmosphérique) avec des mesures directes par satellites pour les dernières décennies (flux radiatifs, précipitations). Grâce aux ajustements réalisés, la circulation thermohaline mondiale se maintient à des valeurs compatibles avec les estimations issues des mesure *in situ*, et le niveau moyen des océans n'augmente que de 25 cm pendant les 54 ans d'expérience. Cette dernière dérive est irréaliste, puisque la montée observée du niveau des océans serait plutôt de

l'ordre de 1 cm pour 50 ans. C'est malgré tout un résultat remarquable puisqu'il est obtenu par un ajustement a priori des précipitations atmosphériques et non par une correction fictive appliquée au cours de l'expérience, une technique utilisée jusqu'à présent au niveau mondial dans toutes les simulations forcées réalisées.

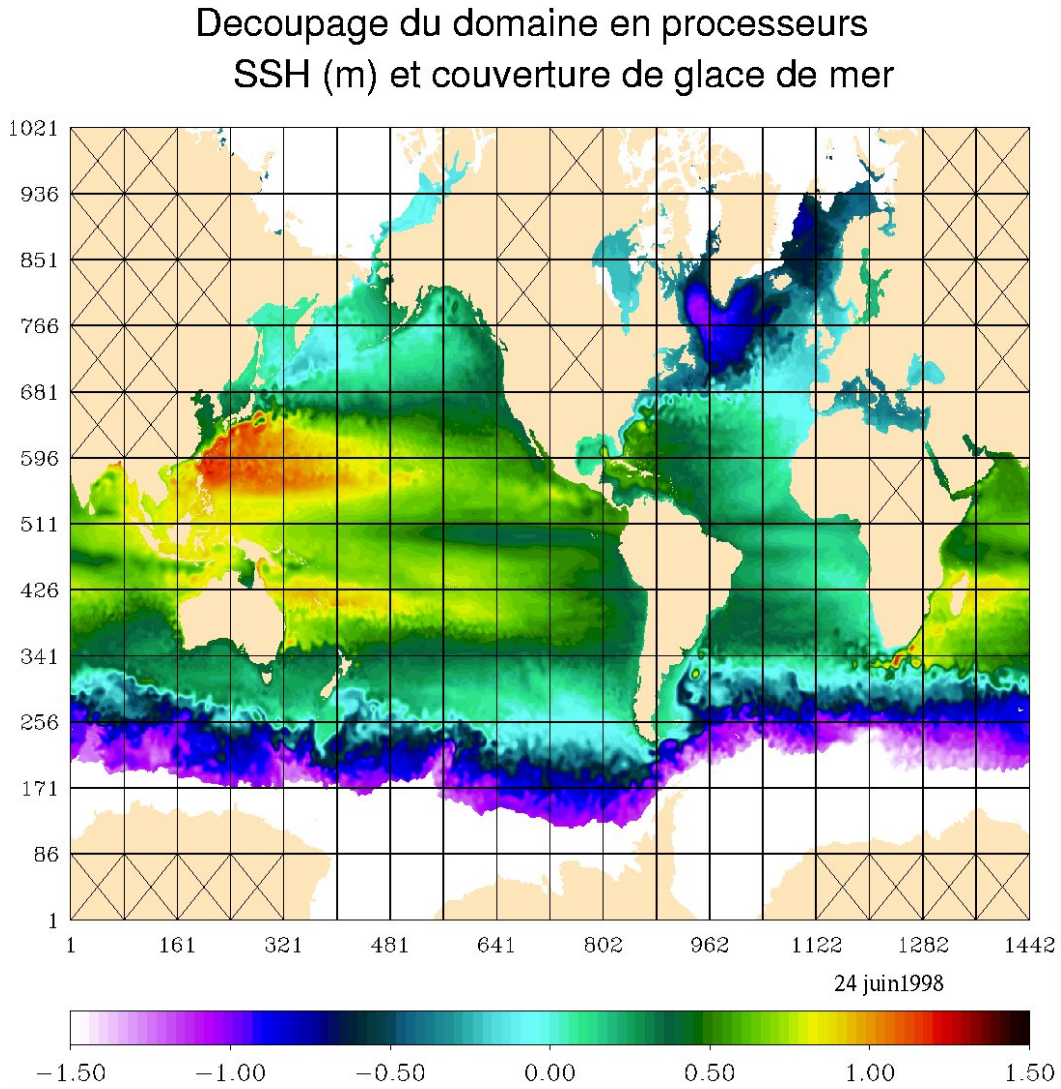

Figure 1 : Découpage du domaine de calcul du modèle de circulation océanique ORCA025 sur 216 processeurs de la machine Zahir de l'IDRIS. Chaque boîte représente le domaine calculé par un processeur. 32 processeurs ne comprenant pas de point océan (marqués d'une croix) ne sont pas pris en compte, ce qui limite le nombre de processeurs utiles à 186 et conduit à une réduction de 15% des coûts de calcul. La variable représentée en couleur sur cette carte est un champ instantané de topographie de la surface océanique (Sea Surface Height); la couverture de glace est indiquée en blanc. Mesurée par altimétrie satellitaire (TOPEX/Poséïdon, JASON, etc.), cette grandeur renseigne sur la direction, l'intensité, les fluctuations des courants et tourbillons de surface. Le modèle numérique permet de compléter en trois dimensions ces données de surface et de mieux comprendre la dynamique océanique non directement observable. On remarque la richesse des structures spatiales représentées par le modèle.

La turbulence d'échelle moyenne

ORCA025 n'est pas le modèle global à plus haute résolution existant aujourd'hui, puisque des modèles globaux avec une maille 1/10° ont été développés aux Etats-Unis (Maltrud and McCLean, 2005), au Royaume Uni (http ://www.soc.soton.ac.uk/JRD/OCCAM/OC12)ou au

Japon (Masumoto et al., 2004). Cependant, grâce à des solutions numériques originales récemment introduites dans le code NEMO, le modèle ORCA025 représente remarquablement bien la turbulence d'échelle moyenne pour un modèle de sa catégorie. Ceci apparaît sur la figure 2, qui compare l'énergie cinétique turbulente des courants de surface en Atlantique Sud mesurée par l'altimétrie satellitaire et simulée par le modèle. On trouve dans cette région de l'océan deux des systèmes de courant les plus énergétiques au monde : le courant des Aiguilles au sud de l'Afrique et la confluence des courants du Brésil et des Malouines au large de l'Argentine. Des études récentes ont montré que le modèle ORCA025 était plus proche de la réalité que les modèles au 1/10° dans cette zone (Barnier et al., 2006), et que ce succès est dû aux efforts particuliers mis sur les schémas numériques (Le Sommer et al., 2006).

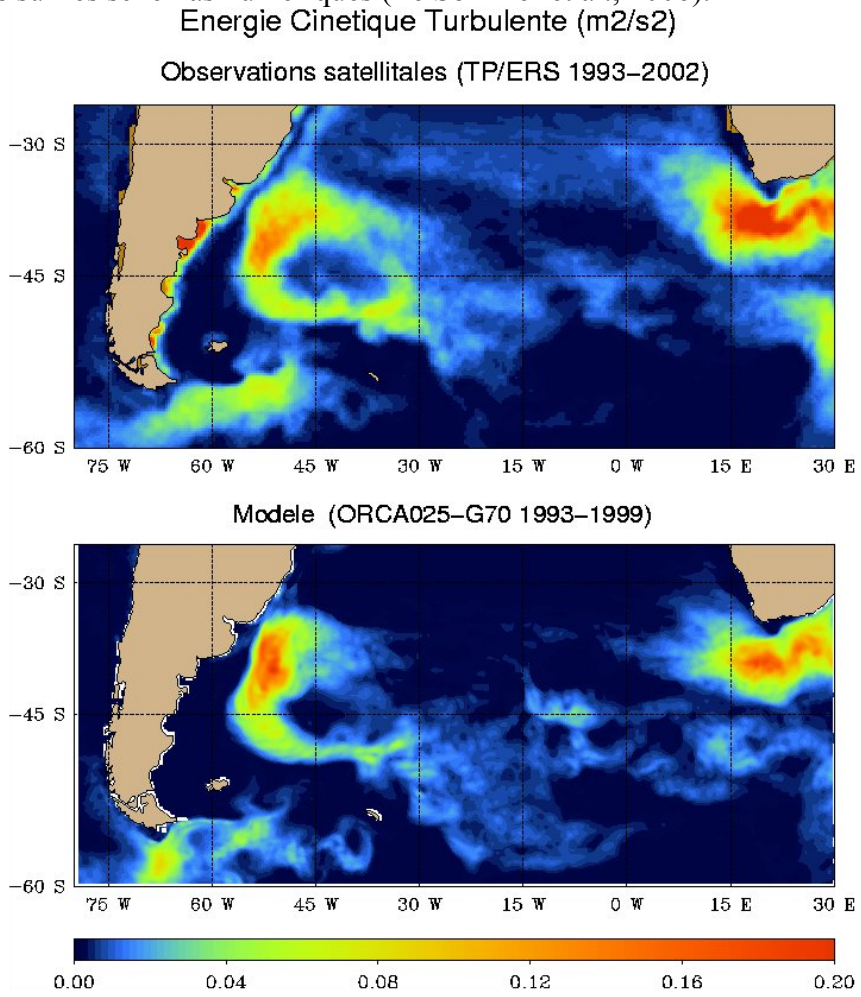

Figure 2 : Energie cinétique turbulente moyenne (en m^2s^{-2}) dans l'océan Atlantique Sud estimée à partir des observations satellitaires, et à partir des vitesses calculées par le modèle global ORCA025. Le très bon accord de la distribution spatiale de cette quantité entre le modèle et les observations indique une représentation satisfaisante des processus d'instabilité des grands courants océaniques de cette région que ce soit au niveau de la pointe sud de l'Afrique ou de autour du Zapiola, un mont sous-marin centré autour de 45°W – 45°S.

Le modèle est bien sur tridimensionnel et fournit des estimations des courants profonds, qui sont beaucoup moins bien connus que ceux de surface car inaccessibles à la mesure par satellite. Ces courants profonds, notamment ceux intensifiés sur les bords Ouest des bassins, sont un maillon clé de la circulation thermohaline mondiale régulant les transferts méridiens de chaleur et donc le climat. Un tel courant de bord ouest est présent au large des côtes du Brésil (Fig.3). Il transporte les eaux froides formées dans les mers Nordiques et subpolaires de l'Atlantique Nord vers l'océan Austral. La déstabilisation de ce courant à 8°S a été récemment décrite dans la revue Nature par

Dengler et al (2004) à partir de mesures courantométriques; le transport des eaux froides par des tourbillons, plutôt que par un courant permanent laminaire, a des implications importantes pour les échanges avec l'intérieur du bassin. Le modèle reproduit bien cette déstabilisation et la formation de tourbillons qui lui est associée (Fig. 3).

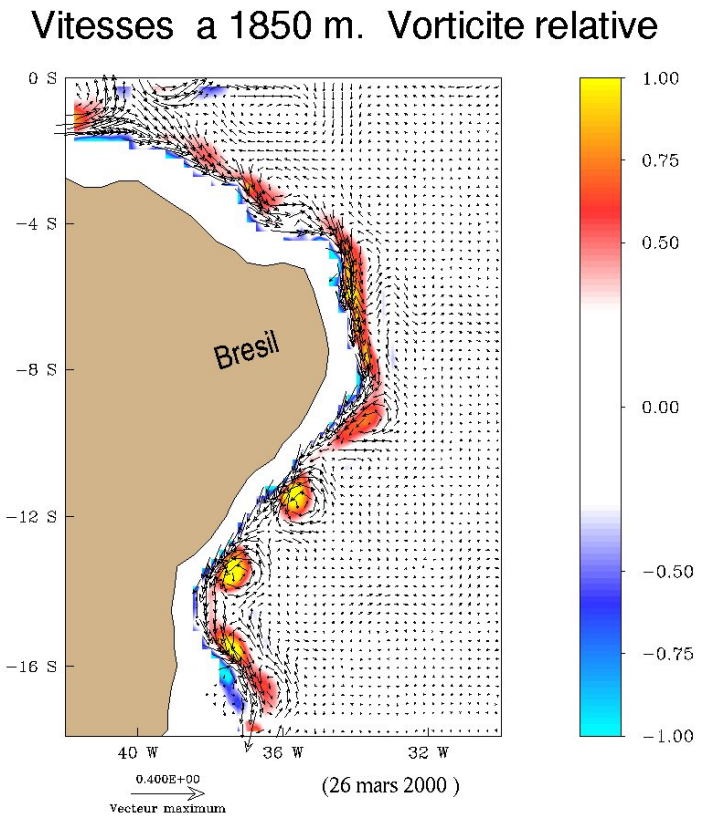

Figure 3 : Destabilisation du courant de bord ouest au large du Brésil à une profondeur de 1850m. Les vecteurs représentent les vitesses horizontales (m/s). La couleur indique la vorticité relative, c'est à dire la composante verticale du rotationnel de la vitesse (unité : 10^{-6} s^{-1}); cette quantité met clairement en évidence les tourbillons présents au sud de 8°S.

Evolution temporelle

Les résultats du modèle vont maintenant permettre aux chercheurs associés au projet DRAKKAR d'étudier la variabilité de l'océan sur les dernières décennies. L'un des modes de variabilité les plus connus est le phénomène "El Niño", qui consiste en un basculement de l'ouest vers l'est du contenu thermique de surface de l'océan Pacifique Tropical, avec des conséquences parfois dramatiques sur les pêcheries et les conditions météorologiques des pays bordant l'océan Pacifique, depuis l'Indonésie jusqu'à la Californie. La figure 4 montre que ce phénomène est très bien reproduit par le modèle pour les décennies récentes. Ce résultat n'est pas surprenant : El Niño est contrôlé au premier ordre par des phénomènes de grande échelle qui sont généralement bien reproduit par les modèles de climat forcés. La maille plus fine de ORCA025 va nous permettre de mieux quantifier certaines contributions à El Niño, comme l'effet des ondes tropicales d'instabilité qui apparaissent clairement de part et d'autre de l'équateur dans la figure 4a.

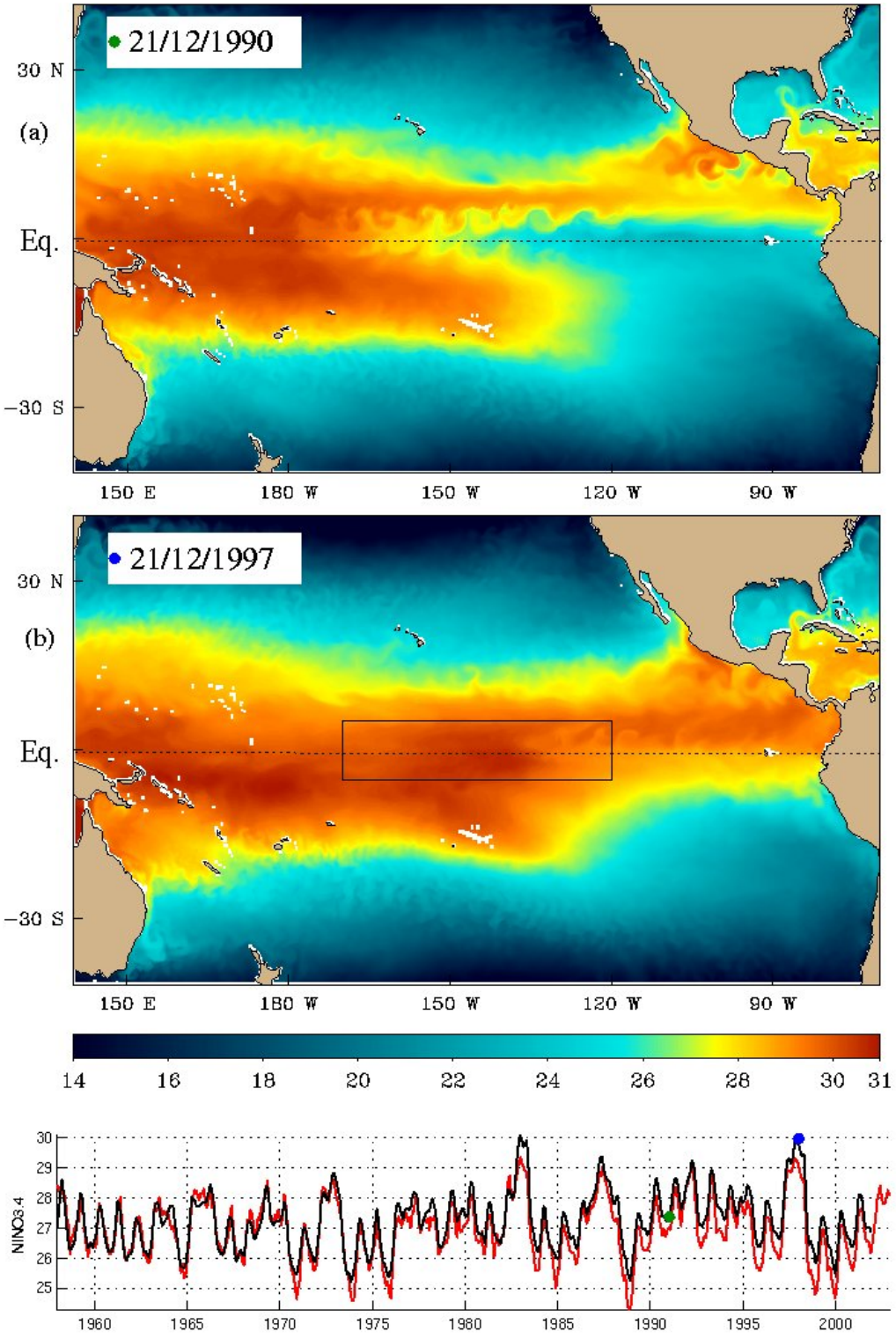

Figure 4 : Température de surface dans le Pacifique Tropical dans le modèle ORCA025. (a) Une situation "normale", hors phénomène El Niño. (b), la situation au maximum de l'El Niño 97-98 : l'eau chaude, habituellement stockée dans le Pacifique Ouest, envahit la partie Est du bassin. Un indicateur de El Niño est la température de surface moyennée dans une boîte (indiquée par un rectangle sur la carte 4b). La série temporelle compare cet indicateur pour le modèle (en noir) et les observations (en rouge, www.cpc.ncep.noaa.gov ; voir par exemple Trenberth et Stepaniak, 2001).Les instants correspondant aux cartes (a) et (b) sont respectivement indiqués par un point vert et bleu .Le biais chaud du modèle est peut-être lié à des vents équatoriaux un peu faibles ou un déficit d'évaporation.

Traceurs transitoires

L'océan stocke une partie importante (de l'ordre d'un tiers) du CO_2 relâché dans l'atmosphère par les activités industrielles. Pour comprendre l'effet de l'augmentation des gaz à effet de serre dans l'atmosphère, il est donc nécessaire d'étudier les mécanismes d'injection d'un traceur dans l'océan ainsi que les échelles de temps mises en jeu. Le CFC-11 (chlorofluorocarbone-11) est un gaz d'origine humaine qui a été injecté dans l'atmosphère à partir de 1930, en de plus en plus grandes quantités jusqu'à l'implémentation dans les années 70s du protocole de Montréal (qui avait pour but de limiter les dommages causés par ce gaz à la couche d'ozone). Le CFC-11 est inactif chimiquement dans l'eau de mer. La mesure de sa concentration dans l'océan a permis de suivre son augmentation dans les eaux de surface et sa lente pénétration dans l'océan profond.. L'inventaire du CFC-11 (intégrale sur la verticale) calculé à partir d'observations de la période 1989-1994, est représenté sur la figure 5a. La quantité de CFC-11 présente sur la colonne d'eau est importante en mer du Labrador et en mer d'Irminger, dans la partie Nord de l'océan Atlantique, car ce sont des zones où se produit de la convection qui mélange les traceurs jusqu'à des profondeurs de plus de 1000m. L'inventaire est également important dans le courant Antarctique Circumpolaire où existe un fort mélange vertical. La distribution de CFC-11 constitue donc un moyen puissant pour évaluer le mélange vertical dans les modèles d'océan (Dutay et al, 2002). Pour une complémentarité d'information sur la circulation et une meilleure contrainte sur l'absorption de CO_2 par l'océan, un autre traceur a été aussi simulé dans le modèle ORCA025 : le carbone ^{14}C injecté dans l'atmosphère par les explosions nucléaires. L'inventaire du CFC-11 dans le modèle (figure 5b) montre que les régions d'injection sont remarquablement bien représentées. Dans certaines région clé, la quantité totale est trop importante, reflétant sans doute une convection trop profonde dans le modèle notamment en mer du Labrador et dans le courant Antarctique Circumpolaire. Les résultats du modèle montrent une structure fine non résolue par les observations (la figure 5a est construite uniquement à partir des lignes hydrographiques représentées en noir). L'examen des distributions en profondeur, non représentées ici, montre que le modèle au 1/4° reproduit bien la progression des CFC le long des bords ouest, beaucoup mieux que les modèles basse résolution examinés par Dutay et al (2002).

Conclusion

Avec cette première expérience longue réalisée grâce aux moyens de l'IDRIS, le modèle ORCA025 du projet DRAKKAR affirme sa position au plus haut niveau international en tant qu'outil d'étude de la variabilité de l'océan sur les dernières décennies. Cette position est appelée à se renforcer, d'une part dans le cadre de collaborations Européennes (partage du modèle et coordination d'expériences avec des groupes Allemands et Anglais) et d'autre part grâce à son utilisation pour réaliser les premières "réanalyses océaniques" globales en combinant le modèle avec les données existantes (action de MERCATOR-Ocean prévue à partir de 2008).

Cependant la simulation réalisée cet été est loin de répondre à toutes nos interrogations sur l'océan et son rôle dans le climat. Comprendre le comportement d'ORCA025 nécessitera de rejouer cette expérience plusieurs fois en modifiant la physique utilisée. Il est également souhaitable d'encore mieux résoudre la turbulence d'échelle moyenne, en particulier dans les régions polaires cruciales pour le climat : c'est l'objet d'un projet de modèle global et d'Atlantique nord au 1/12° qui se heurte actuellement à l'insuffisance des moyens de calcul au plan Européen. Enfin, pour discriminer le réchauffement d'origine anthropique de la variabilité naturelle de l'océan, il faudrait disposer d'une simulation numérique équilibrée, ce qui nécessite une expérience au moins dix fois plus longue (500 ans au lieu de 50 ans) et couplée à un modèle d'atmosphère. La soif des océanographes pour les moyens de calculs n'est donc pas près d'être assouvie!

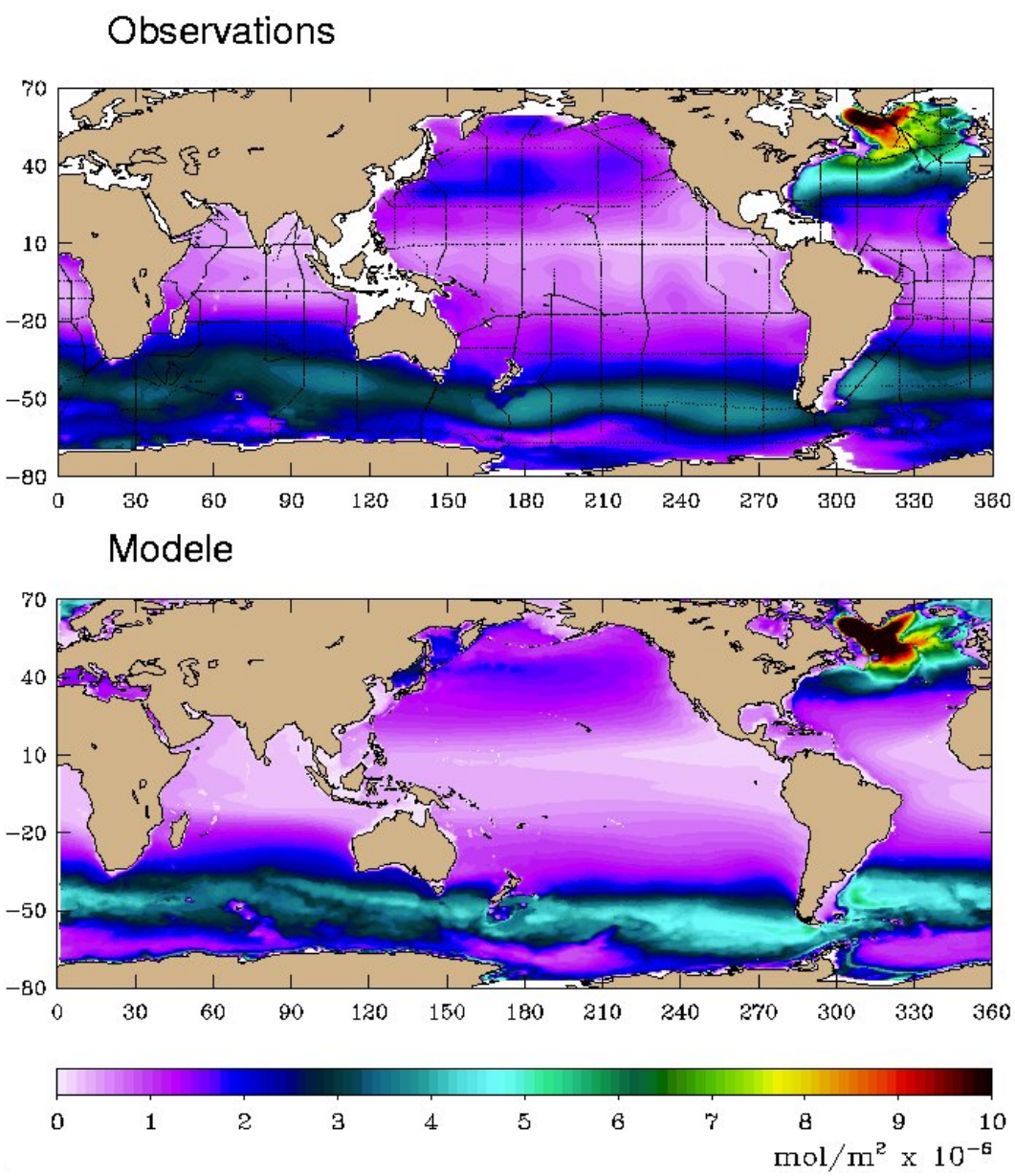

Figure 5 : Inventaire global du CFC-11. a : estimation GLODAP à partir des mesures WOCE collectées entre 1989 et 1994 (lignes hydrographiques indiquées en noir) (Key et al, 2004). b : estimation du modèle basée sur la même période.

Remerciements

Nous remercions bien sûr particulièrement le centre IDRIS qui nous a permis de réaliser cette expérience dans d'excellentes conditions, ainsi que le comité de programmes "Environnement" (CP1) qui a soutenu notre projet. DRAKKAR est financé par le CNRS-INSU, Mercator-océan, le CNES, le SHOM et l'IFREMER.

Références

Barnier B., G. Madec, T. Penduff, J.-M. Molines, A.-M. Treguier, J. Le Sommer, A. Beckmann, A. Biastoch, C. Böning, J. Dengg, C. Derval, E. Durand, S. Gulev, E. Remy, C. Talandier, S. Theetten, M. Maltrud, J. McClean, and B. De Cuevas, 2006 : Impact of partial steps and momentum advection schemes in a global ocean circulation model at eddy permitting resolution. Ocean Dynamics, Vol 4, DOI 10.1007/s10236-006-0082-1.

Dengler M., F. Schott, C. Eden, P. Barndt, J. Fischer, and R. J. Zantopp, 2004: Break-up of the Atlantic deep western boundary current into eddies at 8° S, *Nature* 432, 1018–1020

Dutay,J-C, J.L. Bullister,S.C. Doney,J.C. Or,R. Najjar, K. Caldeira,J.-M. Campin,H. Drange,M. Follows,Y. Gao,N. Gruber, M.W. Hecht,A. Ishida,F. Joos,K. Lindsay,G. Madec,

E. Maier-Reimer,J.C. Marshall,R.J. Matear,P. Monfray,A. Mouchet, G.-K. Plattner,J. Sarmiento,R. Schlitzer,R. Slater,I.J. Totterdell, M.-F. Weirig,Y. Yamanaka,A. Yool, 2002: Evaluation of ocean model ventilation with CFC-11: comparison of 13 global ocean models. Ocean Modelling 4 (2002) 89–120

European Centre for Medium-Range Weather Forecasts, 2002: The ERA-40 Archive. Rapport ECMWF, 40 pp.

Fichefet T, Morales Maqueda MA (1997) Sensitivity of a global sea ice model to the treatment of ice thermodynamics and dynamics. J Geophys Res 102: 12609-12646

Guyon, M., G. Madec, F.-X. Roux, and M. Imbard, 1999 : A Parallel ocean model for high resolution studies. P. Amestoy et al. (Eds.): Euro-Par'99, LNCS 1685, 603-607.

Key, R. M., Lee, C. L. S. K., Wanninkhof, R., Bullister, J., Feely, R. A., Millero, F. J., Mordy, C., and Peng, T.-H, 2004.: A Global Ocean Carbon Climatology: Results from Global Data Analysis Project (GLODAP), Global Biogeochem. Cycles, 18, GB4031, doi:10.1029/2004GB002247.

Large W, Yeager S (2004) Diurnal to decadal global forcing for ocean and sea-ice models: the data sets and flux climatologies. NCAR technical note: NCAR/TN-460+STR. CGD division of the National Center for Atmospheric Research.

Le Sommer J, T. Penduff , S. Theetten , G. Madec, B. Barnier, (2006) How momentum advection schemes affect current-topography interactions in the DRAKKAR 1/4-degree z-coordinate model. Ocean Modelling, submitted.

Madec G, Imbard M (1996) A global ocean mesh to overcome the North Pole singularity. Climate Dyn, 12, 381-388

Madec G, 2006: NEMO, the ocean engine. Notes de l'IPSL, Université P. et M. Curie, B102 T15-E5, 4 place Jussieu, Paris cedex 5, En préparation.

Maltrud ME, McClean JL (2005) An eddy resolving global 1/10° ocean simulation. Ocean Modelling 8: 31-54

Masumoto Y, Sasaki H, Kagimoto T, Komori N, Ishida A, Sasai T, Miyama T, Motoi T, Mitsudera H, Takahashi K, Sakuma H, Yamagata T, (2004) A fifty-year eddy-resolving simulation of the world ocean: Preliminary outcomes of OFES (OGCM for the Earth Simulator). J Earth Simulator, 1, 35–56

Roullet, G. and G. Madec, 2000: Salt conservation, free surface and varying volume: a new formulation for Ocean GCMs. J. Geophys. Res.,105 , 23,927-23,942.

Trenberth K.E. and D.P. Stepaniak (2001) "Indices of El Niño Evolution" Journal of Climate, (14) 1697-1701.

ANNEX 2

SYNERGY BETWEEN OCEAN OBSERVATIONS AND NUMERICAL SIMULATIONS: CLIPPER HERITAGE AND DRAKKAR PERSPECTIVES

Proceeding of Symposium on 15 years of Progress in Radar Altimetry

Venice, 13-18 Mars 2006

SYNERGY BETWEEN OCEAN OBSERVATIONS AND NUMERICAL SIMULATIONS: CLIPPER HERITAGE AND DRAKKAR PERSPECTIVES

Thierry Penduff[(1)], Bernard Barnier[(1)], Anne-Marie Treguier[(2)], Pierre-Yves Le Traon[(2)]

[(1)]LEGI, BP53, 38041 Grenoble Cedex 9, France
[(2)]LPO, IFREMER, B.P.70, 29280 Plouzané, France

ABSTRACT

Between 1996 and 2005, the French CLIPPER project team performed numerical simulations of the Atlantic Ocean over the WOCE years (1980-2000). Since 2002, the DRAKKAR program extends this framework: international collaboration, global and basin-scale simulations of the ocean circulation, sea-ice and biogeochemical tracers over the 1950-2000+ period at increased resolutions with local grid refinement capabilities, improved physics and numerics. Both projects were designed to strengthen the complementarity between ocean simulations and observations, for the study of the oceanic variability. This review paper illustrates the scientific benefits of such synergies as performed during the CLIPPER experiment, and as presently done within the DRAKKAR program.

1. OBSERVATIONAL AND NUMERICAL OCEANOGRAPHY

The quantity and quality of oceanic observations has strongly increased over the last decades, especially during the World Ocean Circulation Experiment (WOCE) and since the advent of spatial oceanography. The global ARGO array of profiling floats extends since 2000 the satellite monitoring of the global oceanic surface to the uppermost 2 kilometers. These datasets have highlighted the complexity and ubiquity of the ocean's variability over a wide range of space and time scales. However, observational datasets remain too short, too superficial (satellites) or too dispersed in time and space (drifters) to allow detailed studies of physical processes across their full range of scales. This is particularly true for nonlinear processes (dynamical interactions across wide time and space scale ranges, complex interplays between ocean physics and biogeochemistry, mesoscale and sub-mesoscale dynamics). Combined investigations of observations and numerical simulations are necessary to investigate such issues.

Primitive equation ocean models have substantially improved in terms of physics and numerics (forcing functions, subgrid-scale parameterizations, etc). Thanks to the growing computational power, the size and resolution of numerical domains and the duration of simulations have increased, thus extending the range of space/time scales that can be explicitly simulated and improving the realism of solutions. These observational and numerical developments, along with improvements of data assimilation techniques, have led to ocean reanalysis experiments and to operational oceanography. Data assimilating systems constitute a well-known example of model-data synergy: ocean models are used as dynamical interpolators between various types of dispersed observations while observations maintain the model trajectories close to reality.

Modeling the ocean realistically is impossible without observations: initial states, boundary forcings, the adjustment of model parameterizations, the scientific validation and analysis of the solutions largely depend on the available data. Despite truncation errors, forcing errors, and imprecise initial states, the realism of ocean simulations generally increase as the model grid allows the explicit resolution of mesoscale dynamics (that are involved in most ocean processes). In high-resolution assimilating experiments, observations are used where and when available to reconstruct the actual evolution of the large-scale circulation and of individual eddies. The approach followed during the CLIPPER and DRAKKAR studies is somewhat different and complementary: models are forced by reconstructed (reanalyzed) atmospheric fields, but mesoscale, regional and large-scale oceanic fields are totally free to interact. Because they are nonlinear and barely constrained, these solutions cannot not be as realistic as their assimilated counterparts with respect to individual observations. But for the same reason, they help analyze complex dynamical responses, generated internally or forced the atmosphere, scale interactions over large time/space scales, feedbacks between dynamics, thermodynamics and biogeochemistry, including over the pre-satellite era when observations were rare. Once their actual realism is evaluated, the oceanic scenarios produced by these models can be precisely analyzed in terms of dynamical balance. The following sections present various aspects of the complementarity between observational datasets and numerical simulations.

2. OVERVIEW OF THE CLIPPER AND DRAKKAR PROGRAMS

In 1996, scientists from five French laboratories designed the CLIPPER Program (http://www.ifremer.fr/lpo/clipper/index.html) with the objective to model and study the variability of the whole

Atlantic Ocean over the WOCE period (1980-2000). About 20 multi-year sensitivity experiments were performed at various resolutions (1°, 1/3°, 1/6°, up to 1/15° regionally) using different surface forcing functions derived from reanalyzed air-sea flux products (mostly from ECMWF). CLIPPER simulations have been to used in about 35 peer-reviewer papers since 1999, most of which in combination with observational datasets. This research program stimulated the development of the OPA8 ocean model for high-resolution basin-scale modeling (numerical schemes, surface and lateral boundary conditions, grid refinement techniques, etc.) The 1/3° North Atlantic CLIPPER configuration has been transferred to the MERCATOR-Ocean centre and is being used since January 2001 for operational forecasts.

The DRAKKAR Program, designed in 2002, extends the framework of its predecessor CLIPPER in terms of scientific objectives, numerical tools, and multi-disciplinary collaborations with associated scientists (http://www.ifremer.fr/lpo/drakkar/index.htm). The DRAKKAR Project Team includes ocean, atmosphere, sea-ice scientists and applied mathematicians from 8 research laboratories in 5 countries and from the MERCATOR-Ocean operational oceanography center. The general objective is to model and study the 3-dimensional evolution of the ocean circulation, sea-ice, and passive tracers (CFCs, bomb ^{14}C) over the last 50 years, in close relationship with observationalists and associated scientists. A hierarchy of models based on the NEMO modeling framework has been constructed and is presently running in coordination among the groups: global configurations at 2°, 1/2°, and ¼° resolution, North Atlantic/Nordic Seas regional models at ¼° and (soon) 1/12°, and idealized configurations. Besides its research applications, the ¼° global model is being used for global ocean forecasting at the MERCATOR operational center since October 2005.

3. MODEL SETUP AND FORCING

The aim of CLIPPER or DRAKKAR simulations is to mimic the real ocean variability with constraints limited to the atmospheric forcing (and lateral boundaries in regional models). Observations are involved for the setting up the discrete domain geometry, adjusting model parameters and building the atmospheric forcing function

3.1 Model setup

Bottom topography strongly affects the dynamics and distribution of eddies, fronts and currents up to the surface [1]. In addition, the representation of topographic constraints in numerical models and their subsequent solutions at regional and basin scales depend on their numerical formulation and on bottom boundary conditions [2, 3, 4]. Unlike in sigma-coordinate models where topographies are smoothed to reduce numerical errors, topographic datasets are generally used as is (i.e. keeping the finest scales present in altimeter-derived fields) in geopotential-coordinate models like OPA/NEMO. A detailed comparison of CLIPPER outputs with all the WOCE current-meter measurements available in the Atlantic showed that these fine structures distort the vertical distribution of mean and eddy kinetic energy [5, 6], especially where the spatial scales of oceanic currents are marginally resolved (high latitudes). This reference to in-situ observations to evaluate CLIPPER dynamics helped setting up the DRAKKAR topographies and interpret several sensitivity experiments: comparison of near-surface [7] and full-depth [8] circulations, and numerical study of the near-bottom origin of these differences [9].

More generally, numerous sensitivity experiments are performed and carefully compared to ocean observations to develop and adapt model parameterizations. They are used to take small-scale processes (eddy fluxes, entrainment/detrainment, surface and bottom non-hydrostatic mixed layer processes, etc.) into account in basin-scale and global ocean simulations. For instance, EQUALANT ADCP velocity measurements [10] were used as a reference to improve the parameterization of near-surface equatorial momentum eddy fluxes in the CLIPPER models [11]. Consistently with dedicated studies of inertial instabilities [12], the representation of the Atlantic undercurrent was improved by the local addition of a down-gradient Fickian diffusion of momentum. The DRAKKAR project team has started collaboration with observationalists from the Grenoble glaciology laboratory (LGGE) to evaluate the sea-ice visco-plastic component of the NEMO model used in DRAKKAR. The simulated sea-ice deformation tensors and distribution variability will be carefully compared to satellite observations with the objective of evaluating and (possibly) improving the model. Other model data-comparisons are being performed presently to improve the fit to globally observed mixed layer depths (parameterization of Langmuir and surface waves) or the three-dimensional density field downstream of topographic sills (entrainment in overflows).

3.2 Model forcing

The choice and formulation of the external forcing is of major importance in ocean modeling and is largely based on observational datasets. CLIPPER simulations were initialized from a seasonal T/S climatology based on historical hydrography [13] that was developed for the project but used in various other studies. The CLIPPER Atlantic models required physically-consistent open boundary conditions (OBCs) able to evacuate outgoing perturbations transparently and to simulate the presence of a variable outer ocean [14]. The aforementioned climatology was used to constrain

tracer and velocity shears along OBCs. Synoptic hydrographic sections were used (with an equivalent barotropic hypothesis and after removing synoptic eddies) to constrain absolute velocities at both openings of the austral Atlantic sector ([15] at 68°W, [16] at 30°E). This combined use of climatological and synoptic hydrography was necessary and proved successful in controlling the model over 20 years [6, 14]. The CLIPPER atmospheric forcing was derived from the ECMWF reanalysis and analysis, and was applied in terms of heat, salt and momentum fluxes. A relaxation term was applied on surface temperatures and salinities to compensate for forcing uncertainties (thus letting the model correct them where needed), and to roughly mimic the ocean feedback on air-sea fluxes [17]. The use of scatterometer winds in CLIPPER was shown to improve the simulated variability at low latitudes.

A more consistent formulation of air-sea interactions has been introduced in DRAKKAR through bulk formulae. These parameterizations provide turbulent air-sea fluxes of heat, freshwater and momentum from the instantaneous simulated ocean and reanalyzed atmospheric variables [7]. The DRAKKAR hierarchy of models (simple planetary boundary layer model, global ocean/sea-ice models at increasing resolutions) is currently used to develop a forcing function that hybridizes reanalyzed atmospheric fields with air-sea interface satellite observations. This "more observational" approach is likely to improve the long-term stability of unconstrained ocean simulations.

4. MODEL VALIDATION

The realism of unconstrained numerical simulations is generally the result of reasonable physics (section 6) and forcings (section 3), and should be systematically assessed with respect to available observations. Most scientific studies that make use of model outputs actually start by such model-data comparisons thus contributing to the validation of large simulations. CLIPPER solutions have been evaluated by several authors who extracted model counterparts of real data colocalized in space (and possibly time), treated both datasets identically and could quantify model-data misfits. For example, lagrangian time/space eddy scales [18], deep subtropical zonal flows [19], Agulhas rings properties [20], interannual variations of Labrador Sea Water characteristics [21] and of basin-scale eddy distribution [22] were validated and studied from colocalized datasets (drifters, ADCP, BRAVO timeseries, and altimeter fields, respectively). More quantitative validation studies have involved model-data correlations for tropical sea level anomalies [23], or stimulated the development of model skills with respect to current meter data [6]. These comparisons contribute to characterize the quality of numerical solutions and evaluate their relevance to interpret observations.

To validate eddy-permitting global ocean simulations more precisely (and to take advantage of the available datasets) requires additional developments that are underway in DRAKKAR with the support of the CNES/NASA Ocean Surface Topography Science Team. Local and global quantities (maps, sections, integral budgets, transports, etc) are computed during model simulations, and regularly compared to corresponding observations when and where available. This monitoring helps comparing various sensitivity experiments mutually and/or against the same references, such as the 3D evolution of temperatures and salinities, mass and heat transport of the main currents, global distribution and properties of the surface mixed-layer, of the sea-ice cover, of passive tracers, or the evolution of surface temperatures in the equatorial Pacific (NINO boxes, Fig. 1). Synthetic observations, colocalized with available observations, are extracted from model outputs and archived as observed databases to facilitate exchanges with real data users. The validation of long DRAKKAR simulations will be based on colocalized model-data comparisons with respect to the main observational datasets (historical hydrography, ARGO and altimeter fields). Identical diagnostics will be applied on real and synthetic observations to characterize model misfits on various periods, in various regions and depths ranges.

5. OBSERVING SYSTEM SIMULATION EXPERIMENTS (OSSE)

Ocean simulations provide a dynamical context to design observing systems and evaluate their performances a priori. Synthetic observations can be extracted from model outputs to assess observation/mapping errors or the potential for combining various datasets. For instance, high-resolution CLIPPER synthetic datasets helped evaluate the representativeness of hydrographic transects in terms of meridional overturning and transports, the impact of eddies on such observational estimates, and the uncertainty linked with the use of neighboring sections in estimating year-to-year changes of the meridional transports [24]. A dedicated high-resolution simulation has also been conducted by the CLIPPER team to characterize the space/time variability of sea-surface salinity over its full range of simulated scales, and their expected observability [25]. This run helped characterizing this virtually unknown field, and to design the SMOS (Soil Moisture and Ocean Salinity) mission. CLIPPER outputs were also used to demonstrate that the fluctuations of the Deep Western Boundary Current transport could be estimated from XBT-derived dynamics heights and SSH measurements in the North and South Atlantic [26]. Other observational systems were also assessed from CLIPPER outputs, including the ARGO float array alone [27] or in combination with SSH and SST satellite data [28], the GRACE (Gravity Recovery And Climate

Experiment) and GOCE (Gravity-field and steady-state Ocean Circulation Explorer) missions [29, 30].

One of DRAKKAR objectives is to pursue such collaborative investigations of observational systems, to characterize their representativeness and the observability of small-scale processes or climate indexes. The DRAKKAR group wishes to produce, distribute and analyze synthetic datasets (satellite, in-situ, up to kilometric resolutions) in collaboration with the OST/ST and observational communities.

6. PHYSICAL PROCESSES AND CIRCULATION FEATURES

The CLIPPER ensemble of 20-year Atlantic Ocean simulations has been widely used to put observed features (in particular WOCE and satellite data) into a broader context and to gain insight into their dynamical origin. These process studies, conducted in a realistic context, have concerned various time/space scales (days to decades, a few kilometers to thousands), regions (subpolar to equatorial, surface to bottom) and processes (water masses, dynamics, mutual interactions). Among other examples, theories and observations were compared with the four-dimensional model solution to investigate the equatorial circulation [31] and wave activity [23, 32], the link between Loop Current Eddy shedding and vorticity fluxes into the Gulf of Mexico [33], or the origin of subtropical zonal flows at depth [34].

Some authors took direct advantage of the wide range of time and space scales resolved in CLIPPER experiments. They showed the importance of mesoscale eddies in processes involved in climate variability, and in several cases, the limits of eddy parameterizations used in most non-turbulent climate models. For instance, the eddy-driven character of the post-convective restratification in the Labrador Sea was demonstrated by nesting a 1/15° model of this region into a 1/3° CLIPPER configuration [35]. Combined examinations of modeled and observed mesoscale activity showed the importance of instabilities and eddies in controlling the Indian-Atlantic heat flux in the Agulhas basin [20], the subduction process and its overall effect on North Atlantic mode waters [36], or the sensitivity the large-scale and mesoscale circulation to the North Atlantic Oscillation [22].

The realism of CLIPPER solutions against mean circulation schemes and water masse properties was shown to improve at each resolution increase (runs performed at 1°, 1/3°, 1/6°, up to 1/15° in the Labrador Sea). This is expected from the improved representation of the currents' natural scales, but three independent studies [22, 37, 38] based on CLIPPER and observed data led to another result, only showed in idealized models at that time. The resolution of mesoscale turbulence in ocean models increases the variance of important large-scale ocean indices (distribution and magnitude of eddies, intergyre heat fluxes) at interannual timescales (possibly slower). Non-linear scale interactions are increased by mesoscale processes and can generate intrinsic fluctuations of these indices (up to 40% of the large-scale interannual variability), even without interannual atmospheric forcing. In non-eddy-admitting coarse-resolution ocean models, these important contributions to climate variability are not resolved and cannot be parameterized through usual Fickian operators.

DRAKKAR extends the dynamical spectrum resolved in CLIPPER toward longer timescales (up to 50 years), larger and shorter space scales (up to global, down to 1/12° over the whole Atlantic). Along with better parameterizations and the explicit simulation of sea-ice and passive tracers, this spectral extension is expected to improve the consistency of simulated dynamics, the value of process studies, and the potential for fruitful collaborations with associated scientists.

7. CONCLUSIONS AND PERSPECTIVES

The aim of this paper was to illustrate various connections between numerical and observational oceanography. Observations are vital for the setup, improvement, validation, and analysis of simulations; simulated fields provide a framework to design and evaluate observing systems, to complement and interpret incomplete pictures of the real ocean. These expectations are certainly fulfilled in assimilation experiments, where the four-dimensional oceanic evolution is reconstructed from dispersed datasets of various origins (reanalyzes). Unconstrained simulations are globally less realistic than their assimilated counterparts with respect to individual observations, but they are complementary to such reanalyzes. Indeed, they are not limited to the years of sea-surface altimetry over which most ocean reanalyzes are performed; their realistic features, i.e. those that were actually observed, can be fully interpreted in terms of discrete primitive equation terms; they are necessary to simulate the free, non-linear oceanic response to changes in physical parameters or atmospheric forcings, thus allowing process studies of cause-to-effect relationships.

Both observational and numerical oceanography have improved and converged toward each other, especially during the WOCE years over which CLIPPER simulations were performed. Just like their observed counterparts, modeled datasets have strongly increased in size and quality, but much remains to be done to improve their complementarity. Quantitative model-data comparison approaches need to be developed on physical bases to distinguish model biases (thus guide numerical improvements) from realistic simulated features (thus orient physical investigations). When

possible, ocean reanalyzes need to be included in these validation exercises and in dynamical investigations.

Theoretical investigations, high-resolution modeling programs, observational missions, and reanalysis efforts tend toward a better understanding of the ocean dynamics in complementary ways. Convergences between the first approach and the other ones were not addressed in this paper, but they are crucial and deserve dedicated efforts. By making model outputs available to associated teams, the CLIPPER and DRAKKAR programs aim at stimulating and extending such interactions within the scientific community.

8. REFERENCES

1. Gille, S.T., Metzger, E.J., and Tokmakian, R. *Seafloor Topography and Ocean Circulation*, Oceanography, 17, 1, 47-54, 2004
2. Barnier B., Reynaud T., Beckmann A., Böning C., Molines J.M., Barnard S. et Jia Y, *On the seasonal variability and eddies in the North Brazil Current: Insights from model intercomparison experiments*, Progress in Oceanography, 48, 195-230, 2001.
3. Böning C., Dieterich C., Barnier B. et Jia Y., *Seasonal cycle of meridional heat transport in the subtropical North Atlantic: Intercomparison of the DYNAMO models and observations near 25 N,* Progress in Oceanography, 48, 231-254, 2001.
4. Penduff T., B. Barnier, K. Béranger, and J. Verron, *Comparison of near-surface mean and eddy flows from two numerical models of the South Atlantic Ocean*, J. Geophys. Res., 106, 16,857-16,867, 2001.
5. Penduff, T., B. Barnier, M.-A. Kerbiriou, and J. Verron, *How topographic smoothing contributes to differences between the eddy flows simulated by sigma- and geopotential-coordinate models*, J. Phys. Oceanog., 32, 1, 122-137, 2002.
6. Penduff, T., B. Barnier, J.-M. Molines, and G. Madec, *On the use of current meter data to assess the realism of ocean model simulations*, Ocean Modelling, 11/3-4, 399-416, 2005.
7. Barnier B., G. Madec, T. Penduff, J.-M. Molines, A.-M. Treguier, J. Le Sommer, A. Beckmann, A. Biastoch, C. Böning, J. Dengg, C. Derval, E. Durand, S. Gulev, E. Remy, C. Talandier, S. Theetten, M. Maltrud, J. McClean, and B. de Cuevas, *Impact of partial steps and momentum advection schemes in a global ocean circulation model at eddy permitting resolution*, Ocean Dynamics, in press.
8. Penduff, T., J. Le Sommer, G. Madec, and A.M. Treguier, *Effects of numerical advection schemes, lateral and boundary conditions in eddy-admitting global ocean simulations*, Ocean Modelling, in preparation.
9. Le Sommer, J., T. Penduff, G. Madec, and S. Theetten, *How momentum advection schemes affect current-topography interactions : sensitivity studies in the North Atlantic 1/4° DRAKKAR model*, Ocean Modelling, in preparation.
10. Bourlès, B., M. D'Orgeville, G. Eldin, Y. Gouriou, R. Chuchla, Y. DuPenhoat, and S. Arnault, *On the evolution of the thermocline and subthermocline eastward currents in the Equatorial Atlantic*, Geophys. Res. Lett., 29(16), 1785, 2002. doi:10.1029/2002GL015098.
11. Michel, S., and A-M Treguier : *Sensitivity of the Equatorial Undercurrent to mixing parameterizations in the CLIPPER model*, DRO/LPO report n°02-16, LPO, IFREMER-Brest, October 2002
12. Richards, K.J., and N.R. Edwards, *Lateral mixing in the equatorial Pacific : The importance of intertial instability*, Geophys. Res. Lett., 30(17), 1888, 2003. doi:10.1029/2003GL017768.
13. Reynaud T., P. Legrand, H. Mercier and B. Barnier, *A new analysis of hydrographic data in the Atlantic and its application to an inverse modelling study*, International WOCE Newsletter, 32, 29-31, 1998.
14. Tréguier A-M., B. Barnier, A. de Miranda, J.-M. Molines, N. Grima, M. Imbard, G. Madec, C. Messager, and S. Michel, *An eddy permitting model of the Atlantic circulation: evaluating open boundary conditions*, J. Geophys. Res., 106, 22115-22129, 2001.
15. Roether W., R. Schlitzer, A.Putzka, P. Beining, K.Bulsiewicz, G. Rohardt, and Delahoyde F., *A chlorofluoromethane and hydrographic section across Drake Passage: Deep water ventilation and meridional property transport*, J. Geophys. Research, 98, 14423-14435, 1993.
16. Park Y. H. and E. Charriaud, *Hydrography and baroclinic transport between Africa andAntarctica on WHP section I6,* International Woce Newsletter, 29, 13-16, 1997.
17. Barnier, B., *Forcing the ocean*, Ocean modeling and parametrization, 45-80, E.P. Chassignet and J. Verron (eds), 1998.
18. Lumpkin, R., A.M. Treguier, K Speer, *Lagrangian eddy scales in the Northern Atlantic Ocean,* J. Phys. Oceanogr., 32, 2425-2440, 2002.
19. Treguier, A.M., N. G. Hogg, M. Maltrud, K. Speer, and V. Thierry, *On the origin of deep zonal flows in the Brazil Basin*. J. Phys. Oceanogr., 33,580-599, 2003.
20. Treguier, A.M., O. Boebel, B. Barnier, and G. Madec, *Agulhas eddy fluxes in a 1/6° Atlantic model*, Deep Sea Res., II, 50, 251-280, 2003.
21. The CLIPPER Group, *Modélisation à haute résolution de la circulation dans l'Océan Atlantique, forcée et couplée océan-atmosphère.,. (http://www.ifremer.fr/lpo/clipper/reports/report2000/final_report.pdf), Final report*, 2001.
22. Penduff, T., B. Barnier, W.K. Dewar, and J.J. O'Brien, *Dynamical response of the oceanic eddy field to the North Atlantic Oscillation: a model-data comparison,* J. Phy. Oceanogr., 34 N°12, 2615-2629, 2004.
23. Illig S., B. Dewitte , N. Ayoub , Y. du Penhoat , G.

Reverdin , P. De Mey , F. Bonjean and G.S. E. Lagerloef*, Interannual Long Equatorial Waves in the Tropical Atlantic from a High Resolution OGCM Experiment in 1981-2000.* J. Geophys. Res., 109, C02022, doi:10.1029/2003JC001771, 2003.

24. Treguier, A.-M., C. Gourcuff, P. Lherminier, H. Mercier, B. Barnier, G. Madec, J.-M. Molines, T. Penduff, L. Czeschel, C. Böning, *Internal and forced variability along a section between Greenland and Portugal in the CLIPPER Atlantic model,* Ocean Dynamics, in press, 2006.
25. Molines, J.M., B. Barnier, C. Boone, P.Y. Le Traon, and M. Espino*, Scientific Requirements and Impact of Space Observation of Ocean Salinity for Modeling and Climate Studies,* ESA/ESTEC Contract n°14273/00/NL/DC., 2001.
26. Montenegro, A., and G. L. Weatherly, *A method for estimating barotropic variability in western boundary currents.* Submitted to J. Geophys. Res., 2004.
27. Guinehut, S., G. Larnicol, and P.Y. Le Traon : *Design of an Array of Profiling Floats in the North Atlantic from Model Simulations*. Journal of Marine Systems, 35, 1-2, 1-9, 2002.
28. Guinehut S., P.Y. Le Traon, G. Larnicol and S. Philipps, *Combining Argo and remote-sensing data to estimate the ocean three-dimensional temperature fields - A first approach based on simulated observations.* Journal of Marine System, 46, Issues 1-4, 85-98, 2004
29. Ganachaud, A., and H. Mercier: *Ocean response to meridional Ekman transport in the Atlantic and implication for gravity missions*, Geophys. Res. Lets., December 14th 2002, DOI 10.1029/2002GL 015291, 2002
30. Legrand, P., *Future gravity missions and quasi-steady ocean circulation*, Earth, Moon and planets, 94(1-2), 57, 2004
31. Elmoussaoui, A., M. Arhan, and A.M. Treguier, *Model-inferred upper ocean circulation in the eastern tropics of the North Atlantic*, Deep Sea Research I, 52, 7, 1093-1120, July 2005.
32. Thierry, V., A. M. Treguier and H. Mercier, *Numerical study of the annual and semi-annual fluctuations in the deep equatorial Atlantic ocean*. Ocean Modelling , 6, 1-30, 2004
33. Candela J, S. Tanahara, M. Crepon, and B. Barnier, *The Yucatan channel flow: observations vs CLIPPER ATL6 and MERCATOR PAM05 models*., J. Geophys. Res., 108 C12, 3385 doi:10.1029/2003JC001961, 2003
34. Treguier, A. M., Hogg, N. G., Maltrud, M., Speer, K., and Thierry, V, *The Origin of Deep Zonal Flows in the Brazil Basin,* Journal of Physical Oceanography 33, 580-599, 2003.
35. Chanut, J., B. Barnier, W.G. Large, L. Debreu, T. Penduff, and J.-M. Molines, *Mesoscale eddies in the Labrador Sea and their contribution to convection and restratification*, in preparation for J. Phys. Oceanogr.
36. Valdivieso Da Costa, M., H. Mercier, A.M. Treguier, *Effects of the Mixed Layer Time Variability on Kinematic Subduction Rate Diagnostics*, Journal of Physical Oceanography, 35, 427-443, 2005.
37. Hall, N. M. J., B. Barnier, T. Penduff and J.M. Molines, *Interannual variation of Gulf Stream Heat transport in a numerical model forced by reanalysis data*, Climate dynamics. 23, 3-4, 341-351, 2004.
38. Cabanes, C., A. Colin de Verdière, and T. Huck, *Contributions of wind forcing and surface heating to interannual sea level variations in the Atlantic Ocean*, Journal of Physical Oceanography, in revision, 2006.

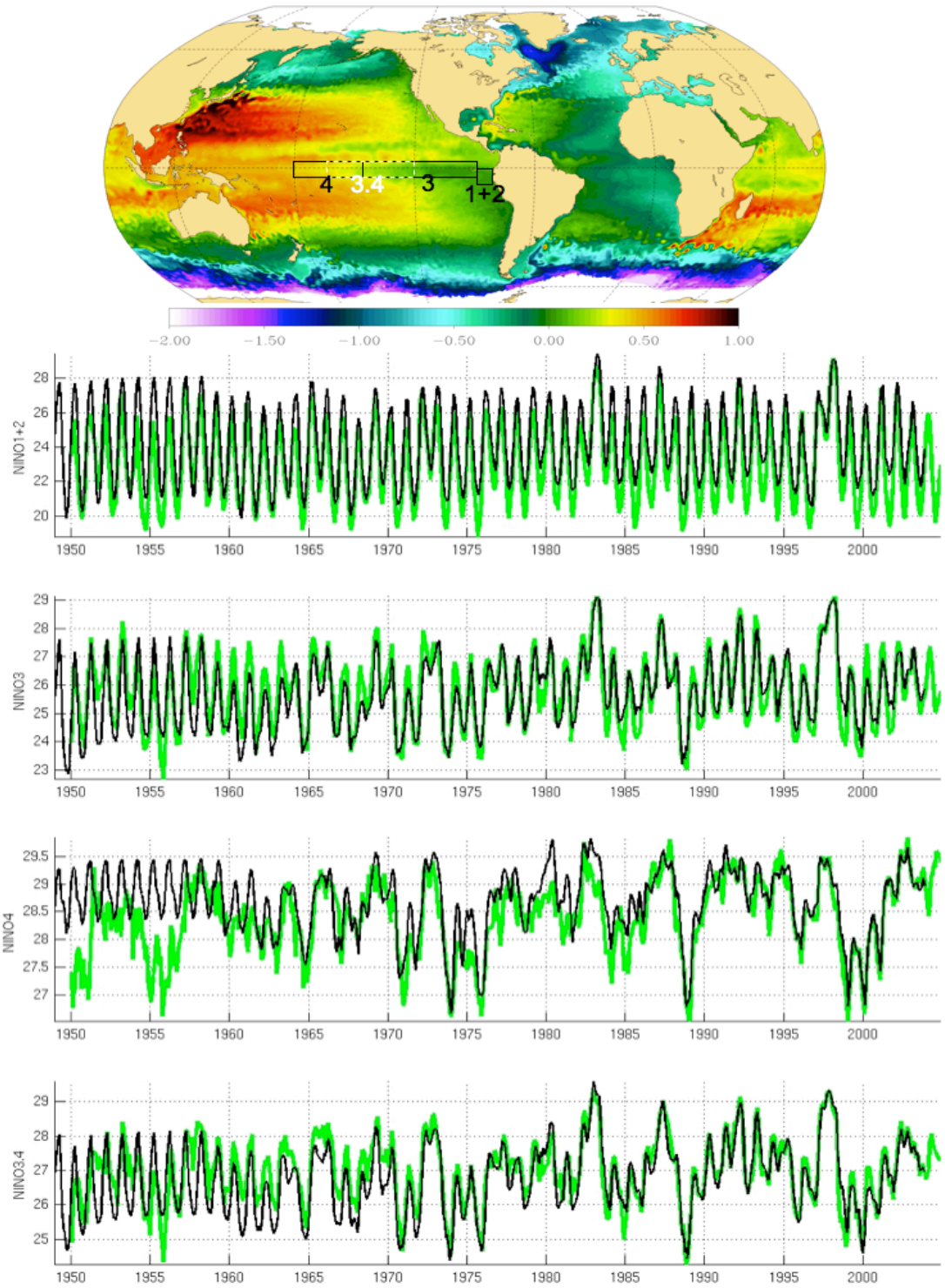

Figure 1: Upper : December snapshot of sea-surface height (m) from the DRAKKAR 1/4° model. Lower : 1949-2003 evolution of observed (green) et simulated (black) monthly sea-surface temperatures (SST) in the Tropical Pacific boxes shown in the upper plot. DRAKKAR 1/2° run, CORE interannual forcing[1]. Over the post-spinup phase (1958-2003), correlation coefficients between model and real SSTs lie between 0.88 et 0.95.

1 Large W., and S. Yeager, 2004. Diurnal to decadal global forcing for ocean and ice models: the datasets and flux climatologies. NCAR technical note: NCAR/TN-460+STR. CGD, National Center for Atmospheric Research.

ANNEX 3

DRAKKAR :modélisation à haute résolution de la variabilité océanique au cours des 50 dernières années

Lettre du PIGB N°19

May 2006

DRAKKAR : modélisation à haute résolution de la variabilité océanique au cours des 50 dernières années

La variabilité océanique affecte sensiblement le climat terrestre aux échelles interannuelles à décennales. Notre compréhension de cette variabilité reste toutefois limitée par la complexité des processus à l'œuvre et le manque d'observations historiques. Le programme DRAKKAR vise à compléter par la modélisation numérique la recherche observationnelle et théorique sur le climat océanique des dernières décennies ainsi que sur les processus qui le contrôlent.

Climat et turbulence océaniques

L'océanographie physique a beaucoup progressé depuis 15 ans grâce à l'observation globale de la surface des océans par satellite. Depuis 2000, le réseau mondial de flotteurs profilants autonomes ARGO (**http://www.argo.ucsd.edu/**) étend progressivement aux masses d'eau des 2 000 premiers mètres ce suivi global océanique en temps réel. Ces données sont précieuses pour l'étude du milieu mais trop superficielles (satellites) ou trop dispersées en espace (flotteurs) pour décrire avec précision la turbulence de méso-échelle océanique (tourbillons de 20 à 200 km de diamètre). Omniprésente du fait de l'instabilité générale des courants océaniques, cette turbulence assez mal connue affecte en retour la dynamique et la thermodynamique des océans. Plusieurs études récentes soulignent également son impact sur la variabilité des bassins à l'échelle interannuelle à décennale, via les flux air-mer (Caniaux *et al.*, 2005), l'évolution des masses d'eau (Mémery *et al.*, 2005 ; Chanut *et al.*, 2005), ou les échanges de chaleur entre bassins (Treguier *et al.*, 2003). Cette dynamique non-linéaire serait ainsi responsable d'une part significative de la variabilité océanique à basse fréquence (Dewar, 1998 ; Hall *et al.*, 2004 ; Penduff *et al.*, 2004).

La plupart des simulations océaniques destinées à l'étude du climat ne représentent pas la turbulence de méso-échelle et ses effets non-linéaires, mais utilisent des paramétrisations dissipatives (viscosité, diffusion turbulente) qui tendent à amortir la variabilité basse fréquence. En effet, les processus qui contrôlent l'évolution océanique occupent une immense gamme d'échelles de temps et d'espace, de la seconde au millénaire, du centimètre à l'océan global. Il est impossible de simuler explicitement les plus fins d'entre eux dans une simulation globale, mais on en représente (imparfaitement) l'impact via des paramétrisations basées sur des lois physiques. Augmenter la résolution des modèles jusqu'à simuler explicitement les effets de la méso-échelle permet de s'affranchir d'une

DRAKKAR : high-resolution modeling of ocean variability over the last 50 years

The ocean variability substantially affects the earth's climate on interannual to decadal time scales. Our understanding of this variability remains limited by the complexity of the processes involved and the lack of historical observations. The DRAKKAR modeling program aims at complementing theoretical and observational research on the oceanic climate and its controlling processes over the last decades.

Ocean climate and turbulence

*Physical oceanography has made a great step forward over the last 15 years of global sea-surface observation by satellite. Since 2000, the global ARGO array of profiling floats (**http://www.argo.ucsd.edu/**) progressively extends this global ocean monitoring to the upper 2 000 meters. These data are crucial for research, but too superficial (satellites) or dispersed in space (floats) to precisely describe the oceanic mesoscale turbulence (20-200km-scale eddies). This turbulence is ubiquitous due to the general instability of ocean currents and, in turn, affects the ocean's dynamics and thermodynamics. Several studies also highlight the impact of mesoscale turbulence on processes implied in the interannual-to-decadal oceanic variability, such as air-sea fluxes (Caniaux et al., 2005), the life cycle of water masses (Mémery et al., 2005; Chanut et al., 2005), or inter-basin heat exchanges (Treguier et al., 2003). These nonlinear features may thus generate a significant part of the oceanic low-frequency variability (Dewar, 1998 ; Hall et al., 2004 ; Penduff et al., 2004).*

Most oceanic simulations dedicated to climate studies do not resolve the mesoscale turbulence and its nonlinear effects, but use dissipative parameterizations (turbulent viscosity and diffusivity) that tend to damp the low-frequency variability. Indeed, the processes that control the ocean's evolution cover a huge range of time and space scales, from seconds to millennia, from centimeters to the global ocean. It is impossible to explicitly simulate the smallest scales in global simulations, so that the impact of certain ones are (imperfectly) represented via physically-based subgrid-scale parameterizations. Increasing ocean model resolutions allows the explicit resolution of mesoscale effects, and avoids the use of certain parameterizations used in present climate models. The representation of entrainment, the impact of small-scale mixing or surface waves still requires parameterizations. Multi-decadal, high-resolution oceanic simulations are thus necessary to improve the representation of the ocean's general circulation (main currents, inter-basin exchanges, the cycle of water masses) and better understand the contributions of mesoscale turbulence to the climatic variability (instabilities, response to the atmosphere, modes of variability).

partie des paramétrisations utilisées dans les modèles climatiques actuels. L'entraînement, le mélange à petite échelle ou l'effet des vagues restent toutefois paramétrés.

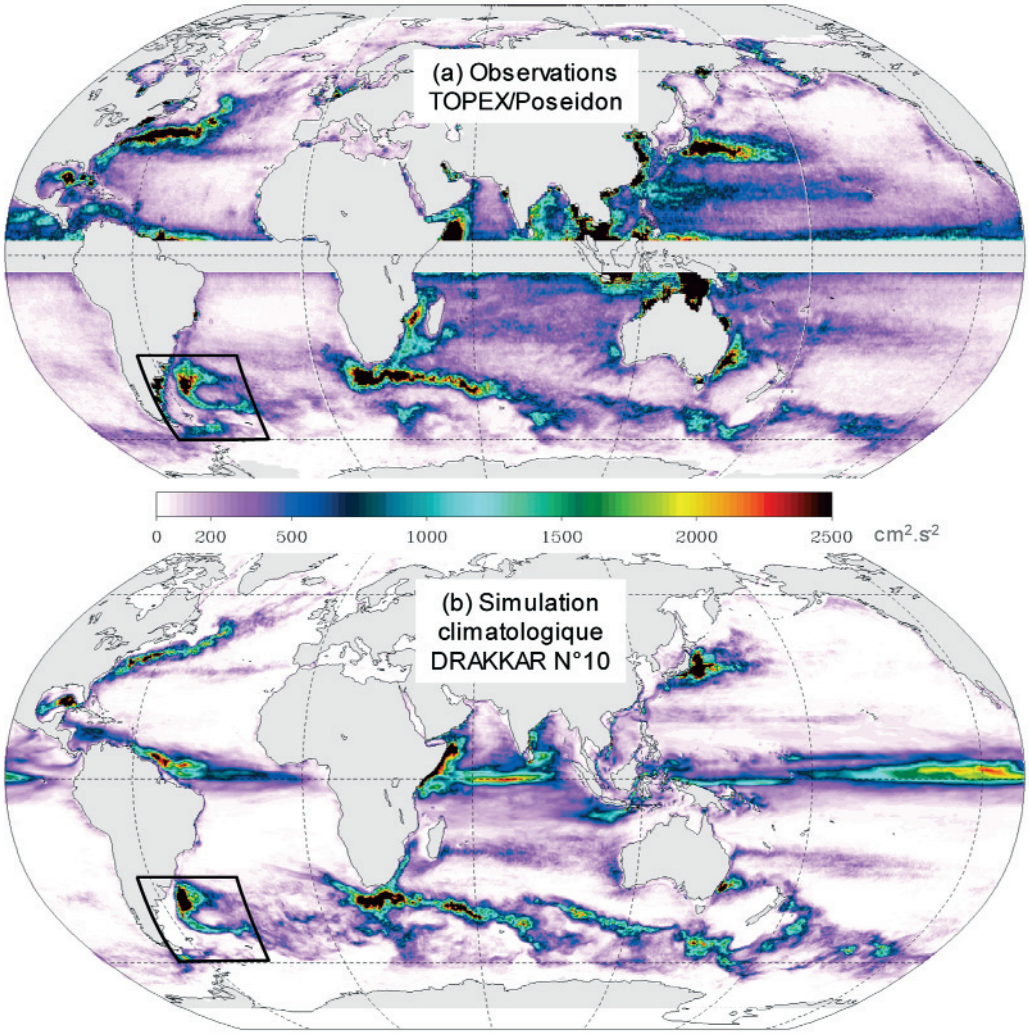

Figure 1 - Energie cinétique climatologique de la turbulence océanique à méso-échelle en surface (en cm²/s²). Image a : déduite de 10 ans de mesures altimétriques du satellite TOPEX/Poseidon (quantité non observable dans la bande tropicale). Image b : déduite de la simulation climatologique globale DRAKKAR n°10. Malgré une sous-estimation globale des niveaux d'énergie due à sa résolution encore modeste, le modèle positionne très correctement les régions de forte activité tourbillonnaire et les grands courants océaniques. Les cadres indiquent la zone de Confluence présentée en figure 2. Modèle NEMO, programme DRAKKAR, 2005.

Climatological surface kinetic energy of mesoscale eddies (cm²/s²). Image a: from 10 years of satellite measurements by the TOPEX/Poseidon altimeter (non observed in the tropical band). Image b: from the global climatological DRAKKAR simulation #10. The model simulates very correctly the regions of strong eddy activity and the main currents, despite a general underestimation of energy levels due to the still modest spatial resolution. NEMO model, DRAKKAR program, 2005.

Des simulations océaniques à haute résolution s'étendant sur plusieurs décennies sont donc nécessaires pour bien représenter la circulation générale océanique (grands courants, échanges entre bassins, cycle des masses d'eau), et mieux comprendre la contribution des tourbillons à la variabilité climatique (instabilités, réponse à l'atmosphère, modes de variabilité).

The DRAKKAR program

The DRAKKAR team includes 12 scientists and engineers from five French laboratories and European teams:

- *LEGI (Grenoble),*
- *LPO (Brest),*
- *LODYC (Paris),*
- *LEGOS (Toulouse),*
- *LSCE (Gif-sur-Yvette),*

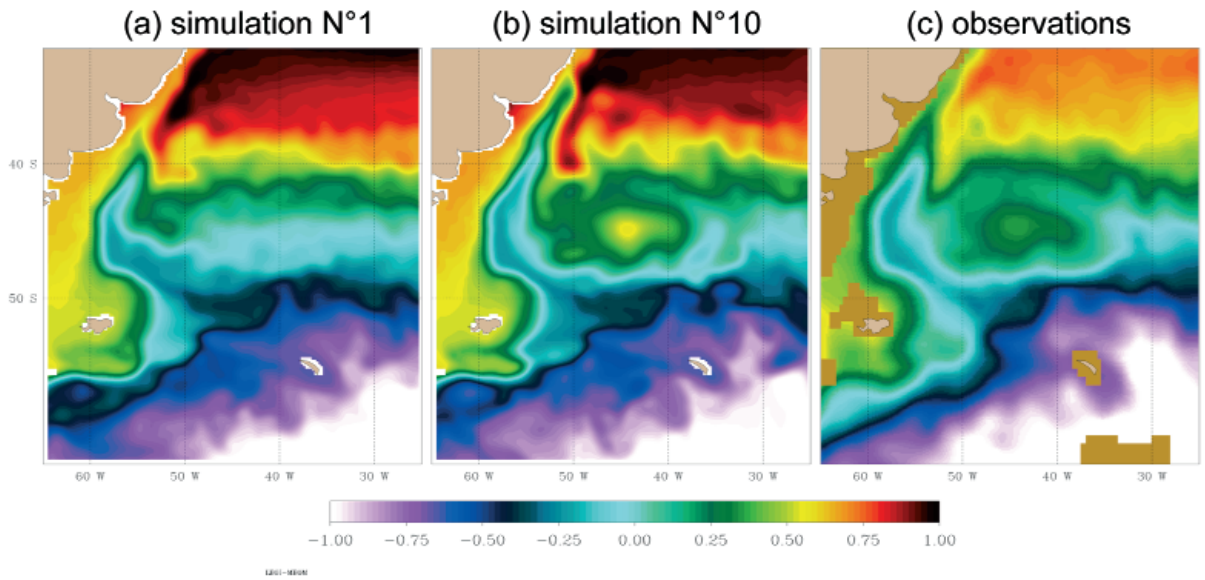

Figure 2 – Topographie de surface moyenne climatologique dans la zone de Confluence au large de l'Argentine (en mètres). Images a et b : déduites respectivement des simulations climatologiques globales DRAKKAR n°1 et n°10. Image c : issue d'une synthèse d'observations sur la période 1992-2002 (Niiler *et al.*, 2003). La topographie de surface océanique indique notamment la direction et l'intensité des courants dans cette région de fort mélange entre des eaux en provenance du Pacifique et de l'Atlantique. Un travail sur les paramétrisations du modèle explique l'amélioration de la solution entre les deux simulations, visibles notamment sur l'Anticyclone de Zapiola (surélévation de la surface centrée sur 45°S-45°W, en vert-jaune) et sur l'extension vers le nord du Courant des Malouines en provenance du Cap Horn (en bleu-vert le long du continent). Modèle NEMO, DRAKKAR program, 2005.

Mean climatological sea surface topography (metres) in the Confluence region off the Argentinian shelf. Images a and b: deduced fromthe global climatological DRAKKAR simulations #1 and #10, respectively. Image c: deduced from a synthesis of observations over the period 1992-2002 (Niiler et al., 2003). The oceanic sea-surface topography indicates the direction and intensity of currents in this region where waters from the Pacific and the Atlantic basins are strongly mixed together. Improved numerical parameterizations in simulation #10 explain the better representation of the Zapiola anticyclone (sea-surface «bump» centered at 45°S-45°W, yellow-green), and of the northward extension of the Malvinas Current coming from Cape Horn along the continent (blue-green). NEMO model, DRAKKAR program, 2005.

Le programme DRAKKAR

L'équipe DRAKKAR est constituée d'une douzaine de chercheurs et ingénieurs issus de cinq laboratoires français et d'équipes européennes :

- LEGI (Grenoble),
- LPO (Brest),
- LODYC (Paris),
- LEGOS (Toulouse),
- LSCE (Gif-sur-Yvette),
- IFM-GEOMAR (Kiel, Allemagne),
- Shirshov Institute of Oceanology (Moscou, Russie),
- Université d'Helsinki (Finlande).

Des équipes de recherche françaises et étrangères sont associées à DRAKKAR ; elles participent à la définition des simulations et contribueront à leur exploitation scientifique. Citons par exemple des projets de recherche sur le couplage entre physique, biologie, et le cycle du carbone, la variabilité à grande échelle (océan austral et tropical, impact des vents catabatiques en Antarctique) ou à l'échelle régionale (archipel Canadien, upwellings côtiers, Golfe du Mexique, etc.).

Le programme DRAKKAR construit une hiérarchie de modèles

- *IFM-GEOMAR (Kiel, Germany),*
- *Shirshov Institute of Oceanology (Moscow, Russia),*
- *University of Helsinki (Finland).*

Additional research teams are associated to DRAKKAR and contribute to the definition and the scientific analysis of numerical simulations. For instance, associated research projects concern the coupling between marine physics, biology, and carbon cycle, the ocean's variability at large scale (Austral and tropical oceans, impact of katabatic winds around Antarctica) or regional scale (Canadian Archipelago, coastal upwelling regimes, Gulf of Mexico, etc.).

The DRAKKAR project team is building a hierarchy of numerical models based on the NEMO system («Nucleus for European Modelling of the Ocean»). This system includes the ocean code OPA9, the sea-ice code LIM, and the biogeochemical tracer code TOP. These models simulate the evolution of the ocean circulation and water masses, sea-ice, and dissolved tracers (CFCs, ^{14}C) over 46 levels distributed between the ocean's surface and bottom. These simulations are forced at the surface by daily global reconstructions of atmospheric winds, temperatures and humidity over the last 50 years.

An eddy-admitting resolution of 1/4° (about 10-25 km) is

numériques sur la base du système NEMO «Nucleus for European Modelling of the Ocean». Ce système inclut l'outil national de modélisation océanique OPA9, le modèle de glace de mer LIM, et le code de traceurs et biogéochimie TOP. Ces modèles simulent sur la période 1950-2005 l'évolution tridimensionnelle de la circulation et des masses d'eaux océaniques, des glaces de mer, et de composants chimiques dissous (CFCs,^{14}C) sur 46 niveaux répartis de la surface au fond. Ces simulations sont forcées en surface par des reconstructions globales journalières des vents, de la température et de l'humidité atmosphériques depuis les années 50.

Une résolution horizontale de 1/4° (soit 10-25 km), qui permet aux tourbillons de se développer, est utilisée dans une configuration de l'océan global, et dans une configuration resserrée autour de l'Atlantique Nord et des Mers Nordiques (de 30°S à 80°N). A l'horizon 2006, l'évolution depuis 1950 de ce dernier bassin sera simulée avec une résolution nettement accrue des tourbillons (résolution de 1/12°). Le logiciel AGRIF (*Blayo et Debreu, 1999*) permettra en outre des accroissements locaux de la résolution de ces configurations pour des études de paramétrisation ou d'océanographie régionale.

La construction de ce dispositif expérimental repose sur une coopération entre océanographes modélisateurs et observateurs, de climatologues, d'atmosphériciens, de numériciens et de biogéochimistes. Ce programme requiert d'importants moyens de calcul car nos objectifs concernent l'impact à long terme (longues intégrations) de processus de fine échelle (haute résolution spatiale) à l'échelle de bassins entiers (vastes domaines).

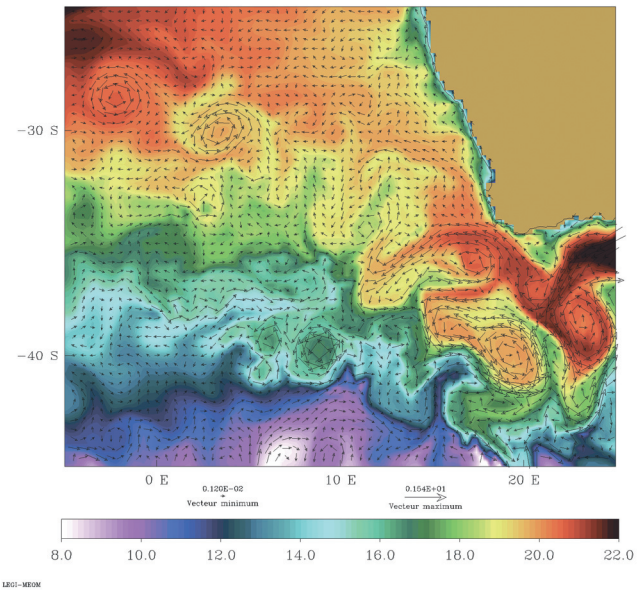

Figure 4 - Température (en °C) et courants instantanés à 30 m de profondeur au sud de l'Afrique, simulés à la fin décembre (dixième année, simulation climatologique globale DRAKKAR n°10). Le courant chaud des Aiguilles quitte la côte au sud de l'Afrique et rétroflecte vers l'est. Les tourbillons produits par l'instabilité de cette rétroflexion piègent des eaux chaudes de l'Océan Indien et les transportent vers l'Atlantique. Modèle NEMO, programme DRAKKAR, simulation climatologique N°10, 2005.

Temperature et currents at 30 m south of Africa. The warm Agulhas Current leaves the coast and retroflects toward the Indian Ocean. The rings produced by instability processes trap warm waters and carry them toward the northwest. NEMO model, DRAKKAR program, 2005.

Objectifs scientifiques

Il s'agit d'une façon générale d'étudier les processus impliqués dans l'évolution de l'océan global, de

used in a global ocean configuration, and in a North Atlantic/Nordic Seas configuration (from 30°S to 80°N). In 2006, the evolution of this latter basin will be simulated over the last 50 years with a much finer resolution of mesoscale structures (1/12°). In addition, the AGRIF package (Blayo and Debreu, 1999) will allow local increases of the resolution of DRAKKAR configurations for regional oceanography or parameterization studies.

The construction of this numerical system relies on the cooperation of ocean modelers, observationalists, climatologists, atmosphericists, numericians, and biogeochemists. This system requires important computational resources because our objectives concern the long-term impact (long integrations) of fine-scale structures (high spatial resolutions) over whole basins (large domains).

Scientific objectives

We plan to study the processes involved in the variability of the global ocean, of the North Atlantic and the Nordic Seas over the last 50 years. The numerical simulations will be compared to available in-situ and satellite observations, and analyzed in terms of dominant processes with respect to existing theories. These simulations will help extend the study of the interactions between oceanic eddies and currents responding to the slow atmospheric variability (Penduff et al., 2004). The 1/4° and 1/12° North Atlantic/Nordic Seas simulations will be forced along their boundaries by global simulation outputs. We will take advantage of the model hierarchy by modifying the lateral and surface forcing of regional simulations, in order to distinguish the local and remotes origins of the North Atlantic variability.

An example of interaction between mesoscale processes and climate: mode waters

Mode waters have an important contribution in the interannual-to-decadal variability of the ocean. They are currently

l'Atlantique Nord et des Mers Nordiques depuis les années 1950. Les simulations numériques seront confrontées aux observations *in-situ* et satellitaires disponibles, analysées et confrontées aux théories existantes en termes de processus dominants. Ces simulations permettront par exemple d'affiner l'étude de la méso-échelle et des courants océaniques en réponse aux lentes fluctuations atmosphériques (Penduff *et al.*, 2004). Les simulations de l'Atlantique Nord et des Mers Nordiques au 1/4° et au 1/12° seront forcées à leurs frontières par les champs issus des simulations globales. Nous tirerons profit de la hiérarchie de modèles en modifiant ces forçages latéraux et atmosphériques, afin de caractériser la part de la variabilité Nord Atlantique forcée localement ou à distance.

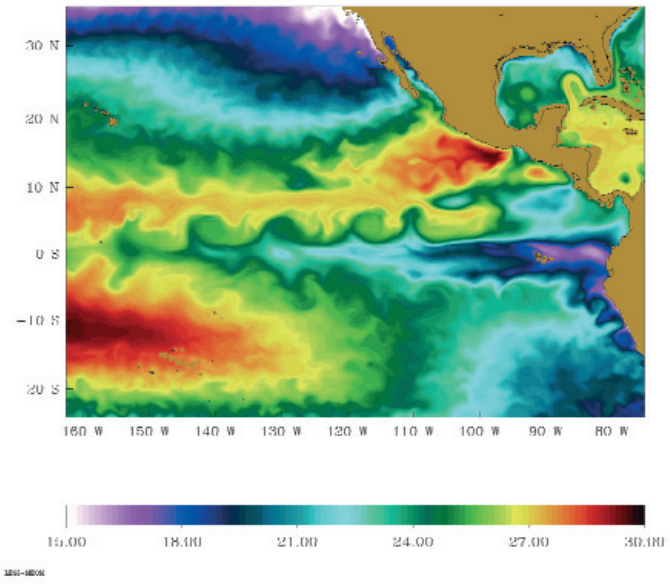

Figure 5 - Température instantanée (en °C) à 30 m de profondeur à l'est du Pacifique Tropical, simulés à la fin décembre (dixième année, simulation climatologique globale DRAKKAR n°10). Le courant d'upwelling transporte des eaux froides (en bleu) vers le nord le long des côtes de l'Amérique du Sud; les tourbillons de méso-échelle qu'il produit mélangent ces eaux avec les eaux environnantes. En atteignant l'équateur, les ondes tropicales d'instabilité modifient le processus de mélange. Modèle NEMO, programme DRAKKAR, simulation climatologique N°10, 2005.

Temperature at 30 m in the eastern tropical Pacific. The unstable upwelling current mixes and brings cold waters (blue) to the north along the South American coast. These waters join the equatorial current and are further mixed by tropical instability waves. NEMO model, DRAKKAR program, 2005.

Un exemple d'interaction entre processus à méso-échelle et climat : les eaux modales

A la fois actrices et témoins de la variabilité océanique interannuelle à décennale, les masses d'eau modales sont surveillées et étudiées dans le cadre des campagnes OVIDE (sections répétées entre Groenland et Portugal. **http://www.ifremer.fr/lpo/ovide/**) et des simulations DRAKKAR. Au cours de leur trajet en Atlantique Nord, ces eaux de surface sont refroidies par l'atmosphère et s'homogénéisent sur plusieurs centaines de mètres, mémorisant ainsi l'état de l'atmosphère en termes de température, salinité ou teneur en CO_2. Une partie de ces eaux va alors être subductée sous la surface pour y circuler plusieurs années, et pourra éventuellement restituer ces signaux vers l'atmosphère dans d'autres régions. Les processus impliqués dans l'évolution de ces eaux modales (interactions air-glace-mer, advection, subduction, diffusion, dispersion) sont affectés par des processus de grande et moyenne échelle dont la contribution relative est mal connue. Ces incertitudes planent aussi sur les mécanismes de propagation des Grandes Anomalies de Sel, suivies en surface du Spitzberg aux moyennes latitudes Atlantiques, et dont l'impact à grande échelle s'est manifesté au cours des dernières décennies (Belkin, 2004).

*monitored and studied within the OVIDE program (repeated transects between Greenland and Portugal. **http://www.ifremer.fr/lpo/ovide/**), and they will be investigated from high-resolution DRAKKAR simulations. These surface waters transfer their heat to the atmosphere during their journey across the North Atlantic. This forms an homogeneous surface layer several hundreds of meter thick that captures part of the atmospheric state in terms of heat, salt or CO_2 content. Part of these waters then subducts and continues its trip beneath the ocean's surface. After several years, they may eventually affect the atmosphere in other regions. The processes involved in the evolution of mode maters (air-sea-ice interactions, advection, subduction, diffusion, dispersion) are sensitive to large- and meso-scale mechanisms whose relative contributions are poorly known. Similar uncertainties also concern the mechanisms involved in the propagation of Great Salinity Anomalies. These anomalies led to substantial large-scale oceanic changes between Spitzbergen and the mid-latitude Atlantic over the last decades (Belkin, 2004).*

Simulation results

The scientific value of our simulations will depend on the models' ability to reproduce, without data assimilation (i.e. without regular corrections of the model state), a variable but globally stable multi-decadal solution which is realistic in terms of processes and with respect to available observations. Since observations are quite rare, our three-dimensional knowledge of the ocean state is often based on observational syntheses typical of the several decades. The DRAKKAR models are thus implemented and adjusted during preliminary 10-year "climatological" simulations (forced by the repetition of a year typical of recent decades). These climatological simulations are compared to observational syntheses in terms of paths and transports of the main currents, cycle and characteristics of water masses, etc. About ten 10-year climatological simulations allowed us to improve the physics of the 1/4° global

Résultats de simulation

La portée des études scientifiques issues de nos simulations dépendra de la capacité des modèles à reproduire, sans assimilation directe de données, (c'est-à-dire sans l'apport régulier de données mesurées qui permettent de recaler le modèle), une circulation variable mais stable sur plusieurs décennies, réaliste en termes de processus et en regard des observations océaniques. Ces dernières étant rares, notre connaissance tridimensionnelle du milieu se base souvent sur des synthèses d'observations représentatives d'une ou plusieurs décennies. Nos modèles sont donc mis au point lors de simulations préliminaires de 10 ans «climatologiques» (forcées par la répétition d'une année atmosphérique typique des décennies récentes) que nous évaluons vis-à-vis de ces synthèses d'observations en termes de trajectoire et transport des courants, cycle et caractéristiques des masses d'eau, etc. Une dizaine de simulations climatologiques de 10 ans a ainsi permis d'affiner la physique du modèle global 1/4°, comme l'illustrent les images présentées plus loin. L'absence d'observations régulières et détaillées complique l'évaluation des simulations, mais plaide aussi pour des investigations conjointes d'observations et de simulations.

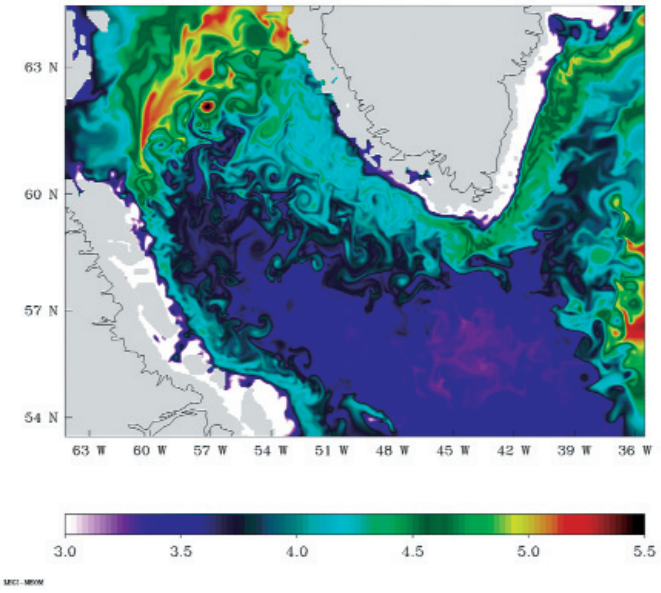

Figure 6 - Température instantanée à 200 m de profondeur (en °C) entre le Groenland et le Canada, simulée au début du printemps. La haute résolution horizontale (3,5 km) permet de simuler finement la turbulence de moyenne échelle dans cette région et d'en étudier l'impact climatique à distance. Les tourbillons mélangent des masses d'eau d'origine Arctique (en blanc) et subtropicales (en rouge et vert) dans cette région fortement refroidie par l'atmosphère. Les eaux produites par la plongée de ces eaux de surface rejoignent ensuite la zone de Confluence le long du continent américain entre 2 000 et 3 000 m de profondeur. Modèle OPA avec raffinement de maillage AGRIF, LEGI (Chanut *et al.*, 2005).

Temperature at 200 m between Greenland and Canada in early spring. The AGRIF package is used to enhance the local resolution up to 1/15°. This resolution is necessary to simulate and study the impact of mesoscale processes, which mix Arctic (white) and subtropical (red and green) waters subjected to strong atmospheric cooling. The deep waters produced by sinking surface waters then flow toward South America along the American shelf. OPA model with AGRIF grid refinement, LEGI, 2004.

Les altimètres satellitaires, comme TOPEX/Poseidon ou son successeur Jason, mesurent à la surface du globe l'énergie cinétique de la turbulence de méso-échelle océanique. La comparaison entre les climatologies qui en sont déduites et leur équivalent simulé (figure 1) montre que le modèle global positionne très correctement la plupart des grand courants et la turbulence qu'ils génèrent. Un travail sur les schémas numériques (Le Sommer *et al.*, 2006 ; Penduff *et al.*, 2006) a permis d'améliorer dans plusieurs régions-clé (exemple de l'Atlantique sud-ouest

model, as shown in the figures commented below. The sparseness of observations makes model-data comparisons difficult, but also encourages combined investigations of numerical simulations and observational data.

Satellite altimeters (e.g. TOPEX/Poseidon, ERS, or its successor Jason) measure the surface kinetic energy (EKE) of mesoscale ocean eddies at quasi-global scale. Comparing altimeter-derived EKE climatologies with their DRAKKAR counterparts (figure 1) shows that the location of the main currents and associated turbulence maxima are fairly well located in the global simulations. Improved numerical schemes (Le Sommer et al., 2006; Penduff et al., 2006) led to improved physics in several key regions (example of the south-west Atlantic in figure 2). The realism of recent DRAKKAR simulations is now comparable to those deduced from more computationally-demanding models (Barnier et al., 2006).

Figures 3 to 6 illustrate in three regions the coexistence of dynamical components involved in the ocean's low-frequency variability:

- *the large-scale circulation, which advects atmospherically-induced and intrinsically-generated climatic anomalies within and between basins;*
- *the sea-ice, that directly affects the ocean's salinity and its interaction with the atmosphere ;*
- *the omnipresent mesoscale eddies, which affect many oceanic processes implied in the climatic variability.*

Grid refinements allow a very detailed simulation of mesoscale processes in particular regions, as illustrated in figure 6. The DRAKKAR hierarchy of models will help study the processes controlling the ocean variability over a wide range of space and time scales.

en figure 2) la physique du modèle. Les simulations récentes approchent désormais le réalisme de modèles nettement plus coûteux en ressources de calcul (Barnier et *al.*, 2006).

Les figures 3 à 6 illustrent dans trois régions climatiquement importantes la coexistence dans le modèle des composantes impliquées dans la variabilité basse fréquence :

- la circulation océanique de grande échelle qui redistribue d'une région à l'autre les perturbations forcées par l'atmosphère ou induites par la dynamique océanique ;
- la glace de mer qui affecte directement la salinité de l'océan et son interaction avec l'atmosphère ;
- les tourbillons de méso-échelle, omniprésents, qui affectent de nombreux processus océaniques impliqués dans la variabilité climatique.

Des raffinements de maillage, dont un exemple d'application est illustré en figure 6, permettent d'accroître localement la représentation de cette méso-échelle. La hiérarchie de modèles construite devrait donc contribuer à une meilleure compréhension des processus impliqués dans la variabilité océanique sur une vaste gamme d'échelles spatio-temporelles.

Collaborations et applications

Ces recherches sont accompagnées d'avancées technologiques (nouvelles configurations océaniques pour l'étude du climat) et d'échanges avec l'océanographie opérationnelle. Ainsi le modèle global 1/4°, développé dans le cadre de DRAKKAR avec la collaboration du GIE Mercator-Océan (**http://www.mercator-ocean.fr/**), est utilisé depuis octobre 2005 pour la prévision océanique et sera transféré prochainement au programme européen MERSEA (**http://www.mersea.eu.org/**). Réciproquement, Mercator-Océan développe une configuration Atlantique Nord 1/12° à des fins opérationnelles, configuration que nous adapterons prochainement pour nos objectifs scientifiques. Avec le soutien du CNES, le groupe DRAKKAR contribue enfin à la valorisation des missions d'observation satellitaire et in-situ (Jason, ARGO, etc.) par ses travaux sur l'intégration des mesures de flux air-mer pour le forçage des modèles océaniques et sur les méthodes de comparaison modèle-données. L'équipe DRAKKAR propose donc de fédérer la recherche dans différentes disciplines autour d'outils communautaires.

Site du programme DRAKKAR :
http://www.ifremer.fr/lpo/drakkar/

Collaborations and applications

These research topics come along with technical outcomes (new ocean configurations for climate studies) and exchanges with operational agencies. The 1/4° global model developed by DRAKKAR in collaboration with Mercator-Océan (http://www.mercator-ocean.fr/) is being used for ocean forecasts since October 2005, and will be transferred to the MERSEA European program (http://www.mersea.eu.org/). Conversely, Mercator-Océan develops a 1/12° Atlantic configuration for operational purposes which will be adapted and used by the DRAKKAR group for research applications. The French Space Agency (CNES) supports the use of in-situ and satellite observations (Jason, ARGO, etc) in DRAKKAR: use of satellite-derived air-sea flux measurements for the forcing of ocean models, improvement of model-data comparison methods, representativeness of observational systems, etc. The DRAKKAR project team thus proposes to federate research in complementary fields around collective tools.

Programme DRAKKAR :
http://www.ifremer.fr/lpo/drakkar/

Contact : Thierry Penduff
Laboratoire des Ecoulements Géophysiques et Industriels,
LEGI, UMR 5519 CNRS/UJF/INPG
BP53, 38041 Grenoble Cedex 9
Thierry.Penduff@hmg.inpg.fr

ANNEX 4

Impact of partial steps and momentum advection schemes in a global ocean circulation model at eddy permitting resolution

Published in Ocean Dynamics

November 2006

Ocean Dynamics
DOI 10.1007/s10236-006-0082-1

Barnier Bernard · Gurvan Madec · Thierry Penduff · Jean-Marc Molines · Anne-Marie Treguier · Julien Le Sommer · Aike Beckmann · Arne Biastoch · Claus Böning · Joachim Dengg · Corine Derval · Edmée Durand · Sergei Gulev · Elizabeth Remy · Claude Talandier · Sébastien Theetten · Mathew Maltrud · Julie McClean · Beverly De Cuevas

Impact of partial steps and momentum advection schemes in a global ocean circulation model at eddy-permitting resolution

Received: 2 September 2005 / Accepted: 22 March 2006

Abstract Series of sensitivity tests were performed with a *z*-coordinate, global eddy-permitting (1/4°) ocean/sea-ice model (the ORCA-R025 model configuration developed for the DRAKKAR project) to carefully evaluate the impact of recent state-of-the-art numerical schemes on model solutions. The combination of an energy–enstrophy conserving (*EEN*) scheme for momentum advection with a partial step (*PS*) representation of the bottom topography yields significant improvements in the mean circulation. Well known biases in the representation of western boundary currents, such as in the Atlantic the detachment of the Gulf Stream, the path of the North Atlantic Current, the location of the Confluence, and the strength of the Zapiola Eddy in the south Atlantic, are partly corrected. Similar improvements are found in the Pacific, Indian, and Southern Oceans, and characteristics of the mean flow are generally much closer to observations. Comparisons with other state-of-the-art models show that the ORCA-R025 configuration generally performs better at similar resolution. In addition, the model solution is often comparable to solutions obtained at 1/6 or 1/10° resolution in some aspects concerning mean flow patterns and distribution of eddy kinetic energy. Although the reasons for these improvements are not analyzed in detail in this paper, evidence is shown that the combination of EEN with PS reduces numerical noise near the bottom, which is likely to affect current–topography interactions in a systematic way. We conclude that significant corrections of the mean biases presently seen in general circulation model solutions at eddy-permitting resolution can still be expected from the development of numerical methods, which represent an alternative to increasing resolution.

Keywords Global ocean · Eddy-permitting ocean model · Momentum advection scheme · Partial step topography · Eddy/topography interactions

Responsible editor: Lee-Lueng Fu

B. Bernard (✉) · T. Penduff · J.-M. Molines · J. Le Sommer
Laboratoire des Ecoulements Géophysiques et Industriels,
Grenoble, France
e-mail: bernard.barnier@hmg.inpg.fr

G. Madec · C. Talandier
Laboratoire d'Océanographie Dynamique et de Climatologie,
Paris, France

A.-M. Treguier · S. Theetten
Laboratoire de Physique des Océans, Ifremer Centre de Brest,
Plouzané, France

A. Beckmann
Department of Physical Sciences, Division of Geophysics,
University of Helsinki,
Helsinki, Finland

A. Biastoch · C. Böning · J. Dengg
IfM-GEOMAR, Leibniz-Institut für Meereswissenschaften an der Universität Kiel,
Kiel, Germany

C. Derval · E. Durand · E. Remy
MERCATOR-Ocean,
Toulouse, France

S. Gulev
Shirshov Institut of Oceanography,
Russian Academy of Science,
Moscow, Russia

M. Maltrud
Fluid Dynamics Group, Los Alamos National Laboratory,
Los Alamos, USA

J. McClean
Scripps Institution of Oceanography, UCSD,
LA Jolla, USA

B. De Cuevas
National Oceanography Centre,
Southampton, UK

1 Introduction

In a special issue honoring the memory of Christian Le Provost, it is fitting for many of us who collaborated with him, sometimes very closely and for almost 20 years, to place the work presented here in relation to scientific

issues he stood by. Christian Le Provost's first involvement in the field of ocean circulation modeling was motivated by the World Ocean Circulation Experiment (WOCE) in the mideighties. His intuition was that among all processes which have a crucial influence in shaping the mean circulation, two of particular importance were overlooked: the mesoscale eddies and the constraint of the bottom topography. His early work therefore concentrated on process studies searching for a better understanding and modeling of the generation of eddies in the presence of topography (Verron and Le Provost 1985; Verron et al. 1987) and the interaction of turbulent large-scale flows with topography (Barnier and Le Provost 1993). He also emphasized the crucial importance of numerics on the realism of model solutions (Blayo and Le Provost 1993). Christian convinced himself and his group that accurate modeling of the effect of bottom topography on ocean nonlinear flows is a key to achieve realistic simulations of the global ocean circulation. This belief underlay the model intercomparison DYNAMO project (DYNAMO Group 1997), which he designed with Jürgen Willebrand (Willebrand et al. 2001).

Building and running ocean models able to simulate the world ocean circulation with great realism require a great variety of scientific skills. Christian Le Provost was aware that gathering all the necessary skills within a single research team as the one he was leading would be difficult. Consequently, he always favored community experiments in the spirit of the Community Model Experiment carried out under WOCE (Bryan and Holland 1989; Böning and Bryan 1996). This concept of community projects, which Christian shared with Jürgen Willebrand, Bill Holland, and others, was at the core of the DYNAMO project. It was at the origin of the French CLIPPER project (Treguier et al. 1999) and is the basis of the international DRAKKAR project, which is briefly presented here. These are projects in which Christian Le Provost actively participated.

The present paper is strongly inspired by the issues mentioned above. It presents recent advances in modeling the general ocean circulation at eddy-permitting resolution achieved in the framework of the European modeling project DRAKKAR. Indeed, eddy-permitting models are still worth exploring and enhancing, despite the existing higher resolution models because they will be the target resolution of the next generation of climate models. Improvements presented here mainly concern the representation of ocean flows in regions where the circulation is dominated by nonlinearities and is strongly constrained by bottom topography. These results were obtained by using a new numerical treatment of the nonlinear advection term in momentum equations and a partial step representation of the bottom topography.

The paper is organized as follows. Section 2 describes the eddy-permitting, global, 1/4° model configuration implemented by the project, ORCA-R025. It also presents the mean circulation produced by ORCA-R025 under a climatological atmospheric forcing. Section 3 evaluates the impact of new numerical choices regarding bottom topography and momentum, in direct relation with Christian Le Provost early intuition, by comparison of ORCA-R025 simulations with observations and other state-of-the-art model simulations at equivalent or higher resolution. Section 4 identifies key issues where problems remain and ways of improving.

2 Global 1/4° DRAKKAR configuration ORCA-R025

2.1 DRAKKAR project

During the last decade, scientists participating in the DRAKKAR[1] project fostered cooperative activities within the European project DYNAMO (Dynamics of North Atlantic Models, DYNAMO Group 1997) and between their respective national projects, CLIPPER in France (Treguier et al. 1999) and FLAME (Family of Linked Atlantic models) in Germany (Böning et al. 2003). The challenge of developing realistic global ocean models suited for a wide range of applications will be better met with an effective integration and coordination of activities and complementary expertises of the groups. This yielded the DRAKKAR concept, a European modeling project, which provides the framework for joint and coordinated modeling studies between research groups in France, Germany, Russia, and Finland.

One primary concern of the project is related to the circulation and variability in the North Atlantic Ocean as driven by the atmospheric forcing, by interactions between processes of different scales, by exchanges between basins and regional circulation features (including the Nordic Seas), and by the influence of the world ocean circulation (including the Arctic and Southern Oceans and the Agulhas retroflection region). To achieve these scientific objectives, DRAKKAR is carrying out coordinated realistic simulations of the ocean circulation at regional and global scales with pertinent atmospheric forcing and resolutions high enough to ensure physical consistency over the range of scales which are dynamically important (i.e., from eddy to global and from day to decade).

For its first objective, the project has built a hierarchy of numerical model configurations from global to regional scale, each based on the NEMO[2] modeling system, which presently includes the latest version of the primitive equation, free surface (Roullet and Madec 2000) ocean circulation code OPA9 (Madec et al. 1998) coupled to the multilayered sea-ice code LIM2 (Fichefet et al. 1997). This hierarchy of models includes the ORCA-R025 configuration, an eddy-permitting, global ocean/sea-ice configuration with a resolution of 1/4° described below.

[1] http://www.ifremer.fr/lpo/drakkar.

[2] NEMO: Nucleus for European Models of the Ocean.

2.2 Global 1/4° DRAKKAR configuration ORCA-R025

2.2.1 ORCA grid common to all DRAKKAR configurations

In the OPA numerical code (Madec et al. 1998), the primitive equations are discretized on a C-grid centered at tracer points. A family of tripolar grids, ORCA grids, was developed by Madec (personal communication) for global models (see Timmmerman et al. 2005 for an application of the ORCA grid at 2° resolution). The geographical South Pole is conserved and from 80°S to 20°N, the grid is a regular Mercator grid (isotropic, getting finer at high latitude as the cosine of latitude). Following Murray's (1996) idea, the singularity of the North Pole is treated by changing the coordinate system using two poles, one in Canada and the other in Asia. Starting at 20°N, latitude circles of the Mercator grid are progressively distorted into ellipses, the great axes of which are oriented along a line joining the two poles of the northern hemisphere. The grid is computed following the semianalytical method of Madec and Imbard (1996). The deformation of the grid is such that it remains quasi-isotropic and is quasi-uniform in the Arctic. Because the resolution of the grid is variable, the resolution of an ORCA grid is referred to the latitude of the equator where it is the coarsest. This family of grid is used for all DRAKKAR configurations, including the regional ones (North Atlantic and Nordic Seas).

2.2.2 Model grid, bathymetry, and initial conditions

ORCA-R025 is a global configuration of NEMO implemented on an ORCA grid at 1/4° resolution. Grid, masking, and initial conditions are inherited from the global configuration of the operational oceanography center MERCATOR-Ocean[3] (Remy et al., personal communication). This configuration has 1,442×1,021 grid points and uses 46 vertical levels. Vertical grid spacing is finer near the surface (6 m) and increases with depth to 250 m at the bottom. The maximum depth in the model is 5,844 m. The effective resolution, which gets finer with increasing latitudes, is ~27.75 km at the equator and ~13.8 km at 60°S or 60°N. It gets to ~7 km in the Weddell and Ross Seas and ~10 km in the Arctic.

The bathymetry is derived from the 2-min resolution Etopo2 bathymetry file of National Geophysical Data Center, which is a combination of the satellite-based bathymetry (Smith and Sandwell (1997) and International Bathymetric Chart of the Arctic Ocean (Jakobsson et al. 2000). It was merged with the Bedrock Mapping Project data (Lythe and Vaughan 2001) beyond 72°S in the Antarctic. The interpolation onto the model grid was carried out by taking all the Etopo2 grid points falling into an ORCA-R025 grid box and taking the median of those points. This produces a smoothing of the subgrid scale topography. Penduff et al. (2002) showed that topographic smoothing has a strong influence on the model's circulation. We believe that topography should not vary too much at the grid scale to avoid numerical noise. For this reason, we have applied an additional smoothing (two passes of a uniform shapiro filter). Hand editing was performed in a few key areas. Initial conditions for temperature and salinity are derived from the Levitus et al. (1998) data set for the middle and low latitudes. For high latitudes, we chose the PHC2.1 climatology (Steele et al. 2001) and for the Mediterranean Sea, the Medatlas climatology (Jourdan et al. 1998).

2.2.3 Numerical characteristics

A purpose of developing the NEMO code is to improve model physics and numerical algorithms. Perhaps the most significant problem in eddy-permitting *z*-coordinate ocean models is the misrepresentation of flow–topography interactions (Penduff et al. 2005). The previous version of OPA (OPA 8.1, Madec et al. 1998) represented the topography as staircases whose steps have the size of the model vertical levels: This is the "full step" (*FS*) topography, which approximates the true ocean depth to the closest model level. By making the depth of the bottom cell variable and adjustable to the real depth of the ocean, it is possible to better represent small topographic slopes: This is the "partial step" (*PS*) topography, first introduced by Adcroft et al. (1997) and also named partial cells in the literature (Pacanowski and Gnanadesikan 1998). This PS representation of the topography is now available in NEMO.

In OPA, the momentum equations are expressed in their vector invariant formulation (i.e., as a relative vorticity term plus a gradient of kinetic energy and a vertical advection) instead of the flux form (i.e., divergence of momentum fluxes plus a metric term) used in most ocean general circulation models. At this point, several options are possible to discretize the total (relative + planetary) vorticity term. Two distinct schemes are used in the present paper. One is the standard scheme used in the former versions of OPA (referred to as the *ENS* scheme) and has the property to conserve enstrophy (Sadourny 1975) in flows with no mass flux divergence. The other, which is newly available in NEMO, is an adaptation of the scheme of Arakawa and Lamb (1981) to the primitive equations. Referred to as the energy–enstrophy conserving (*EEN*) scheme, it conserves total energy for general flow and potential enstrophy for flows with no mass flux divergence. These two new options (PS + EEN) have a drastic impact on the model solution as will be demonstrated in Section 3.

Other options worth noting in ORCA-R025 and all DRAKKAR configurations are: (1) a total variance diminishing advection scheme for tracers (Lévy et al. 2001), which, compared to the centered scheme, avoids the generation of overshoots in case of sharp gradients; (2) a Laplacian lateral isopycnal diffusion on tracers (300 m^2 s^{-1} at the equator and decreasing poleward, proportionally to

[3] MERCATOR-Ocean: http://www.mercator-ocean.fr.

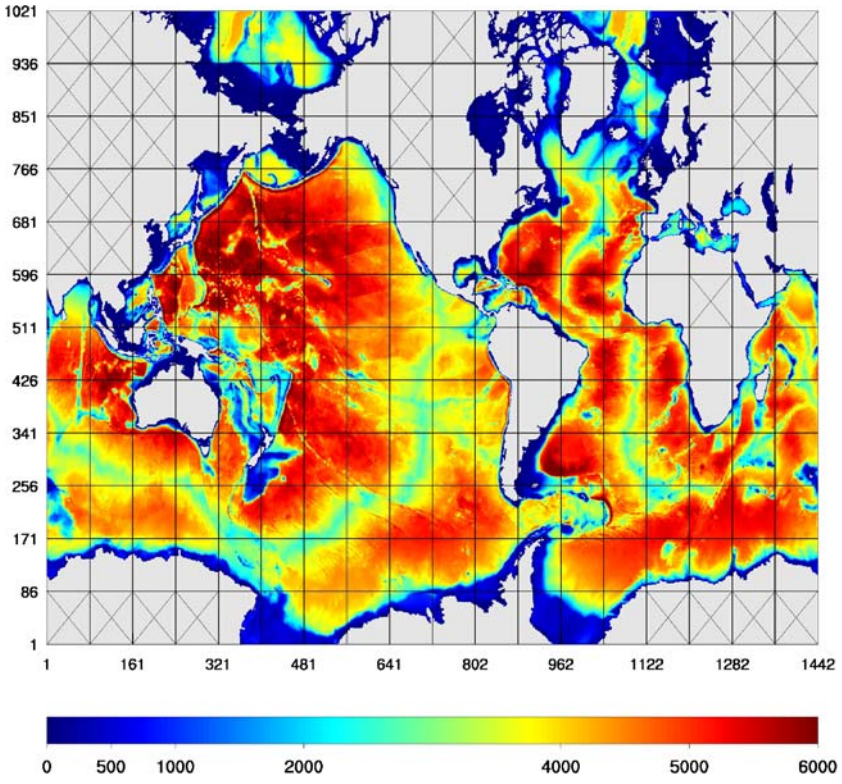

Fig. 1 Domain decomposition on 186 processors of the DRAKKAR global 1/4° ocean circulation model ORCA-R025. *Colors* indicate the model bathymetry in meters. Every single *box* represents the domain accounted for by a processor. *Boxes with a cross* are "land processors" not retained in the calculation. *Numbers* in abscissa and ordinate indicate model grid points

the grid size); and (3) a horizontal biharmonic viscosity for momentum (-1.5×10^{11} m^4 s^{-1} at the equator and decreasing poleward as the cube of the grid size). In the equatorial waveguide, a Laplacian viscosity (500 m^2 s^{-1}) is added to the biharmonic operator at levels included in the upper 100 m to better control the speed of the Equatorial Undercurrent. This method gave satisfying results in the CLIPPER model (M. Arhan et al. 2006, in revision).

Surface boundary layer mixing and interior vertical mixing are parameterized according to a turbulent closure model (order 1.5) adapted to OPA by Blanke and Delecluse (1993). In case of static instability, a viscosity/diffusivity enhancement up to 10 m^2 s^{-1} is used.

2.2.4 Forcing

The atmospheric forcing, which drives the simulations presented here, is a climatological seasonal cycle forcing applied in a cycling way. It is the same forcing used by Timmermann et al. (2005) in their application of older versions of OPA and LIM at coarser resolution (2°), except for the wind forcing, which here, uses European Space Agency remote sensing satellite (ERS) scatterometer winds.

Surface momentum flux is directly provided to the ocean/sea-ice model as a wind stress vector. A climatological daily mean wind stress vector is used. It is a combination of ERS scatterometer data (CERSAT 2002) and National Centers for Environmental Prediction/National Center for Atmospheric Research (NCEP/NCAR) reanalysis (Kalnay et al. 1996) built as follows: ERS wind stress between 50°N and 50°S, a linear combination of ERS winds with NCEP between 50°and 60°, and NCEP winds poleward of 60°. The daily climatology is built using years 1992 to 2000 with an 11-day running mean filter to remove synoptic variability.

Surface heat fluxes (solar, infrared, latent, and sensible heat) and freshwater flux for ocean and sea-ice are calculated using the empirical bulk parameterization described by Goosse (1997). Evaporation is derived from the latent heat flux. The set of atmospheric variables used in these flux calculations consists of climatological daily mean values of air temperature from NCEP/NCAR reanalysis, climatological monthly mean precipitation from CMAP (Xie and Arkin 1997), monthly mean humidity (Trenberth et al. 1989) and cloud cover (Berliand and Strokina 1980), and climatological daily mean wind speed from the blend of ERS and NCEP/NCAR reanalysis described above. River runoff was provided by MERCATOR-Ocean (Remy, personal communication). No relaxation to any sea surface temperature or sea surface salinity (*SSS*) is used.

2.2.5 Performance

ORCA-R025 is implemented on a massively parallel machine at IDRIS.[4] We applied a domain decomposition technique and split the global computational domain into 18×12 subdomains (216 in all). To streamline efficiency,

[4] Institut du Développement et des Ressources en Informatique Scientifique, Orsay, France.

Table 1 List of the 10-year-long sensitivity experiments carried out with ORCA-R025

Simulation	Vorticity scheme	Bottom topography*
G03	EEN (new)	FS
G04	ENS (old)	FS
G22	EEN (new)	PS

The present study mainly uses the results from the G04 and G22 simulations. No relaxation to SSS is applied in any of these experiments. A free slip sidewall boundary condition is used in all simulations

**FS* Full step and *PS* partial step

we used only processors having ocean grid points (186 processors). Each processor thus had 82×87×46 grid points. A one-row overlapping halo (1 row) is shared with the neighboring processors, using explicit communications between processors, (Message Passing Interface library). Figure 1 gives a global view of the domain broken-down into individual processors. The time step of the ocean component is 1,440 s (60 time steps per day) and the sea-ice component is called once every five time steps. One year of model simulation requires 2,200 h of CPU on 186 IBM SP4 processors and takes about 12.6 h of elapsed time. Maximum memory is 0.479 Gb per processor and total memory is 84 Gb.

2.3 Sensitivity tests with ORCA-R025

A series of 10-year simulations were run to evaluate the contribution of various numerical choices to the solution. The focus is on the *PS representation of topography* and the *EEN vorticity scheme* used in the calculation of momentum advection, which produced the greatest improvements to the model solution. Therefore, we compare (in Section 3) a simulation that does not include these two features, referred to as G04, with a simulation that includes both, referred to as G22, (Table 1). Other numerical options were tested. In particular, a FS simulation using the EEN vorticity scheme was run (simulation G03, Table 1) so the effects of the PS could be separated. Some results from this experiment will be used in Section 3.

Before we provide (in Section 3) an assessment of the changes induced by the numerics, we provide a brief overview of simulation G22 (with PS and the EEN momentum advection scheme). Our analysis will remain rather descriptive. A full understanding of how the numerics impact on the physics of the model requires a large number of sensitivity experiments and complex diagnostics, which are currently under way in a North Atlantic configuration of the code (J. Le Sommer et al. 2006, in preparation). Preliminary results from this work are used in the discussion of Section 4 to illustrate possible

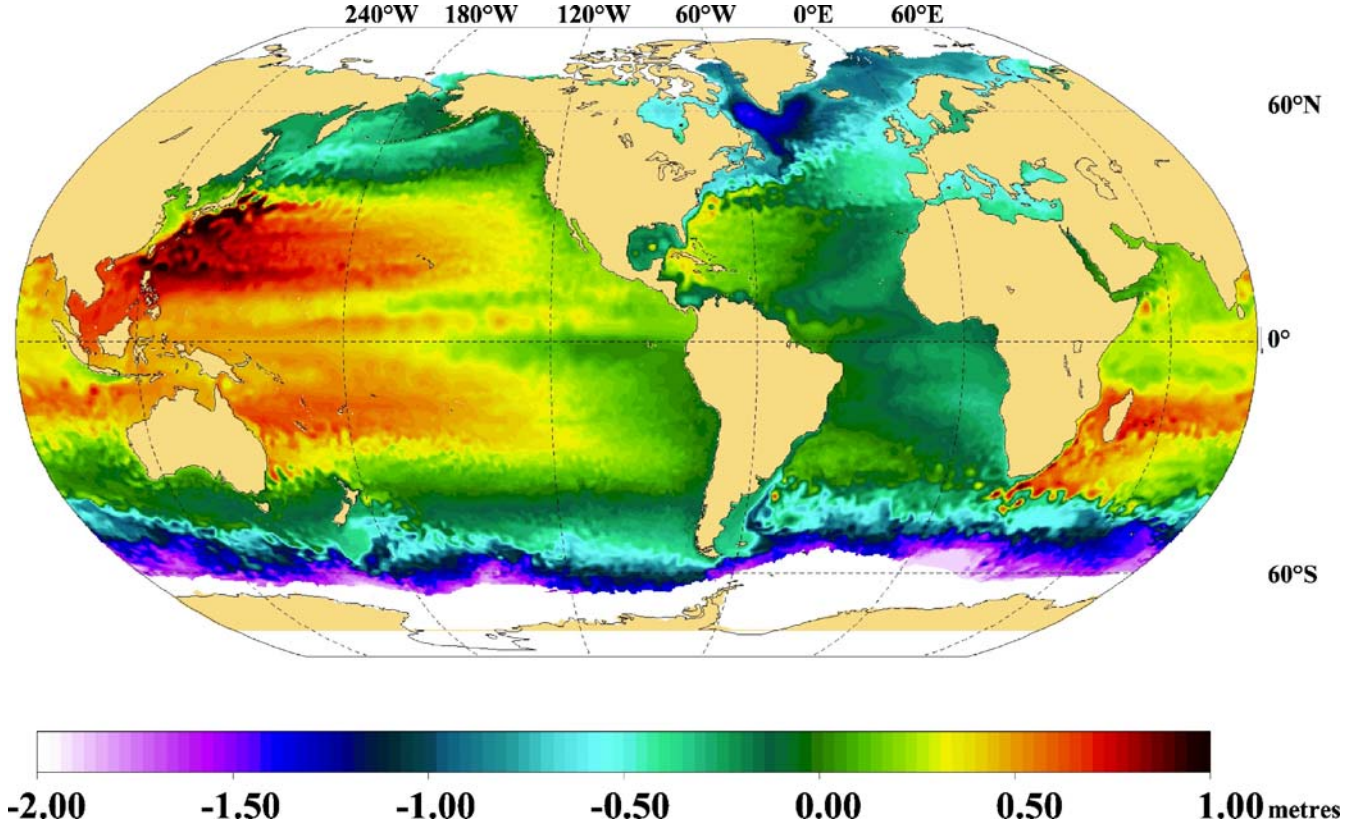

Fig. 2 Simulation G22 (partial step topography, new EEN vorticity scheme for momentum advection): snapshot of the sea surface height (*ssh*, in *color*) and ice cover (in *white*) in Austral winter in year 10 of the simulation

reasons of improvements when the combination PS + EEN is used.

2.4 Mean general circulation in simulation G22

2.4.1 Upper ocean circulation

A first overview of the large-scale upper circulation is presented in Fig. 2 with a snapshot of the sea surface height (*ssh*) and sea-ice cover in year 10 of the simulation. It shows the known general circulation features that are seen in similar model simulations (Maltrud et al. 1998; Maltrud and McClean 2005): the well-marked subpolar and subtropical gyres, the strong and meandering western boundary currents, the large upwelling systems of eastern ocean basins, and the equatorial current systems with waves and eddies. The strong Antarctic Circumpolar Current (ACC, almost a 2-m change in ssh) shows many mesoscale features. Agulhas Rings are drifting northwestward in the South Atlantic. Western boundary currents, the North Brazil Retroflection area, and the Caribbean Sea are rich in mesoscale features. Loop Current eddies are found in the Gulf of Mexico.

The distribution of the eddy kinetic energy (*eke*) compares remarkably well with the satellite estimate of Ducet et al. (2000) considering the medium resolution (1/4°) of the model (Fig. 5). There are regions where a significant improvement is found compared to other experiments (see next section). One is the Brazil–Malvinas Confluence Zone in the South Atlantic with the characteristic C-shape and the minimum of eke inside the Zapiola anticyclone (de Miranda et al. 1999a). Another is the Agulhas region where the paths of Agulhas Rings tend to be more realistic than in experiments with FS topography. The Gulf Stream and the North Atlantic Current system are also regions where the distribution pattern of eke is clearly improved, in particular, in the Northwest Corner. As shown in following sections, the distribution pattern of eke is sometimes better in simulation G22 than in 1/6° and even 1/10° experiments.

Sea-ice is not the focus of the present paper and only a quick overview is presented (the Austral winter sea-ice cover is shown in Fig. 2). A first look at the sea-ice component of simulation G22 shows reasonable performance in high latitudes. In the Arctic, the climatological winter sea-ice extent, area, and thickness are reproduced quite well with many small-scale details in the marginal ice zone present (e.g., ice tongues in the Greenland Sea, off Newfoundland, in the Okhotsk Sea, and partial coverage of the Baltic Sea). The summer ice distribution is characterized by a general overestimation of the ice cover. For the Antarctic Marginal Seas, we find larger differences between observed climatology and the model results. While the winter extent is acceptable, the thickness shows a systematic bias: too thick in all coastal regions and too thin offshore. The former leads to an overestimation in ice surviving the summer. Simulations with other global configurations of NEMO (at 1/2 and 2° resolutions) run within the DRAKKAR project show that this is a general feature of the coupled model system, not related specifically to the high-resolution case presented here. It will be investigated in more detail in a separate study.

2.4.2 Meridional circulation

The meridional overturning cell (MOC) or streamfunction and the meridional heat transport (MHT) provide a zonally averaged view of the meridional circulation. They are quantities of important climate relevance that ocean models aim to simulate accurately. In 10-year-long simulations as presented here, these quantities are still far from a state of equilibrium. However, they are systematically analyzed in similar model studies (Maltrud and McClean 2005; Lee and Coward 2003). An initial assessment of the strength of the meridional circulation in our model is useful because it characterizes the global dynamical regime in which simulations are compared.

We choose to comment on simulation G22 because it is representative of all three simulations in that respect, the MOC being very similar in simulations G03 and G04. Note that the simulations discussed here do not include a bottom boundary layer to improve the deep overflows, usually not reproduced well in *z*-coordinate models.

The MOC and MHT of G22 are shown in Figs. 3 and 4. It is very clear from Fig. 4 that the simulation is still far from equilibrium, as displayed by the large discrepancies between the advective MHT (i.e., estimated from correlation of the meridional velocity with the temperature) and the MHT diagnosed from the meridional integration of the surface fluxes (under the hypothesis of a state of equilibrium). These differences are indicative of significant trends in the model heat storage.

In the Atlantic, the maximum overturning is 24 Sv (Fig. 3a) with over 6 Sv of dense water overflow across the sills of the Nordic Seas. The MOC of G03 and G04 (not shown) are identical to that of G22 in that respect. These values are in the upper bounds of the values found in the literature, indicating a particularly strong meridional circulation in the northern North Atlantic under the present forcing conditions in all our simulations. The southward flow of North Atlantic Deep Water shows a significant decrease in the South Atlantic from 16 Sv at the equator to 9 Sv at 30°S. Northward flow of Antarctic Bottom Water is 4 Sv below 3,800 m. The maximum MHT is 1.28 PW at 28.5°N (Fig. 4a), a realistic value at this latitude. However, the MHT is generally weaker than the estimates obtained by an inversion of hydrographic sections by Ganachaud and Wunsch (2003). The comparison of the advective MHT with the MHT diagnosed from surface fluxes indicates a heat storage (i.e., warming) of the North Atlantic at latitudes higher than 30°S and a cooling elsewhere (between 30°S to 30°N). The model, therefore, is far from adjusted to the forcing field, limiting a quantitative interpretation of the above numbers.

In the Indo-Pacific, the MOC structure of G22 (Fig. 3b) and those of G034 and G04 (not shown) shows a relatively

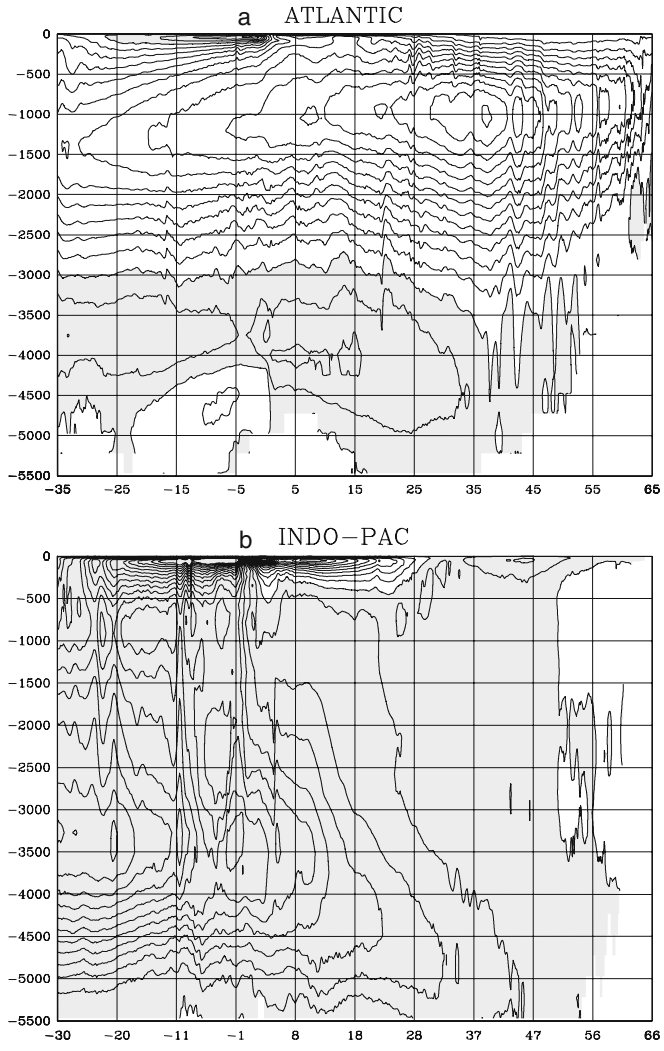

Fig. 3 Meridional overturning streamfunction (in Sv) averaged over year 8 to 10 of the G22 simulation (PS + EEN) for the Atlantic (**a**) and the Indo-Pacific ocean basins (**b**). Contour interval is 2 Sv

deep reaching shallow overturning cell; the equatorward subsurface flow, which compensates the poleward Ekman transport spreads down to 500 m. The equatorial upwelling is quite strong. Beneath the shallow cell, there is almost no net cross equatorial transport above 3,500 m, the equatorial upwelling reaching almost to that depth. Below 4,000 m, the northward flow of bottom water crossing the equator is of the order of 12 Sv.

The MHT maximum divergence (i.e., zero crossing) is located at about 4°N (Fig. 4b). The northern hemisphere maximum is 0.55 PW northward at 20°N. The poleward MHT is greater in the southern hemisphere and reaches its maximum of 1.7 PW at 13°S. The quantitative agreement with Ganachaud and Wunsch (2003) estimates is certainly fortuitous. The discrepancies observed between the advective MHT and the MHT diagnosed from surface fluxes indicate that the Indo-Pacific basin is being cooled between 20 and 60°N (i.e., the North Pacific sector), and between the equator and 10°S (strong cooling). From the equator to 20°N and from 10°S to 35°S, the difference between the two curves of Fig. 4b does not vary with latitude, indicating a quasiequilibrium between the surface flux and the model heat transport.

At global scale, the MHT (Fig. 4c) shows a relatively good symmetry with regard to the equator, a pattern common to estimates obtained from atmospheric analyses (see Trenberth and Caron 2000 for example) with a large

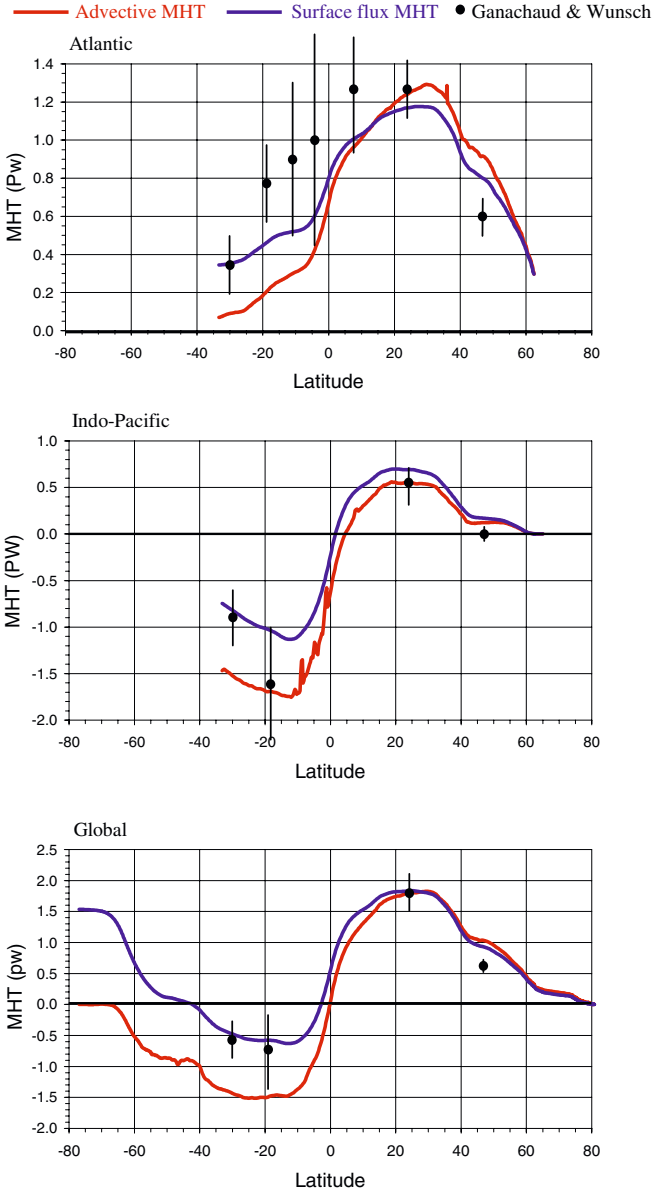

Fig. 4 Meridional heat transport (in PW) averaged over year 8 to 10 of the G22 simulation for the Atlantic, Indo-Pacific, and Global oceans. The advective MHT (*red curve*) is calculated using a 5-day mean model meridional current velocities and temperatures. The surface flux MHT (*blue curve*) is calculated as the meridional integration of surface fluxes. Differences between the *curves* indicate trends and storage. *Black dots* are estimates (with *error bars*) from an inversion of hydrographic data by Ganachaud and Wunsch (2003)

maximum of southward heat transport in the southern hemisphere (1.5 PW at 13°S). Global models usually tend to produce smaller values for the southern hemisphere maximum MHT [for example, 1.2 PW at 12°S in the 1/10 Parallel Ocean Program (POP) model], in agreement with the hydrographic estimate of Ganachaud and Wunsch (2003). Note that an experiment similar to G22 but using a relaxation of SSS to climatological value reduced the southern hemisphere maximum to a value comparable to hydrographic estimates. The sensitivity of MHT to the details of the forcing is thus quite large.

The comparison with the global MHT diagnosed from surface fluxes (Fig. 4c) suggests a quasiequilibrium between heat advection and surface fluxes north of 20°N. In fact, this equilibrium at the global scale is the result of a balance between the warming of the North Atlantic and the cooling of the North Pacific. Between 20°N and 20°S, the global ocean is cooling, the Atlantic providing the major contribution to this cooling from 20°N to the equator, and the contribution of the Indo-Pacific being dominant from the equator to 20°S. The imbalance between both MHT estimates is of the order of 1.0 PW at 60°S, mainly coming from the cooling at tropical latitudes. It will be interesting to see in future sensitivity experiments with different forcing fields how the MHT characteristics presented here are modified.

This brief overview of the model solution indicates that the ORCA-R025 broad circulation patterns correspond to what is expected from a state-of-the-art ocean general circulation model. It also shows that the global meridional circulation, yet too far from steadiness to be quantitatively interpreted, is of very similar strength in all ORCA-R025 simulations compared here, so changes in the MOC intensity between experiments will not be an issue when comparing their respective regional circulation features.

3 Effects of PS and EEN vorticity scheme

We assess the impact of the PS and EEN advection scheme on the model solution by looking at local dynamical circulation features whose spin-up is almost complete after 10 years and whose characteristics should not change significantly (i.e., not to the point of invalidating the conclusions of the present study) during the slow adjustment of the internal thermohaline structure of the ocean to the forcing.

3.1 Global analysis

To identify where the PS and the EEN vorticity scheme produce significant changes in the model solution, we compare the 3-year mean barotropic streamfunction (*BSF*) of simulations G22 and G04 (Fig. 6a). To separate the effects of PS and EEN, we also do this comparison for simulations G03 and G04 (Fig. 6b), both using FS but with only G03 using the EEN scheme (See Table 1). Only changes above 10 Sv are looked at here, which limits our investigation to regions of strong currents (i.e., where the impact of nonlinear terms is strong). The first look at Fig. 6a identifies the region around Antarctica as a region of great impact of the new schemes, the use of which reduces the ACC transport (from 160 to 140 Sv at Drake Passage). This reduction is clearly due to the PS because the map of the BSF differences between the two FS simulations, which only differ by the momentum advection scheme (G03 and G04, Fig. 6b), does not show this pattern. The smaller transport at Drake Passage in G22 (141 Sv compared to 154 Sv in G04) is therefore a consequence of the PS topography. This is consistent with former studies, which demonstrated how crucial the bottom topography is to establish the momentum balance of the ACC (Rintoul et al. 2002; Grezio et al. 2005).

Other regions of great differences are basically the regions of high eke levels shown in Fig. 5: western boundary current systems with the largest impact in the Argentine Basin and the Gulf Stream, the Agulhas Current retroflection region and its extension in the southern Indian ocean, the most intense branches of the ACC in the Indian Ocean sector, and in the Pacific Ocean sector around the Campbell Plateau and beyond. Smaller changes, still significant because they are slightly above 10 Sv, are seen in the Labrador Sea, mainly due to the use of PS as deduced from Fig. 6a,b. This is consistent with the findings of Käse et al. (2001) and Myers (2002) who showed that the use of PS topography strengthened the North Atlantic subpolar gyre. Changes in BSF are also noticeable in the Caribbean Sea and in the east Australian Current.

All the above remarks strongly suggest that the impact of the new schemes is localized where the flow is highly nonlinear and where the topographic constraint is strong, as briefly illustrated in Section 4 (detailed explanation in J. Le Sommer et al. 2005, in preparation). Figure 6a,b indicates that except for the region around Antarctica where the PS topography appears to drive the changes, the EEN advection scheme and PS have comparable contribution.

In the following, we concentrate our analysis on six regions (outlined in Fig. 6a) where changes are particularly large. The impact of PS and EEN on the mean circulation will be assessed by comparing mean sea surface height (*mssh*) and the mean eke of simulation G22 with estimates from observations and from various model experiments. The "observed" mssh used here as reference is the output of the surface drifter and satellite altimetry analysis of Niiler et al. (2003). The observed eke used here as reference is that derived from satellite altimetry by Ducet et al. (2000). Although referred to as observed quantities in the following, we should keep in mind that these are estimates derived from observations and that they have their own inaccuracies and biases generally depending on data coverage (which is quite unequal from a region to another for surface drifters). Model results used are from simulations G04 and G22 performed with the ORCA-R025 model (Table 1) and from simulations carried out with different models: the Ocean Circulation and Climate Advanced Modeling (OCCAM) Project (Webb et al. 1998; Coward and de Cuevas 2005), the POP1/10 model (Maltrud and

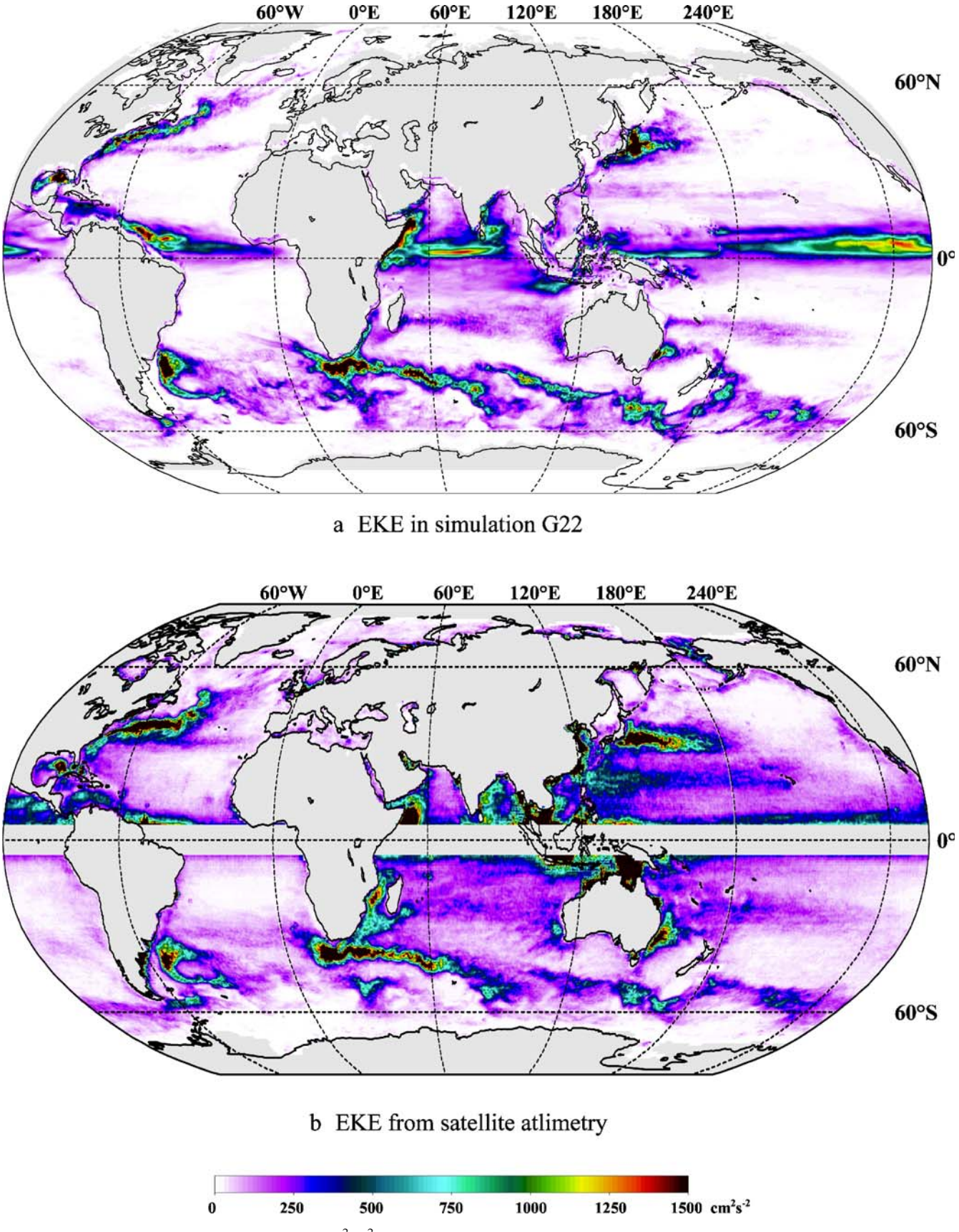

Fig. 5 Global map of eddy kinetic energy (in $cm^2\ s^{-2}$) in simulations G22 (3-year mean) and from satellite altimetry (Topex/Poseidon and ERS; Ducet et al. 2000)

McClean 2005), and the CLIPPER ATL6 model (Penduff et al. 2005). The main characteristics of these latter models are summarized in Table 2. Note that the version of OCCAM uses PS and a large number (66) of vertical levels.

We have to mention here the ocean general circulation model for the earth simulator (OFES). It is a 50-year-long simulation carried out on the Earth Simulator in Japan (Masumoto et al. 2004) with a global implementation of the Modular Ocean Model (MOM)3 code at 1/10° resolution (thus, similar to POP1/10). OFES outputs were not available when we carried out our analyses so this simulation is not included in the present study. However, public Internet access[5] to the OFES 50-year climatological simulation is now available. This simulation uses a PS topography and OFES mean fields could, in future studies, be compared to the POP1/10 solution to assess the impact of the PS at eddy-resolving resolution. We mention some results of this simulation in Section 3.3.

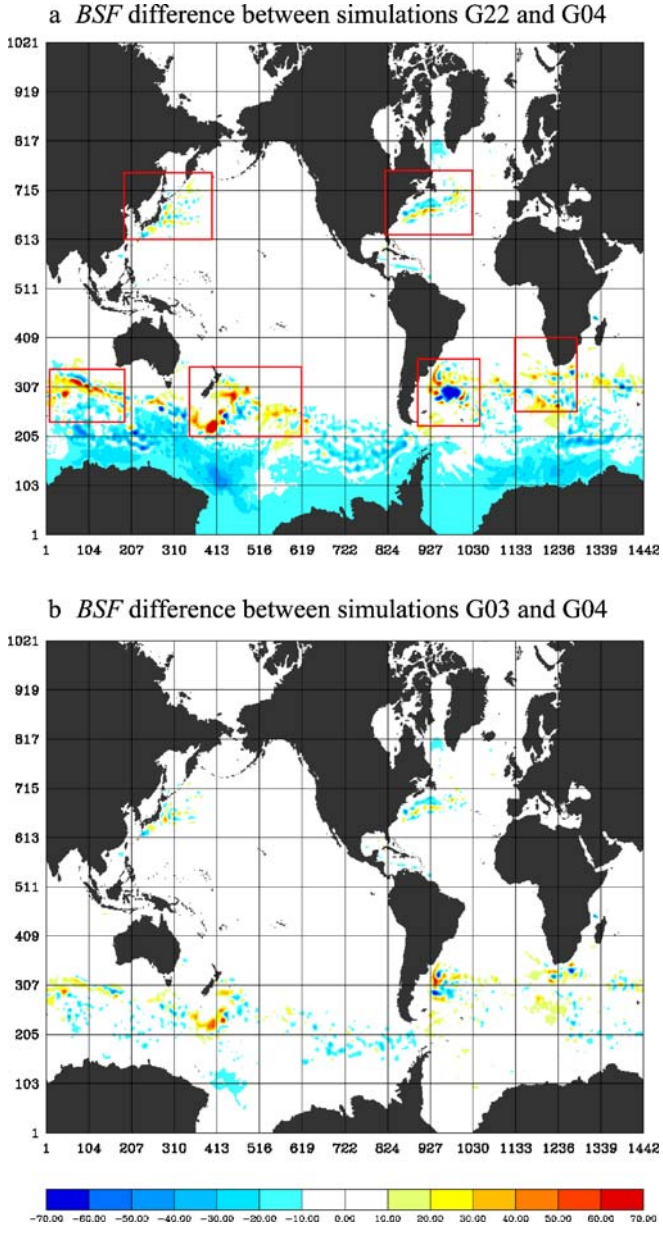

Fig. 6 Difference in the mean barotropic streamfunction (in Sv) between **a** simulations G22 (PS + EEN) and G04 (FS + ENS) indicating where both the partial step topography and EEN scheme play a role, and **b** between G03 (FS + EEN) and G04 (FS + ENS), both full step topography, indicating where advection scheme only has an impact. The *red boxes* identify the regions where model solution is compared to observation and other models. *Color palette* indicates Sv. *Axes* are subdivided by grid point numbers

3.2 The Gulf Stream and North Atlantic Current system

Figure 7 shows several mssh estimates obtained from observations (Fig. 7a) and from various model experiments (Fig. 7b–f). Observed characteristics of the mean path of the Gulf Stream outlined in Fig. 7a are: a clear separation at Cape Hatteras, an elongated anticyclonic southern recirculation cell, the presence of a cyclonic northern recirculation cell indicating the presence of cold slope waters on the Grand Banks, and a crossing of the 40°N line at 60°W. Beyond this point, the path of the North Atlantic Current (NAC) is characterized by a well marked Mann Eddy at 42° N, 43°W and a North West Corner at 50°N, 40°W. Thus, east of 40°W, the path of the NAC is always north of 50°N and follows the topography.

The ORCA-R025 simulation G22 (which includes PS + EEN) reproduces rather well all these features (Fig. 7b), except for the separation of the Gulf Stream, which still shows a slight overshoot and standing inertial oscillations in the current characterized by a standing eddy off Cape Hatteras (the unrealistic *Hatteras eddy*). Nevertheless, the transport of the Hatteras eddy (20 Sv in G22) is significantly reduced compared to the simulation without the new schemes (55 Sv in simulation G04 in Fig. 7d), and even compared to the solutions provided by other models at similar resolution (OCCAM in Fig. 7c) or higher resolution (POP1/10 and ATL6 in Fig. 7e,f). Concerning the other observed characteristics of the Gulf Stream and the NAC, the G22 simulation is by far the most consistent with observations. The path of the mean current in G22 (including the northwest corner and the presence of slope waters) is remarkably accurate for a model of such resolution, despite a weaker Mann Eddy and a stronger mssh gradient between the subtropical and subpolar gyre.

Figure 8 shows several estimates of the eke obtained from satellite altimeter observations (Fig. 8a) and from various model experiments (Fig. 8b–f). In numerical models, the value of this quantity depends on how well the deformation radii are resolved (i.e., on the fact that the model is eddy resolving, like POP1/10, or eddy-permitting, like ORCA-R025 or OCCAM). Therefore, comparing eke levels between models must be moderated by considerations about their differences in resolution. The present analysis gives more attention to the distribution pattern of eke, which reflects the position of the main currents and eddy pathways, rather than comparing values.

[5] http://www2.es.jamstec.go.jp/ofes/eng/index.html.

Table 2 Main characteristics of the 10-year-long sensitivity experiments, G22 and G04, carried out with ORCA-R025, and of the other model simulations compared in this study

Model name	Code	Area	Resolution	Topography	Momentum advection
G22–ORCA-R025	NEMO	Global	1/4°	Partial step	EEN (Arakawa and Lamb 1981)
G04–ORCA-R025	NEMO	Global	1/4°	Full step	ENS (Sadourny 1975)
OCCAM	MOM	Global	1/4°	Partial step	Flux form
POP1/10	POP	Global	1/10°	Full step	Flux form
ATL6	OPA8.1	Atlantic	1/6°	Full step	ENS (Sadourny 1975)

The distribution of eke confirms the improvements due to the PS and the EEN advection scheme to the simulation of the mean currents. Among all 1/4° simulations presented here (G22, G04, and OCCAM), G22 is the one whose eke pattern (Fig. 8b) is the most consistent with observations (Fig. 8a), in particular, along the path of the NAC. Simulation G04, performed with the same model without the new numerical methods, is clearly deficient with regard to the path of the Gulf Stream beyond the Grand Banks. OCCAM shows extremely intense standing eddies at the separation point of the Gulf Stream. The eke pattern in the path of the NAC and the Northwest Corner indicates that this current system is shifted southward, a picture that is usual at this resolution for the MOM. It is interesting to note that models with higher resolution do not perform better in terms of eke distribution pattern. Both POP1/10 and ATL6 show a strong eke maximum at the Gulf Stream separation point and a wide spread of eke east of the Grand Banks. This indicates a misrepresentation of the main path of the NAC. Note, however, that in a regional simulation of the North Atlantic carried out with the POP model at 1/10° resolution by Smith et al. (2000), the path of the Gulf Stream was quite realistic and the distribution of eke was very comparable to the one observed from satellite.

Therefore, the distribution of the eke satellite estimate confirms the picture provided by the observed mssh that the use of PS and EEN advection has considerably reduced the major dynamical biases found in the simulation of the current system of the western North Atlantic by most numerical models.

3.3 Western South Atlantic

Observed and model mssh estimates are shown in Fig. 9 for the western South Atlantic. Improvements due to PS and EEN in the South Atlantic are even more striking than for the North Atlantic, in particular, because the G22 experiment (Fig. 9b) is the only one among all other models to reproduce the high mssh anomaly observed in the center of the Argentinian Basin at 45°W, 45°S (Fig. 9a). This high-pressure pattern is the signature of the standing Zapiola Eddy, first reported from observations by Saunders and King (1995), and clearly seen in float data (Boebel et al. 1999). The first realistic simulation of the Zapiola Eddy was obtained with a sigma coordinate model by de Miranda et al. (1999a) with a resolution of 1/3°. These authors demonstrated that this strong flow pattern, which transports over 100 Sv, is the result of an interaction between the eddies generated in the highly turbulent confluence of the Brazil and the Malvinas currents with the Zapiola drift, a deep depositional topographic feature rising only 1,000 m above the abyssal plain of the Argentinian Basin. In agreement with the theory developed by Dewar (1998), the convergence of the eddy mass flux above the Zapiola drift generates a high pressure above the topography and a large anticyclonic circulation around it. The circulation pattern reaches its equilibrium when the eddy mass flux is balanced by the export of mass in the Ekman bottom boundary layer. de Miranda et al. (1999a) suggested that standard z-coordinate models (i.e., using FS topography) could not simulate this feature because of a poor representation of f/h contours and an increased numerical dissipation due to lateral friction induced by the step-like topography. This has since been confirmed with the ATL6 model simulations (Penduff et al. 2005) and the POP1/10 experiment (Maltrud and McClean 2005), which could not reproduce this first-order feature despite a significantly higher resolution. Our G03 simulation, which includes the EEN vorticity scheme but uses a FS topography (see Table 1), also does not reproduce the Zapiola Eddy. Comparing the BSF differences of Fig. 6 subpanels a and b, it becomes obvious that the use of PS topography is required to simulate this circulation pattern, in agreement with the discussion of de Miranda et al. (1999a).

This requirement may not be sufficient because OCCAM does not reproduce the Zapiola Eddy despite a PS formulation of the topography. A reason could be that the no-slip boundary condition used by default in the MOM code prevents the formation of the anticyclonic circulation, known to be very sensitive to bottom dissipation (de Miranda et al. 1999a). Still, the OCCAM results are contradicted by those of the OFES simulation (Masumoto et al. 2004) because this 1/10° MOM3 global simulation with partial cell topography simulates a well-marked Zapiola Eddy (Sasaki, personal communication). Understanding the behavior of the PS version of the MOM code is likely challenging and certainly deserves a specific investigation.

In addition to the Zapiola Eddy, the representation of the Malvinas and Brazil currents confluence is also significantly improved with PS and EEN (simulation G22, Fig. 9b) when compared to G04. This improvement is also remarkable when compared to solutions produced by the other models, including POP1/10 and ATL6, which used much higher resolutions (1/10 and 1/6°, respectively). G22

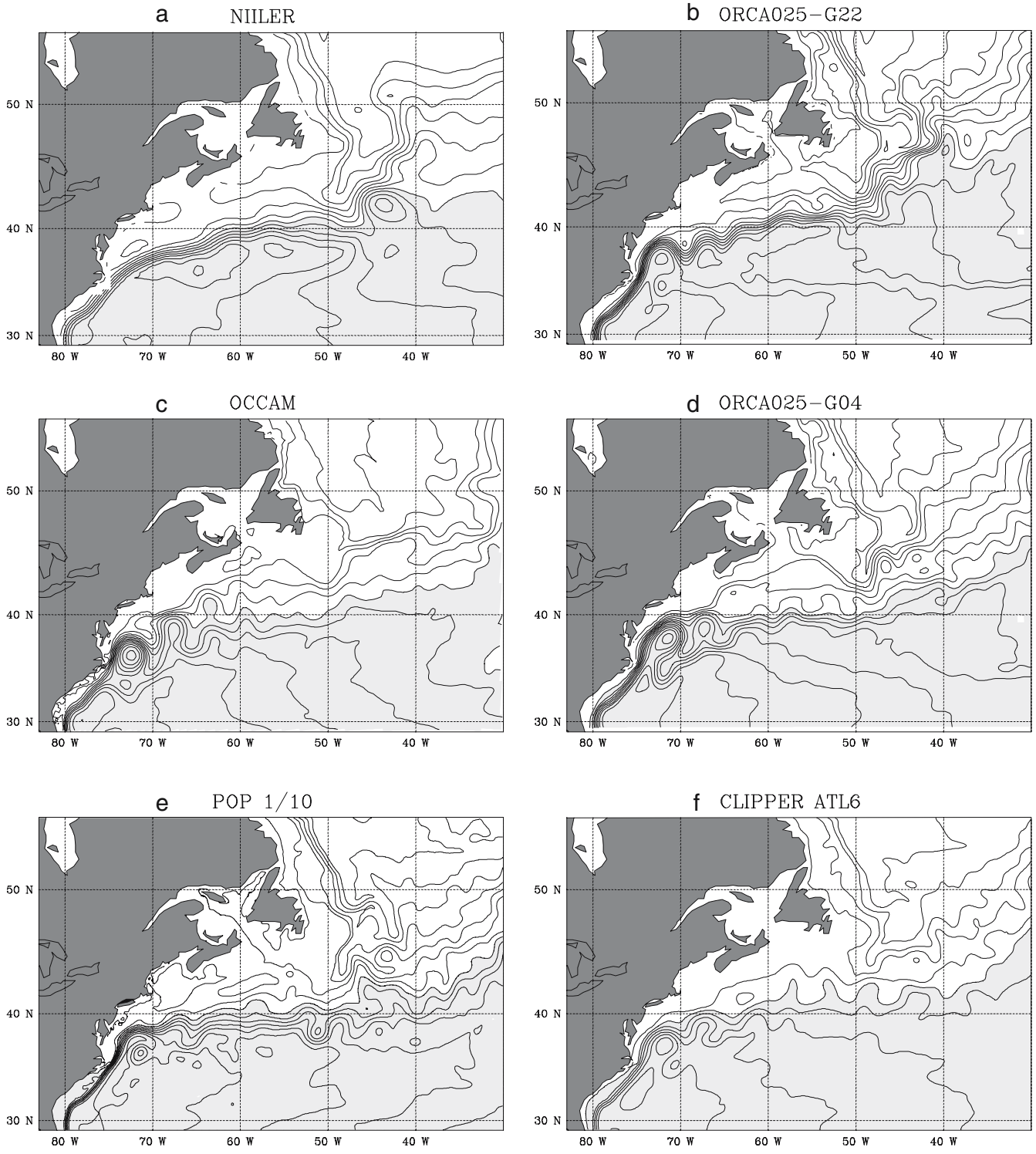

Fig. 7 Estimates of mean sea surface height (*mssh* in cm) in the North Atlantic from **a** observations (Niiler et al. 2003), **b** global ORCA-R025 model simulation G22 (PS + EEN), **c** global OCCAM model simulation, **d** global ORCA-R025 model simulation G04 (FS + ENS), **e** global POP1/10, and **f** Atlantic CLIPPER ATL6 model simulation. All model results present a 3-year mean. To remove mean biases between estimates, the area mean was subtracted for each plot, and thus, *gray* (*white*) areas indicate region of mssh higher (lower) than the area mean. Contour interval is 10 cm

is the only simulation for which the Confluence region is offshore of the Rio de La Plata (36–38°S). In every other simulation, independent of the numerical model used and of resolution, the Confluence region is located beyond 40° S (and as far as 43°S).

The distribution pattern of eke (Fig. 10) confirms this picture. Simulation G22 and Topex/Poseidon exhibit very

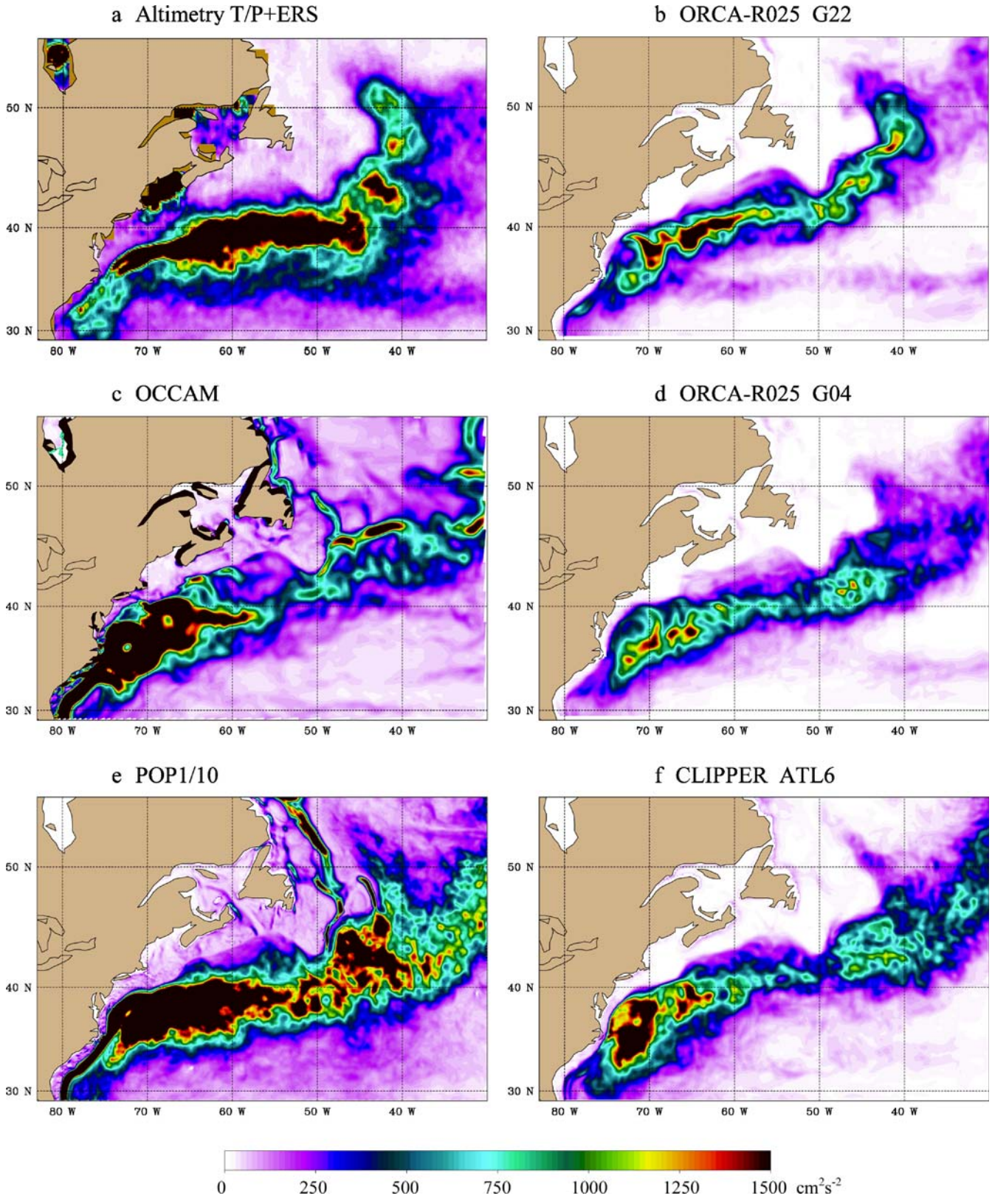

Fig. 8 Estimates of the mean eddy kinetic energy (*eke* in $cm^2\ s^{-2}$) in the North Atlantic from **a** observations (Ducet et al. 2000), **b** global ORCA-R025 model simulation G22 (PS + EEN), **c** global OCCAM model simulation, **d** global ORCA-R025 model simulation G04 (FS + ENS), **e** global POP1/10, and **f** Atlantic CLIPPER ATL6 model simulation. All model results present a 3-year mean

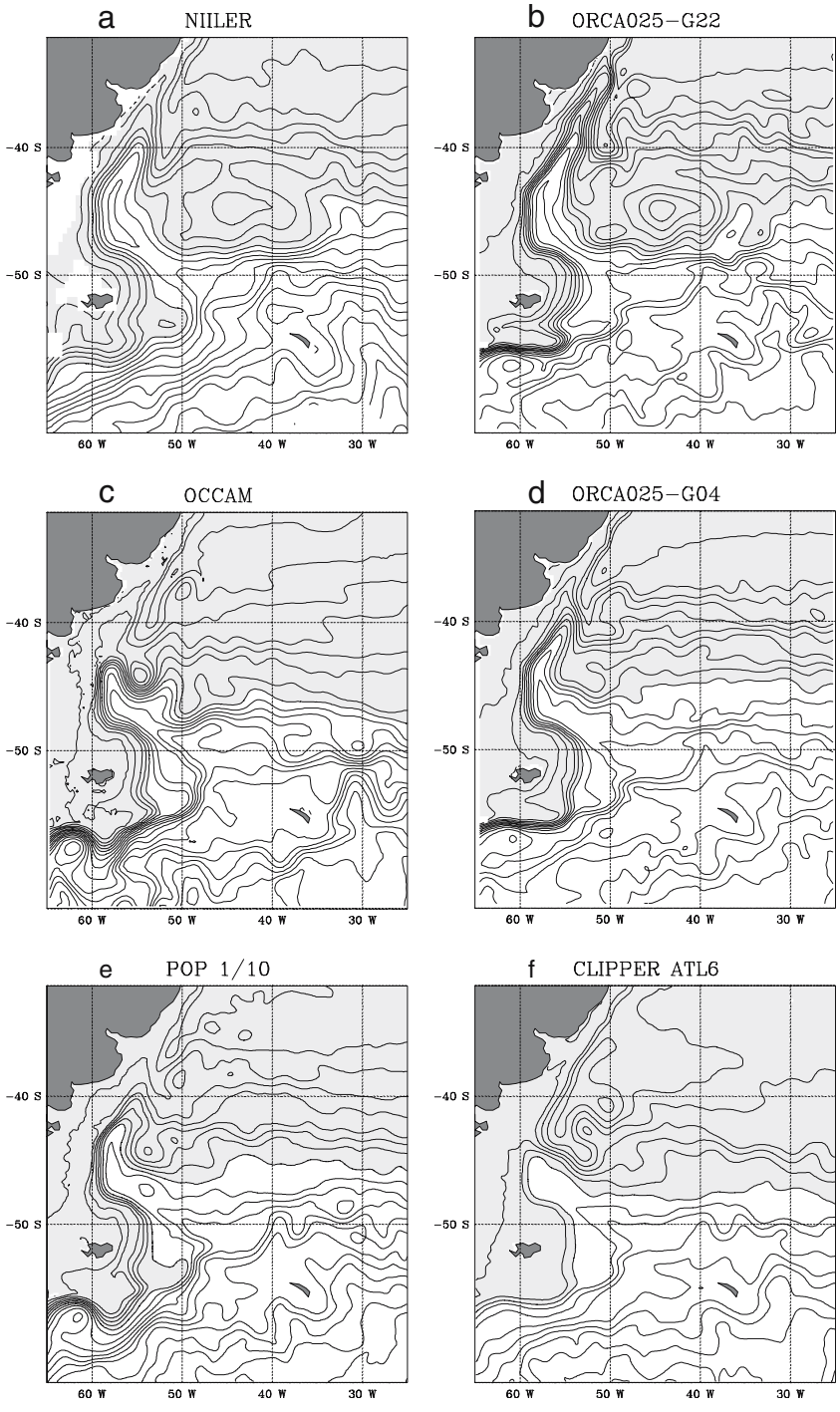

Fig. 9 Same as Fig. 7 (plots of *mssh* in cm) for the western South Atlantic. Contour interval is 10 cm

similar distributions with the characteristic C-shape of high eke levels around the core of the Zapiola Eddy and the small eke levels above. Other models, in particular OCCAM and ATL6, exibit eke patterns characteristic of a strong overshoot to the south of the Brazil Current and no sign of the Zapiola Eddy.

3.4 Cape Basin

The simulation of the Agulhas Current system is also greatly influenced by the new numerical schemes. First, the stability of the Agulhas Current as it flows along South Africa is clearly different in simulations G22 and G04, as illustrated by the snapshots of current speed shown in Fig. 11. When PS and EEN advection are not used (simulation G04, Fig. 11b), the Agulhas Current resembles a train of large eddies rather than a continuous stream as in G22 (Fig. 11a). In G04, the retroflection produces pairs of

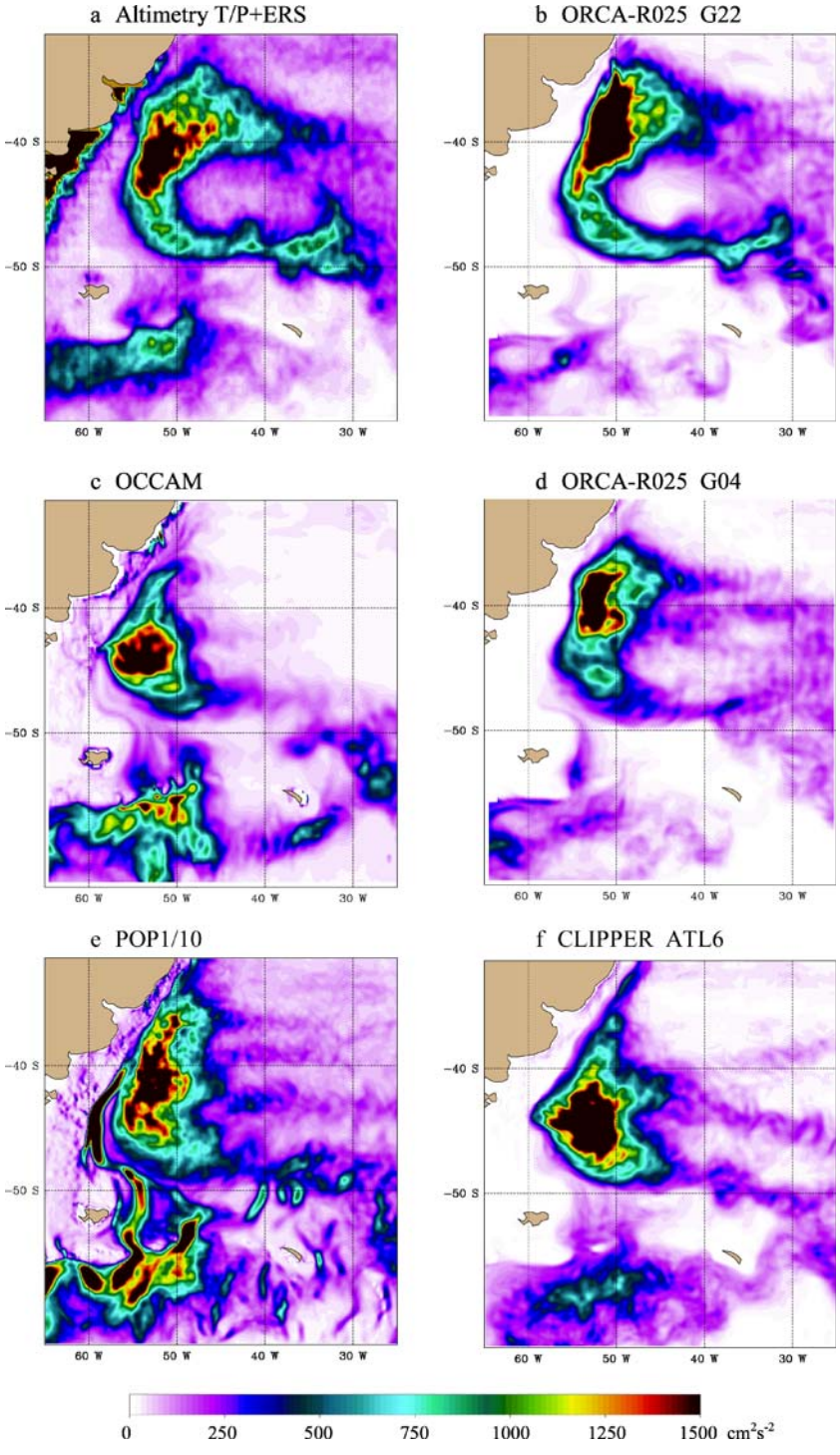

Fig. 10 Same as Fig. 8 (plots of *eke* in $cm^2\ s^{-2}$) for the western South Atlantic

very large eddies (or rings), which later drift into the South Atlantic. The ring generation is very regular in time; rings shed from the retroflection are quite large in size and all use the same pathway to the northwest. Their signature in the distribution of eke (Fig. 12d) is a band of high eke stretching from the retroflection region across the Cape Basin. The ring-generating process is dominated by shear instability. This picture is that usually provided by eddy-permitting numerical models since the Fine Resolution Antarctic Model experiment (Stevens and Killworth 1992) with the very few exceptions of the regional models of Biastoch and Krauss (1999) and de Miranda et al. (1999b), which, although at slightly coarser resolution (1/3°), did not show that bias. In these later regional experiments, the shear instability could be underestimated due to a lack of resolution. Recent models based on the same numerical code from Geophysical Fluid Dynamics Laboratory (OCCAM in Fig. 12c or POP1/10 in Fig. 12e) and on the OPA8.1 code (at 1/3° resolution, Treguier et al. 2001) also present the same type of bias. The ATL6 (1/6°) model

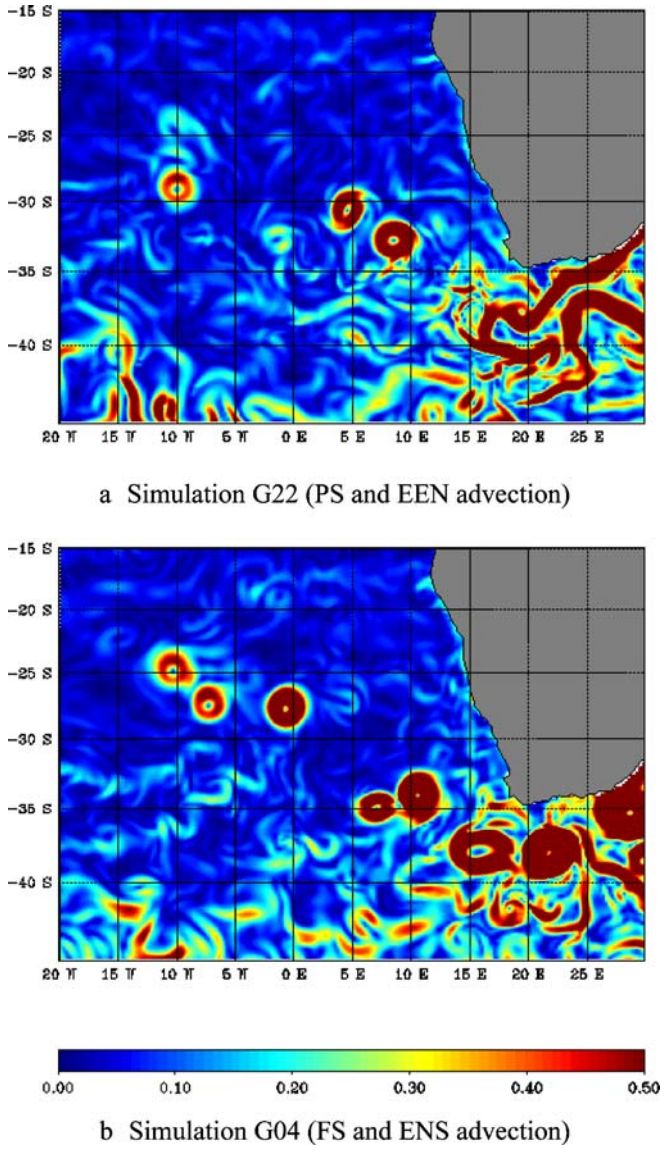

Fig. 11 Snapshot of current speed (in m/s) at 25 m depth in the Cape Basin and the region of the retroflection of the Agulhas Current for **a** simulation ORCA-R025 G22 (PS + EEN) and **b** simulation ORCA-R025 G04 (PS + ENS)

simulations run with OPA8.1 during the CLIPPER project provided a better representation of the Agulhas retroflection region (Treguier et al. 2003). It is possible that the use of a climatological open boundary across 30°E in this later simulation prevented the growth of the inertial eddies seen in Fig. 11b, resulting in a better simulation of the Agulhas Current. Nevertheless, the path of the Agulhas Rings in the South Atlantic was not correctly simulated.

The picture of the circulation in this region provided by simulation G22 with the PS and EEN scheme is significantly different from those described above and is more consistent with observations. In the snapshot of the current speed shown in Fig. 11a, the Agulhas retroflection appears as a large loop of a continuous stream, which extends into the south Atlantic, sometimes as far as 16°E, before it closes and sheds from the main stream. After shedding, this loop breaks into smaller eddies (the Agulhas Rings). Although the above scenario is by far the most frequent during the 10 years of the G22 simulation, we noticed a few periods when the Agulhas Current behaved in a way similar to that observed in G04. But overall, the eddy field in G22 is more chaotic than in G04, the Agulhas Rings rarely produced by pair and their path across the South Atlantic not as regular. We expect to reach a more complete understanding of the model behavior with the longer interannual forcing experiment of the Common Ocean-ice Reference Experiment (50 years) that will be performed in the near future.

Discrepancies noted above regarding the generation and pathway of the Agulhas Rings have drastic consequences on the Cape Basin eke distribution shown in Fig. 12. The eke pattern of simulation G22 (Fig. 12b) is by far the most consistent with that provided by satellite altimetry (Fig. 12a), although a tendency for a preferred path of the eddies in their westward drift still remains. As in satellite observations, largest eke values in G22 are found in the retroflection loop and in the returning Agulhas Current. In the other model simulations, quite large eke values are also found along the east African coast (i.e., in the Agulhas Current before the retroflection loop) and in the path of the rings in the South Atlantic—features not found in the Topex/Poseidon data. Maps of mssh (not shown) show a main path of the returning Agulhas Current along the northern flank of the Agulhas Plateau in simulation G22, very similar to that of the observed mssh of Niiler et al. (2003). This explains the "pinching" of the eke pattern at 25°E, 39°S, high eke levels being found at the north side of the plateau in the mean current, and minimum eke levels being found on the plateau itself. The other models do not show such pinching of the eke pattern at the Agulhas Plateau, which suggests that the G22 simulation is more realistic in accounting for the effects of topography on the mean flow.

3.5 Kuroshio

The simulation of the mean position of the Kuroshio along the coast of Japan is improved by the new schemes. The comparison of the mssh simulated by experiments G22 (Fig. 13b) and G04 (Fig. 13c) shows that G22 is again closer to the observations (Fig. 13a). In this latter simulation, location and meandering of the main stream along the Ryukyu Archipelago and southern Japan (i.e., before the current separates from the coast of Japan) compare very well with observations. The separation is marked by a slight overshoot with two standing eddies aligned offshore, and the path of the mean current is shifted 1°N of the observed position. Without PS and EEN advection (simulation G04), the overshoot and the mean current location are shifted even more to the north, and the standing eddies are now aligned along the coast reaching beyond 40°N. This is reflected in the pattern of the BSF difference of Fig. 6a, which shows negative values (i.e., reduced transport) on the north side along the Kuroshio

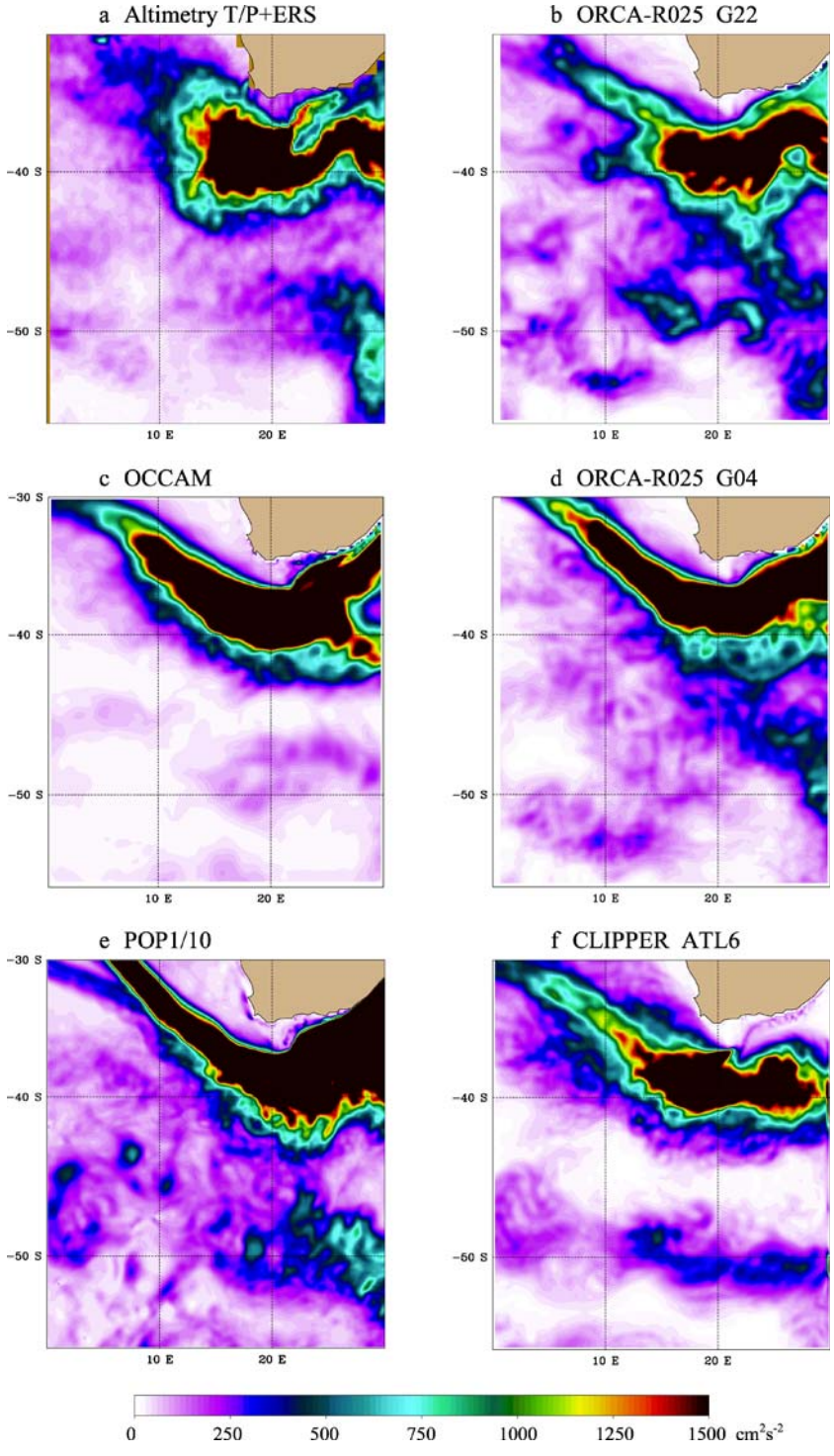

Fig. 12 Same as Fig. 8 (plots of *eke* in $cm^2\ s^{-2}$) for the Cape Basin in the South Atlantic

extension and positive values (i.e., increased transport) on the south side. This indicates a southward shift of the mean current path in simulation G22 compared to G04. The path of the Kuroshio after its separates from Japan is better located in POP1/10 (but not in OCCAM), but the intense high/low dipole of mssh south of Japan (also seen in OCCAM, Fig. 13c,e) is in strong disagreement with observations.

Eke shows a significant reduction in the Kuroshio extension in simulation G22 (Fig. 5a). In the observations, high eke levels are found much farther to the east (see Fig. 5b). POP1/10 (no figure shown, see Maltrud and McClean 2005) simulates a rather realistic eastward extension of eke in the North Pacific Ocean, indicating that simulating this feature could be more a resolution issue than a current topography interaction issue.

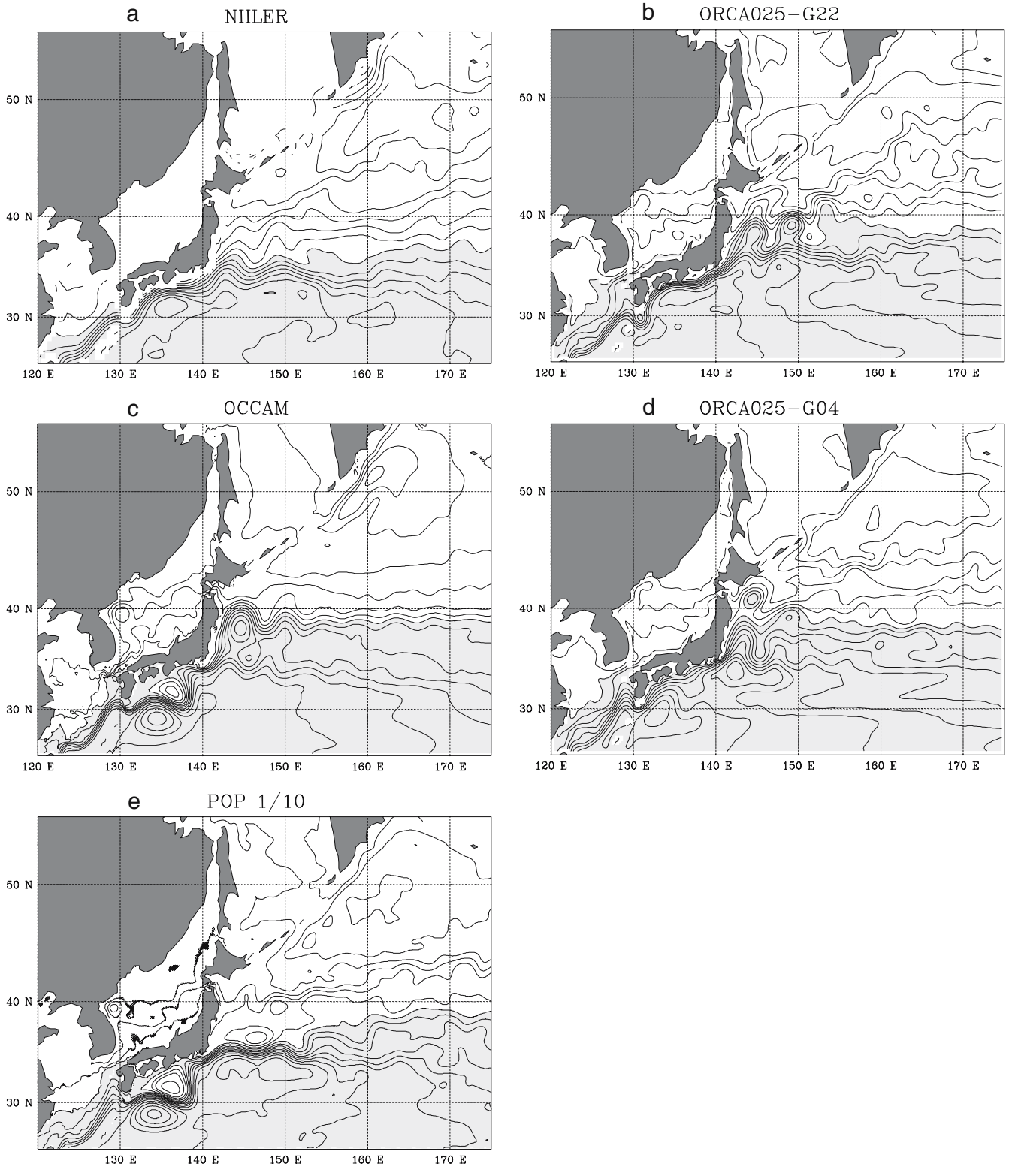

Fig. 13 Same as in Fig. 7 (plots of *mssh* in cm) for the western Pacific (without the CLIPPER model, which only covers the Atlantic). Contour interval is 10 cm

3.6 South Indian Ocean

The south Indian Ocean (the red box to the southwest of Australia in Fig. 6a) is another region where the BSF difference between simulations G22 and G04 shows a pattern indicating a meridional shift of the mean current. The bottom topography of the region (Fig. 15) is characterized by the Kerguelen Plateau in the southwest

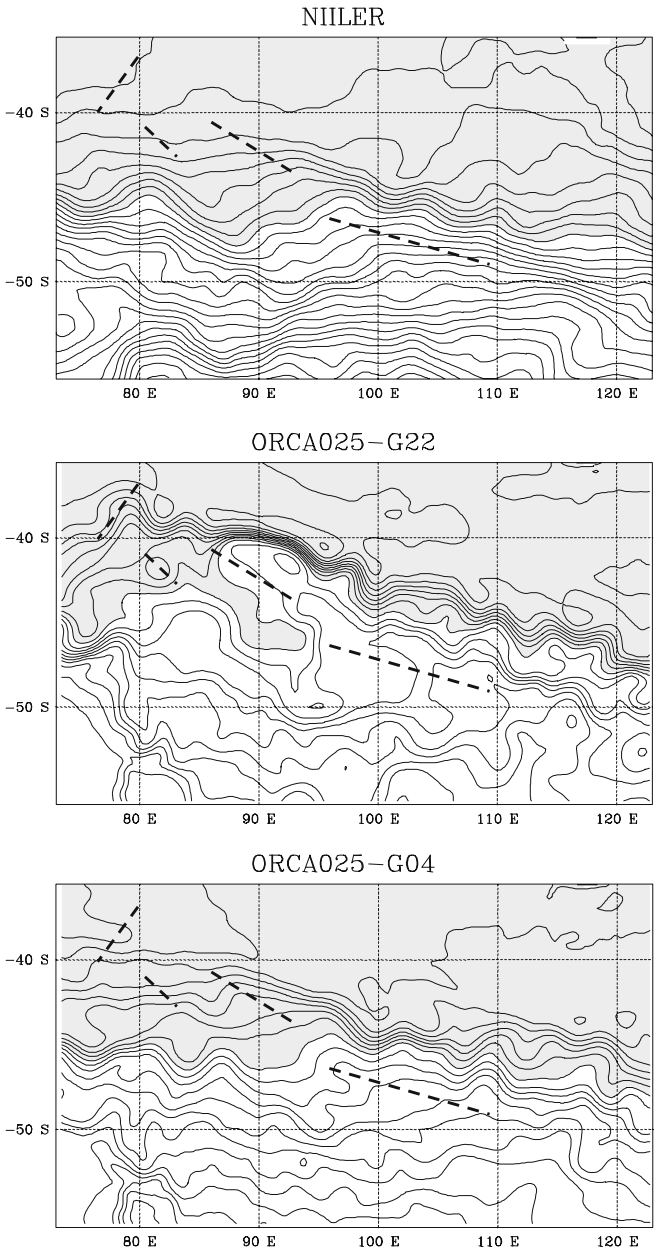

Fig. 14 Estimates of mean sea surface height (*mssh* in cm) in the South Indian Ocean from (*top*) observations (Niiler et al. 2003), (*middle*) global ORCA-R025 model simulation G22 (PS + EEN), and (*bottom*) global ORCA-R025 model simulation G04 (FS + ENS). All model results present a 3-year mean. Mean biases between estimates were removed by subtracting the area mean for each plot. Thus, *gray* (*white*) areas indicate region of mssh higher (lower) than the area mean. Contour interval is 10 cm. The *bold dashed lines* indicate the location of the main topographic features of the South Indian Ridge as reported in the topography map of Fig. 15

corner of the domain and the Amsterdam Island in the northwest corner at 41°S, 78°E from where the Southeast Indian Ridge (SIR) stretches to the southeast. The passage between the islands of Kerguelen and Amsterdam at 75°E features a rise of the bottom topography of 1,500 m above the abyssal plains of the western and eastern Indian basins, and is likely to influence the path of the ACC to the east.

The observed flow in the area can be described from the mssh of Niiler et al. (2003) shown in Fig. 14 and the eke distribution obtained from Topex/Poseidon (Fig. 15). The ACC enters this region passing between Kerguelen and Amsterdam as a broad current spreading between 45 and 50°S. In its eastward route, the main stream of the ACC makes a large meander at 80°E while the topography rises slightly between the Kerguelen–Amterdam passage. Further down stream, the ACC crosses the SIR between 90 and 100° E. It then tilts southeastward to flow along the northern flank of the ridge. The ACC shows significant eke levels as it passes the Kerguelen Plateau (between 70 and 90°E) and after crossing the ridge (from 105 to 120°E, Fig. 15a). This circulation scheme is very consistent with that recently deduced from autonomous floats drifting at 900 mb (Davis 2005), suggesting a significant barotropic component of the flow.

The mssh in simulation G04 (no PS and EEN advection) exhibits a similar behavior to the observed one, the ACC crossing the SIR at the same location (Figs. 14c and 15c). OCCAM and POP1/10 simulations (no figure shown) are very similar to G04. However, both these models tend to produce more zonal flows and to show less sensitivity to the bottom topography. This is well illustrated by their respective eke patterns (Fig. 15c,e), which do not exhibit the observed tilt according to the orientation of the SIR.

In contrast to the observed estimate, the mssh in simulation G22 reveals a strong topographic influence and a significant branching of the ACC (Fig. 14b). At the entrance of the domain (75°E) the main stream of the ACC is split in two branches. One branch, not present in the observed mssh, flows north up to Amsterdam Island where it crosses the SIR. It continues to flow southeastward along the northern side of the ridge and significantly intensifies, probably by topographic influence between 80 and 100°E. The other branch, which enters the domain along the eastern Kerguelen Plateau, behaves in a way similar to the observed mssh. The flow meanders eastward, part of it crossing the SIR in the same passage as suggested by the observed mssh between 90 and 100°E. The northward split of the ACC at the longitude of the Kerguelen Plateau is not related to PS alone (although its contribution is dominant). Simulation G03, which uses the FS topography and the new EEN scheme, already differs from G04 (Fig. 6b) and also shows this split of the ACC path (no figure shown).

The circulation branches described above correspond to regions of high eke (Fig. 15). The high eke values seen in G22 on the northern side of the SIR in the (80°E, 100°E) longitude band (Fig. 15b) is the direct result of the instability of the northern branch of the ACC. In the eastern part of the domain (100°E, 120°E), the eke is rather similar in pattern between G22, G04, and the estimate derived from altimeter observations; high eke values are found on the north side of the SIR aligned along the topography.

Considering the remarkably good agreement of G22 with observations in most regions, this unrealistic behavior of the ACC in this longitude band is rather disconcerting. It is likely that the behavior of the northern branch and, in particular, the intensification of the current by the strong

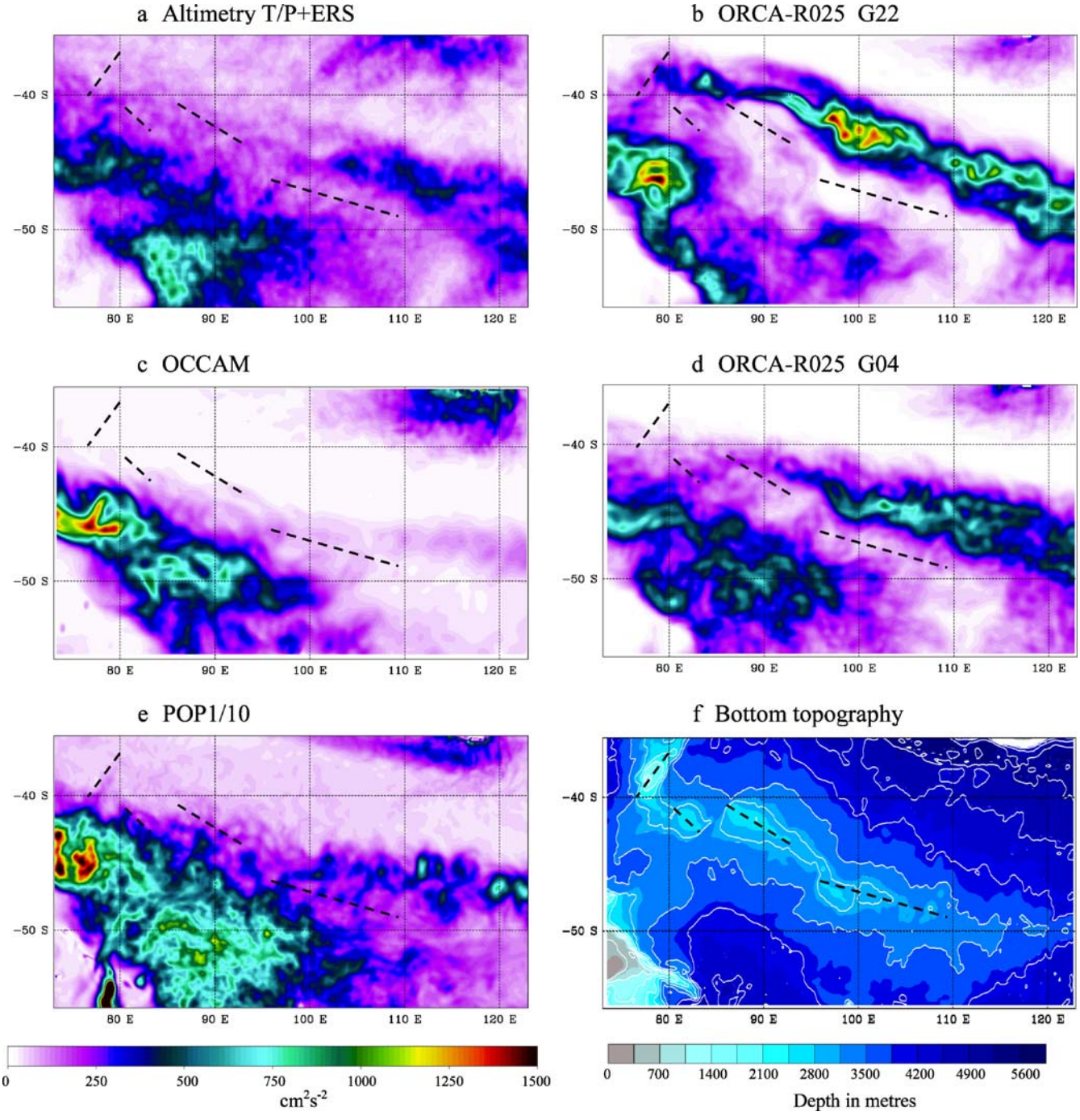

Fig. 15 Same as in Fig. 8 (plots of *eke* in $cm^2\ s^{-2}$) for the South Indian Ocean (without the CLIPPER model, which only covers the Atlantic). The bottom topography of the area is shown (*bottom right plot*) with a contour interval of 500 m. The *bold dashed lines* indicate the location of the main topographic features of the South Indian Ridge

topography of Amsterdam Island and the SIR is the downstream consequence of the splitting of the ACC as it reaches the longitude of the Kerguelen Plateau. This split, which seems to be related to the topographic slopes and its relation to the use of the PS and EEN numerical schemes deserves a more detailed investigation.

The difference between the G22 and G04 simulations may be partly explained by the differences between the PS and the FS representations of the topography of the Kerguelen–Amsterdam passage. Because the bottom depth is adjusted to the local *z*-level in the FS topography, a flat channel exists in G04, which connects the western and eastern abyssal plains at the depth of 3,530 m (the 37th level of the model). This channel does not exist in the original Etopo2 topography nor in the PS topography, which both have a sill in the passage at the depth of nearly 3,300 m. The existence of this channel in G04 may

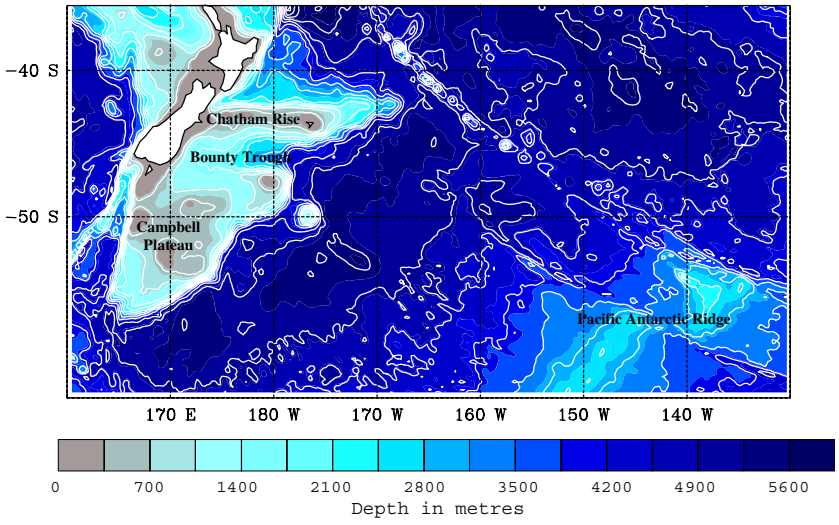

Fig. 16 Bottom topography (in meters) of the South Pacific around New Zealand. *Colors* indicate the depth. Contour interval is 500 m

influence the path of the ACC between the islands, which may thus agree with observations for the wrong reasons.

3.7 Campbell Plateau

The region south and west of New Zealand is also characterized by large changes in BSF due to the use of both PS and EEN (Fig. 6). Major BSF changes between G22 and G04 are localized along the topography of the Campbell Plateau and the Chatham Rise (see the bottom topography map in Fig. 16). Figure 17 shows the various estimates of mssh. As noted for most regions we have already looked at, there is a remarkable agreement between the observed mssh and that simulated in G22, the latter showing currents at finer scale. Every circulation feature, like the branching of the ACC at the tip of the Campbell Plateau (55°S, 165°E), the trapping of the ACC on the slope of the east side of the Campbell Plateau, the well-marked anticyclonic circulation far inside the Bounty Trough (reaching the coast of New Zealand and flowing out the trough along Chatham Rise), are reproduced. Even farther to the west (between 150 and 130°W), the model reproduces the ACC splitting into two branches while it crosses the Pacific Antarctic Ridge. The G04 simulation, although rather realistic in this region, does not show the same amount of details. In particular, flows trapped on topographic slopes are weaker. However, one could wonder whether the G22 could overemphasize the topographic constraint, as suggested for the South Indian region. This will have to be investigated in the future with additional in situ data and by looking at the baroclinic structure of the flow. Note that recent subsurface float observations presented by Davis (2005, Fig. 3) show a very consistent circulation inside Bounty Trough, trapped on the topographic slope, very much like the circulation pattern simulated in G22. OCCAM and POP1/10 models do not simulate the flow with similar details despite similar or higher resolution. In particular, the intrusion of the ACC into the Bounty Trough is not reproduced. An interesting model feature is the standing cyclonic eddy found in the abyssal plain south of the Campbell Plateau at 55°S, 172°E. This feature is seen in every model and corresponds in the observed mssh to a "flat" (i.e., no gradient) mssh, separating two branches of the ACC. Models and observations are thus consistent, indicating that the mean flow does not go through but around the abyssal plain.

4 Discussion and conclusion

We have provided an overview of progress in modeling the ocean general circulation at eddy-permitting (1/4°) resolution achieved within the European project DRAKKAR. The main focus was on modeling issues whose importance was continuously emphasized by Christian Le Provost, which are the numerical treatment of nonlinearities and bottom topography. We introduced this paper with a brief presentation of the DRAKKAR community project, the birth of which Christian Le Provost actively participated. We have described the eddy-permitting, global 1/4° resolution, model configuration implemented by the project ORCA-R025. This ocean/sea-ice general circulation model uses the NEMO code, which is a new version of the OPA primitive equation, *z*-level, ocean circulation model coupled to the LIM2 sea-ice model. The characteristic of the new code, which is evaluated here, lies in a new advection scheme for momentum equations (the EEN scheme) and the use of a PS representation of the bottom topography. Ten-year-long sensitivity simulations with and without EEN and PS numerics were run with ORCA-R025 under a climatological atmospheric forcing. The impact of the new numerical choices on the model solution were assessed by comparing the model mssh and eke with their equivalent in the observations and with other state-of-the-art model simulations at equivalent or higher resolution.

Although our analysis remained quite descriptive, it demonstrated that the combination of the EEN scheme with PS yields a remarkable improvement in the major circulation patterns. Well-known biases in the representation of

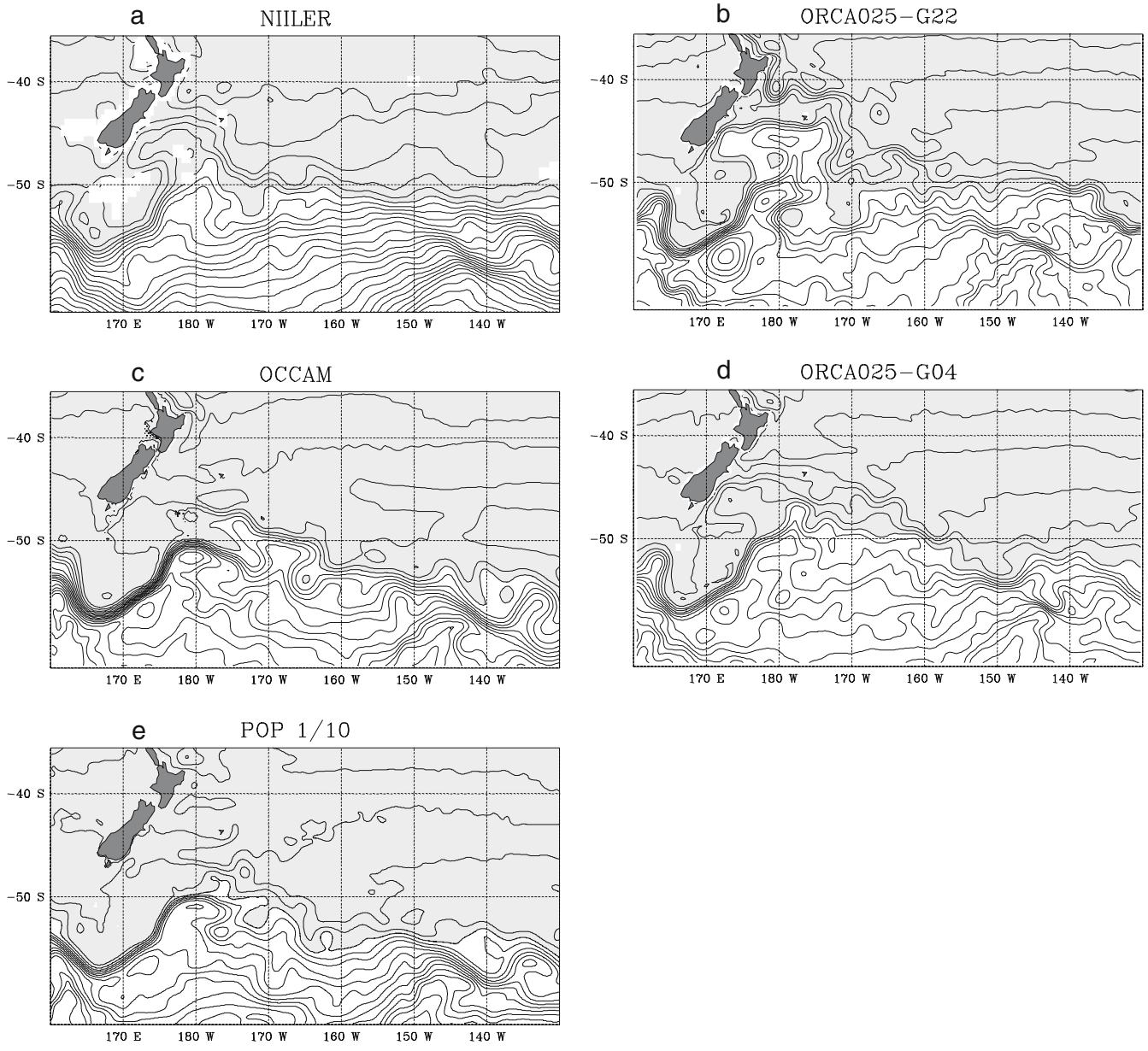

Fig. 17 Same as in Fig. 7 (plots of *mssh* in cm) for the Campbell Plateau in the South Pacific (without the CLIPPER model, which only covers the Atlantic). Contour interval is 10 cm

western boundary currents, such as in the Atlantic, the separation of the Gulf Stream, the path of the North Atlantic Current at the Northwest Corner, the location of the Brazil–Malvinas Confluence, and the strength of the Zapiola Eddy, are significantly corrected. Similar improvements are found in the Pacific, Indian, and Southern Oceans, and characteristics of the simulated mean circulation patterns are generally much closer to observations. In comparison with other models at similar resolution (the 1/4° OCCAM), the ORCA-R025 configuration generally performs better. In addition, the ORCA-R025 solution is often comparable to (or even better than) solutions obtained at 1/6° (CLIPPER model) or 1/10° (POP Model) resolution in some aspects concerning mean flow patterns and distribution of eke. Note that the improvements in mssh and eke presented here generally correspond to improvements in the deep circulation (not discussed in this paper) and, in particular, in a stronger and quite coherent deep western boundary current.

The impact of the new numerical schemes is not a uniformly positive one. The flow pattern of the ACC in the South Indian Ocean is different from that suggested by both mssh and eke observations when PS and EEN are used. Moreover, the solution with this later combination seems degraded when compared to the solution with the FS topography and the former ENS advection, although this could be due to compensating errors in the FS representation of topography. The unrealistic branching of the ACC at the longitude of the Kerguelen plateau (Section 3.6) suggests a strong local sensitivity of the model solution

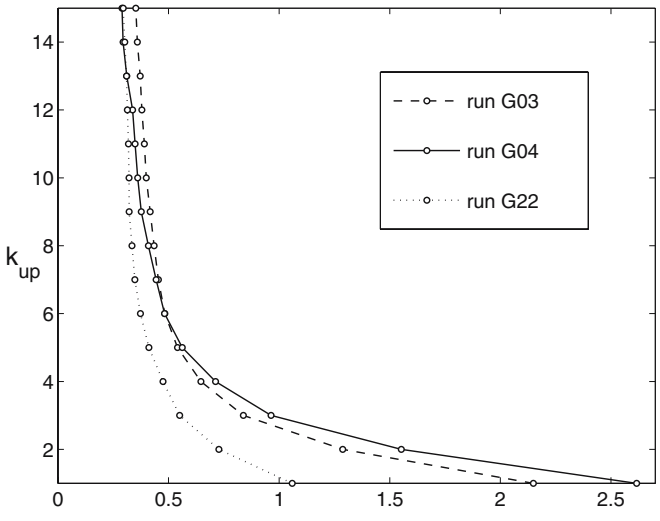

Fig. 18 Snapshot of the normalized grid scale irregularities in vertical velocity fields as a function of the level above the bottom (k^{up}), averaged over the Gulf Stream area in simulations G04 (FS + ENS), G03 (FS + EEN), and G22 (PS + EEN). The difference (δw) between the vertical velocity (w) and its nine cell average ($\overline{w}$) was computed on each model level. The vertical levels were reindexed from the bottom ($k^{up}=i$ is the ith level above the bottom). The grid scale irregularity, which is plotted, is the ratio between the averages at constant k^{up} of $|\delta w|$ and $|\overline{w}|$.

to the bottom topography, which we do not understand yet. Additional simulations, driven by different atmospheric forcing, produced a MOC and an ACC of different strength from G22 but still presented a similar flaw in the region, and the same happened with a different algorithm to calculate the pressure gradient between partial cells. Additional simulations are underway, but at present, we are not able to explain this local behavior of the solution.

The use of PS topography and EEN advection scheme thus dramatically affects the ORCA-R025 model solution in regions, which are subject to strong current–topography interactions. Understanding in full the dynamical origin of these improvements is beyond the scope of the present paper, but first analyses point to the presence of small-scale noise near the bottom as a crucial factor. Figure 18 shows a measure of the vertical velocity noise (the deviation of the vertical velocity from its nine-point average) in the Gulf Stream region as a function of depth (a similar picture is obtained in all regions of the global model). In all three cases (G03, G04, and G22), we find this noise to increase significantly toward the bottom. Near the bottom layer (approximately eight levels up from the bottom), the noise is drastically reduced by the use of the EEN scheme in combination with PS topography (G22). According to J. Le Sommer et al. (2006, in preparation), it is plausible that the noise level has time–mean effects through the diffusion of momentum and tracer, and that the choice of bottom cell and advection schemes consequently affects the vertical energy distribution near sloping topography and thereby the larger scale flow.

We conclude that significant corrections of the mean biases seen in general circulation model solutions at eddy-permitting resolution, which were not obtained by increasing resolution, were obtained by changing the numerical methods used. Studies searching for a full understanding of the impact of the EEN and PS numerics on the model dynamical solution are currently under way. It was already shown that the impact of the EEN scheme is greatest at grid cells nearest a side wall (J. Le Sommer et al. 2006, in preparation), suggesting a great sensitivity of the momentum advection to the lateral and bottom boundary condition. The numerical treatment of momentum advection has somewhat been overlooked in global and climate ocean models, except perhaps for the dynamics of the Equatorial Undercurrent. This contrasts with numerous studies dealing with the importance of advection schemes for temperature, salinity and other tracers (see, for example, Lévy et al. 2001). It also contrasts with the Regional Oceanic Modeling System where special effort was put into developing new advection schemes for momentum (Shchepetkin and McWilliams 2005).

In recent years, improvement of global ocean models was sought through an increase in horizontal resolution, and global model simulations were performed at 1/10 and 1/12° resolutions (Maltrud and McClean 2005; Kara et al. 2005; Coward and de Cuevas 2005). Our results bring forward a different view and point out the numerical treatment of momentum advection and bottom topography and, more generally, the improvement of the model numerics as an issue of prime importance for eddy-permitting climate modeling.

But eddy-permitting models were shown to perform worse than coarse resolution models in the representation of important small-scale processes such as the restratification after a deep convection event (J. Chanut et al. 2006, submitted for publication; Czeschel 2005) or the deep overflows. It is clear that physical parameterizations developed at coarse resolution (for example, the "bolus velocity" of Gent and McWillams 1990 or the "bottom boundary layer" of Beckmann and Döscher 1997) are not suited for that resolution. It is likely that development or adaptation of parameterizations of these key subgrid scale processes at eddy-permitting resolution should be coordinated with the development of numerics because their efficiency could depend on the model numerical schemes.

The complexity of the global ice–ocean system is such that the sensitivity of an eddy-permitting model is still poorly known. Nevertheless, it is expected that many ocean models used for climate prediction, which provide our only means to assess future changes, will begin to operate in the eddy-permitting regime within a few years. Hence, developing an improved understanding of how this regime plays a key role in controlling global ocean dynamics has become a high priority.

Acknowledgements This work is a contribution of the DRAKKAR project. Support to DRAKKAR comes from various grants and programs listed hereafter. French national programs GMMC, PATOM, and PNEDC. PICS 2475 from Institut National des Sciences de l'Univers (INSU) and Centre National de la Recherche Scientifique (CNRS). Kiel SFB460 and CLIVAR-marin (03F0377A/B) supported by Deutsche Forschungsgemeinschaft. European integrated project MERSEA. Computations presented in this study were performed at Institut du Développement et des Ressources en Informatique Scientifique (IDRIS). Finally, we would like to thank P. Niiler, N. A. Maximenko, and J. C. McWilliams who kindly made their data sets available from the Web.

References

Adcroft A, Hill C, Marshall J (1997) Representation of topography by shaved cells in a height coordinate ocean model. Mon Weather Rev 125:2293–2315

Arakawa A, Lamb VR (1981) A potential enstrophy and energy conserving scheme for the shallow water equations. Mon Weather Rev 109:18–36

Barnier B, Le Provost C (1993) Influence of bottom topography roughness on the jet and inertial recirculation of a mid-latitude gyre. Dyn Atmos Oceans 18:29–65

Beckmann A, Döscher R (1997) A method for improved representation of dense water spreading over topography in geopotential-coordinate models. J Phys Oceanogr 27:581–591

Berliand ME, Strokina TG (1980) Global distribution of the total amount of clouds. Hydrometeorological, Leningrad, p 71 (in Russian)

Biastoch A, Krauss W (1999) The role of mesoscale eddies in the source regions of the Agulhas current. J Phys Oceanogr 29:2303–2317

Blanke B, Delecluse P (1993) Variability of the tropical Atlantic Ocean simulated by a general circulation model with two different mixed-layer physics. J Phys Oceanogr 23:1363–1388

Blayo E, Le Provost C (1993) Performance of the capacitance matrix method for solving Helmholtz type equations in ocean modelling. J Comp Physiol 104:347–360

Boebel O, Davis RE, Ollitrault M, Peterson RG, Richardson PL, Schmid C, Zenk W (1999) The intermediate depth circulation of the western South Atlantic. Geophys Res Lett 26(21):3329–3332

Böning CW, Bryan FO (1996) Large-scale transport processes in high resolution circulation models. In: Borntraeger G (ed) The warm watersphere of the North Atlantic. Berlin, pp 91–128

Böning CW, Rhein M, Dengg MJ, Dorow C (2003) Modeling CFC inventories and formation rates of Labrador Sea Water. Geophys Res Lett 30(2):1050. DOI 10.1029/2002GL014855

Bryan FO, Holland WR (1989) A high resolution model of the wind- and thermohaline-driven circulation in the North Atlantic Ocean. In: Muller P, Henderson D (eds) Aha Huliko'a parameterization of small-scale processes. Hawaii Institute of Geophysics, Hawaii, pp 99–115

CERSAT (2002) Mean wind fields (MWF product), vol. 1. In: ERS-1, ERS-2 & NSCAT user manual. Ref C2-MUT-W-05-IF, version 1.0

Coward AC, de Cuevas BA (2005) The OCCAM 66 level model: model description, physics, initial conditions and external forcing. Southampton Oceanography Centre internal document 99, Southampton, UK, p 83

Czeschel L (2005) The role of eddies for the deep water formation in the Labrador Sea. Ph.D. thesis, Kiel University, Institut f. Meereswissenschaften, p 101

de Miranda A, Barnier B, Dewar WK (1999a) On the dynamics of the Zapiola anticyclone. J Geophys Res Ocean 104:21137–21149

de Miranda A, Barnier B, Dewar WK (1999b) Mode waters and subduction rates in a high resolution South Atlantic simulation. J Mar Res 57:213–244

Davis ER (2005) Intermediate-depth circulation of the Indian and South Pacific Oceans measured by autonomous floats. J Phys Oceanogr 35:683–707

Dewar WK (1998) Topographic and barotropic transport control by bottom friction. J Mar Res 56:295–328

Ducet N, Le Traon PY, Reverdin G (2000) Global high resolution mapping of ocean circulation from Topex/Poseidon and ERS-1 and -2. J Geophys Res Ocean 105(C8):19477–19498

DYNAMO Group (1997) DYNAMO: dynamics of the North Atlantic models: simulation and assimilation with high resolution models. Ber Institute für Meereskunde, Universität Kiel, pp 294–334

Fichefet T, Morales Maqueda MA (1997) Sensitivity of a global sea ice model to the treatment of ice thermodynamics and dynamics. J Geophys Res 102:12609–12646

Ganachaud A, Wunsch C (2003) Large-scale ocean heat and freshwater transports during the World Ocean Circulation Experiment. J Climate 16:696–705

Gent PR, McWillams JC (1990) Isopycnal mixing in ocean circulation models. J Phys Oceanogr 20:150–155

Goosse H (1997) Modeling the large scale behaviour of the coupled ocean–sea ice system. Ph.D. thesis, Université Catholique de Louvain, Louvain-la-Neuve, Belgium, p 231

Grezio A, Wells NC, Ivchenko VO, de Cuevas BA (2005) Dynamical budgets of the Antarctic Circumpolar Current using ocean general-circulation models. Q J Roy Meteor Soc Part A 607(28):833–860

Jakobsson M, Cherkis NZ, Woodward J, Macnab R, Coakley B (2000) New grid of arctic bathymetry aids scientists and mapmakers. Eos Trans Am Geophys Union 81(9):89, 93, 96

Jourdan D, Balopoulos E, Garcia-Fernandez MJ, Maillard C (1998) Objective analysis of temperature and salinity historical data set over the Mediterranean Basin. IEEE Press, Piscataway, NJ

Kalnay E, Kanamitsu M, Kistler R, Collins W, Deaven D, Gandin L, Iredell M, Saha S, White G, Woollen J, Zhu Y, Chelliah M, Ebisuzaki W, Higgins W, Janowiak J, Mo KC, Ropelewski C, Leetmaa A, Reynolds R, Jenne R (1996) The NCEP/NCAR 40-year reanalysis project. BAMS 77:437–471

Kara AB, Barron CN, Martin PJ, Smedstad LF, Rhodes RC (2005) Validation of interannual simulations from the 1/8° global Navy Coastal Ocean Model. Ocean Model 11:376–398

Käse RH, Biastoch A, Stammer DB (2001) On the mid depth circulation in the Labrador and Irminger seas. Geophys Res Lett 28:3433–3436

Lee MM, Coward AC (2003) Eddy mass transport in an eddy-permitting global ocean model. Ocean Model 5/3:249–266

Levitus S, Boyer TP, Conkright ME, O'Brian T, Antonov J, Stephens C, Stathopolos L, Johnson D, Gelfeld R (1998) World ocean database 1998. NOAA Atlas NESDID 18, US Government Printing Office, Washington, DC

Lévy M, Estublier A, Madec G (2001) Choice of an advection scheme for biogeochemical models. Geophys Res Lett 28 (19):3725–3728. DOI 10.1029/2001GL012947

Lythe MB, Vaughan DG (2001) BEDMAP: a new ice thickness and subglacial topographic model of Antarctica. J Geophys Res Solid Earth 106:11335–11351

Madec G, Imbard M (1996) A global ocean mesh to overcome the North Pole singularity. Climate Dyn 12:381–388

Madec G, Delecluse P, Imbard M, Levy C (1998) OPA 8.1 general circulation model reference manual. Notes de l'IPSL, Université P. et M. Curie, B102 T15-E5, 4 place Jussieu, Paris cedex 5, No. 11, p 91

Maltrud ME, McClean JL (2005) An eddy resolving global 1/10° ocean simulation. Ocean Model 8:31–54

Maltrud ME, Smith RD, Semtner AJ, Malone RC (1998) Global eddy-resolving ocean simulations driven by 1985–1995 atmospheric fields. J Geophys Res Ocean 103:30825–30853

Masumoto Y, Sasaki H, Kagimoto T, Komori N, Ishida A, Sasai T, Miyama T, Motoi T, Mitsudera H, Takahashi K, Sakuma H, Yamagata T (2004) A fifty-year eddy-resolving simulation of the world ocean: preliminary outcomes of OFES (OGCM for the Earth Simulator). J Earth Simulator 1:35–56

Myers PG (2002) SPOM: a regional model of the sub-polar North Atlantic. Atmos-Ocean 445–463
Murray RJ (1996) Explicit generation of orthogonal grids for ocean models. J Comput Phys 126:251–273
Niiler PP, Maximenko NA, McWilliams JC (2003) Dynamically balanced absolute sea level of the global ocean derived from near-surface velocity observations. Geophys Res Lett 30 (22):2164. DOI 10.1029/2003GL018628
Pacanowski RC, Gnanadesikan A (1998) Transient response in a z-level ocean model that resolves topography with partial cells. Mon Weather Rev 126:3248–3270
Penduff T, Barnier B, Verron J, Kerbiriou MA (2002) How topographic smoothing contributes to differentiating the eddy flows simulated by sigma- and z-level models. J Phys Oceanogr 32:122–137
Penduff T, Barnier B, Molines J-M, Madec G (2005) On the use of current meter data to assess the realism of ocean model simulations. Ocean Model 11(3–4):399–416
Rintoul SR, Hughes CW, Olbers D (2002) The Antarctic Circumpolar Current system. In: Siedler G, Church J, Gould J (eds) Ocean circulation and climate, international geophysics series, vol. 77. Academic, New York
Roullet G, Madec G (2000) Salt conservation, free surface and varying volume: a new formulation for ocean GCMs. J Geophys Res 105:23927–23942
Sadourny R (1975) The dynamics of finite-difference models of the shallow-water equations. J Atmos Sci 32(4):680–689
Saunders PM, King BA (1995) Bottom currents derived from a ship borne ADCP on the WOCE cruise A11 in the South Atlantic. J Phys Oceanogr 25:329–347
Shchepetkin AF, McWilliams JC (2005) Regional ocean model system: a split–explicit ocean model with a free surface and topography—following vertical coordinate. Ocean Model 9:347–404
Smith WHF, Sandwell DT (1997) Global sea-floor topography from satellite altimetry and ship depth soundings. Science 277:1956–1962
Smith RD, Maltrud ME, Bryan FO, Hecht MW (2000) Numerical simulation of the North Atlantic Ocean at 1/10°. J Phys Oceanogr 30:1532–1561
Steele M, Morley R, Ermold W (2001) PHC: a global ocean hydrography with a high quality Arctic Ocean. J Climate 14:2079–2087
Stevens DP, Killworth PD (1992) The distribution of kinetic energy in the Southern Ocean. A comparison between observations and an eddy-resolving general circulation model. Phil Trans Royal Soc B 338:251–257
Timmmerman A, Goosse H, Madec G, Fichefet T, Ethe C, Dulière V (2005) On the representation of high latitude processes in the ORCA-LIM global coupled sea-ice ocean model. Ocean Model 8:175–201
Treguier AM, Reynaud T, Pichevin T, Barnier B, Molines JM, de Miranda A, Messager C, Beismann JO, Madec G, Grima N, Imbard M, Le Provost C (1999) The CLIPPER project: high resolution modelling of the Atlantic. Int WOCE Newsl 36:3–5
Treguier AM, Barnier B, de Miranda A, Molines JM, Grima N, Imbard M, Madec G, Messager C, Michel S (2001) An eddy permitting model of the Atlantic circulation: evaluating open boundary conditions. J Geophys Res 106:22115–22129
Treguier AM, Boebel O, Barnier B, Madec G (2003) Agulhas eddy fluxes in a 1/6° Atlantic model. Deep-Sea Res Part 2 Top Stud Oceanogr 50:251–280
Trenberth KE, Caron JM (2000) Estimates of meridional atmosphere and ocean heat transports. J Climate 14:3433–3443
Trenberth KE, Olson JG, Large WG (1989) A global ocean wind stress climatology based on ECMWF analyses. National Center for Atmospheric Research, boulder, NCAR/TN-338+STR, p 93
Verron J, Le Provost C (1985) A numerical study of quasi-geostrophic flow over isolated topography. J Fluid Mech 154:231–252
Verron J, Le Provost C, Holland WR (1987) On the Effects of a midocean ridge on the general circulation: numerical simulations with an eddy-resolved ocean model. J Phys Oceanogr 17:301–312
Webb D J, de Cuevas BA, Coward AC (1998) The first main run of the OCCAM global ocean model. Internal document no. 34, Southampton Oceanography Centre, UK
Willebrand J, Barnier B, Böning C, Dieterich C, Killworth PD, Le Provost C, Jia Y, Molines JM, New AL (2001) Circulation characteristics in three eddy-permitting models of the North Atlantic. Prog Oceanogr 48:123–162
Xie P, Arkin PA (1997) Global precipitation: a 17-year monthly analysis based on gauge observations, satellite estimates, and numerical model outputs. Bull Am Meteorol Soc 78 (11):2539–2558

ANNEX 5

Ocean surface forcing and surface fields

Mercator News Letter

July 2006

News: Ocean surface forcing and surface fields

By Bernard Barnier, Laurent Brodeau and Thierry Penduff

Equipe de Modélisation des Ecoulements Océaniques à Moyenne et grande échelle (MEOM)
Laboratoire des Ecoulements Géophysique et Industriels, Grenoble

Exchanges of energy and water occurring at the air-sea interface establish links and feedbacks between the atmosphere and the ocean, and are key processes in the climate and weather systems. There are great needs in climate and oceanographic research for high quality estimates of large scale fluxes of heat, freshwater and momentum. There has been substantial progress in our knowledge of the ocean surface fluxes in recent years. Nevertheless, new challenges have emerged, stimulated by the use of eddy-resolving ocean general circulation models (OGCMs) to investigate the ocean decadal variability and by the rapid development of operational oceanography. The state of our knowledge in the field of air-sea exchanges of energy and water is comprehensively covered in the report on air-sea fluxes from the WCRP working group (1). For in-depth considerations on the need of surface fluxes in operational ocean analysis and forecasting systems, we recommend the book chapter by W. Large (2).

Surface flux estimates

Attempts to produce climatologies and long-term (decadal) time series of the air-sea flux fields differ in many aspects. For example, Figure 1 compares over a 17-years period, the downward radiations provided by the CORE data set (3) (basically a satellite observation based product), with the one from the ERA40 data set (4) (the recent atmospheric re-analysis performed at ECMWF). Both data sets are considered as state of the art products in terms of flux estimates. In the long term mean, the ERA40 product compared to the CORE one shows a deficit of radiation on the equatorial band and an excess at higher latitudes (Figure 1a). Globally, the ocean receives more radiation (between 2 to 5 Wm-2) with ERA40 (Figure 1b). But the most striking difference between the two data sets is found in their representation of the inter-annual variability (Figure 1cd): ERA40 is showing a quite unrealistic decreasing trend in the inter-tropical band. Similar differences are found between climatologies and time series of the other heat and freshwater fluxes (5).

Reasons for that are many, and the lack of observational data is one. But there is one major difficulty for heat flux estimation which is intrinsic to the nature of the fluxes: while the magnitude of individual heat flux components is of the order of a few 100 Wm-2, the net heat flux and the inter-annual variability of the fluxes are of the order of a few 10 Wm-2, and the long-term changes in heat content (or heat transport) of the world ocean is consistent with changes in surface heat flux of a few Wm-2. Thus, the difference of a few W/m2 pointed out in radiative fluxes of CORE and ERA40 (Figure 1b) is significant. This places stringent requirements on the accuracy of flux calculations, since a 10% error on a flux component may introduce a first order bias in the net heat balance. This likely explains why biases can be observed between flux estimates using different sources and retrieval methods.

The accuracy of flux calculations is therefore a critical issue. If uncertainties on air-sea fluxes are difficult to quantify because of a lack of direct measurements, they decrease as time and space averaging is performed. The best known constraint is that the long-term mean heat and freshwater fluxes should balance near zero at global scale. However, the use of high resolution ocean models in research and operational systems demands fluxes and surface variables with global coverage at spatial-scales of the order of 10 km and time-scale of a few hours. To meet this demand on every flux or variable entering the forcing function of an OGCM is presently out of range. The accuracy of flux calculation at these scales is thus a new challenge, which is presently taken up with satellite measurements and numerical weather prediction models. Two papers in this newsletter focus on this issue, and present on-going efforts to estimate a consistent set of wind fields at a 6 hour sampling from satellite measurements (paper by A. Bentamy and D. Croize-Fillon), and to produce highly sampled SST (paper by H. Roquet).

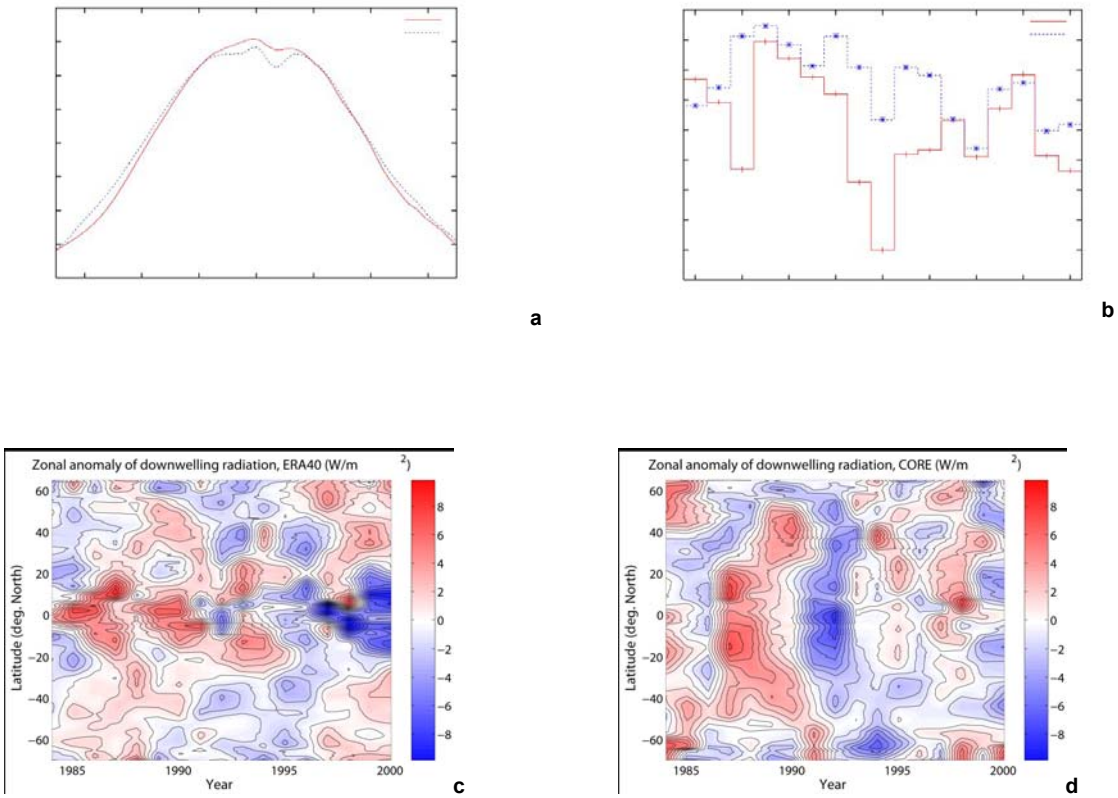

Figure 1
Comparison over the period 1984-2000 of the zonal average of the total down-welling radiation (solar plus infrared) provided by CORE (red line) and ERA40 (blue line) data sets. Are shown: a) the distribution with latitude of the long term (17 years) mean, b) the global averaged annual mean for individual years, and the year to year variations in ERA40 (c) and CORE (d).

Ocean surface forcing

At first thought, the ocean/atmosphere coupling in the surface exchanges is so strong that driving an ocean-only model (i.e. not coupled with an atmospheric model) with observed surface fluxes (i.e. fluxes obtained from observation of surface variables) could be considered as a silly exercise. Nevertheless, oceanographers have been very successful in running ocean-only models in those conditions, provided that some kinds of parameterisation of the ocean feedbacks were used. Therefore, in the process of constructing a forcing function for OGCMs, it would be an error to separate the problem of the estimation and accuracy of surface fluxes and other surface variables, from that of the formulation of the surface boundary condition used by the model. In the NEMO community, two different methods are commonly used to account for the ocean feedbacks on the forcing fluxes, which put different requirements on the surface fields.

The flux correction method [6] simply utilizes the global observed flux fields (radiative fluxes (solar and infrared), turbulent fluxes (wind stress, sensible and latent heat, evaporation), precipitation and river runoff). The ocean feedback is parameterised by a relaxation to an observed sea surface temperature (SST) (with a time scale which varies with space and time expressing the sensitivity of the surface fluxes to small changes in SST. The operational MERCATOR analysis system presently uses a simplified version where the relaxation time scale is kept constant.).

There are several criticisms levelled at this method. One is that the model SST is not fully prognostic (but it allows a prognostic meridional heat transport). This criticism can be ignored when performing ocean analysis or re-analysis (i.e. with data assimilation) for which a prognostic SST is not an issue. In that case the feedback term may be seen as a "physically consistent nudging" of the model solution to the observed SST and it contributes to constrain the model to remain close to observations (albeit not in an optimal way). Another serious criticism is that the physical consistency between the various components of the forcing (like between evaporation and latent heat) could be lost or seriously degraded when the flux correction become large, which happens frequently in model simulations. In forecast model calculation (i.e. with no data assimilation) this may deteriorate the model solution.

NDLR:

Per definition, Latent Heat flux (Q_E) and Evaporation (E) are proportional [W. Large, 2] (eq. 1).

Eq. (1) $Q_E=-\Lambda E$ where $\Lambda=2.5 \times 10^6$ j/kg

In numerical simulation using the flux correction method, Q_E and E are initially proportional. However, as the simulation is being performed, Q_E and E end up not to be proportional anymore. Indeed, the largest part of the flux correction is attributed to a correction of Q_E, without any proportional correction applied to the E field. The initial E stays out the same during the whole simulation, whereas Q_E is being modified because of the flux correction. Hence, the physical consistency between Q_E and E is being lost or degraded throughout the simulation when the flux correction becomes large.

The bulk method (7) utilizes bulk aerodynamic formulae and the model SST to calculate the turbulent fluxes (which are locally most sensitive to changes in SST). Observed flux fields are used for the downward solar and infrared radiation, precipitation and river runoff just as in the flux correction method. The representation of the ocean feedbacks is not explicit but lies in the bulk formulae. Air-sea physics are better accounted for in this formulation than in the flux correction method, which introduces additional degrees of freedom. However, as we already mentioned, uncertainties on the exchange coefficients are quite large at the eddy permitting/resolving resolution, and the coefficients used in bulk formulae may need to be adjusted. An interesting approach to that issue is presented in this newsletter by S. Skachko et al., who investigate the possibility to estimate the turbulent exchange coefficients using sequential data assimilation of ARGO heat and salinity profiles in a realistic coarse resolution global model.

The demand of air-sea fluxes expressed by the ocean modelling community is increasing rapidly: the need to resolve the diurnal cycle at global scale with a few km scales is already strong. But increasing the accuracy of flux estimation at global scale is a particularly difficult problem. Meeting the demands expressed by our community will certainly require important additional observational means and long term efforts. It is thus likely that uncertainties in the forcing function of ocean models will remain large for some time. It is therefore important that we increase our understanding of the sensitivity of our models to uncertainties in the forcing function. This issue is addressed in this Newsletter from two different angles. A paper by N. Ayoub et al. explores on monthly time scales the errors induced in the surface layers of a ¼ North Atlantic model by uncertainties in the atmospheric forcing fields. Interestingly, this study is among the first using ensemble simulations with an eddy-permitting model. Another paper by A.L. Dhomps et al. investigates the sensitivity of a South East Pacific regional Mercator configuration to presently available high resolution surface wind fields (obtained from blending Quickscat satellite winds and ECMWF analysis).

Concluding remarks

Our experience in the Clipper and Drakkar projects is that every time we undertook a new series of simulations with a given model configuration, we had to do an empirical correction and adaptation of the available forcing data. Unfortunately, there is no simple methodology to define the forcing function of a simulation. A common approach to decide which forcing data to select is to carry out flux calculations using bulk aerodynamics formulae and observed SST. Fluxes obtained are then extensively compared to other flux data sets, and empirical corrections are performed on various fields, usually in order to correct obvious biases, and to have mean heat and freshwater fluxes balanced to nearly zero at global scale and providing acceptable meridional heat transports. However, this does not assure that these properties of the corrected fluxes will be conserved during model integration (due to the parameterisation of ocean feebacks). We have many examples of models going in a way opposite to that expected using the above procedure (8). Our present impression is that an accurate definition of the forcing requires dedicated sensitivity experiments using the model configuration. It is not clear that significantly coarser resolution models can be used for such sensitivity experiments. Examples with NEMO are that the 2° global configuration ORCA2 shows, in long term calculations, a sensitivity to the forcing fields different than that shown by the 1/2° configuration ORCA05, whereas ORCA05 and ORCA025 (1/4° configuration) tends to show a similar sensitivity. And we may have different sensitivity with eddy permitting model (as the 1/12° resolution future Mercator configuration).

References

WGASF, 2000: Intercomparison and validation of ocean-atmosphere energy flux fields, Final report of the joint WCRP/SCOR Working Group on Air Sea Fluxes, WCRP-112, WMO/TD-No 1036, 303 pp.

Large W., 2006: Surface fluxes for practitioners of global ocean data assimilation, in Ocean Weather Forecasting, Springer, E.P. Chassignet and J. Verron (eds.), 229-270.

Large, W. G. and Yeager, S. G. 2004, Diurnal to Decadal Global Forcing For Ocean and Sea-Ice Models: The Data Sets and Flux Climatologies. NCAR technical note, 62 pp.

European Centre for Medium-Range Weather Forecasts, 2002: The ERA-40 Archive.

Béranger K., B. Barnier, S. Gulev and M. Crépon, 2006 : Comparing twenty years of precipitation estimates from different sources over the world ocean. Ocean Dynamics, Vol. 56-2, 104-138, DOI: 10.1007/s10236-006-0065-2 2006.

Barnier B., 1998: Forcing the Ocean, in Ocean Modeling and Parameterization. E. P. Chassignet and J. Verron (eds.), Kluwer Academic Publishers, The Netherlands, 45-80.

Large W. G., G. Danabasoglu, S. C. Doney, J. C. McWilliams, 1997: Sensitivity to surface forcing and boundary layer mixing in a global ocean model: annual mean climatology. J. Phys. Oceanogr., 27, 2418-2447.

Brodeau L., T. Penduff, and B. Barnier, 2006: Sensitivity of DRAKKAR global simulations to two existing and a hybrid atmospheric forcing functions. Proceedings of the OSTST meeting, Venice, 16-18 March 2006

ANNEX 6

A study of model errors in surface layers due to uncertainties in the atmospheric forcing fields

Mercator News Letter

July 2006

A study of model errors in surface layers due to uncertainties in the atmospheric forcing fields

By Nadia Ayoub[1], Marc Lucas[1], Bernard Barnier[1], Thierry Penduff[1], Guillaume Valladeau[2] and Pierre De Mey[2]

(1) LEGI/CNRS - Grenoble, (2) LEGOS/CNRS - Toulouse

Introduction

Estimates of model errors should be available to users of OGCM simulations for research purposes or operational applications. They are necessary for the evaluation of the degree of realism of the simulation as well as for better interpreting model-data misfits. In particular, data assimilation or state estimation methods require the specification of model errors. The latter are given as the covariance matrix of forecast or background errors on the control variables. Estimation of model errors is sometimes based on model-data comparisons, but this is not an easy approach because model-data discrepancies include uncertainties on the observations themselves and representation errors that should be distinguished from intrinsic model errors. Finally, it implies some limitations on the space and time scales over which the evaluation is made (since data are not available everywhere at every model time step); stationarity and isotropy hypotheses are then usually made to extrapolate towards the non-observed scales. Ensemble methods offer the possibility to quantitatively estimate model errors and test the robustness of a simulation in response to given perturbations on state variables, parameters and boundary/initial conditions. They constitute the basis of the so-called Ensemble Kalman Filter (Evensen, 2003), where the forecast error covariance matrices are computed from statistics on an ensemble of simulations generated by randomly perturbing initial conditions (or any parameters or boundary conditions). The estimation of errors in OGCM is an issue which has not really been addressed yet, in all likelihood because of complexity of the problem and of numerical computation limitations. Recently, it has received more attention in particular through the use of ensemble methods (see among recent studies: Wirth and Ghil (2000), Auclair et al. (2003)).

Model errors arise from various sources: non-represented or mis-represented physics (approximations in the equations, parameterizations for unresolved processes, uncertainties of parameters values), discretization (of the equations) and boundary conditions (initial, surface, lateral and at the bottom). Errors in the atmospheric forcing are expected to have significant impact at different space and time scales. For example, a local error on the wind velocity amplitude influences the local and 'instantaneous' vertical mixing in the mixed layer but has a cumulated and remote effect as well through the generation of waves. Atmospheric forcing errors include errors in the atmospheric fields themselves and errors in the air-sea exchange formulation (e.g. bulk formulae). Most of the time, OGCMs are forced with NWP fields such as the ECMWF or NCEP (re)analyses, for which uncertainties are usually not provided. According to the different sources of atmospheric uncertainties that one considers, many questions arise on the induced ocean response. For example, how deep is the impact of the uncertainties in the water column? To what extent does it depend on the state of the ocean (e.g. stratified or well-mixed)? What are the relative impacts of small-scale errors and large-scale trends? What is the ocean feedback to small-scale perturbations in the atmospheric forcing?

Our project aims at answering some of these questions in the context of an eddy-permitting simulation in the North Atlantic. The objective is to explore the model errors in surface layers and at monthly time scales due to uncertainties in the atmospheric forcing fields. We use an ensemble method where the forcing is perturbed and we characterize the errors from the ensemble statistics of the induced ocean perturbations. The period of study is September 1994 – March 1995. In parallel, we have started a sensitivity study on interannual runs comparing the impacts of using two different reanalysis products to force our model. This work is in progress. This note presents our method and preliminary results.

Description of the circulation model and the numerical experiments

Ocean circulation model

We use the NEMO-OPA9 model in the NATL4 configuration from the DRAKKAR project (Theetten and Tréguier, 2004). The model is discretized on an irregular ¼° so-called "ORCA" grid with 46 vertical levels. Bottom topography is represented with partial steps. The domain covers the North and Tropical Atlantic, from 20°S to 80°N. Lateral boundaries at the south, north, in the eastern Mediterranean Sea and north of Scandinavia are closed, with relaxation to climatological temperature and salinity (hereafter T,S) fields. OPA is coupled to the LIM sea-ice model at high latitudes. Vertical diffusion is handled by a TKE scheme. Air-sea fluxes are formulated via the Large and Yeager (2004) bulks. The atmospheric variables are the air temperature, relative humidity, zonal and meridional wind fields at 10 m every 6 hours, short-wave and long-wave radiative heat fluxes every 24 h and precipitations every 24 h. In the reference and ensemble runs (see § 2.2), the atmospheric fields come from the ERA40 reanalysis (Uppala et al., 2005); in other runs, we use the CORE products of Large and Yeager (2004) derived from the NCEP/NCAR reanalysis and satellite observations. ERA40 and CORE fields have the same temporal sampling (except for the

precipitation that is given as monthly averages in CORE) and comparable horizontal resolution (1.125º on longitude and latitude for ERA40; 1.875º for longitude and ~1.9º in latitude for CORE). There is no relaxation for temperature and salinity to climatological values at surface or at depth.

Numerical experiments

The so-called 'reference run' consists of a 14-year simulation, from Jan. 1987 to Dec. 2000, forced with the ERA40 atmospheric fields. The model starts from rest and from climatological T, S fields. A second 14-year simulation is performed using CORE atmospheric forcing fields ('CORE run'). Then a third simulation is made over the period Sep. 94 – Mar. 95; the initial conditions are the Reference run fields for Aug. 31st 1994 whereas the atmospheric forcing fields are the CORE products ('Mixed run'). The associated runs are listed in Table 1.

Simulations	Atmospheric forcing		
	Jan. 87 – Aug. 94	Sep. 94 – Mar. 95	Apr. 95 – Dec. 2000
Reference	ERA40	ERA40	ERA40
CORE	CORE	CORE	CORE
Mixed	ERA40	CORE	
Ensemble	ERA40	ERA40+perturbations	

Table 1

The study is made of two complementary approaches. The first approach is a 'classical' sensitivity study where simulations with different atmospheric forcing are compared. By comparing the CORE and Reference runs, one can estimate the integrated effect of different forcings with similar space/time sampling over a long period. From Sep. 94 to Mar. 95, the discrepancies between the Reference and Mixed runs should help us to understand the impact of different forcings on short time scales, in addition to the analysis based on the ensemble method (see below). Lastly, comparing the differences Reference-Mixed and CORE-Mixed runs should underline the effect of forcing vs. the effect of initial conditions. The second approach is based on an ensemble method over the period Sep. 94 –Mar. 95. The period from September to March corresponds to the seasonal deepening of the mixed-layer at mid and high latitudes; we therefore expect the impact of atmospheric uncertainties in subsurface to be maximum during these months. The ERA40 fields are perturbed and an ensemble of simulations is then generated with the perturbed forcing. The impact of atmospheric perturbations is analyzed from the ensemble statistical properties. 50 members are generated. This number is a compromise between the large number of members needed for statistical significance and what we can computationally afford with such a model.

Comparisons between ERA40 and CORE forced simulations

Our work is in three steps; the analysis is currently in progress and we present here a few examples of the kind of analysis we are doing at each step. We first attempt to evaluate qualitatively the realism of the reference run; this includes comparisons over the period 1993-2000 with satellite data of Sea Surface Temperature (SST) and Sea Level Anomaly (SLA, computed with respect to the mean surface height over 1993-1998) . SLA data consist in 10-day maps of objectively interpolated TOPEX/POSEIDON and ERS1/2 observations on a 1/3° grid; this is an AVISO/CLS product made available to us by the CTOH at LEGOS (Toulouse, France). Figure 1 compares the SLA variability over 1993-2000 as modeled in the reference run and deduced from satellite data. The model variability is lower than the observed one over the whole basin, with maximum values of 30 cm in the Gulf Stream whereas they reach more than 80 cm in the data. Several reasons may account for this underestimation: the insufficient resolution of turbulence at mesoscale, possible errors or missing small time/spatial scales in the atmospheric forcing fields, and to a lesser extent the non-representation of steric effects in the model. However, the spatial distribution in terms of areas of minimum (North-East Atlantic and western equatorial region) and maximum (Gulf Stream and Azores Current regions) variability is well represented in the model.

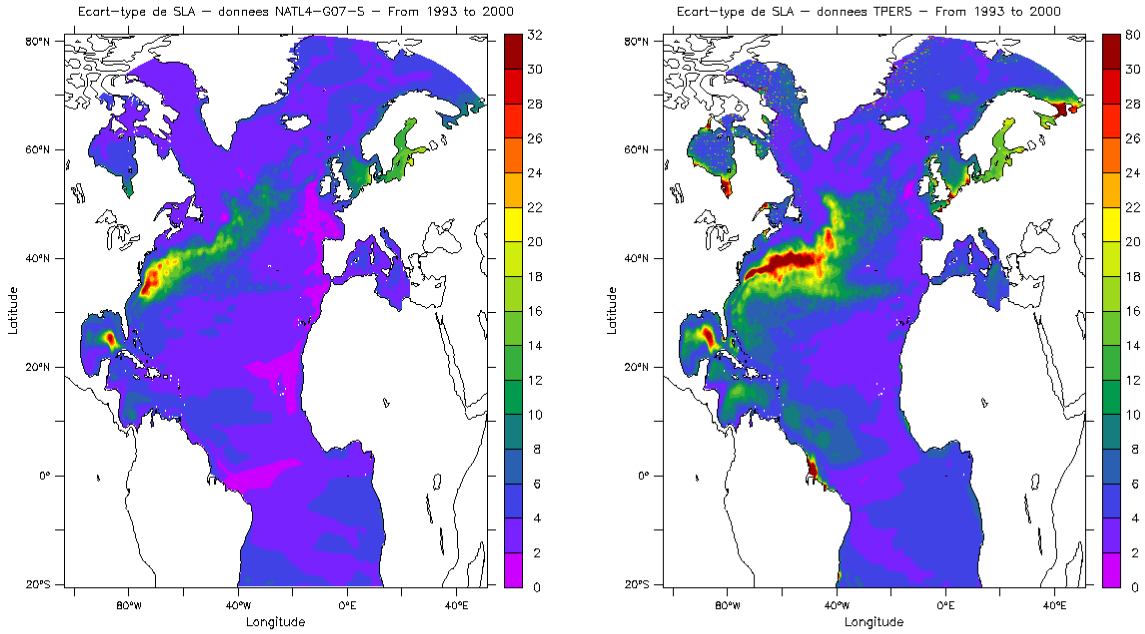

Figure 1
SLA standard deviation a) over 1993-2000 in the Reference run (left) and b) the observations(right). Unit is cm.

As a second step, we compare the mean circulation over 1993-2000 and its variability as represented in the Reference and CORE simulations. Figures 1a and 2 show that both forcing datasets lead to the similar overall underestimation of the SLA variability. There are however significant local differences, such as at 30°W-55°N and in the western tropical area, where the variability is slightly higher in the CORE simulation; ERA40 and CORE wind stress display some differences in the tropical area (not shown), confirming as previously assumed, that errors in the wind stress fields may be responsible for local underestimation of SLA variability.

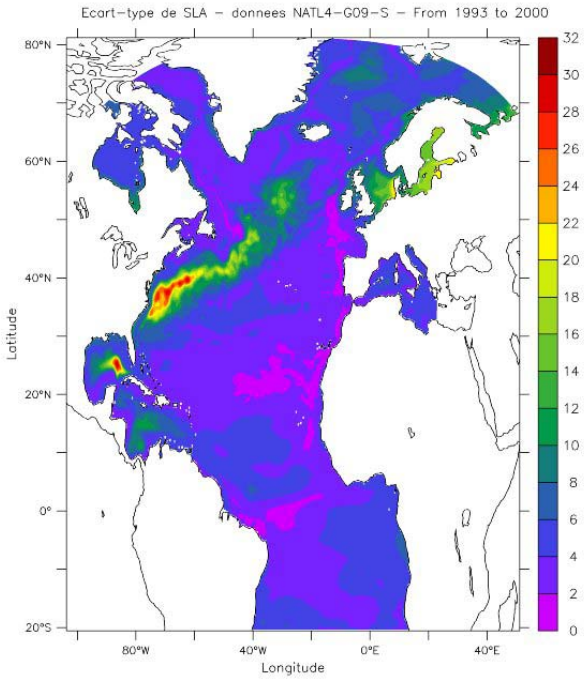

Figure 2
SLA standard deviation over 1993-2000 in the CORE run. Unit is cm.

Finally, we focus over the period Sep. 94 – Mar. 95 and analyze differences between the Reference, CORE and Mixed runs, mainly in terms of the representation of surface heat content. The simulations lead to significant differences in the mixed-layer depth (MLD) estimate. For example, at high latitudes, in late winter, the mixed-layer depth tends to be overestimated in the three simulations (not shown) with respect to observations; this is due to the lack of spatial resolution in NATL4 which results in the underestimation of the summer re-stratification (Barnier, pers. comm., 2005). However, differences in the MLD of about 400 to 1000 m are obtained in the Labrador and Irminger seas between the runs, with the deepest mixed-layer in the CORE simulation. In the Mixed run, mixed-layer depths have values varying between those in CORE and Reference runs. In the Gulf Stream area and North-East Atlantic, the influence of initial conditions seems larger than the forcing influence, whereas in the deep convection area of the Labrador Sea it is the inverse situation (i.e. larger impact of the forcing). At 5°N (Figure 3), striking differences appear in the mixed-layer depth zonal distribution and time evolution. For example, in the Reference run we observed a shallowing episode of about 50 m in December that is not reproduced in the two other simulations. It is interesting to note that, west of 40°W in November-December, the mixed-layer depth in the Mixed run offers little resemblance with both the CORE and ERA40 runs, illustrating the non-linear combination of the effects due to changes in initial conditions and atmospheric forcing.

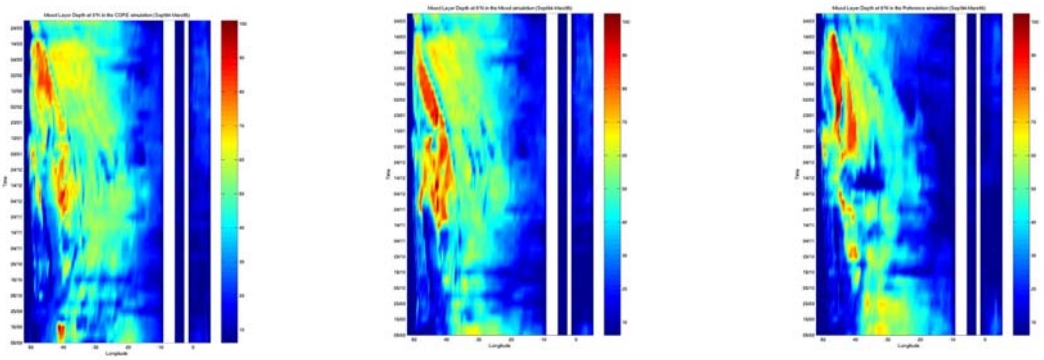

Figure 3
Variations as a function of time and longitude of the mixed-layer depth at 5°N in the Reference (left), Mixed (center) and CORE (right) runs. Unit is m.

Ensemble runs

Estimation of the a priori uncertainties of ERA40 fields

The perturbations to generate are meant to represent uncertainties on the ERA40 fields. This supposes an a priori quantitative knowledge of these uncertainties all over the basin and over the whole period of study. To our knowledge, there is no such estimate. At this point, several choices can be made to estimate the uncertainties for a limited range of scales and/or of physical processes. Perhaps, the most straightforward method consists in taking random fields with a priori space and time decorrelation scales (e.g. Andreu-Burillo et al., 2002). Such a method supposes that one can perform a large ensemble since the a priori error space itself has a large dimension. To reduce it, one can choose to consider non-biased errors whose variability (for a given variable) is the same as the variability of the variable itself. This is done, for example, by computing EOFs of the atmospheric fields over the period of study and restricting the error space as the subspace spanned by the dominating EOFs (e.g. Auclair et al., 2003;. Lamouroux et al., 2006). At ECMWF, within seasonal forecasting projects (e.g. Vialard et al., 2003), errors on wind stress are estimated by comparing ECMWF analyses to monthly fields built from observations at NOC (Southampton, Josey et al., 2002). The perturbations are then interpolated in time to get daily perturbations. This method gives an objective estimate of ECMWF uncertainties, although it supposes that the NOC fields are errors free, which is unlikely.

In our case, we attempt to get an uncertainties estimate for the space and time scales contained in the ERA40 fields. To achieve it, we build the perturbations from the differences between ERA40 fields and their equivalent in the CORE products that have a comparable sampling. Such a choice has been made as well by Leeuwenburgh (2005) in a data assimilation study in the Tropical Pacific ; its motivations and the detailed method to generate the perturbations are however different from ours. It is clear that by this approach, our errors estimate do not represent the full range of errors in the ERA40 variables, mainly because both ECMWF and NCEP NWP models are based on similar physical assumptions and also because common observations are used in both assimilations systems or as boundary conditions. As a consequence, the main features of the large scale atmospheric circulation and variability are expected to be similarly represented in the two reanalyses. The ‘errors’ defined by the differences between ERA40 and CORE are the signature of 1) the differences between the ECMWF and NCEP atmospheric models (physical parameterizations, numerical schemes), 2) the differences between the data assimilation systems and 3) the adjustments made by Large and Yeager (2004) on the original NCEP/NCAR reanalysis to create the CORE products. However, the differences in terms of radiative fluxes have a different nature since, in the CORE datasets, they are derived from satellite observations (International Satellite Cloud Climatology Project flux products). Finally, we choose not to include in our a priori errors the time mean of the differences between ERA40 and CORE.

Generation of the perturbations

We perturb the following atmospheric variables: the 10 m air temperature (t10) and wind velocity (zonal and meridional components, u10 and v10) every 6 hour and the short-wave solar radiation (Qsol) every day. During the model integration, this leads to changes on wind stress, heat and fresh water fluxes. The perturbations are computed as follows: we first compute the EOFs of the differences between ERA40 and CORE for each variable over the period of study. The EOFs are multivariate for t10, u10 and v10, and univariate for Qsol. The first multivarite and univariate EOFs explain 8% and 14% of the variance respectively. The EOFs are characterized by a high-temporal variability. The latter is superimposed to seasonal-like signals for the first 2 modes (both multivariate and univariate). The first EOF for Qsol (Figure 4) has a large amplitude in the tropics where ERA40 solar fluxes are indeed known to suffer from large inaccuracies (Brodeau et al., 2006). For u10 and v10, the EOFs

display 'sub-basin' spatial scales and coastal small-scales features; t10 EOFs scales tend to be smaller, with larger amplitude at high latitudes. We keep the first 20 EOF modes that explain 50% of the variance in the univariate and multivariate cases. The perturbations on the atmospheric variables are then built from random combinations of the first 20 EOF modes. The model is integrated with the perturbed atmospheric forcing from the same initial conditions, from Sep. 94 to Mar. 95. We generate an ensemble of 50 simulations. As the analysis is in progress, results presented here are based on the first 30 ensemble members. The model outputs are 5-day averages.

Spatial distribution of the ensemble spread

Figures 4 to 7 shows the distribution of the ensemble standard deviation in SST, Sea Surface Height (SSH), temperature at 100 m and net heat flux at the end of the integration period (March 1995). We first note that significant perturbations are obtained on the surface fields; maximal values reach 1°C and 12 cm in SST and SSH respectively (Figures 4 and 5). The maximum spread is observed in regions of high mesoscale activity and strong currents (Gulf Stream, Labrador Sea boundary currents) in both SST and SSH. The impact of atmospheric perturbations on SST is significant in the whole tropical region, whereas it is confined to the Northern Brazilian coast for SSH. The impact is significant in subsurface since it reaches 1°C at 100 m (Figure 6) and 0.5°C at 1000 m (not shown) in Mar. 95. In contrast, it is very weak in the North East Atlantic both in surface and at depth. Note the intensification in subsurface in the Equatorial region and off the Brazilian coast in the northern Tropics (Figures 4 and 6). In agreement with the ensemble variability on SST, the perturbations on the net heat flux (Figure 7) are mainly located in the Gulf Stream with values between 30 and 100 W/m2 and, to a lesser extent in the Labrador Sea and tropical region. They are very weak in the North East Atlantic. We suggest that the ocean feedback on air-sea fluxes (through the bulk formulae) tends to reduce the impact of perturbations on the net heat flux everywhere except in the Gulf Stream area. Whether this is linked to the space/time characteristics of the atmospheric variables perturbations is a possibility that we cannot exclude. The ensemble spread in both wind stress components (not shown) show significant values in the western tropical region between 0 and 10°N, in the western subtropical gyre, in the Labrador and Nordic Seas. Except close to the Greenland coasts, the perturbations do not exceed 10% of the zonal and meridional wind stress amplitudes at the same date. The patterns of wind stress and SSH perturbations are very coherent.

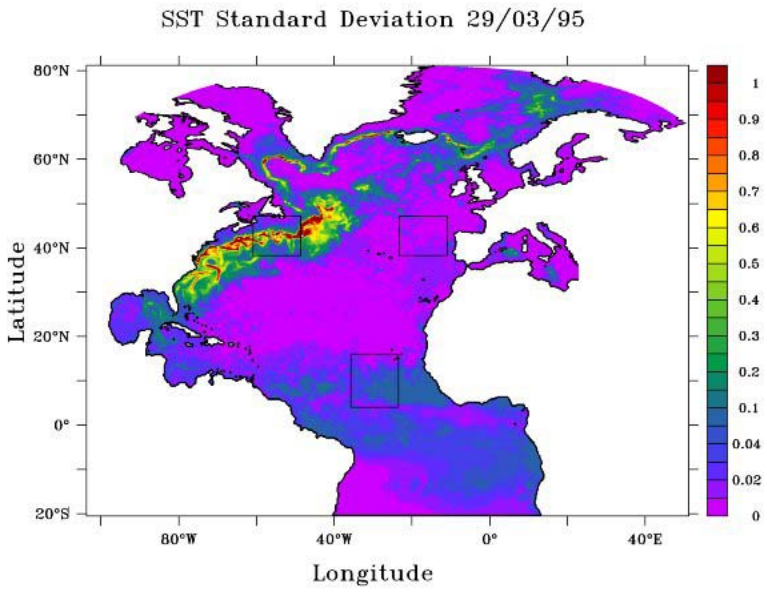

Figure 4
Ensemble standard deviation for SST (in °C) on 29/03/1995

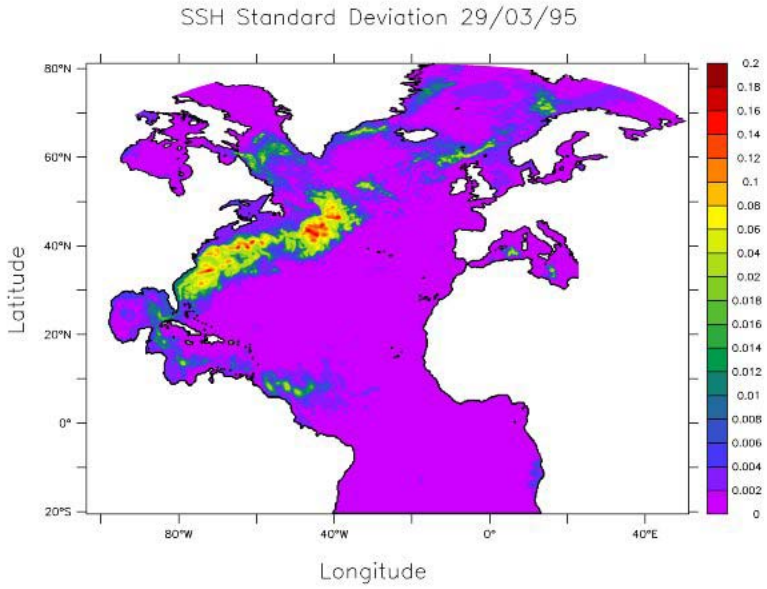

Figure 5
Ensemble standard deviation for SSH (in m) on 29/03/1995.

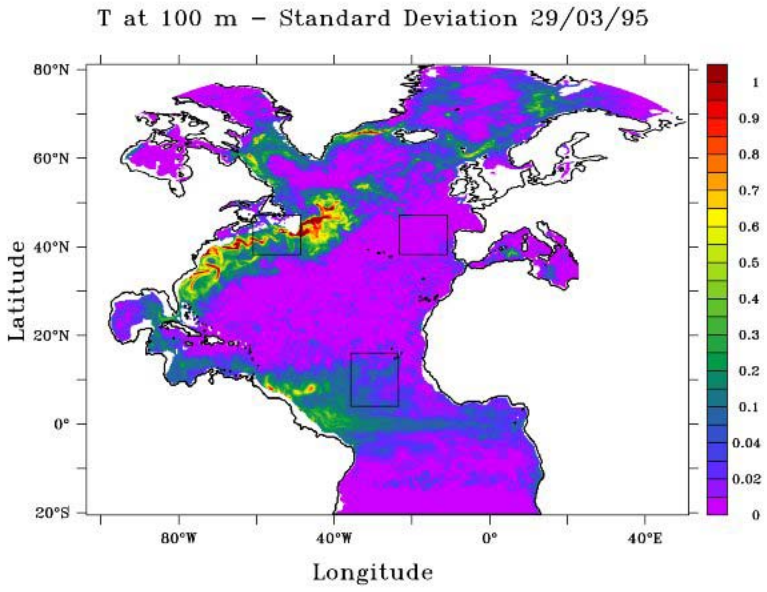

Figure 6
Ensemble standard deviation for the temperature (in °C) at 100 m on 29/03/1995

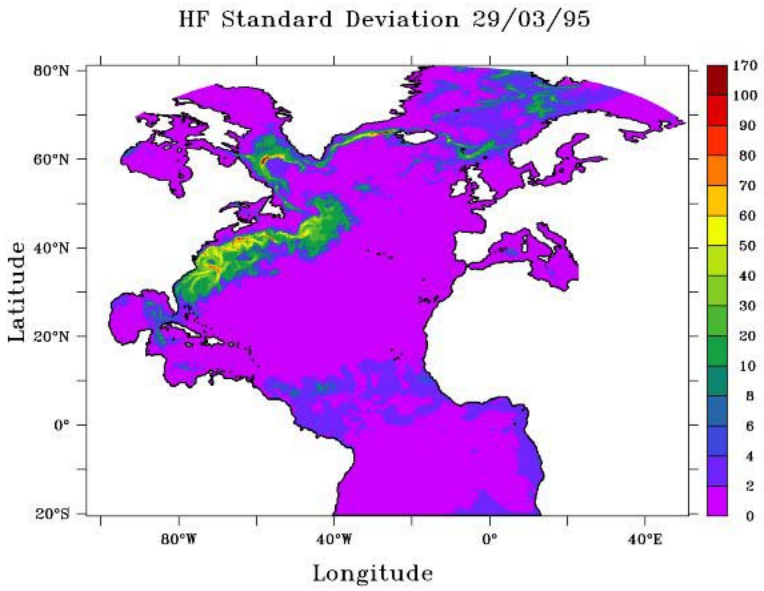

Figure 7
Ensemble standard deviation for the net heat flux at surface (in W/m2) on 29/03/1995

The maps of Figures 4 to 7 are representative of the situation at the end of the study period. The ensemble spread varies along with time, displaying significant changes in amplitude and spatial patterns. However, the regions of maximum and minimum spread remain the same through the integration.

Time evolution of the ensemble spread

The analysis in the previous section indicates large discrepancies in the ocean response to atmospheric perturbations between different regions, with differences in amplitude and in horizontal, vertical and time distributions. We have therefore decided to focus on three regions and on the impact of the atmospheric perturbations on temperature profiles. This study is reported in a paper in preparation (Lucas et al., 2006). We just comment here one of the figures showing the temporal evolution of the ensemble spread for the mean SST in three boxes (Figure 8). The boxes are about 12°x12° and are located in the Gulf Stream area (Region 1), in the Northern Tropics (Region 2) and in the North Eastern Atlantic (Region 3) – see Figure 4. Figure 8 illustrates the very different behaviors from one region to the other. In Region 1, we observe a monotonic increase of the spread; the latter is generated by the Gulf Stream instabilities (eddies, meanders). In Region 2, the spread widens until November, then become very narrow and, from the end of January increases again. In Region 3, it narrows from November-December and starts to widen again at the end of March; these variations are clearly linked to the deepening of the mixed layer as winter progresses and its rapid shallowing in March. As the mixed-layer deepens, perturbations on SST are ‘mixed’ over a deeper water column and are therefore dampened.

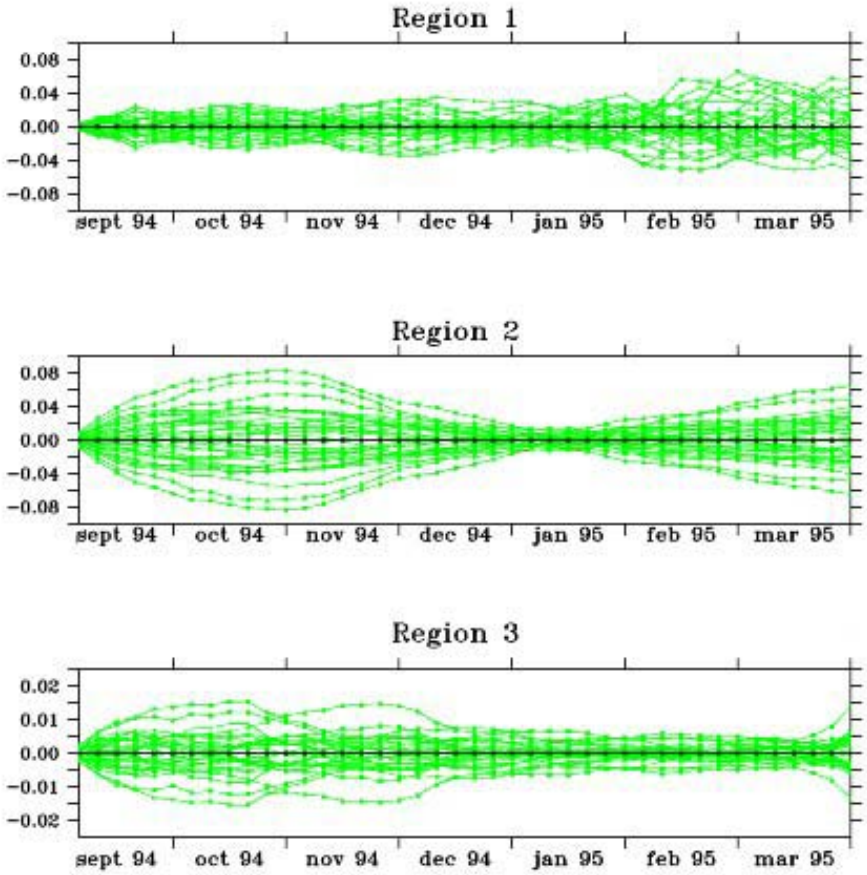

Figure 8
Evolution as a function of time of the differences between each member and the ensemble mean in SST. The SST is first averaged over the three regions of interest before computing the difference with the ensemble mean. Unit is °C.

Conclusion

This study aims to characterize the sensitivity of a simulation to atmospheric forcing at interannual and monthly time scales. A first approach allows us to discuss the impact on ocean circulation that one can expect when forcing a model with the ERA40 reanalysis or with CORE products. We show here the impact on the surface variability over 1993-2000 after a 7-year spin-up as well as the differences obtained on the mixed-layer depth estimate and variability on a few months time scales. The second approach is based on an ensemble method and leads to a quantitative estimate of 'errors' due to perturbations on the atmospheric forcing. These are intended to represent uncertainties on ERA40 fields. We show however that the limited knowledge of 'objective' errors on ERA40 leads us to restrict the space of ERA40 uncertainties that we explore by choosing to estimate them from the differences between ERA40 and CORE variables. To our knowledge, it is the first time that model errors at basin scale, over several months and in a realistic configuration are estimated with such a method. Preliminary results show the complexity of the oceanic response and illustrate the richness of the method. In particular, they underline the degree of non-stationarity and non-isotropy of model errors – as already clearly demonstrated in coastal models (e.g. Auclair et al., 2003; Jordà, 2005). The impact of the perturbations on oceanic variables is clearly linked to the dynamics and evolves according to different processes (advection, vertical mixing, vertical diffusion). For this reason, the errors space-time structure might be predictable at least to some extent. However, in some regions, the ocean feedback on air-sea fluxes seems to dampen the effect on fluxes of perturbations on atmospheric variables; this might be due to our specific choice of perturbations but it makes the prediction of errors amplitude difficult locally. This study is in progress; current and future works are mainly dedicated to the estimation of errors on other surface fields and on covariances between different variables.

It is clear that, as long as there is no objective and realistic information on the forcing uncertainties, it remains very difficult to estimate the contribution of the errors due to atmospheric uncertainties to model-data discrepancies. One expects however that

data assimilation (with ocean variables only being constrained) tends to reduce these errors. Specifying them in the forecast or background covariance matrices (e.g. Leeuwenburgh, 2005) should make the data constraint more efficient. Another possibility is to include in the control variables the atmospheric forcing, i.e. parameters in the air-sea exchanges formulation (see for example the paper by S. Skachko et al., this issue) or the atmospheric forcing fields (e.g. Stammer et al., 2004 ; Ayoub, 2006 ; Lamouroux et al., 2006). Such methods lead to adjustments on the forcing fields. These should be consistent with the a priori uncertainties statistically specified in the background error covariances but they provide very interesting information on the forcing fields errors 'as seen by the model', i.e. depending on the ocean model characteristics (e.g. resolution, vertical physics). It is therefore another kind of estimate of forcing uncertainties.

Acknowledgments

Many thanks for the help with NATL4 simulations and interesting discussions on the project to J.-M. Molines, J.-M. Brankart, S. Theetten, A.-M.Tréguier and L. Brodeau. This work is supported by MERCATOR (GMMC), SHOM, CNES (OSTST-Jason project). Numerical simulations are made at IDRIS (Paris) on the IBM Power4 parallel machine.

References

Andreu-Burillo I., G. Caniaux, M. Gavart, P. De Mey and R. Baraille, 2002: Assessing ocean model sensitivity to wind forcing uncertainties, Geophys. Res. Lett. 10, 1-8.

Auclair F., P. Marsaleix and P. De Mey, 2003. Space-time structure and dynamics of the forecast error in a coastal circulation model of the Gulf of Lions, Dyn. Atmos. Oceans, 36, 309-346.

Ayoub N., 2006. Estimation of boundary values in a North Atlantic circulation model using an adjoint method, Ocean Modelling, doi: 10.1016/j.ocemod.2005.06.003.

Brodeau L., T. Penduff and B. Barnier, 2006, Sensitivity of DRAKKAR global simulations to two existing and a hybrid atmospheric forcing functions. Proceedings of the OSTST meeting, Venice, 16-18 March 2006

Josey, S. A., E. C. Kent and P. K. Taylor, 2002, On the Wind Stress Forcing of the Ocean in the SOC Climatology : Comparisons with the NCEP/NCAR, ECMWF, UWM/COADS and Hellerman and Rosenstein Datasets. J. Phys. Oceanog., 32(7), 1993-2019.

Evensen G., 2003, The Ensemble Kalman Filter: theoretical formulation and practical implementation, Ocean Dynamics, 53, 343-367, doi 10.1007/s10236-003-0036-9.

Jordà-Sanchez G., 2005, Towards data assimilation in the Catalan continental shelf - from data analysis to optimization methods, PhD thesis, Universidad Politècnica de Catalunya, Barcelona, 2005.

Lamouroux J., P. De Mey, F. Lyard and E. Jeansou, 2006, Control of a barotropic model of the Bay of Biscay in presence of atmospheric forcing errors, J. Geophys. Res., in revision.

Large W. and S.G.Yeager, 2004, Diurnal to decadal global forcing for ocean and sea-ice models: the data sets and flux climatologies, NCAR Technical Note.

Leeuwenburgh O., 2005, Assimilation of along-track altimeter data in the Tropical Pacific region of a global OGCM ensemble, Quart. J. Roy. Meteor. Soc, doi: 10.1256/qj.0 4.146.

Lucas M., N. Ayoub et al., 2006, Vertical propagation of the atmospheric induced temperature anomaly in the ocean: an ensemble study, in preparation.

Stammer D., K. Ueyoshi, A. Köhl, W.G. Large, S.A. Josey and C. Wunsch, 2004, Estimating air-sea fluxes of heat, freshwater and momentum through global ocean data assimilation, J. Geophys. Res., 109, C05023, doi:10.1029/JC002082.

Theetten S. and A.-M. Tréguier, 2004, Validation and analysis of the first NATL4 run of the DRAKKAR project, Rapport interne DOPS/LPO, www.ifremer.fr/lpo/drakkar/index.htm.

Uppala S.M. and co-authors, 2005, The ERA40 re-analysis, Quart. J. Roy. Meteor. Soc., 131, 2961-3012.

Vialard J., F. Vitart, M. A. Balmaseda, T. N. Stockdale, D. L.T. Anderson, 2003, An ensemble generation method for seasonal forecasting with an ocean-atmosphere coupled model, ECMWF Technical Memorendum n°417.

Wirth, A., and M. Ghil, 2000: Error evolution in the dynamics of an ocean general circulation model, Dyn. Atmos. Oceans, 32, 419–431

ANNEX 7

Sensitivity of DRAKKAR global simulations to two existing and a hybrid atmospheric forcing functions

Proceeding of Symposium on 15 years of Progress in Radar Altimetry

13-18 March 2006

Sensitivity of DRAKKAR global simulations to two existing and a hybrid atmospheric forcing functions

L. Brodeau[1], T. Penduff[1] and B. Barnier[1]

[1]{Laboratoire des Ecoulements Géophysiques et Industriels, Grenoble, France}

Correspondence to: L. Brodeau (*brodeau@hmg.inpg.fr*)

Abstract

The present work is aimed to provide the ocean modeler with an overview of the main features that differentiate two reference atmospheric datasets, CORE[(1)] and ERA40[(2)], within the period of 1984-2000.

Variables of interest are air temperature, specific humidity, and wind components, together with radiative down-welling fluxes components (short-wave and long-wave).

After a comparison of input variables, heat air/sea fluxes resulting from each dataset, are computed with the same climatic SST[(4)] and bulk formulae. These fluxes are then analyzed and compared. As a third test, three inter-annual simulations are conducted on a 2° resolution OGCM: CORE, ERA40 and HYB. The HYB forcing set mixes ERA40 turbulent variables with the ISCCP[(3)] radiative product implemented into CORE.

Concerning turbulent variables, the CORE dataset has stronger winds and moister air while air temperature is comparable to ERA40. Surprisingly, computation of bulk fluxes with the fixed SST shows that the warming effect of moister air partially decreases the cooling effect of evaporation due to stronger winds. By globally evaporating less than CORE and receiving more radiation, ERA40, is expected to warm the ocean more than CORE.

Results from the simulations, where SST is freely evolving, point out an inverse trend as the CORE-driven run lets the ocean gain much more heat than the two other tested runs, this is partly explained by the formation of a cooler SST in the CORE-driven simulation. This proves that climatic SST offline tests are not sufficient to predict the answer of the model to a given data set. Finally, the HYB configuration is shown to lead to a better behavior of our coarse model.

Introduction

The DRAKKAR community modeling program aims at better understanding the ocean variability and scale interactions over the last 50 years. The project team is building a hierarchy of models of the global ocean (horizontal resolutions: 2°, 1/2°, 1/4°) and of the North Atlantic/Nordic Seas basin (1/4°, 1/12°) based on the NEMO system, with the explicit simulation of the 3-dimensional ocean circulation, sea-ice, 14C and CFC tracers. DRAKKAR models are driven at the surface by momentum, heat and water fluxes partly computed online via bulk formulae from prognostic model SST and atmospheric variables.

Two gridded atmospheric datasets, CORE[(1)] (NCAR/NCEP) and ERA40[(2)] (ECMWF), both built from reanalyzes, stand as serious candidates for inter-annual forcing of the DRAKKAR models. They have the advantage to cover most of the last 50 years with variables at high time resolution. The work presented here reveals the first elements for determining the most suitable forcing function for conducting these inter-annual simulations.

One singularity of CORE is the implementation of a new satellite radiative product from the ISCCP[(3)] available since 1984, which is why the study is conducted from 1984 to 2000. These satellite data are expected to be more reliable than products of reanalyzes, this motivates the evaluation of a third forcing function, named HYB, constructed by hybridizing long- and short-wave down-welling radiation fields from the ISCCP satellite-derived dataset into the ERA40 function.

This study is done in three steps; first, input atmospheric variables and radiative fluxes of each dataset are compared. Then, prior to ocean simulations and given a reference climatic SST

dataset[4], a stand-alone tool named FOTO is used to estimate the impact of the three different surface forcing functions on air-sea fluxes. Three coarse-resolution global simulations (DRAKKAR model at 2° resolution) are then performed with each forcing function. This third step extends the former results by representing the feedback of large-scale ocean dynamics on SST and air-sea interactions (e.g. advection/subduction of forced buoyancy anomalies).

I. Comparison of input data

Differences between CORE and ERA40 are mainly found on down-welling radiation, surface winds and air humidity.

Despite a very similar time variability pattern, CORE winds are stronger than ERA40 at every latitude (*Fig. 1a*) CORE forcing is thus more likely to strengthen heat loss by evaporation and lead to a stronger wind-driven surface circulation.

Concerning the radiative product, ERA40 shows its main weakness, the time variability pattern is inconsistent with the satellite-observed data implemented by CORE (*Fig. 2*). ERA40 shows a deficit of radiation on the equatorial band and an excess at higher latitudes (*Fig. 1b*). Globally, the ocean receives more radiation with ERA40 (*Fig. 3*).

ERA40 has dryer air than CORE except at the equator (*Fig. 1c*).

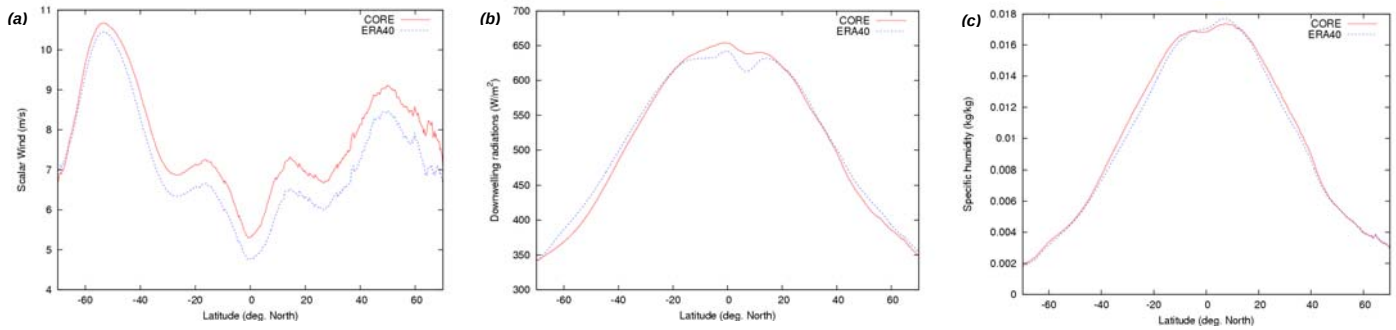

***Fig. 0** : Zonnally-averaged values for 3 input data of each dataset for period 1984-2000 : scalar wind, total down-welling radiation (SW + LW) and specific humidity.*

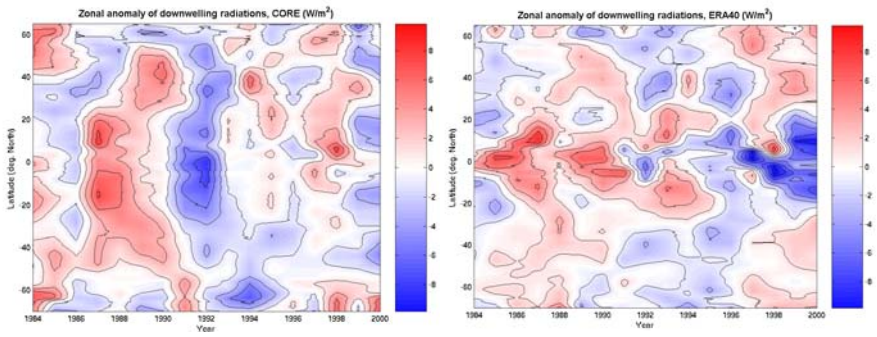

***Fig. 2** : Annual zonal variability of total down-welling radiation for CORE and ERA40*

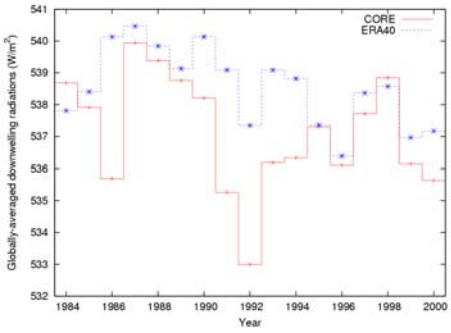

***Fig. 3** : Globally-averaged total down-welling radiation.*

II. Expectations with prescribed SST

Prior to model integrations, the FOTO tool is used to compare the bulk air-sea fluxes derived from available forcing functions and climatic SST[4] (Hurrell et al. 2003) fields. The iterative algorithm used to compute air/sea exchange coefficients (C_D, C_E and C_H) is provided by Large & Yeager (2004)[1].

This procedure shows, that as expected (because of stronger CORE winds), ERA40 injects more heat into the ocean at almost every latitude (*Fig. 4* and *Fig. 7*). Lower humidity of ERA40 tends to narrow the gap between the two datasets. Despite its lower winds, ERA40 leads to more heat loss through evaporation, except under low latitudes (*Fig. 5*), where CORE has a dryer air (*Fig. 1c*).

FOTO predicts a very similar heat gain in the tropics for both sets. In this region, the excess of radiation of CORE is compensated by high evaporation, mainly due to drier air. The HYB configuration confirms this trend, when CORE radiation is used, the net heat flux becomes much higher in the tropics and lower at higher latitudes (*Fig. 4*).

The latitude band [40°S , 15°S] is the only region where the strong evaporation, resulting from ERA40's much drier air, lets the ocean gain less heat than CORE (*Fig. 4* and *Fig. 5*).

Plotting the global heat flux imbalance within the period (*Fig. 6*), shows a trend to global warming for all three forcing sets, with the highest values for ERA40.

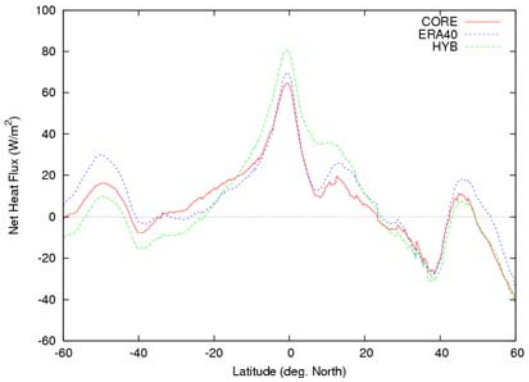

Fig. 4 : *Zonnally averaged net heat flux computed with climatic SST, 1984-2000.*

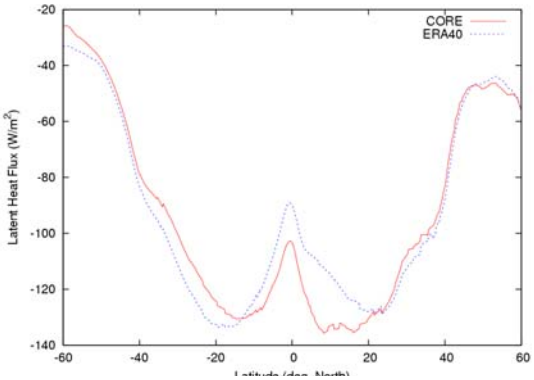

Fig. 5 *: Zonnally averaged latent heat flux computed with climatic SST, 1984-2000.*

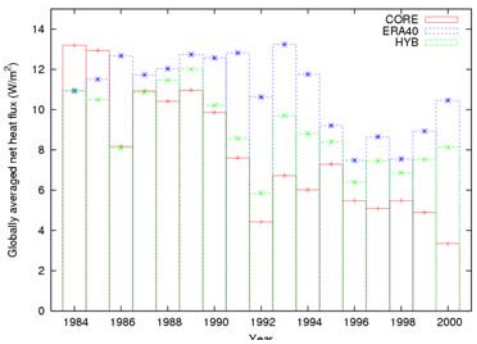

Fig. 6 *: Annual global net heat flux imbalance from climatic SST.*

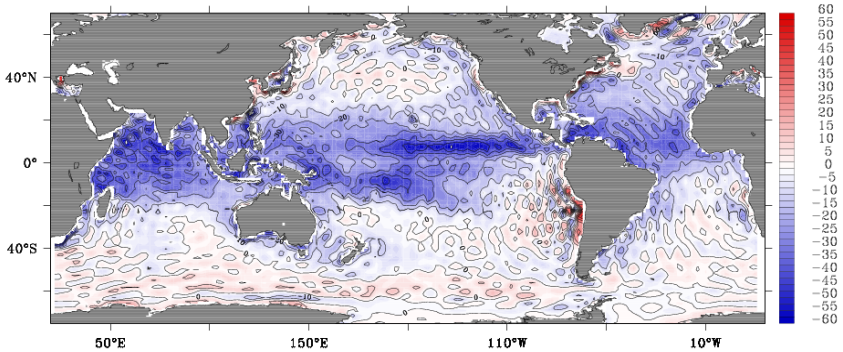

Fig. 7 *: Difference of mean net heat flux, Q_{net}(CORE) - Q_{net}(ERA40). Wave-like spatial features come from input atmospheric fields of CORE. (Units are in W/m²)*

III. 2º model simulations

The 2° global ocean/sea-ice DRAKKAR OPA9-LIM[5] model has been forced over 17 years (1984-2000) by **CORE**, **ERA40** and **HYB** (SSS restoring, no SST restoring, free surface, partial steps).
The first striking difference compared to the previous *fixed-SST investigation* is the damping effect of the model SST feedback on the heat flux through bulk formulation. The zonally-averaged flux profiles show good agreement for the three run (*Fig. 8*) compared to (*Fig. 4*).
Without any expectations, and contrary to former results, the globally integrated thermal trend shows that this is actually the CORE-driven run that warms the ocean the most (*Fig. 11*).
The CORE-driven run leads to a lower SST (*Fig. 10* and *Fig. 14*), that naturally decreases turbulent and infra-red heat loss for a constant down-welling radiative flux. This is especially noticeable in the eastern equatorial region (*Fig. 15*). This process seems to be responsible for the excessive global trend to warming for the CORE run.
The HYB run getting globally less heat from down-welling radiation is naturally warming the ocean less and gives the best results from a heat balance point of view (*Fig. 9* and *Fig. 12*). All 3 runs show a net trend to heat storage, but HYB has the lowest imbalance over the 17 years (*Fig. 9*).

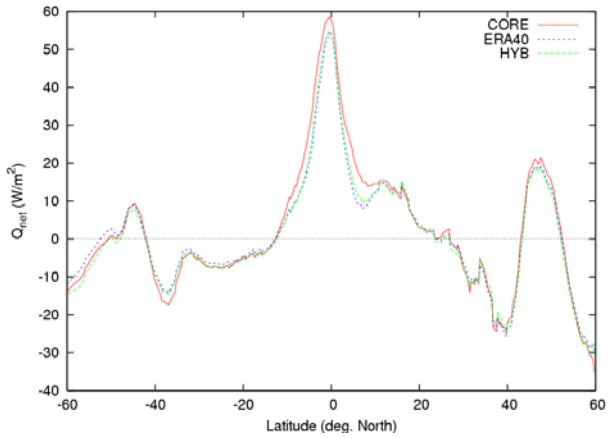

***Fig. 8** : Zonnally-averaged net heat flux from simulations, 1984-2000.*

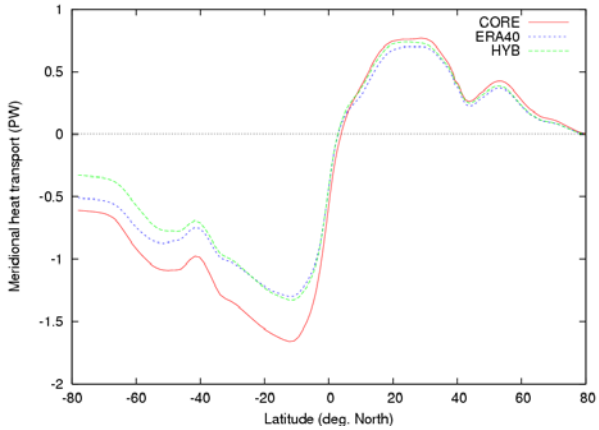

***Fig. 9** : Global meridional heat transport, 1984-2000.*

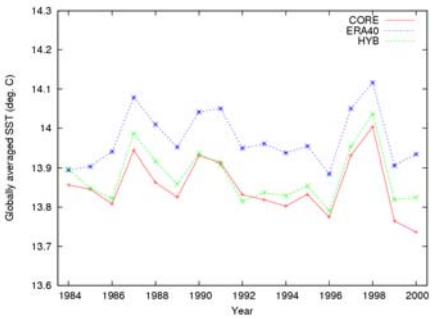

***Fig. 10** : Evolution of the annual globally-averaged SST for the 3 simulations.*

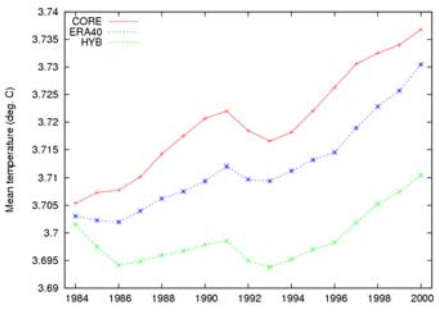

***Fig. 11** : Evolution of the annual globally-averaged temperature for the 3 simulations.*

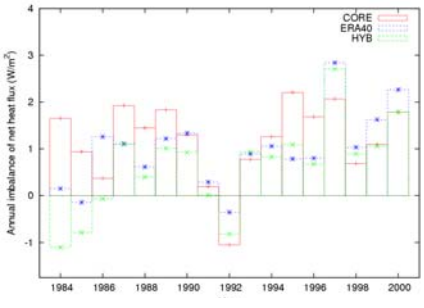

***Fig. 12** : Annual net heat flux imbalance for the 3 simulations.*

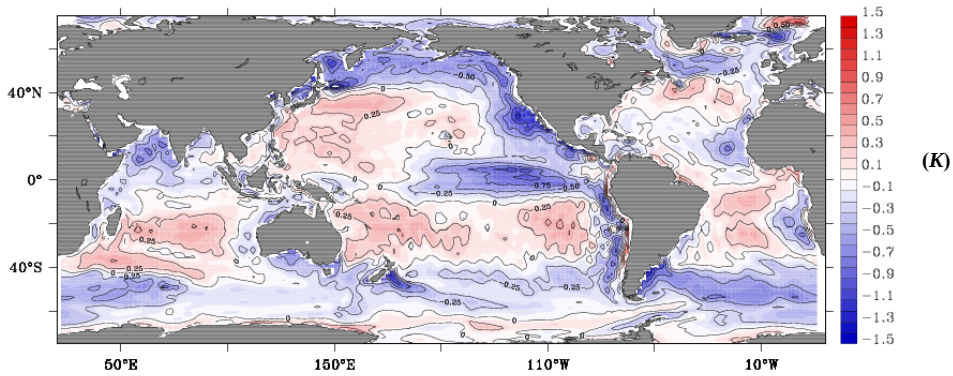

Fig. 14 *: Difference of mean prognostic SST, SST(CORE) - SST(ERA40), 1984-2000.*

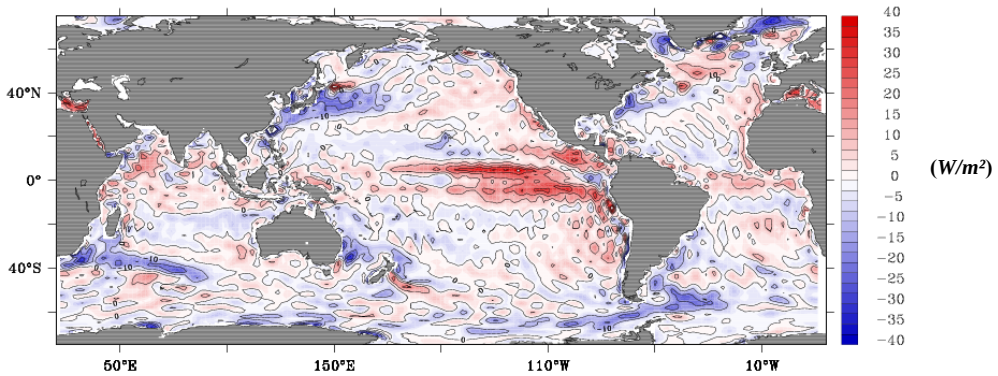

Fig. 15 *: Difference of mean prognostic net heat flux, Q_{net}(CORE) - Q_{net}(ERA40), 1984-2000.*

IV. Conclusion

This study points out the need to use a model, in which at least the dynamics of the mixing layer are solved, in order to truly mimic the answer of the ocean to a given forcing dataset. The model simulations give a totally opposite thermal trend than a simple offline test with a fixed SST. It is thus not sufficient to rely on climatologic fluxes. By letting the SST freely evolve, one can take advantage of the damping feedback of bulk formulae, adding a degree of freedom to the model.
Humidity is also shown to play a non-neglecting role as latent heat flux is one of the major heat loss contributor for the ocean.
Considering a "global heat-budget" concern, the use of ERA40 turbulent variables with the observed radiative ISCCP product (HYB) seems to be the most relevant choice. A major drawback of the CORE dataset is also the presence of unnatural spatial perturbations on the available data fields, likely resulting from bad interpolation from the NCEP/NCAR spectral model.

References

(1) Large, W. G. and Yeager, S. G. 2004, *Diurnal to Decadal Global Forcing For Ocean and Sea-Ice Models: The Data Sets and Flux Climatologies*. NCAR technical note, 62 pp.
(2) European Centre for Medium-Range Weather Forecasts, 2002: The ERA-40 Archive.
(3) Zhang, Y-C., W.B. Rossow, A.A. Lacis, V. Oinas, and M.I. Mishchenko, 2004. *Calculation of radiative fluxes from the surface to top of atmosphere based on ISCCP and other global data sets: Refinements of the radiative transfer model and the input data*. J. Geophys. Res., 109, (27 pp).
(4) Hurrell, J., Caron, J., Hack, J. & Shea, D. 2003, *A New Surface Temperature and Sea Ice boundary data set for the Community Atmosphere Model*, Geophys. Res. Lett. pp. 0-999.
(5) Madec, G., P. Delecluse, M. Imbard, and C. Lévy, 1998: OPA 8.1 Ocean General Circulation Model reference manual. Note du Pôle de modélisation, Institut Pierre-Simon Laplace, N°11, 91pp.

ANNEX 8

Comparing 20 years of precipitation estimates from different sources over the world ocean

Ocean Dynamics

April 2006

Ocean Dynamics (2006) 56: 104–138
DOI 10.1007/s10236-006-0065-2

Karine Béranger · Bernard Barnier · Sergei Gulev · Michel Crépon

Comparing 20 years of precipitation estimates from different sources over the world ocean

Received: 1 December 2004 / Accepted: 7 December 2005 / Published online: 21 April 2006

Abstract The paper compares ten different global precipitation data sets over the oceans and discusses their respective strengths and weaknesses in ocean regions where they are potentially important to the salinity and buoyancy budgets of surface waters. Data sets (acronyms of which are given in Section 2) are categorised according to their source of data, which are (1) *in situ* for Center for Climatic Research (Legates and Willmott, 1990; Archive of Precipitation Version 3.01, http://climate.geog.udel.edu/~climate), Southampton Oceanography Centre (SOC) (Josey et al., *J Clim* 12:2856–2880, 1999) and University of Wisconsin-Milwaukee (UWM) (Da Silva et al. 1994); (2) *satellite* for Microwave Sounding Unit (MSU) (Spencer, *J Clim* 6:1301–1326, 1993), TOPEX (Quartly et al., *J Geophys Res* 104:31489–31516, 1999), and Hamburg Ocean Atmosphere Parameters and Fluxes from Satellite (HOAPS) (Bauer and Schluessel, *J Geophys Res* 98:20737–20759, 1993); (3) *atmospheric forecast model re-analyses* for European Centre for Medium-range Weather Forecast (ECMWF) (Gibson et al. 1997) and National Center for Environmental Prediction (NCEP) (Kalnay et al., *Bull Am Meteorol Soc* 77:437–471, 1996); and (4) *composite* for Global Precipitation Climatology Project (GPCP) (satellites and rain gauges, Huffman et al., *Bull Am Meteorol Soc* 78 (1):5–20, 1997) and Climate Prediction Center Merged Analysis of Precipitation (CMAP) (satellites, rain gauges and atmospheric forecast model, Xie and Arkin, *Bull Am Meteorol Soc* 78(11):2539–2558, 1997). Although there is no absolute field of reference, composite data sets are often considered as the best estimates. First, a qualitative comparison is carried out, which provides for each data set, a description of the geographical distribution of the climatological mean precipitation field. A more careful comparison between data sets is undertaken over periods they have in common. First, six among the ten data sets (SOC, UWM, ECMWF, NCEP, MSU and CMAP) are compared over their common period of 14 years, from 1980 to 1993. Then CMAP is compared to GPCP over the 1988–1995 period and to HOAPS over the 1992–1998 period. Usual diagnostics, like comparison of the precipitation patterns exhibited in the annual climatological means of zonal averages and global budget, are used to investigate differences between the various precipitation fields. In addition, precipitation rates are spatially integrated over 16 regional boxes, which are representative of the major ocean gyres or large-scale ocean circulation patterns. Seasonal and inter-annual variations are studied over these boxes in terms of time series anomalies or correlation coefficients. The analysis attempts to characterise differences and biases according to the original source of data (i.e. in situ or satellite, etc.). Qualitative agreement can be observed in all climatologies, which reproduce the major characteristics of the precipitation patterns over the oceans. However, great disagreements occur in terms of quantitative values and regional patterns, especially in regions of high precipitation. However, a better agreement is generally found in the northern hemisphere. The most significant differences, observed between data sets in the mean seasonal cycles and interannual variations, are discussed. A major result of the paper, which was not expected a priori, is that differences between data sets are much more dependent upon the ocean region that is considered than upon the origin of the data sets

Responsible editor: Jörg-Olaf Wolff

K. Béranger (✉)
ENSTA, UME, Chemin de la Hunière,
91761 Palaiseau Cedex, France
e-mail: Karine.Beranger@ensta.fr
Tel.: +33-169319753
Fax: +33-169319997

B. Barnier
LEGI-IMG, CNRS UMR 5519, BP 53,
38041 Grenoble Cedex, France

S. Gulev
P. P. Shirshov Institute of Oceanology,
RAS, 36 Nakhimousky ave.
117851, Moscow, Russia

M. Crépon
LOCEAN,
Tour 45-55, 4e Etage, 4 Place Jussieu,
75252 Paris Cedex 05, France

Convergence Zone (SPCZ), and pointed out an improvement of the re-analysis compared to the analysis. Other comparisons between GPCP and Climate Prediction Center Merged Analysis of Precipitation (CMAP, Xie and Arkin 1997) by Gruber et al. (1999) and Kidds (2001) show a good spatial and temporal correlation between GPCP and CMAP products in general. Nevertheless, GPCP estimates show higher P in the mid-latitudes and lower P in the tropics than those of CMAP. The use of different analysis procedures and of additional types of input data could explain the disagreement observed between estimates. However, these papers, which often focus on the production of a particular climatology, provide only a qualitative and piecewise view of the relative strengths and weaknesses between data sets.

All the above studies highlight the difficulty to determine the quality of the different data sets and speak in favour of continuous inter-comparison studies. It is the objective of the present study to carry out a quantitative inter-comparison of available global P climatologies, in an attempt to answer the following questions for which we have only very scattered elements:

- Are there any systematic differences between the various data sets according to their source (i.e. in situ, satellite, NWP, composite)?
- How well do the different available climatologies agree in their representation of the mean, of the seasonal cycle and of the interannual variability?

We approach the above questions from an ocean modelling perspective, in an attempt to provide information useful in selecting a P field as a component of the freshwater forcing of an OGCM. Therefore, the present analysis aims to reveal and document differences between various precipitation estimates, which are studied, but not to explain the reasons for these differences. Rather than comparing locally the details of the P fields, we compare the precipitation spatial average over pre-defined areas (called budgets hereafter) where the total amount of rain is suspected to have an impact on the ocean salinity. These areas are basically the major large-scale closed circulation features (ocean gyres).

We have selected ten different P data sets. Their sources, main characteristics and the period they cover are described in Section 2. Climatological annual means of each data set are compared in Section 3, and six data sets covering the same 14-year period (1980–1993) are retained for a quantitative analysis over specific ocean regions relevant to ocean main circulation patterns. Sections 4 to 6 are comparing these six selected data sets (UWM, SOC, ECMWF, NCEP, MSU and CMAP) over their common period. In Section 4, the climatological means are computed and compared. Differences are studied in terms of zonal averages, spatial patterns and regional P budgets. In Section 5, the climatological seasonal cycles (described in terms of climatological monthly mean anomalies) are studied. Then in Section 6, an analysis is undertaken to quantify how the different available data sets agree in their representation of the interannual variability. Again, the focus is on anomalies of the P budget over ocean regions of relevance to physical oceanography. Correlations between low-frequency time series of precipitation are investigated. In Section 7, the analysis of two other major data sets (HOAPS and GPCP), which do not cover the previous common 14-year period, is performed following the same methodology as before. A conclusion summarises the major findings of our comparison analysis and draws, whenever possible, quantitative statements on the strengths and weaknesses of the different data sets.

2 Precipitation data sets

P estimates over sea can be derived from three major sources which are (1) observations at sea (ship reports, ship and buoy measurements), (2) satellite observations and (3) forecasts carried out at NWP centres with atmospheric general circulation models. The reader is referred to the

Table 1 Characteristics of the various ocean precipitation data sets referenced in this study

Data Set	Reference	Period	Grid (deg)	Spatial coverage
Ships and buoys data				
CCR	Legates and Willmott (1990)	1950–1996	0.5	89.75°N–89.75°S
UWM	Da Silva et al. (1994)	1945–1993	1	89.5°N–89.5°S
SOC	Josey et al. (1999)	1980–1993	1	84.5°N–84.5°S
Satellite and rain gauge data				
TOPEX	Quartly et al. (1999)	1993–1999	5×2.5	70°N–67.5°S
HOAPS	Bauer and Schluessel (1993)	1992–1998	1	79.5°N–79.5°S
MSU	Spencer (1993)	1979–1993	2.5	58.75°N–58.75°S
Forecast: surface, meteorological, and satellite data with assimilation in NWP				
ECMWF	Gibson et al. (1997)	1979–1993	1.125	90°N–90°S
NCEP	Kalnay et al. (1996)	1958–1996	gauss 1.8	88.5°N–88.5°S
Satellite, rain gauge data or forecast (composite)				
CMAP	Xie and Arkin (1997)	1979–1999	2.5	88.75°N–88.75°S
GPCP	Huffman et al. (1997)	1988–1995	2.5	88.75°N–88.75°S

report WCRP-115 (2001) for a discussion of the various techniques and methods used to estimate *P*. The various *P* data sets or climatologies discussed in the present study are listed in Table 1, and their respective climatological annual mean is shown in Figs. 1 and 2.

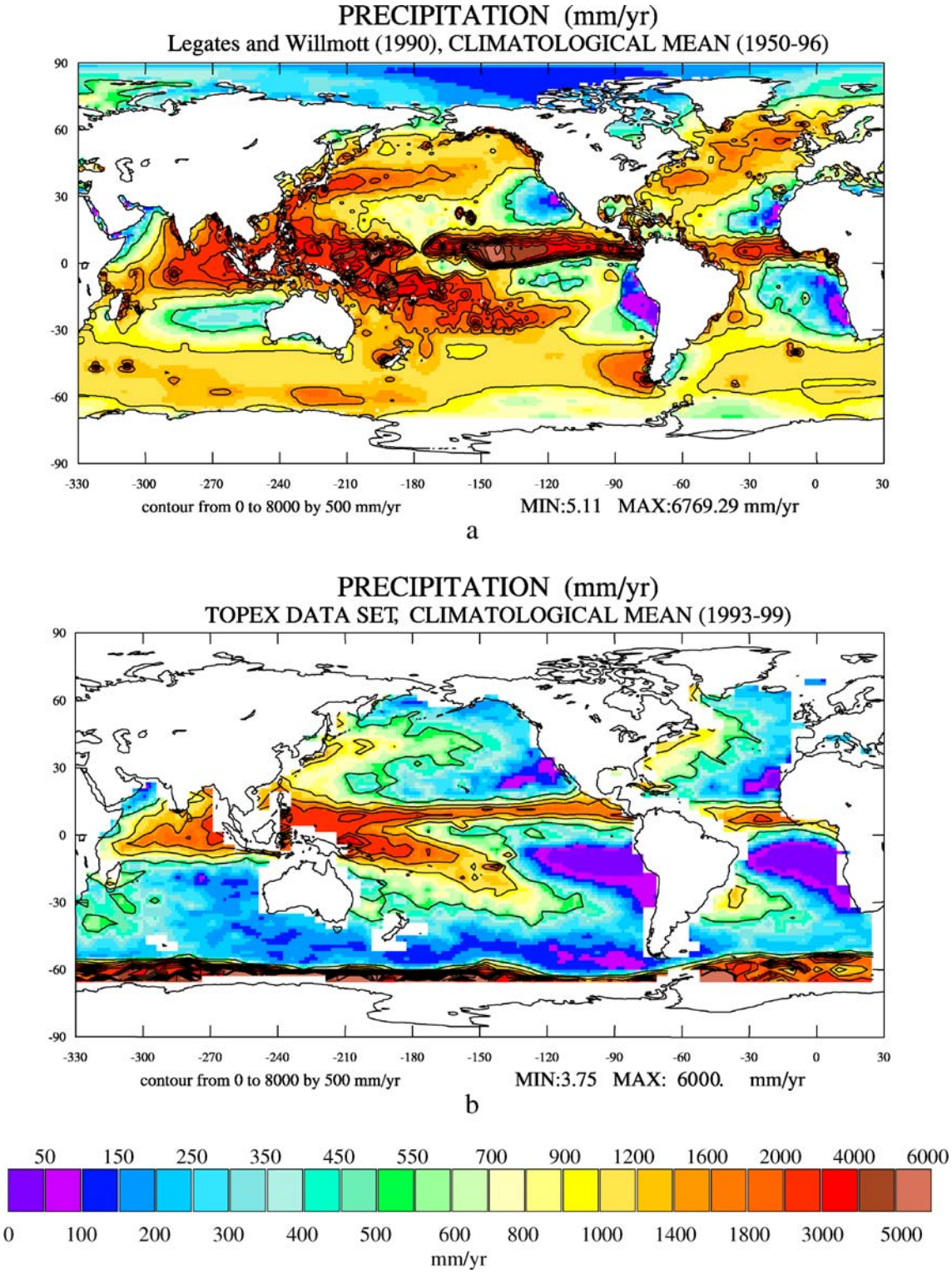

Fig. 1 Climatological mean precipitation over oceans for four data sets averaged over their whole record length. *Colours* indicate local values in millimetre per year. Contour intervals (in millimetre per year) range from 0 to 8,000 per 500. **a** The CCR data set (average from 1950 to 1996). **b** The TOPEX data set (average from 1993 to 1999). **c** The HOAPS data set (average from 1992 to 1998). **d** The GPCP data set (average from 1988 to 1995)

(in situ vs satellite vs model, etc.). Our analysis did not provide enough objective elements, which would allow us to clearly recommend a given data set as reference or best estimate. However, composite data sets (GPCP, and especially CMAP), because they never appeared to be really "off" when compared to other data sets, may represent the best recent data set available. CMAP would certainly be our first choice to drive an ocean GCM.

Keywords Global ocean precipitation · Freshwater · Seasonal variability · Interannual variability

1 Introduction

The freshwater input in the ocean comes from precipitation, river runoff, sea ice and glacial melt. It can strongly increase the ocean vertical stability and exert a significant control on water mass transformation (Speer and Tziperman 1992). The increasing attention given to the distribution of sea surface salinity and its variations (Font et al. 2004) allowed the demonstration that, even in regions of strong advection, the behaviour of the sea surface salinity could not be dissociated from precipitation and evaporation rates (Delcroix et al. 1996). Thus, precipitation (*P* hereafter), which is a major component of the ocean freshwater input, is undeniably an essential contributor to the ocean buoyancy forcing, and its importance to ocean dynamics is fully recognised.

Nevertheless, most ocean General Circulation Models (OGCMs) used to study ocean processes and ocean variability are still using some relaxation to climatological values of the sea surface salinity in their freshwater forcing parameterisation (Large et al. 1997; Barnier 1998). A reason given is the great inaccuracy of mean *P* (and evaporation) estimates over the ocean, which must be compensated by some control on the sea surface salinity, although an inaccurate representation of the salinity seasonal cycle is often attributed to the relaxation itself (Killworth et al. 2000; Ferry and Reverdin 2004).

The need for suitable global *P* estimates over long time series has been brought out in an acute way by the societal concern to understand and predict climate changes in the atmosphere and in the ocean (Schmitt 1995) and by the application of OGCMs to a growing variety of problems. Frequent OGCM applications are made at very high resolution to investigate the driving mechanisms of the mean and variable ocean circulation (Smith et al. 2000; Willebrand et al. 2001; Tréguier et al. 2003). Interdisciplinary applications are emerging, investigating the natural variability of large marine ecosystems (Carmillet et al. 2001; Marchesiello et al. 2003), and ocean forecasting is developing rapidly (Ballabrera-Poy et al. 2002) with the management of ocean resources as perspective. All these applications require realistic driving functions, thus including accurate *P* estimates over wide ocean regions.

Consequently, the determination of the global hydrological cycle over the ocean has become a concern of prime importance to most fields of ocean and atmospheric sciences, and *P* has received an increasing attention in the last 15 years under of the World Climate Research Programme (WCRP), which frames the Global Energy and Water Cycle Experiment (GEWEX). This experiment studies the global freshwater budget, and carries out the Global Precipitation Climatology Project (GPCP, Huffman et al. 1997), with the objective to establish the best possible climatology of *P* at a global scale, over lands and oceans.

P is particularly patchy and intermittent, and due to both spatial and temporal scales at which *P* events occur, the estimation of a global *P* field is an extremely difficult exercise. Ways to estimate *P* rates over the sea have been reviewed in detail by the Working Group on Air–Sea Flux (WCRP-115 2001). Major sources of information are direct (or in situ) measurements, ship reports, satellite observations of several kinds, and Numerical Weather Prediction (NWP) centres, which have significantly improved the capability of their atmospheric models to produce reasonable estimates of *P*. As a consequence, several *P* data sets over the global ocean, built from one or a combination of the possible sources, are now available for periods longer than 10 years.

Inter-comparison projects have been carried out. The Algorithm Inter-comparison Program (Erbert et al. 1996) was an attempt to validate different satellite algorithms against in situ (rain gauges and radar) estimates. Therefore, attention was given to regional areas under different weather conditions. The Precipitation Inter-comparison Project (Adler et al. 2001), with the objective of improving satellite estimates, compared a set of monthly rainfall products. They showed the existence of large discrepancies among the products and proved the usefulness of combining multi-sensor observations with rain gauges. The main findings of these inter-comparison projects, which have been summarised in the WCRP-115 (2001) report, highlight the difficulty of selecting the best estimate, and there is still no recognised field of reference. However, the above studies, whose main objective was to improve satellite products, focused on short periods and gave little insight on long-term *P* climatologies.

Elements of comparison of *P* estimates over long periods can be found in several papers associated with the appearance of new climatologies (see Section 2.1 and Table 1 for a list of references). For example, Quartly et al. (1999) compared the spatial patterns of *P* in the Inter-Tropical Convergence Zone (ITCZ) using *P* climatologies derived from the TOPEX/POSEIDON satellite and GPCP. In fact, a double ITCZ is found in the two data sets in 1993–1996, which could be interpreted as an interannual signal (see Section 6.1). Estimates from TOPEX/POSEI DON are lower by 25% than GPCP values. Mean *P* field of the European Centre for Medium-range Weather Forecast (ECMWF) have been compared by Béranger et al. (1999) and Garnier et al. (2000) with the estimates provided by GPCP and those derived from the Comprehensive Ocean Atmosphere Data Set (COADS, Woodruff et al. 1987) by Da Silva et al. (1994) and Josey et al. (1999). These studies showed that ECMWF presents the highest value of *P* of all data sets, especially in the ITCZ and South Pacific

Fig. 1 (continued)

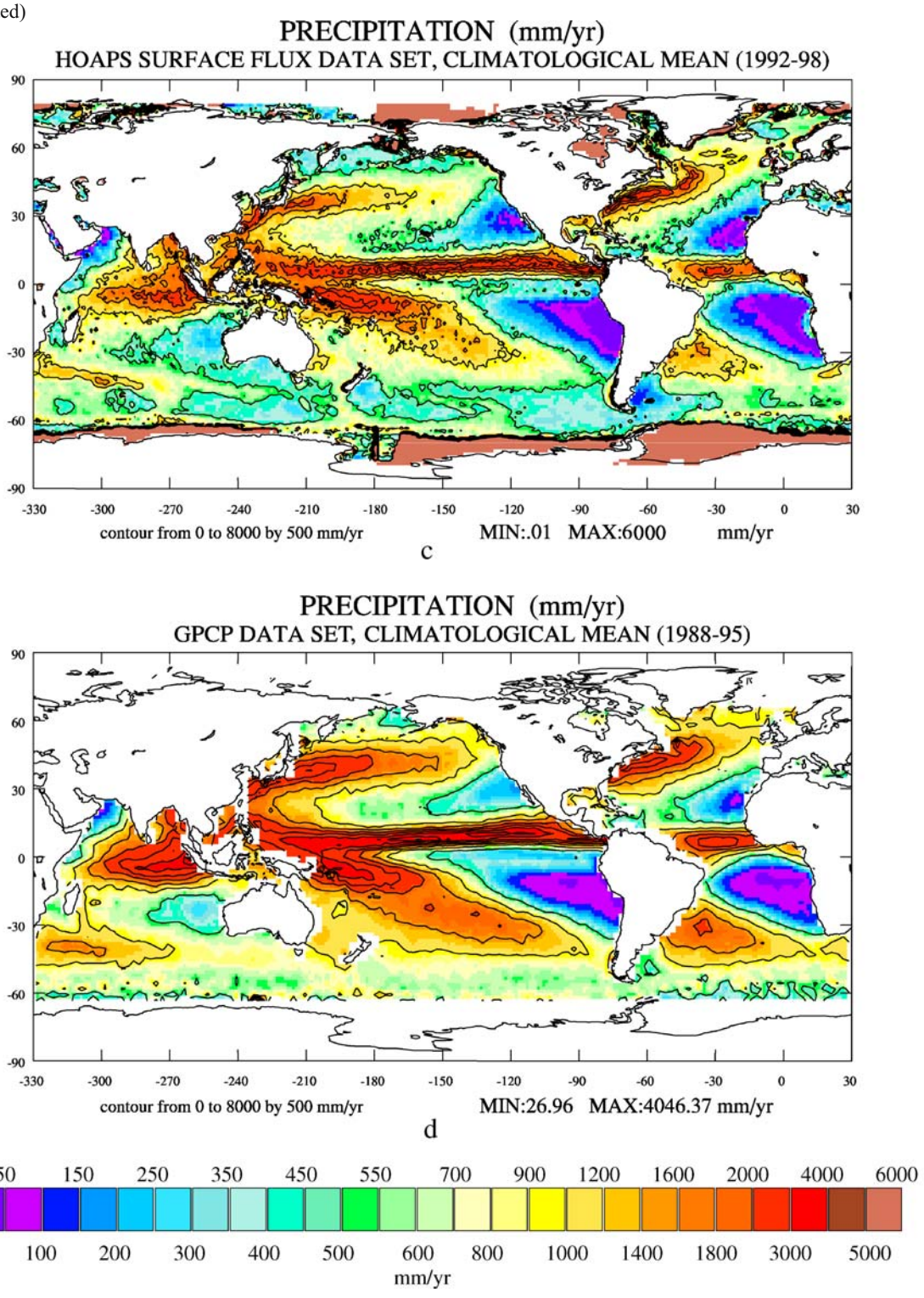

2.1 Precipitation data sets based on observations at sea

Local *P* estimates can be derived from ship reports (which do not measure *P* but report *P* conditions) or obtained from direct rain gauge measurements on ships and buoys (or radar on ship only). However, there are not enough direct measurements of *P* to establish a climatological (long-term) or a monthly mean over the global ocean, and a large recourse to ship reports is used.

The first global *P* climatology over lands and oceans was established by Baumgartner and Reichel (1975). Over land, runoff and *P* were based on direct hydrological measurements. Over oceans, very few data were available in the 1960s–1970s, and Baumgartner and Reichel constrained

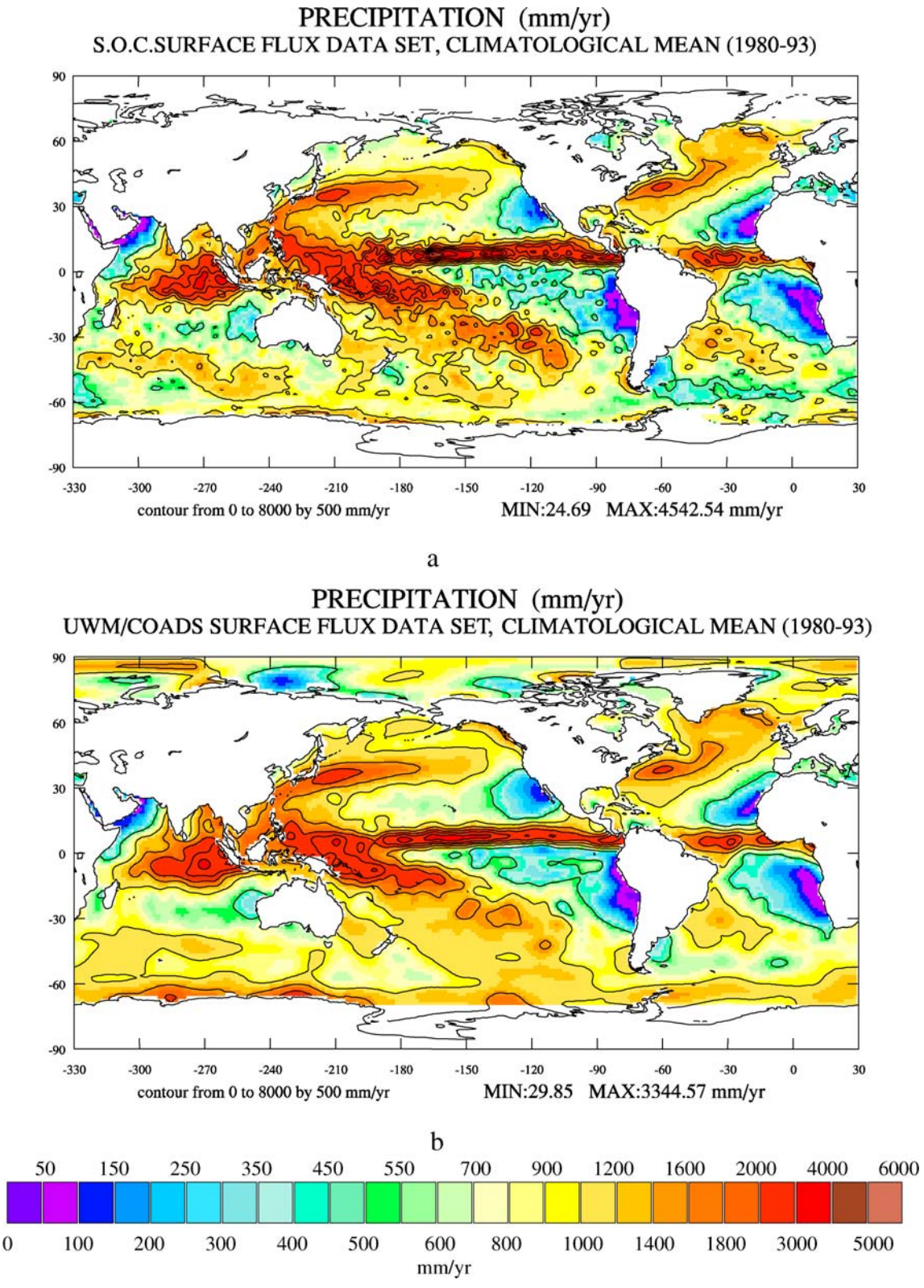

Fig. 2 Climatological mean (14-year average from 1980 to 1993) precipitation over oceans for six data sets having this period in common. *Colours* indicate local values in millimetre per year. Contour intervals (in millimetre per year) range from 0 to 8,000 per 500. **a** The SOC data set. **b** The UWM data set. **c** The MSU data set (lack of data in December). **d** The CMAP data set. **e** The ECMWF re-analysis data set. **f** The NCEP/NCAR re-analysis data set

Fig. 2 (continued)

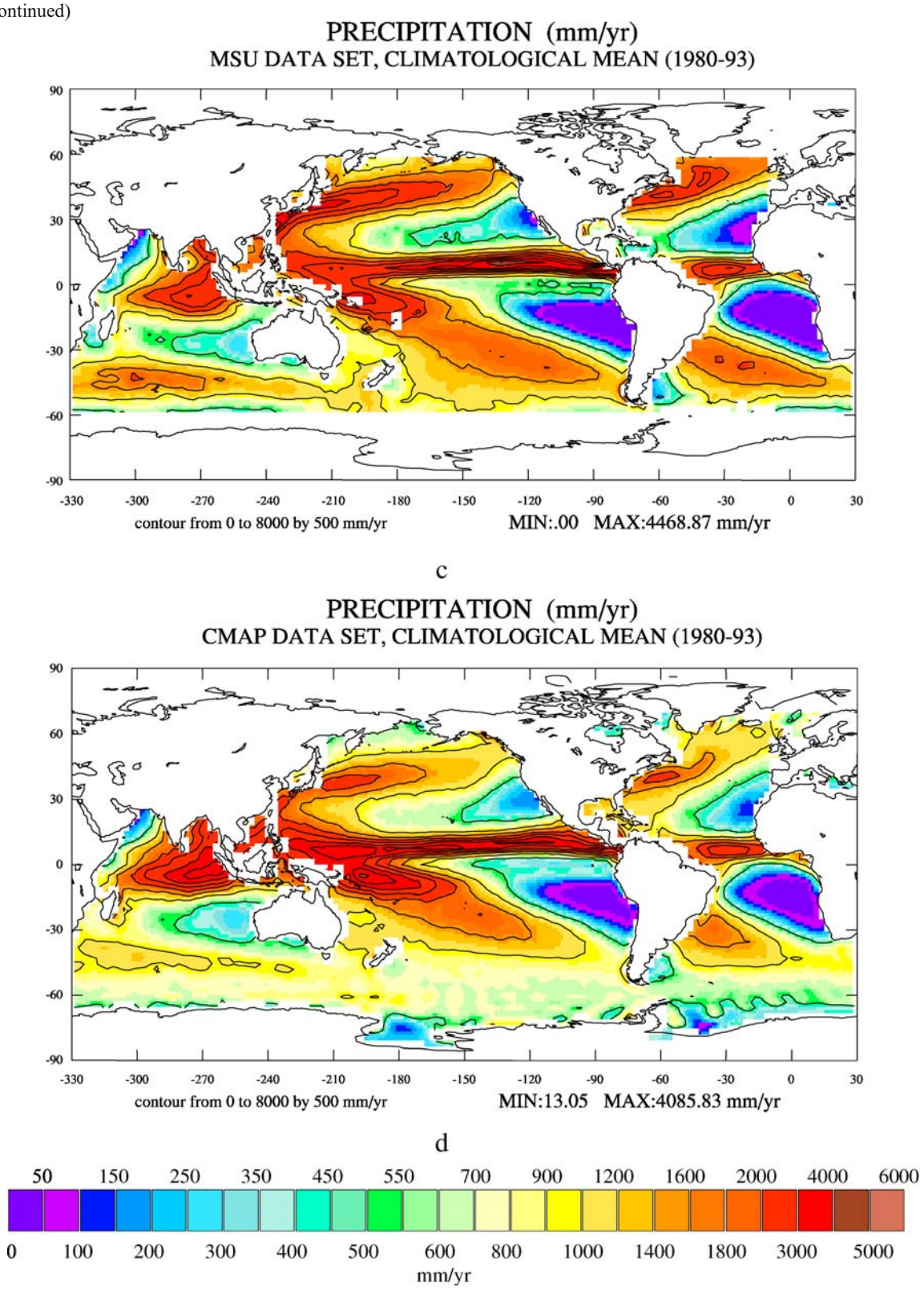

their ocean values with land values using a balanced freshwater budget. The main interest of this climatology over ocean lies in the balanced budget.

Recent ocean P climatologies, such as the three presented below, make a large use of COADS, which compiles almost all existing P measurements, and Volun-

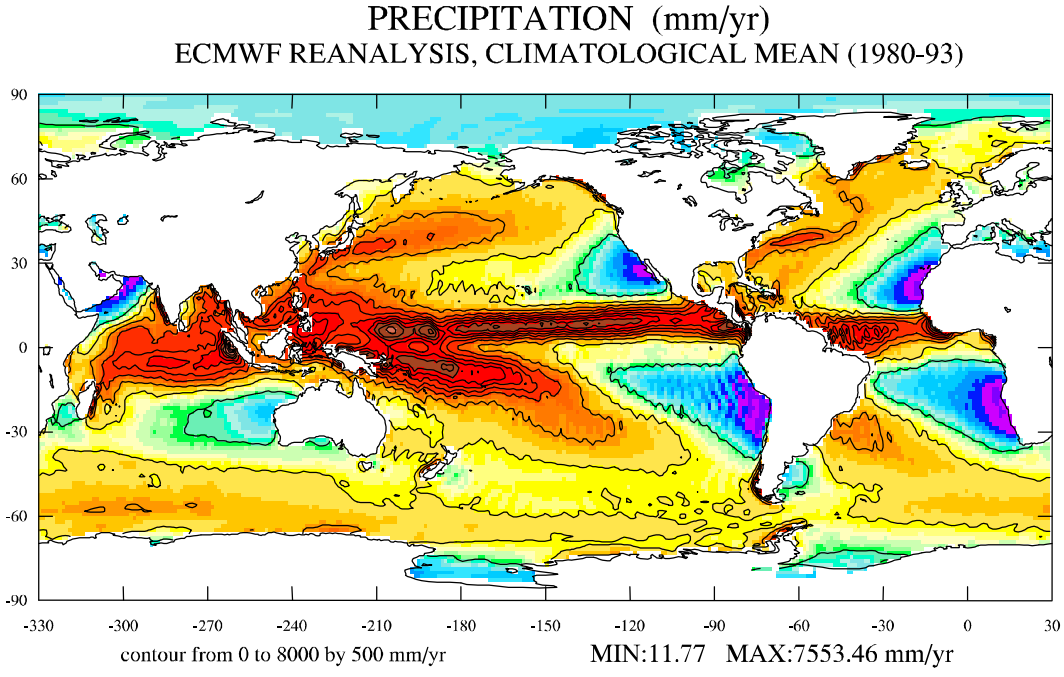

e

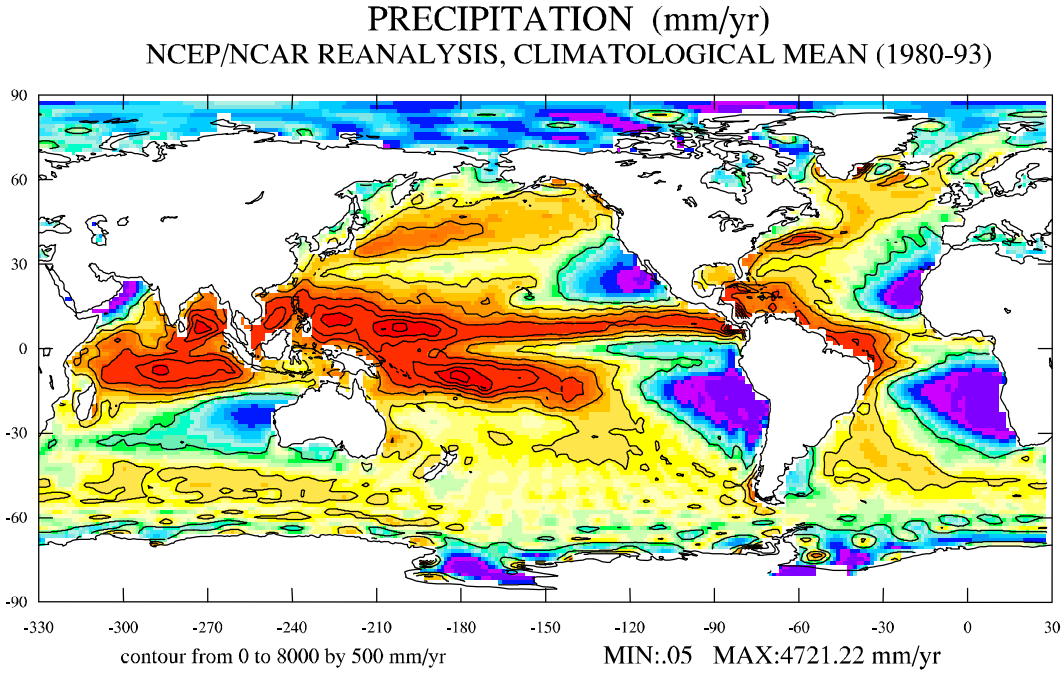

f

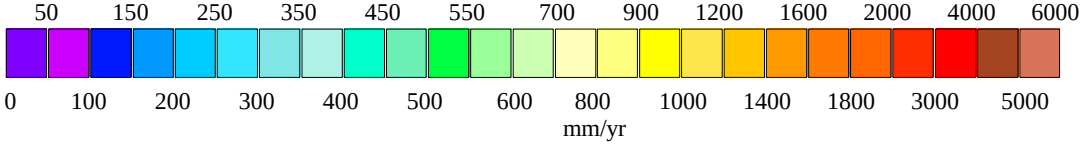

tary Observing Ship (VOS) reports for the last century. Precipitation estimates based on the VOS weather code may be influenced by the sampling errors, which consist of random sampling errors and fair weather bias. It has been pointed out that the fair weather bias may result in a systematic underestimation of the turbulent heat fluxes and wind speeds in case of stormy conditions (Gulev et al., submitted for publication). However, there is no clear

conclusion concerning the systematic or random character of the fair weather bias for precipitation.

CCR climatology Willmott and Matsuura at the Center for Climatic Research (CCR hereafter) extended the work of Legates and Willmott (1990) and proposed a climatology of *P* over ocean and land. Climatological monthly values were produced from a compilation of records obtained between 1950 and 1996 (http://climate.geog.udel.edu/~climate). Legates and Willmott have used the method developed by Tucker (1961). This method uses the present weather information of standard ship reports and relates it to precipitation rates according to a regression formula. Besides, in the tropics, an additional correction from Dorman and Bourke (1978) has been applied. To provide regular space coverage, the CCR climatology used an interpolated algorithm based on an enhanced distance weighting method and a neighbour-finding algorithm based on spherical distance.

UWM climatology A time series of monthly mean air–sea fluxes extending from 1945 to 1993 have been produced at the University of Wisconsin-Milwaukee (UWM hereafter) by Da Silva et al. (1994), in collaboration with the National Oceanographic Data Center and the National Oceanic and Atmospheric Administration. This analysis (Da Silva and White 1996) provides monthly *P* over the global ocean using surface observations or reports collected by ships and buoys.

SOC climatology Monthly air–sea flux estimates for the period 1980 to 1993 have been produced by Josey et al. (1999) at the Southampton Oceanography Centre (SOC hereafter). Flux estimates are obtained from in situ data, which are ship reports and buoy observations. Although using basically the same data as the UWM climatology, the processing is different. In particular, the radius of influence used in the interpolation method is smaller in the SOC analysis.

Both UWM and SOC climatologies were produced with a method of successive correction, a frequently used technique that is likely to introduce errors with irregularly sampled data. It does not require information about the temporal and spatial patterns of the fields. Data with different radii of influence are weighted by distance and averaged in successive passes of the smoothing process. This changes the characteristics of the data, degrades good measurements due to the overall lack of observations and creates a bias in the poorly sampled southern hemisphere due to southwards extrapolation of northern values. Thus, the quality of these estimates is considered as good in the northern hemisphere but poor in the southern hemisphere, particularly South of 30°S, where the number of observations considerably decreases and uncertainties on fluxes increase (White 1995; Glecker and Weare 1997). In this study, when we do not especially distinguish between SOC and UWM data sets, we refer to both of them as the COADS climatologies.

2.2 Precipitation data sets based on one kind of satellite observations

Satellite detection of *P* is likely to provide the best possible spatial and temporal coverage and is receiving strong support. An important difficulty is that space-borne sensors (radiometers or microwave radars) estimate an area-integrated quantity of water in the atmosphere rather than the actual rainfall, and thus provide precipitation rates different from those measured by pluviometers.

Another difficulty in satellite estimation of *P* resides in both spatial and temporal variability of this variable. Big cloud systems are few and small cloud systems are frequent and often last less than 1 h. Thus, to obtain a correct sampling remains a serious challenge. Several methods are being developed, which combine different sensors from different satellites (for a review, see Kidds 2001), and multi-sensor products are presently being improved. Four *P* climatologies are presently available, which use observations from a single satellite or combine different sources of data to construct an optimised estimate.

MSU climatology Monthly global *P* estimates based on Microwave Sounding Unit (MSU hereafter) measurements are available from January 1979 to May 1994 (Spencer 1993). A direct method is used, which consists in observing the effects of precipitating particles on radiation emitted by a radiometer at several frequencies. According to Spencer (1993), estimates in the extra-tropics are doubtful during the cool season. The MSU time series contains gaps due to the occurrence of failures in the retrieval of data, particularly in December over the whole 1980–1993 period. The MSU is insensitive to non-precipitating cirrus clouds and provides a robust signal in the tropics.

HOAPS climatology The Hamburg Ocean Atmosphere Parameters and Fluxes from Satellite (HOAPS hereafter) database provides *P* and fluxes obtained from processing Special Sensor Microwave Imager (SSM/I) and Advanced Very High Resolution Radiometer (AVHRR) (Bauer and Schluessel 1993). Indirect methods are used to retrieve the AVHRR data (radiometric observations in the visible and infrared), which catch the diurnal cycle. Recently developed methods have been applied and retrieval methods have been validated in comprehensive comparison studies with in situ measurements over the 1992–1998 period (Grassl et al. 2000). The HOAPS data set we worked with was not corrected for corrupted or spurious values. Precipitation values as large as 400 m/year were found in few places. Therefore, we masked the points where the climatological mean precipitation is above 9 m/year.

TOPEX climatology Estimates of *P* have been determined from dual-frequency altimeter radar measurements of the TOPEX/POSEIDON satellite (Chen et al. 1997; Quartly et al. 1999). Precipitation rates are bi-monthly values due to the sampling restriction of using a single altimeter and for a period extending from November 1992 to December 1999. This data set is referenced to as TOPEX hereafter. As for HOAPS, the TOPEX data set we worked with showed spurious values. The same masking (threshold of 9 m/year on the climatological mean) was applied.

2.3 Precipitation data sets based on NWP forecasts

Precipitation provided by weather forecasts carried out with atmospheric general circulation models at NWP centres remained very unrealistic for quite a time, mainly due to inaccurate cloud parameterisations. In fact, the low vertical resolution of the models did not allow describing narrow thermal inversions and then did not detect the strati-formed and cumuli-formed clouds, which are stopped under these inversions. Realistic inclusion of clouds with optical and convective properties in NWP models has been constantly improving in the 1990s, when new parameterisations were developed. Clouds of boundary layers were parameterised as a function of the intensity of the thermal inversion and of the humidity at the bottom of the inversion. Another improvement was to introduce a variable "liquid water rate". As a result of these new parameterisations and an increase in resolution, *P* forecasts considerably improved, and the monthly mean rain rates they produce became comparable to estimates from other sources.

The re-analysis projects carried out at the ECMWF and at the National Center for Environmental Prediction (NCEP) in collaboration with the National Center for Atmospheric Research (NCAR) provided long and consistent time series of *P* (and air–sea fluxes), which operational analyses could not provide due to continuous changes in the analysis/forecast system.

An analysis combines the output of a model forecast and observations (both relative to the same period of 6 h) to produce the state of the model that is the closest to the observations in an optimal sense (which depends on the data assimilation technique that is used). Therefore, the analysed fields are the prognostic model variables, which do not include the surface fluxes. In consequence, values of *P* are not obtained from the analysis, but are accumulated over forecast periods (from 6 to 24 h). Snowfall, large-scale and convective precipitation are included in the total *P*. It is worth mentioning that although many atmospheric observations of different kinds are assimilated in the model during the analysis, no *P* measurement is used during the forecast, so *P* is not constrained by any rain observation. Known problems of NWP forecasts are the representation of stratus clouds in regions of subsidence, and the excess of *P* during the model spin-up. The first re-analyses performed at ECMWF and NCEP are studied here. These meteorological centres have carried out second re-analyses, which are presently being evaluated.

ECMWF first re-analysis The re-analysis of ECMWF (ECMWF hereafter, Gibson et al. 1997) consists in an analysis carried out with a fixed state of the analysis/forecast system (the version of 1995), which includes a prognostic cloud scheme (Tiedtke 1993). The re-analysis was run for 15 years, from 1979 to 1993. Therefore, it presents a homogeneous record in comparison to operational analyses (Siefridt et al. 1999; Béranger et al. 1999). In this paper, we use the monthly mean of total *P* obtained from averaging the 12-h forecast (Garnier et al. 2000).

NCEP first re-analysis The NCEP/NCAR re-analysis (NCEP hereafter, Kalnay et al. 1996) consists in a re-analysis performed jointly by NCEP and NCAR (with the fixed NCEP analysis/forecast system as defined in 1995. This re-analysis runs for more than 40 years, from 1957 to present. Differences with the ECMWF re-analysis mainly reside in the atmospheric model and the assimilation process.

2.4 Precipitation data sets based on a combination of several satellite estimates, rain gauge observations or NWP forecasts

CMAP climatology The CMAP (Xie and Arkin 1997) produced a global *P* data set by merging rain gauge

Table 2 Annual period covered by the various precipitation data sets

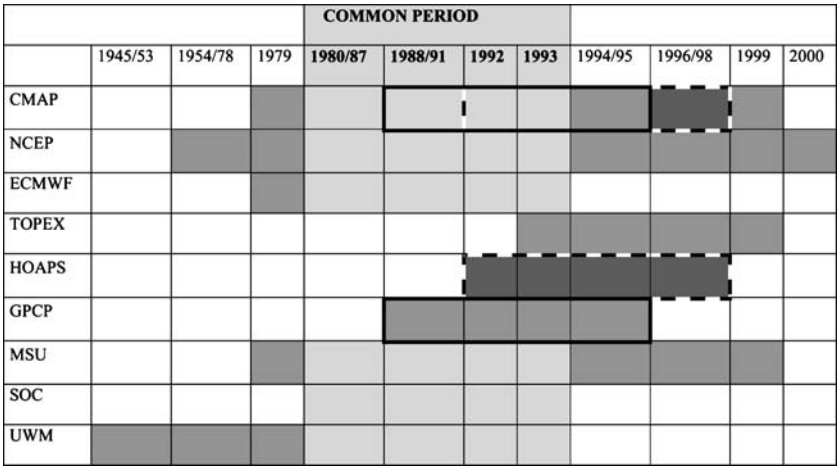

The period common to CMAP, NCEP, ECMWF, MSU, SOC, and UWM (14 years from 1980 to 1993) for which these six data sets are compared is shading in light grey. CMAP and GPCP are compared over the period 1988–1995 (thick dark frame). CMAP and HOAPS are compared over the period 1992–1998 (thick dashed frame)

measurements, *P* forecast from NCEP/NCAR re-analysis and five kinds of satellite estimates (CMAP hereafter). The CMAP product provides monthly means of *P* for the period from January 1979 to October 1999. In this study, CMAP will be considered mainly as a satellite product except at high latitudes (beyond 60°) where input from satellite becomes negligible. There, CMAP is basically equivalent to NCEP.

GPCP climatology A global monthly *P* data set for the period from July 1987 to December 1995 has been produced in the framework of the GPCP (Huffman et al. 1997). The analysis combines only rain gauge data from the Global Precipitation Climatology Centre (Rudolf et al. 1996), radiometer data from geosynchronous and orbiting satellites, and microwave data from the SSM/I. This data set is referenced to as GPCP in the following sections.

3 Overview of climatological mean *P* fields

Climatological mean *P* fields are displayed in Figs. 1 and 2 for the ten different data sets referred to in Table 1. Precipitation units used in this study are *millimetre per year* (*or millimetre per month*) *per unit surface of the ocean*, but are noted *mm/year* (or *mm/month*). Here, the climatological mean is the time average over the period 1980–1993 for the data sets which cover that period (SOC, UWM, MSU, CMAP, ECMWF, NCEP), and over their full record length for data sets which do not (CCR, TOPEX, HOAPS, GPCP). Note that for MSU, the annual climatological mean is only calculated with 11 months due to the lack of values in December over the whole period, which makes comparison with the other data sets inaccurate. The overview of climatological *P* fields presented in this section could be misleading because the analysis period of several data sets (especially HOAPS and GPCP) barely overlaps the period of 1980–1993 common to most other data sets. To avoid a misleading comparison, we also performed the analysis on the 1993 mean, which is common to almost all data sets (see Table 2), and verified that comments and conclusions relative to the comparison of climatological means are consistent with the analysis of the 1993 mean.

The comparisons of *P* maps (Figs. 1 and 2) demonstrate a qualitative agreement at the largest scales, contrasting regions of high and low *P* values. Precipitation is high in the ITCZ, the ascending branch of the Hadley Cell in the Atlantic, Pacific and Indian Oceans, and in the SPCZ. High values of *P* are also observed in the western part of the subtropical gyres, along the path of the warm western boundary currents. Regions of low *P* (<100 mm/year) are found in the eastern part of the tropical and subtropical ocean basins. For example in the descending branch of the Walker Cell, the quasi-constant subsidence of dry air limits convective phenomena, and rainfalls are particularly small in the eastern part of the subtropical ocean gyres. Quantitatively, the agreement between the various *P* estimates is generally poor. Differences between *P* fields can be locally very large, and before a detailed comparison is carried out (Sections 4 and 5), several examples of extreme discrepancies between *P* fields seen in Figs. 1 and 2 are pointed out in this section. Our comments are organised according to geographical areas defined in Fig. 3. The primary motivation for splitting the global ocean into regions is to perform regional budgets. Regions of Fig. 3 have been defined to idealistically represent the major large-scale ocean circulation features (i.e. eastern or western subtropical gyres, subpolar gyres, equatorial waveguide, the Southern Ocean). Precipitation budget (in the form of a spatial average) for a given region will thus be relevant to the salinity budget of the corresponding circulation feature.

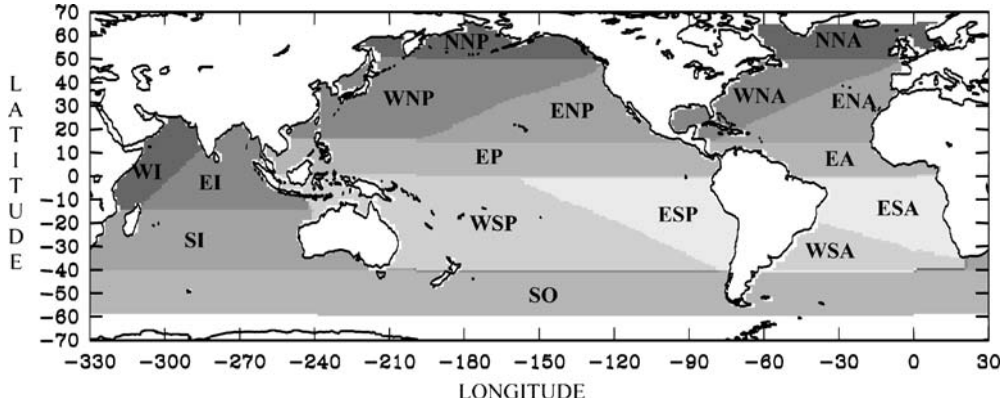

Fig. 3 Definition of 16 ocean regions for which precipitation budget has been calculated. Total precipitation over the region is calculated and normalised by the region area. These budgets are thus expressed in millimetre per year (or millimetre per month) per unit area. For convenience, mm/year (or mm/month) is used in the text and figures. *NNP* is the northern North Pacific region, *WNP* is the western North Pacific region, *ENP* is the eastern North Pacific region, *EP* is the equatorial Pacific region, *WSP* is the western South Pacific region, *ESP* is the eastern South Pacific region, *NNA* is the northern North Atlantic region, *WNA* is the western North Atlantic region, *ENA* is the eastern North Atlantic region, *EA* is the equatorial Atlantic region, *WSA* is the western South Atlantic region, *ESA* is the eastern South Atlantic region, *WI* is the western Indian region, *EI* is the eastern Indian region, *SI* is the southern Indian region and *SO* is the Southern Ocean region

3.1 Equatorial oceans

In the equatorial Pacific (EP in Fig. 3), mean *P* values range for most data sets from 2,000 to 3,000 mm/year, except for TOPEX (1,000 to 1,500 mm/year only) and CCR and ECMWF (over 4,000 mm/year). In addition, CCR shows a much broader ITCZ with a discontinuity near 180°W that is probably due to a lack of data.

In the equatorial Atlantic (EA in Fig. 3), *P* means range between 1,500 and 2,500 mm/year, except in TOPEX and HOAPS where they are less than 1,000 mm/year.

In the eastern Indian (EI in Fig. 3), *P* values range in the Gulf of Bengal between 2,000 and 3,000 mm/year from one data set to another, except for TOPEX and HOAPS, which again exhibit the lowest values (about 1,500 mm/year).

The western Indian (WI in Fig. 3) is characterised by a great *P* contrast between the Arabian coast (a dry area) and the coast of the Indian Peninsula (a wet area) as seen in all data sets.

3.2 Western tropical and subtropical oceans

In the western North Pacific (WNP in Fig. 3), *P* maxima are localised along the path of the Kuroshio Current. Highest values of *P* are found in MSU and GPCP (2,500 mm/year), almost 500 mm/year more than other data sets, whereas TOPEX (800 mm/year) and HOAPS (1,000 mm/year) present the lowest values.

The major *P* pattern of the western South Pacific (WSP in Fig. 3) is the SPCZ and is differently represented in the various data sets. The maximum of *P* is located to the East of New Guinea. ECMWF has the greatest value among all data sets there, with more than 4,000 mm/year, twice the value proposed by TOPEX or COADS (2,000 mm/year). HOAPS is also lower than average there, with only 2,500 mm/year. The poleward extent of the SPCZ is similar between all data sets except CCR. From its *P* maximum off New Guinea, the SPCZ extends to the Southeast to about 45°S-100°W, and exhibits a secondary *P* maximum at 30°S-150°W clearly separated from the one off New Guinea in some data sets. Maximum *P* values found there vary from 1,400 to 2,000 mm/year, according to the data set considered. In CCR, the extent of the SPCZ is limited to 30°S (a consequence of the limited number of observations South of this latitude).

In the western North Atlantic (WNA in Fig. 3), *P* maximum is localised along the path of the Gulf Stream and the North Atlantic Current, where values range from 500 to 1,500 mm/year. Differences between data sets are similar to those noted above in the western North Pacific. The maximum of *P* (1,500 to 2,000 mm/year) in this region closely follows the path of the Gulf Stream in every climatology except for TOPEX. The spatial distribution of *P* in this region, however, is similar between NWP's and satellite-derived products (except TOPEX).

In the western South Atlantic (WSA in Fig. 3), all satellite products except TOPEX and HOAPS (i.e. GPCP, MSU, CMAP) provide by far the largest *P* values.

3.3 Eastern tropical and subtropical oceans

These regions (identified by ENP, ESP, ENA, ESA and SI in Fig. 3) are characterised by a strong atmospheric subsidence associated with very low precipitation. Large areas of *P* rates under 50 mm/year are found in eastern mid-latitude ocean basins in all data sets, except those derived from observations at sea (i.e. CCR, SOC and UWM). In those latter data sets, the smallest *P* values are above 50 mm/year. The extent to the West of these areas of low precipitation appears to be similar among most satellite products (CMAP, MSU, GPCP, HOAPS), but does vary quite significantly between the other data sets.

3.4 Southern ocean

Data sets appear to agree with regard to the spatial distribution of precipitation in the Southern Ocean (SO in Fig. 3). This region is limited to 60°S in our study because most data sets do not provide *P* estimates beyond this latitude. A band of high *P* is found in the Indian sector of the Southern Ocean, along the eastward extension of the return flow of the Agulhas Current. Elsewhere, the Antarctic Circumpolar Current is characterised by rather uniform *P*. Large *P* is found confined along the coast of Chile (upwind of the Andes) and low *P* East of South Argentina (downwind of the Andes). Again, differences between data sets are mainly quantitative, but are quite large. TOPEX presents *P* rates, which seem abnormally small (below 150 mm/year almost everywhere). HOAPS also presents small *P* values, but they are generally above 300 mm/year. Other data sets show values from 500 mm/year to above 1,000 mm/year in the Antarctic Circumpolar Current (more than 100% difference).

3.5 Remarks

Spatial patterns and magnitude of *P* over oceans are very differently reproduced by the data sets discussed here. Two particular data sets, TOPEX and CCR, appear to be especially far from the others. In particular, TOPEX does not reproduce several important patterns of *P* that all other satellites do. A significant amount of precipitation does fall in light events and the inability of TOPEX to detect them may explain part of the observed deficiencies. The same remark holds in extra-tropical bands, where other satellite-based estimates of *P* are twice greater than for TOPEX. CCR shows unrealistic local extremes, characteristic of an inadequate smoothing method to account for the lack of data and the irregular sampling (see Section 2.1).

The qualitative analysis carried out above demonstrates that local values of *P* may differ significantly (by more than 100% in very specific areas) from a data set to another. However, it is difficult with such a visual analysis of global maps to clearly identify systematic differences between the various data sets according to their source.

Eastern subtropical gyres (i.e. regions of *P* minimum) are regions where such systematic differences are noticeable. Satellite products exhibit the areas of low *P* of greatest extent, whereas in situ (i.e. COADS-derived) products show the smallest, likely due to the poor sampling of central tropical oceans (especially in the southern hemisphere) by ships from the Voluntary Ocean Ship program. NWP products seem to lie in between.

However, it is the integrated value of *P* rather than its local value which matters for the salinity budget of ocean circulation patterns. Therefore, the mean and variability of the budget of *P* in regions relevant to ocean dynamics (see Fig. 3) are studied in the next four sections, an approach that allows quantitative comparisons.

If we expect to find geophysical signals or trends and to point out artificial bias in the various data sets, their comparison must be performed over a common period. According to Table 2, six of the ten data sets have 14 years in common during 1980 to 1993, distinguishing between the three major sources of *P* estimates: in situ (i.e. COADS) derived data sets with SOC and UWM, NWP products with ECMWF and NCEP, and satellite products with MSU and CMAP. In the following three sections, we shall concentrate on these particular data sets, over this particular 14-year period. HOAPS and GPCP will then be studied separately over the period each has in common with CMAP (Section 7).

4 Climatological mean (1980 – 1993)

In this section, we proceed to a quantitative comparison of the climatological mean *P* estimates provided by the six data sets covering the 1980–1993 period. The 14-year (i.e. climatological) mean *P* fields relative to these data sets are shown in Fig. 2 and were qualitatively compared in the previous section. First, these mean fields are compared from their zonal average. Then, area averages of precipitation are calculated for 16 oceanic regions (Fig. 3). These spatial averages, which are called regional budgets hereafter because they are related to the total amount of precipitation in the region, are quantitatively compared.

4.1 Zonal average of annual mean precipitation

In a first attempt to quantify the differences between the various precipitation climatologies, we compare their zonal average noted $\overline{P}$ (Fig. 4). As in many other studies (White 1995; Béranger et al. 1999; Gruber et al. 1999; Adler et al. 2001; Kidds 2001), the 10°S–10°N latitude band is where precipitation is the largest and where largest disagreements occur.

Although all data sets place the $\overline{P}$ maximum of the ITCZ around 6.5°N, the value of the maximum differs quite a lot from one data set to another. The difference between the two NWP products is extremely large, with ECMWF showing the greatest value (3,222 mm/year) of all data sets and NCEP nearly the smallest (2,206 mm/year). This represents a discrepancy of 30%. The satellite products CMAP (2,817 mm/year) and MSU (2,507 mm/year) also present high $\overline{P}$ values but differ by only 310 mm/year

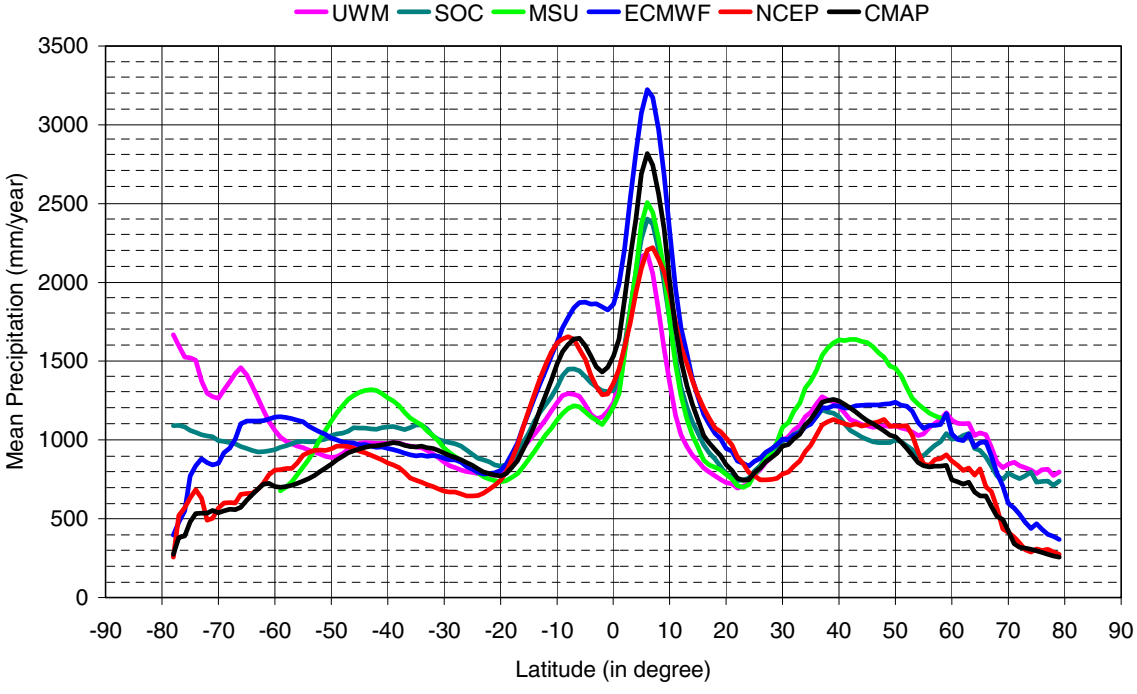

Fig. 4 Zonal average of climatological mean (14-year mean from 1980 to 1993) precipitation over the global ocean for the six data sets, which have this period in common

(≈12%). In situ products SOC (2,402 mm/year) and UWM (2,180 mm/year) are those showing the better agreement since their difference barely exceeds 220 mm/year (≈10%).

Large disagreements between data sets are also found at the latitude of the SPCZ (between 5 and 8°S). The value of $\overline{P}$, provided there by ECMWF, is again significantly above all the other estimates (1,875 mm/year), but NCEP value of $\overline{P}$ is now among the highest (1,654 mm/year), so the discrepancy between the two NWP products (12%) is not as large as for the ITCZ. The discrepancy between the two satellite products is drastically increased at this latitude. Whilst CMAP estimate of $\overline{P}$ remains among the highest (1,646 mm/year), the one from MSU falls last (1,217 mm/year), revealing a discrepancy of 25% (against 12% in the ITCZ). Agreement between the in situ products is again rather good because their difference remain of the order of 10% at this latitude. Note that in this band of latitude, the agreement about the place of maximum $\overline{P}$ is not as good as for the ITCZ. ECMWF and CMAP place it at 5.5°S, NCEP at 7.5°S, and it is placed at 6.5°S in the other climatologies.

All data sets converge to more comparable values in regions of low precipitation. In the southern tropics at 20°S, the difference between the highest value (i.e. SOC with 840 mm/year) and the lowest value (i.e. NCEP with 711 mm/year) does not exceed 15%. The same is noticed in the northern tropics at 24°N. As expected from the distribution of *P* shown in Fig. 2, in situ products (i.e. SOC and UWM) are those which exhibit the highest values in zonal average at the latitudes of the southern tropics (20°S), in relation to their smaller extent of regions of *P* minimum in the East of the ocean basins (see Section 3.5). Note that NCEP places the tropical minimum of $\overline{P}$ at higher latitudes than the other data sets. For the southern minimum (placed at 24.5°S instead of 20°S), this is due to a more zonal pattern of the SPCZ, which has a lesser poleward extent in the South Pacific, and a stronger *P* minimum in the East of the southern Indian (see Fig. 2). For the northern minimum (placed at 27.5°N instead of 22.5°N), this is likely due to the band of low *P* found between 28 and 30°N all across the Pacific Ocean (see Fig. 2).

In subtropical and subpolar regions (from 30° to 60° latitude in both hemispheres), MSU estimate of $\overline{P}$ (1,634 mm/year at 40°N) is well above all other estimates (which all agree within 5% or better of their average value of 1,187 mm/year at this latitude). This large overestimation of *P* in the MSU data set is also obvious in Fig. 2. NCEP provides smaller values of $\overline{P}$ than other data sets in subtropical gyres (about 200 mm/year less than ECMWF), which reveal smaller *P* over the warm western boundary currents (see Fig. 2).

Divergence between data sets increases again at latitudes higher than 60°. However, we do not comment on the respective behaviour of the various data sets for several reasons. Satellite product does not provide reliable values of *P* beyond 60°. So there is no available estimate for MSU and CMAP, which is a composite product similar to NCEP at high latitudes where the input from satellite is reduced. In situ estimates of *P* are not reliable at high latitudes because of a lack of observations in both hemispheres, although this is more crucial in the South. Therefore, our comparison is limited to NWP products. ECMWF and NCEP show a similar behaviour in zonal average in the northern hemisphere (ECMWF being roughly 200 mm/year greater than NCEP). They are very different in the Southern Ocean, with NCEP showing a continuous poleward decrease of $\overline{P}$ starting at 50°S, whereas in ECMWF, $\overline{P}$ increases continuously from the tropics to 65°S before showing a sharp decrease at higher latitudes.

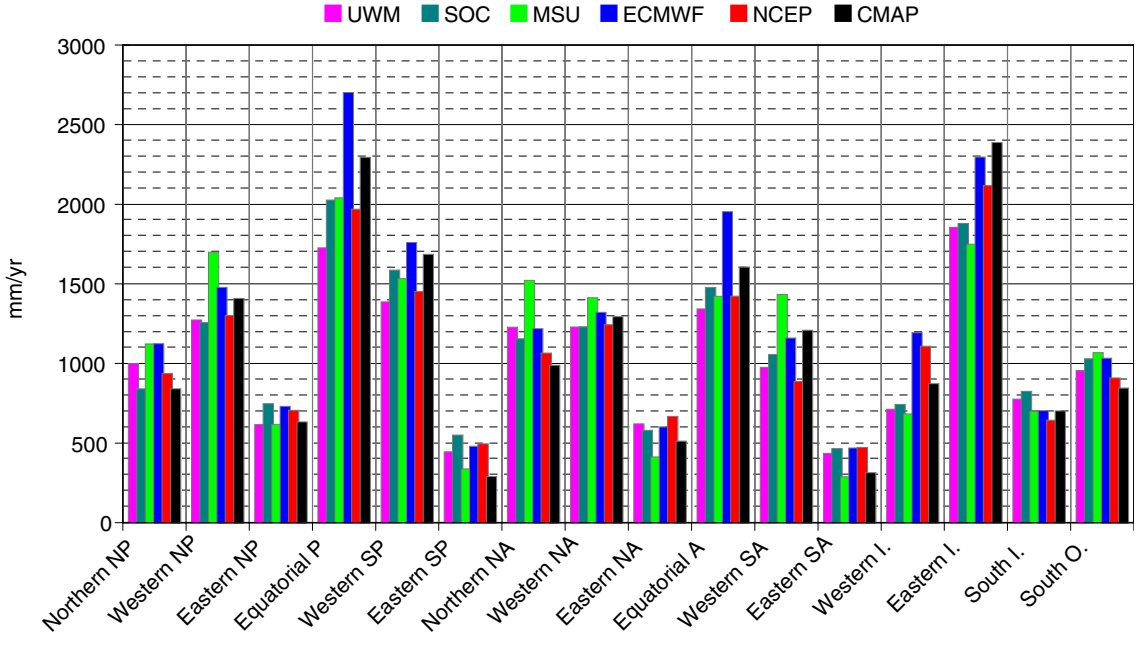

Fig. 5 Spatial average of the mean (1980–1993) precipitation (in millimetre per year) for every ocean region defined in Fig. 3. The six data sets, which have in common the 1980–1993 period, are plotted

4.2 Spatial patterns and regional budgets

The comparison of the climatological mean precipitation provided by the six selected data sets is continued by looking at regional budgets (i.e. area averages) calculated over the 16 oceanic regions defined in Fig. 3. Each region is relevant to ocean circulation patterns for which the total amount of precipitation is important for the salt budget. These regional budgets of *P* are shown in Fig. 5. Our analysis also makes use of the spatial patterns of *P* associated with each region as they appear in Fig. 2.

4.2.1 Equatorial regions of high precipitation

Equatorial pacific This area (EP in Fig. 3) is marked by the band of high precipitation associated with the ITCZ along the equator (see Fig. 2). Within this band, a maximum in *P* is found to stretch across the central Pacific (120°W to 180°W) in all data sets, except in NCEP where the *P* maximum is clearly placed in the western Pacific (180°W to 240°W). In fact, all data sets exhibit some kind of maximum of *P* in the western Pacific, as well seen in ECMWF and CMAP and barely noticeable in MSU. Highest local values of *P* above 4,000 mm/year are found in several places in ECMWF and in one spot of the central Pacific in SOC and in MSU (not in the same place).

The precipitation budget of the EP box (Fig. 5) shows that SOC, MSU and NCEP estimate the area-averaged precipitation in the equatorial Pacific to a value close to 2,000 mm/year, despite the different origin of the data. ECMWF and CMAP, with a budget of 2,600 and 2,300 mm/year, respectively, provide quite a large and likely unrealistic amount of precipitation in the equatorial Pacific. UWM shows the lowest budget with 1,700 mm/year.

Equatorial Atlantic The pattern of the band of high precipitation associated with the ITCZ in the equatorial Atlantic is quite different according to the origin of the data sets (see Fig. 2). In the satellite products MSU and CMAP, the maximum of *P* is placed in the central Atlantic near 30°W. In situ products SOC and UWM also place the maximum *P* at 30°W, but also show an increase of *P* at 10°W along the coast of Sierra Leone. In NWP data sets, two maximum of *P* are seen, the higher being placed in the West and the lower in the East. ECMWF exhibits the greatest values of *P*. All data sets more or less show an increase of *P* in the Gulf of Guinea.

Despite these significant differences in precipitation patterns, most climatologies propose a very comparable budget over the equatorial Atlantic. The area average of *P* is around 1,400 mm/year for all data sets, except for CMAP (1,600 mm/year) and ECMWF (1,900 mm/year).

Eastern Indian The tropical part of the Indian Ocean (i.e. North of 20°S) is characterised by a strong East–West precipitation contrast (see Fig. 2). The eastern part of this basin (EI in Fig. 3) is under the influence of the Indonesian atmospheric rise and is a place of high precipitation. In all data sets but NCEP, *P* maximum is placed off Sumatra and stretches westward, highest *P* occurring South of the equator. In NCEP, the coast of Sumatra is characterised by a relative minimum in *P* (1,000 mm/year lower than values around), which stretches westward along the equator, separating two areas of *P* maximum in the Gulf of Bengal to the North, and in the central Indian Ocean to the South. In situ products SOC and UWM have the lowest *P* estimates in the Gulf of Bengal among all data sets.

In terms of budget, this is the region of second highest precipitation after the equatorial Pacific (see Fig. 5). The in situ products SOC and UWM have very comparable budgets, each showing an area-averaged *P* of nearly 1,800 mm/year. The ECMWF again shows large area-averaged *P* (≈2,300 mm/year, nearly 200 mm/year more than NCEP); it is the CMAP climatology, which has the largest *P* budget (≈2,400 mm/year). The MSU climatology shows the smallest budget from all data sets (1,700 mm/year).

4.2.2 Tropical and subtropical regions of high precipitation

Western North Pacific This region (WNP in Fig. 3) comprises the China Seas and the Kuroshio Current. Whereas most data sets show comparable patterns of precipitation in this area (see Fig. 2), the MSU climatology shows a clear bias towards high *P* values, particularly in the region of the Kuroshio. In the area-averaged budget over the WNP region (Fig. 5), MSU reaches 1,700 mm/year, the greatest value among data sets. SOC, UWM and NCEP agree on a budget of nearly 1,300 mm/year. The area-averaged precipitation of CMAP (≈1,400 mm/year) and ECMWF (barely below 1,500 mm/year) are again on the side of the high estimates.

Western South Pacific This region (WSP in Fig. 3) includes the SPCZ, the influence of which on the area-averaged budget is dominant. The pattern of the SPCZ (Fig. 2) is the more zonal in NWP products. It has a greater extent to the Southeast across the Pacific in satellite estimates (it almost goes across in MSU), and appears as two separated regions of high *P* in the COADS derived climatologies.

In terms of budget (Fig. 5), this region is very similar to other regions of tropical convergence (EP and EA in Fig. 3), with ECMWF and CMAP showing greater area-averaged values.

Western North Atlantic This region includes the Gulf of Mexico and the Gulf Stream current systems (WNA in Fig. 3). MSU climatology shows a clear bias towards high *P* values in the region of the Gulf Stream (see Fig. 2). Other data sets show comparable patterns of precipitation in this area. The area-averaged budget over the western North Atlantic is 1,500 mm/year for MSU, the greatest value among data sets. Other data

sets agree (within a few percent) on a budget of nearly 1,200 mm/year, with again ECMWF showing the largest value (1,300 mm/year).

Western South Atlantic The region (WSA in Fig. 3) is characterised by a pattern of high *P*, which extends over the Brazil current system and its eastward extension. Satellite estimates are greater than all the others (Fig. 2), MSU being the greatest, by far. Therefore, MSU and CMAP show the largest budgets (Fig. 5) with 1,400 and 1,250 mm/year, respectively. Contrary to the northern subtropical gyres (WNP and WNA), differences are large between data sets in pattern as in budget (850 mm/year for NCEP and 1,150 mm/year for ECMWF the other NWP product).

4.2.3 Tropical and sub-tropical regions of low precipitation

Regions of atmospheric subsidence In Fig. 3, regions of atmospheric subsidence are the eastern North and South Pacific (ENP and ESP), and the eastern North and South Atlantic (ENA and ESA). There is an obvious consistency between data sets of same origin. SOC and UWM show very alike *P* patterns (Fig. 2) and present a reasonable agreement on the budget, *P* being usually greater in SOC except in the ENA (Fig. 5). The same comment goes for NCEP and ECMWF, with *P* being usually greater in NCEP except in the ENP. MSU and CMAP satellite *P* estimates provide the largest areas of very small precipitation, which is revealed in lowest budget values in Fig. 5.

Western Indian The Arabian Sea (WI in Fig. 3) is a region of small precipitation. In SOC, UWM and MSU, the *P* minimum is seen along the Arabian Peninsula (Fig. 2) and stretches southward along Somalia to reach Madagascar. Local values of *P* and area-average budgets are very similar between these three data sets (agreement is better than 5%, Fig. 5). The three other climatologies (ECMWF, NCEP and CMAP) show much greater *P* budgets (1,250 mm/year in ECMWF against 700 mm/year for MSU) due to the westward extent of the *P* maximum in the equatorial Indian in the Mozambique Channel. Discrepancies can reach 40% in area averages over the region between data sets, with NWP products showing the largest values.

Southern Indian The subtropical gyre of the Indian Ocean (SI in Fig. 3) is characterised by quite low precipitation in the East (Fig. 2). The *P* minimum off Australia is most marked in NCEP, which also presents the smaller area-averaged budget (650 mm/year). This minimum is not as well seen and does not extend as far to the West in in situ *P* estimates (SOC and UWM), which consequently exhibit the highest budget (750 to 800 mm/year). However, the general agreement between the data sets is better than 20% on the area-averaged budget (Fig. 5), so the southern Indian is a region where the various *P* estimates are in a relatively good agreement on the climatological mean.

4.2.4 High latitudes regions

Northern subpolar gyres Agreement between data sets of the same source is poor on the *P* budgets (Fig. 5) of the northern North Pacific and the northern North Atlantic (respectively, NNP and NNA in Fig. 3). As already mentioned, CMAP and NCEP become similar at high latitudes when the weight of satellite data in the CMAP estimate becomes insignificant. In the northern North Pacific, SOC is 20% higher than UWM, as is ECMWF compared to NCEP, and MSU is 30% larger than CMAP. These discrepancies are reduced to 10% in the northern North Atlantic for in situ and NWP products, which show comparable budgets. On the contrary, the *P* estimate by MSU in the North Atlantic subpolar gyre is 30 to 40% above the others. NCEP (and consequently CMAP) is with SOC, the only data set to propose *P* values below 1,000 mm/year in the Aleutian low-pressure system.

Southern Ocean The Southern Ocean (SO in Fig. 3) is comprised between 40 and 60°S, because the validity of the data sets beyond 60° latitude, particularly in situ and satellite products, is questionable. As for the subpolar regions of the northern hemisphere, CMAP is equivalent to NCEP. The distribution of *P* (Fig. 2) shows the highest values in the Indian sector, and from there, *P* continuously decreases across the Pacific sector and is minimum in the Atlantic sector. All data sets qualitatively agree with this distribution. However, ECMWF places the Indian *P* maximum at 58°S, whereas every other data set places it between 45 and 50°S. This high *P* is much greater in MSU. ECMWF estimates are generally the highest. Note that regional minima along the southwestern coast of Argentina and at the east of New Zealand are well seen in all climatologies, as is the local maximum south of Chile.

The area-averaged budget (Fig. 5) ranges between 800 mm/year for the smallest estimate (CMAP) and 1,100 mm/year for the largest (MSU), for a 30% scatter.

In situ products seem in agreement with each other, as their discrepancy does not exceed 100 mm/year (or 10%) over the whole area. Discrepancy between NWP products is again over 20%.

4.2.5 Remarks

The analysis of the climatological mean of the six data sets covering the same 14-year period has demonstrated that large discrepancies exist between data sets, which cannot generally be attributed to the origin of the data (i.e. in situ, satellite or NWP), although in some regions, a generic bias may exist.

Two important *P* data sets, HOAPS and GPCP, were not part of the above analysis because they cover a different period.

The climatological mean *P* of GPCP (Fig. 1) seems in agreement with CMAP (Fig. 2) with similar patterns and smoothing, although it shows greater values in western subtropical gyres and in the central equatorial Pacific. The two products are very alike and a comparison over their common period (Gruber et al. 1999) showed a good spatial and temporal correlation between them, except in the tropics. HOAPS *P* estimate is a satellite product very

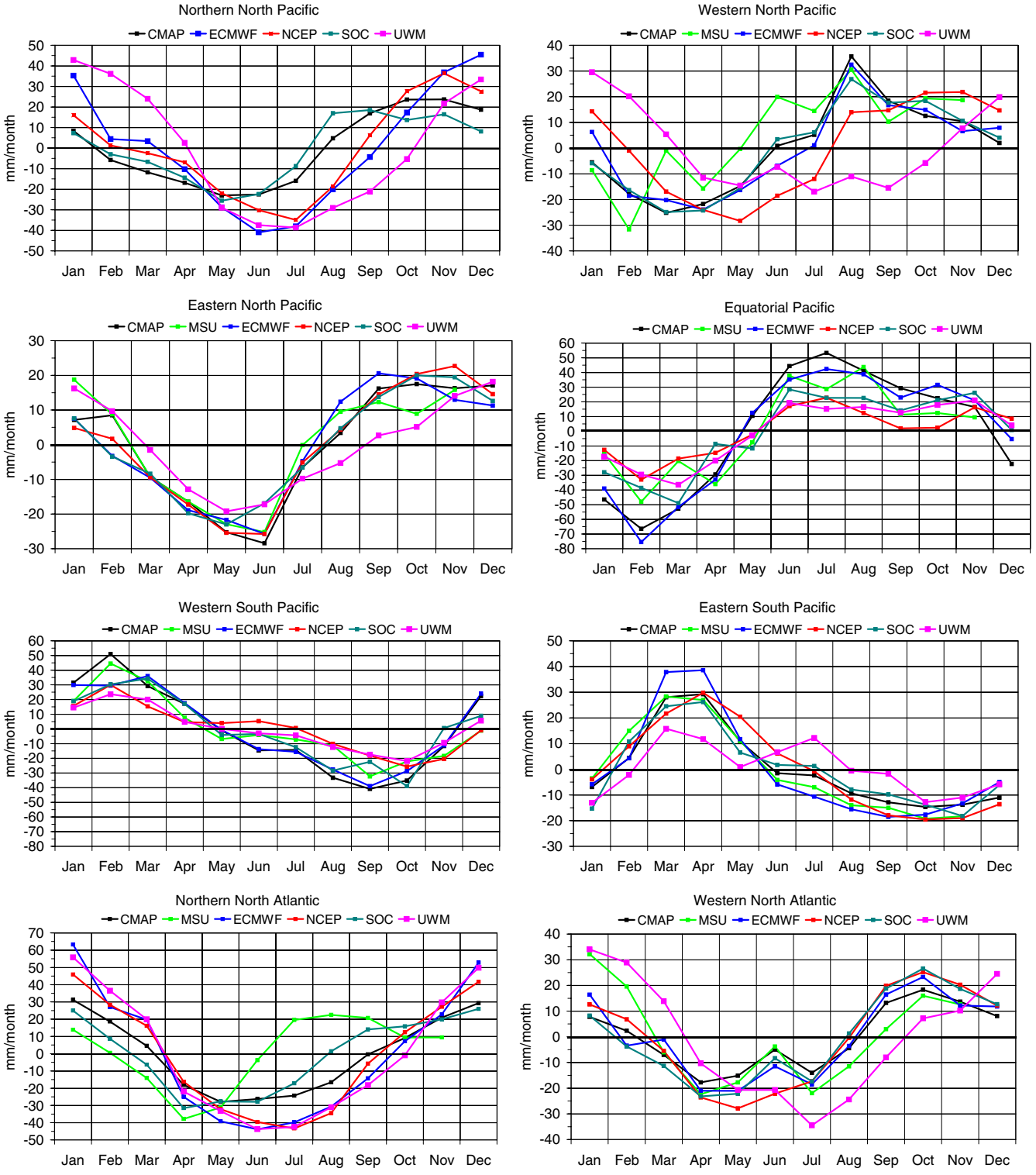

Fig. 6 Climatological seasonal cycle of precipitation (i.e. monthly mean precipitation anomalies) for the 16 ocean regions defined in Fig. 3, for the six data sets, which have in common the 1980–1993 period. The climatological annual mean (1980–1993 mean) for each data set has been subtracted to the climatological monthly means, and a spatial average over the region was performed. There were not enough MSU data in the NNP to provide a seasonal signal

Fig. 6 (continued)

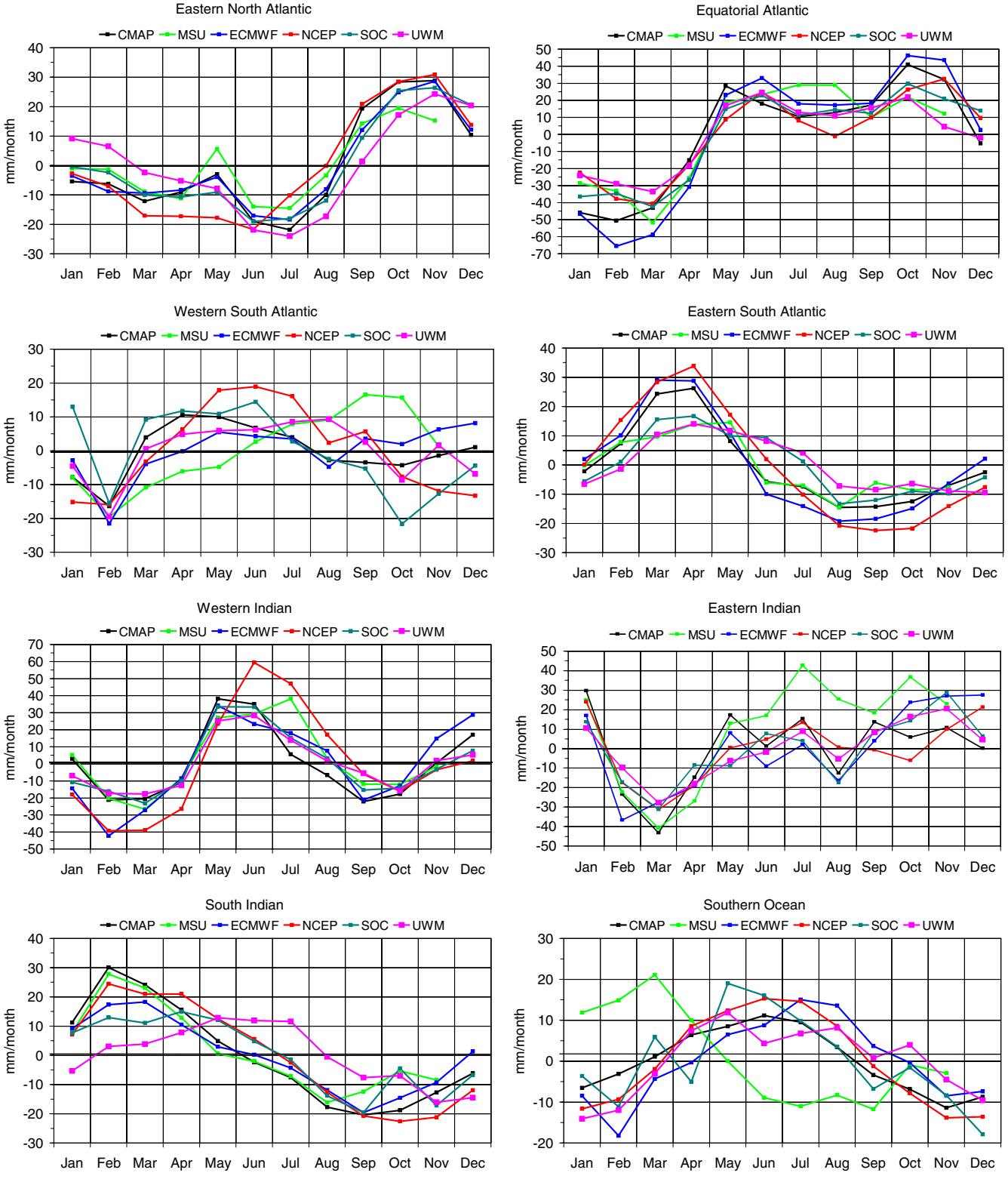

different from any other data sets. Compared to other satellite products and even to NWP products, HOAPS is remarkable by its high resolution (Fig. 1). It resolves smaller *P* features and shows greater *P* contrasts. A finer band of high *P* in the equatorial Pacific, a finer definition of the patterns of high *P* in the western boundary currents (as in the Agulhas Current and the Gulf Stream), pools of low *P* in the Indian and Pacific sectors of the Southern Ocean (east of New Zealand and over the Argentinian shelf for example) and the pool of low *P* in the Mozambique

Channel suggested, but not resolved by most of the other data sets, are the most remarkable features, and a well-defined region of low *P* is the Pacific subtropical gyre. The reality of these fine patterns are often suggested in in situ or other satellite products, which cannot resolve it due to averaging or smoothing. However, their quantitative significance has to be discussed. The comparison of HOAPS and GPCP with CMAP over their respective common periods is presented in Section 7.

5 Seasonal variability

In this section, we make a comparison of the climatological mean seasonal cycle of the *P* estimates provided by the six data sets covering the common 14-year period 1980–1993. We focus on the area averages (over the 16 regions of Fig. 3) of climatological monthly mean *P* anomalies (annual mean removed). This seasonal cycle is presented in Fig. 6 for every region. Unit used is millimetre per month per unit area (mm/month). Note that significant gaps in the MSU data set prevented an accurate calculation of *P* anomalies in polar regions (the NNP and NNA regions) and in December for most regions.

5.1 Pacific ocean

In the northern North Pacific, all data sets agree on a well-marked seasonal cycle, but the amplitude of the cycle varies significantly from one data set to another. Both NWP estimates exhibit a large amplitude seasonal cycle (85 mm/month for ECMWF and 70 mm/month for NCEP). They disagree about the occurrence of maximum/minimum precipitation (December/June in ECMWF and November/July in NCEP). Both data sets agree within 10 mm/month or better on month-to-month value except for December and January (20-mm/month difference). Comparing the two COADS-derived data sets, we find a large difference in the amplitude of the cycle (80 mm/month for UWM and 45 mm/month for SOC) and a shift in the occurrence of the winter maximum (September in SOC and January in UWM) and the summer minimum (May in SOC and July in UWM). The only satellite product available at this latitude (CMAP) shows a seasonal cycle similar to SOC in amplitude (50 mm/month), a summer minimum in May and a winter maximum spread between October and November.

In the western North Pacific, ECMWF, CMAP and SOC show a remarkably similar seasonal cycle (agreement is always better than 5 mm/month), low *P* occurring in March and April and high *P* in August. The amplitude of the cycle is nearly 60 mm/month. NCEP cycle appears shifted by 2 or 3 months, low *P* being observed in May and high *P* in October and November. UWM differs (sometimes by more than 20 mm/month) from every other data set in summer. The satellite product MSU appears noisy (significant month to month changes) and hardly compares with CMAP.

In the eastern North Pacific, all data sets show a well-marked seasonal cycle of amplitude 40 to 50 mm/month, with a summer minimum in May/June and *P* maximum in the fall (spread between September to November according to the data set). Agreement on month-to-month values is generally within 10 mm/month except for UWM.

In the equatorial Pacific, satellite and NWP products agree on the occurrence of *P* minimum in February, whereas COADS-derived products have it in March. All data sets agree on a season of high *P* spreading from June to October. CMAP and ECMWF exhibit the seasonal signal of largest amplitude (nearly 120 mm/month) and a month-to-month agreement generally better than 10 mm/month. SOC and MSU are similar (both are noisy), and when compared to CMAP and ECMWF, they show higher *P* anomalies during the season of low precipitation, and comparable *P* anomalies during the season of high precipitation (except in July). NCEP and UWM exhibit the seasonal signal of the smallest amplitude (55 mm/month). In this region so important for the freshwater budget of the Pacific Ocean, differences between data sets are mostly found in the amplitude (up to 60 mm/month in February) rather than in the phase of the cycle.

In the western South Pacific, place of the SPCZ, the seasonal cycle is qualitatively similar in all data sets, with precipitation reaching a maximum in February/March and a minimum in September/October. This cycle is out of phase with the cycle of the equatorial Pacific region (with a smaller amplitude) due to the southward shift of the ITCZ in the Austral winter, a signal well-captured by all data sets. Discrepancies in the amplitude of the cycle are similar to those noticed in the equatorial Pacific region.

In the eastern South Pacific, a region of low precipitation, the seasonal cycle of *P* is remarkably similar in phase and amplitude for all data sets except UWM. Agreement is generally better than 5 mm/month, except during the rainy season of March and April for ECMWF. The seasonal cycle in UWM does not seem coherent.

5.2 Atlantic Ocean

The northern North Atlantic shows, for most data sets, a seasonal cycle with high *P* in December/January and low *P* in June/July. Discrepancies between data sets are significantly smaller than in NNP. NWP products agree with each other (and with UWM) within less than 10 mm/month. SOC and CMAP look alike and differ from the others by 20 to 40 mm/month. Their *P* minimum occurs earlier (in May) and the amplitude of the cycle is smaller (55 mm/month compared to 110 mm/month for the others). There is no reliable MSU observation for this latitude.

The western North Atlanticand the eastern North Atlantic are regions where many air–sea observations exist, and we expect NWP analyses to be well-constrained, and the sampling of COADS to be the densest. Good agreement, or at least better than elsewhere, is therefore expected between in situ and model estimates of precipitation. Indeed, agreement is quite good for all data sets,

except for MSU and to a larger degree for UWM. In the WNA, most data sets indicate June as an anomaly of higher *P* in the middle of the dry season (which lasts from April to July), but its amplitude is smaller in NCEP and UWM. The same kind of anomaly is observed in the ENA with the month of May. Agreement between data sets is generally within 5 to 10 mm/month for a cycle whose amplitude is nearly 60 mm/month in the western North Atlantic (except for UWM and MSU), and within 5 mm/month for a cycle of 50 mm/month amplitude in the eastern North Atlantic (except for UWM).

In the equatorial Atlantic, all data sets agree on the occurrence of the dry season in February/March, and a long rainy season (May to November) with two peaks of precipitation, one in May/June and another of slightly greater amplitude in October/November. This pattern is not so well-reproduced in MSU, which exhibits its maximum in July/August. The amplitude of the seasonal cycle is the largest in ECMWF (110 mm/month) and CMAP (90 mm/month) due to larger peak values. It is of the order of 65 mm/month for the other data sets, which generally agree with each other within 10 mm/month.

In the western South Atlantic, all data sets draw different seasonal cycles. They all agree (within 5 mm/month), however, on the February minimum. But for other individual months, differences are usually as large as 15 mm/month (and can rise up to 35 mm/month) for a seasonal cycle whose amplitude is of the order of 35 to 40 mm/month.

In the eastern South Atlantic, the seasonal cycle of CMAP and NWP products follow each other within 10 mm/month (with a cycle of amplitude of 50 mm/month). COADS-derived products agree with each other within 5 or 10 mm/month, but present a cycle of smaller amplitude (30 mm/month). MSU is again peculiar, close to COADS in fall and to CMAP for the rest of the year.

5.3 Indian Ocean

In the western Indian, the mean seasonal cycle is characterised by two periods of high precipitation in May–July and November–December in every data set. Most data sets agree on the amplitude of the cycle (around 60 mm/month) except the two NWP products (80 mm/month for ECMWF and 100 mm/month for NCEP). COADS-derived products are very similar to each other (agreement better than 5 mm/month for every individual month) and are close to satellite products CMAP and MSU.

In the eastern Indian, agreement between data sets is found only for the first 5 months of the year (January to May), a period that includes the occurrence (in March) of the low *P* anomalies. For the rest of the year, there is no obvious coherence in the month-to-month variations of the various data sets, which may differ one from each other by 10 to 20 mm/month (and sometimes over 30 mm/month for MSU) for an amplitude of the cycle which is of the order of 50 mm/month or less (for SOC).

In the southern Indian, the seasonal cycle is characterised by a regular decrease of *P* from its maximum in February to its minimum in September or October. Only UWM shows a significantly different cycle, placing the rainy season between May and July. Despite this qualitative agreement in the phase of the cycle, a large disagreement remains on the amplitude, which varies from 30 to 50 mm/month, according to data sets. MSU and CMAP are almost identical from January to August, but diverge by more than 10 mm/month the rest of the year.

5.4 Southern Ocean

In the Southern Ocean, CMAP and NCEP show a seasonal cycle in good agreement (5 mm/month or better), as expected at high latitudes. Both show regular variations from a dry summer season (November to January) to a rainy period in June and July. However, NCEP cycle has greater highs and smaller lows; thus, its amplitude (30 mm/month) exceeds that of CMAP by 10 mm/month. ECMWF lags by a month and presents a doubtfully low *P* anomaly in February. Its amplitude is similar to that of NCEP. Both COADS-derived data sets do not reproduce this smooth seasonal cycle, presenting a significant month-to-month noise. MSU is not coherent at these high latitudes.

5.5 Remarks

The agreement between data sets in their representation of the climatological seasonal cycle remains very qualitative and is generally better on the phase than on the amplitude. Considering that the above analysis has been made on quantities integrated over large spatial areas and averaged over 14 years, it is not encouraging to find discrepancies of the order of 20 mm/month (20% or more of the amplitude of the seasonal cycle).

A remarkable agreement is sometimes observed, like between SOC and CMAP in the western Indian, between ECMWF and SOC in the western North Atlantic, or between ECMWF and NCEP in the northern North Atlantic. But these appear as exceptions.

UWM and MSU are the two data sets which differ most often from the others. The best consistency is generally found between the two NWP products and the satellite CMAP product, especially in the regions of low *P* of the eastern mid-latitude ocean basins (in both hemispheres) and in equatorial regions.

6 Interannual variability

6.1 Observation of peculiar events

Peculiar events have been observed during the 1993–1996 period in the tropical Pacific Ocean using TOPEX or GPCP estimates of *P* (Quartly et al. 1999). These events are the splitting of the ITCZ in March–April, and the cut of the

SPCZ in July–August. These events are not present every year. In this section, we investigate the splitting of the ITCZ in March 1993.

According to Quartly et al. (1999) and as noticed in TOPEX and GPCP in March–April in 1993–1996, the distribution of precipitation shows two zonal bands, one along 8°N and another (with lower values of *P*) a few degrees South of the equator. These two bands of high precipitation in the eastern Pacific were interpreted as resulting from a temporary split of the ITCZ.

The distribution of *P* in March 1993 is shown for the various data sets in Fig. 7 and is compared to the *P* fields of GPCP and TOPEX.

We first note that in 1993, this two-band pattern is better marked in GPCP than in TOPEX. It is most marked in the satellite products CMAP, MSU and HOAPS. There is no clear split in any of the COADS-derived data sets (no figure shown for SOC), and we cannot say if it is because of an under-sampling or because of the interpolation procedure. It is reproduced by NWP models, although ECMWF does not show a clear separation of the bands of high *P* as shown in satellite products, and NCEP shows a very wide southern band. The same pattern occurred again in March 1994 in all data sets which had it in 1993 (no figure shown), again well seen in satellite estimates but with different intensity.

Concerning the cutting of the SPCZ, according to the study of Quartly et al. (1999) with the GPCP data set, it was observed to occur in July–August 1993 at about 225°E-30°S, resulting in a second *P* maximum centred at 250°E-30°S. This pattern is relatively well-seen in August 1993 in every satellite-based *P* estimate and is also reproduced by NWP models (no figure shown). COADS-derived products do not reproduce this event, showing a limitation to reproduce regional events at the interannual time scale.

6.2 Low-frequency variability

In this section, we proceed to a comparison of the low-frequency variability of the *P* estimates provided by the six data sets covering the common 14-year period 1980–1993.

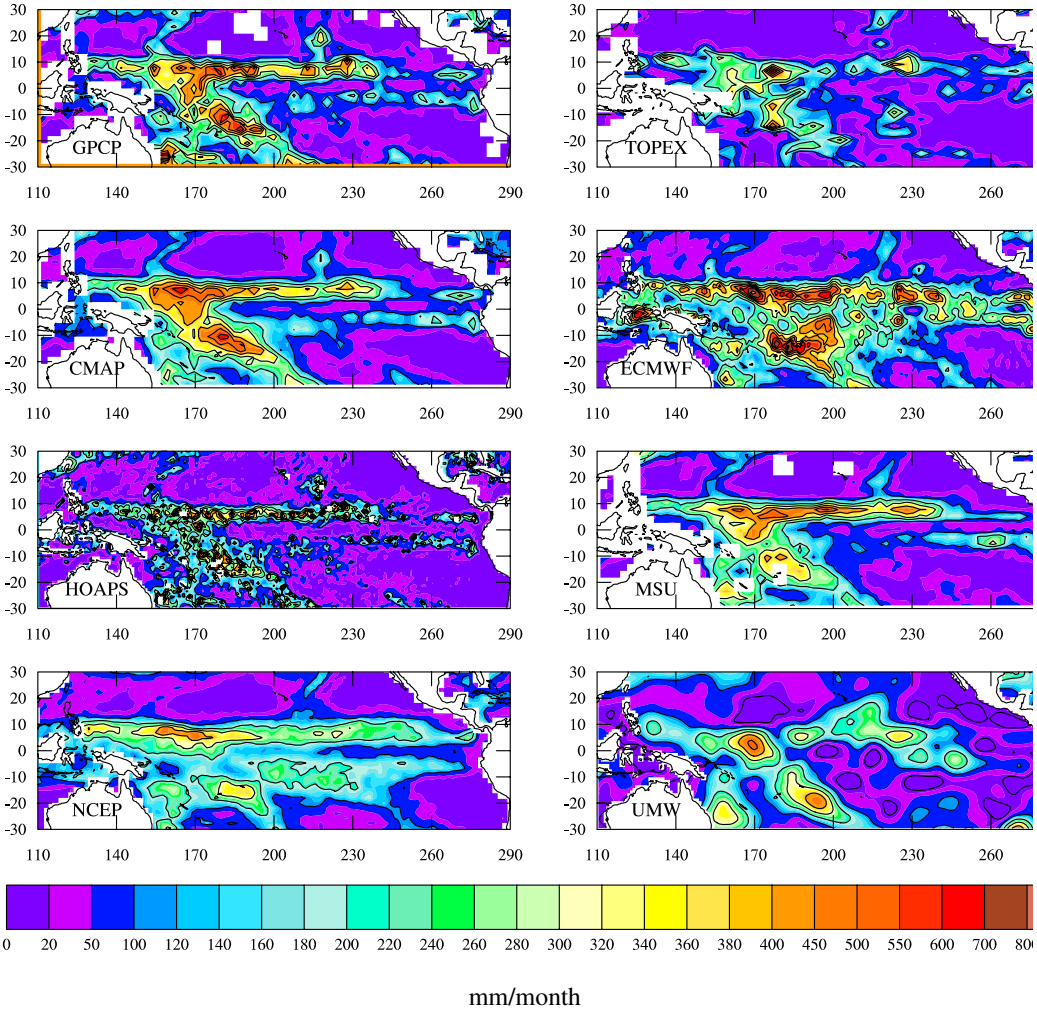

Fig. 7 Monthly precipitation over the equatorial Pacific Ocean in March 1993 for eight data sets. The *colour bar* ranges from 0 to 900 mm/month with irregular spacing. Contour intervals in *dark lines* range from 0 to 800 mm/month with a regular spacing of 100 mm/month

Low-frequency anomalies of P over the 16 areas defined in Fig. 3 are obtained as follows: The climatological mean is subtracted from the 14-year long monthly mean time series, and a 12-month running average is performed, followed by single Hanning filter. The resulting time series are shown in Fig. 8. Due to the smoothing applied, series

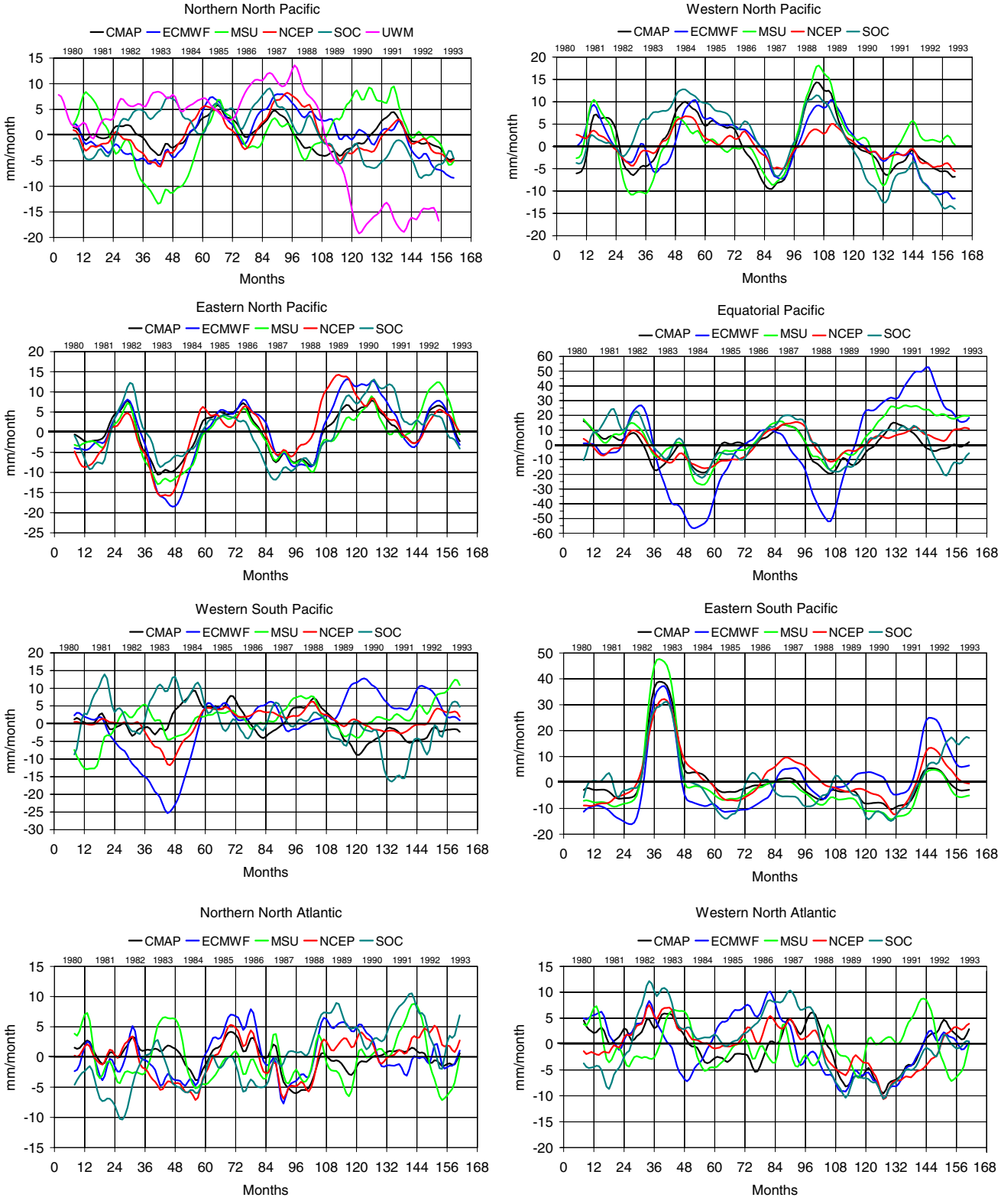

Fig. 8 Monthly mean time series of low frequency precipitation anomalies over the period 1980–1993 for the 16 ocean regions defined in Fig. 3, for the six data sets having the period 1980–1993 in common

Fig. 8 (continued)

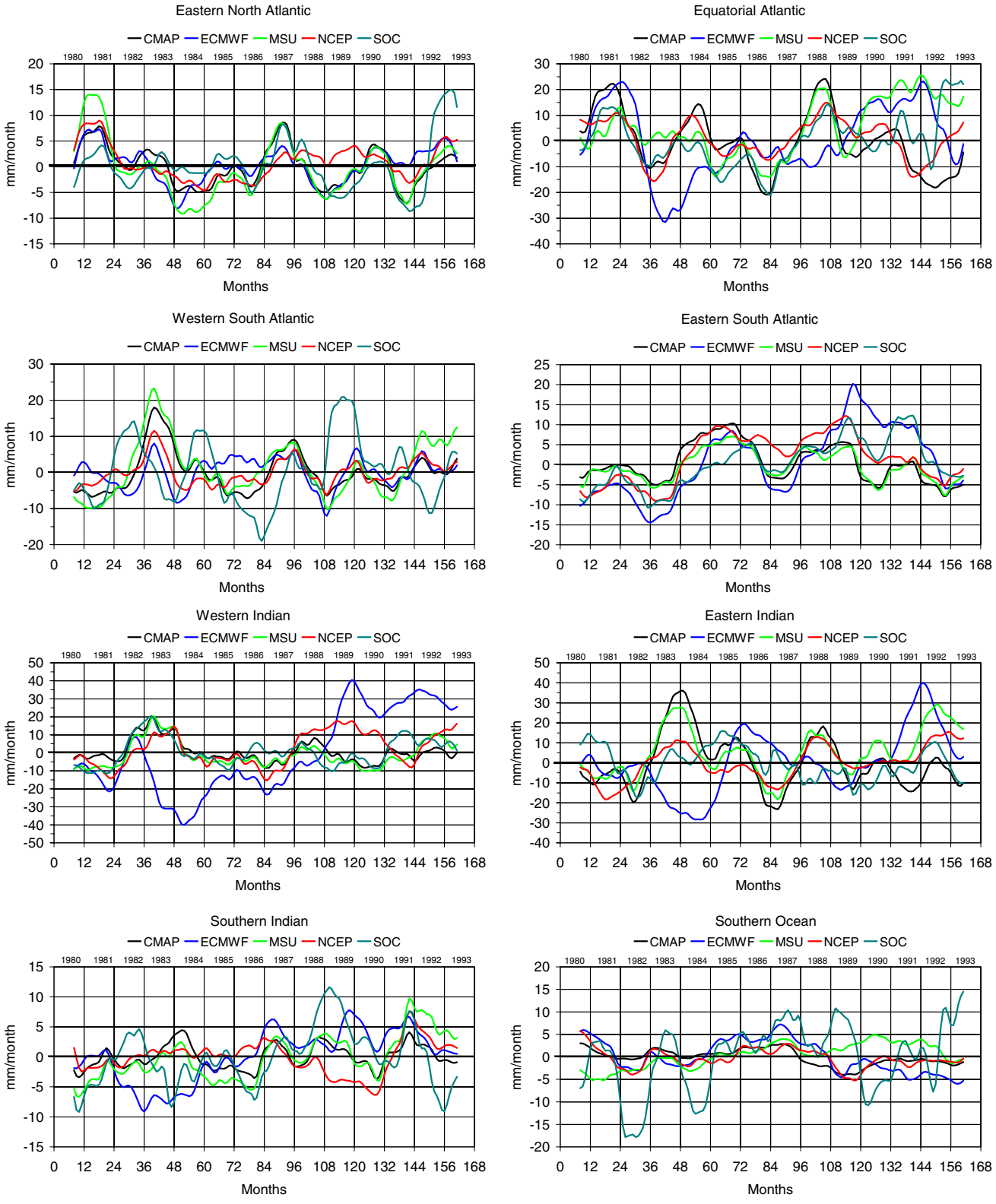

are not complete in 1980 and 1993. Note that the correlation coefficients between all series are shown for all regions in Table 3. In the following, we consider that two series are well-correlated when the correlation coefficient is above the 99% significance level and the variance explained by this correlation is above 50% (i.e. correlation coefficient above 0.7).

UWM, whose record begins in 1945, suffers from two different processing algorithms before and after 1989. Starting in 1989, monthly mean anomalies have been calculated from the mean of 1945–1989 and not for the whole data record. The effect of this is a shift of the series in 1989, as shown in the first plot of Fig. 8 (for the NNP region). It is therefore meaningless to investigate the interannual variability of this data set, which will not be shown in the other regions in Fig. 8. It will not be discussed any longer in this section. It is clear that it should not be used for any purpose related to interannual variability.

6.2.1 Pacific Ocean

In the western North Pacific, the phase of the low-frequency *P* anomalies compares rather well among data sets. Occurrences of periods of positive anomalies in 1981, 1984–1986 and 1988–1989, and of negative anomalies in 1982–1983, 1986–1987 and 1990–1993 are shared by all data sets. Correlation coefficients between series (Table 3) are generally high (i.e. above the critical value of 0.7). The highest correlation is obtained between the two NWP products ECMWF and NCEP (0.88), and the lowest between MSU and SOC (0.38) and MSU and ECMWF (0.57). Note, however, that MSU is well-correlated with the

Table 3 Correlation coefficients between the low frequency anomalies of CMAP, ECMWF, MSU, NCEP and SOC over the period 1980–1993

	CMAP	ECMWF	MSU	NCEP	SOC
	Northern North Pacific NNP				
CMAP		0.59	0.41	0.65	0.36
ECMWF	0.81		0.42	0.85	0.39
MSU	0.81	0.57		0.21	-0.45
NCEP	0.83	0.88	0.62		0.39
SOC	0.75	0.75	0.38	0.79	
	Western North Pacific WNP				

	CMAP	ECMWF	MSU	NCEP	SOC
	Eastern North Pacific ENP				
CMAP		0.94	0.91	0.82	0.80
ECMWF	0.59		0.86	0.88	0.77
MSU	0.77	0.89		0.70	0.71
NCEP	0.68	0.72	0.83		0.64
SOC	0.73	0.43	0.53	0.60	
	Equatorial Pacific EP				

	CMAP	ECMWF	MSU	NCEP	SOC
	Western South Pacific WSP				
CMAP		-0.30	0.09	0.19	0.40
ECMWF	0.75		0.08	0.66	-0.53
MSU	0.99	0.76		0.37	-0.16
NCEP	0.91	0.83	0.91		-0.16
SOC	0.81	0.70	0.81	0.75	
	Eastern South Pacific ESP				

The 99% significance level estimated through the z-Fisher transform (von Storch and Zwiers 1999) is 0.21

Table 3 (continued)

	CMAP	ECMWF	MSU	NCEP	SOC
	Northern North Atlantic				
CMAP		0.44	0.48	0.52	-0.10
ECMWF	0.48		-0.10	0.77	0.21
MSU	0.11	-0.08		0.05	0.29
NCEP	0.75	0.62	-0.21		0.29
SOC	0.66	0.57	-0.09	0.88	
	Western North Atlantic WNA				
	CMAP	ECMWF	MSU	NCEP	SOC
	Eastern North Atlantic ENA				
CMAP		0.72	0.93	0.64	0.56
ECMWF	0.10		0.81	0.55	0.41
MSU	0.16	0.48		0.80	0.49
NCEP	0.76	0.12	0.11		0.41
SOC	0.35	0.29	0.64	0.51	
	Equatorial Atlantic EA				
	CMAP	ECMWF	MSU	NCEP	SOC
	Western South Atlantic WSA				
CMAP		0.29	0.90	0.79	0.05
ECMWF	0.37		0.35	0.48	-0.21
MSU	0.95	0.45		0.79	-0.04
NCEP	0.73	0.70	0.79		0.11
SOC	0.33	0.88	0.48	0.68	
	Eastern South Atlantic				

Table 3 (continued)

	CMAP	ECMWF	MSU	NCEP	SOC
	Western Indian WI				
CMAP		-0.23	0.87	0.34	0.65
ECMWF	-0.51		-0.05	0.45	0.12
MSU	0.68	0.03		0.42	0.78
NCEP	0.54	0.05	0.88		0.15
SOC	0.23	0.08	0.08	-0.13	
	Eastern Indian EI				
	CMAP	ECMWF	MSU	NCEP	SOC
	South Indian SI				
CMAP		0.13	0.77	0.36	0.37
ECMWF	0.68		0.41	-0.04	0.33
MSU	-0.21	-0.11		0.44	0.39
NCEP	0.75	0.70	-0.09		-0.22
SOC	0.00	0.17	0.29	0.27	
	Southern Ocean SO				

other satellite product CMAP. The amplitudes of the peaks and troughs of the anomalies vary significantly (5 to 10 mm/month) from one data set to another, but no systematic difference is observed according to the origin of the data. For example, the positive *P* anomaly of 1983–1985 is the largest in SOC, it is comparable in CMAP and ECMWF, and it is the smallest in NCEP and MSU. In the following period of positive anomalies in 1988–1989, the two satellite products are above all the others, SOC and ECMWF are similar, and NCEP is again the smallest. In general, inter-annual variations are of the order of 15 to 25 mm/month (from peak to trough) to be compared to a climatological annual mean of the order of 110 mm/month (or 1,300 mm/year, Fig. 5).

Other regions of the Pacific where the low-frequency variability of *P* appears to be in agreement between data sets are the eastern North Pacific, the equatorial Pacific and the eastern South Pacific. In these regions, and as already noticed in the western North Pacific, the various data sets agree roughly about the occurrence of the periods of high and low *P*, generally in a tight relation with the occurrence of El Nino (1982–1983, 1986–1987 and 1991–1992) and La Nina (1983, 1988–1989) events. Correlation coefficients obtained from the time series of *P* anomalies are high and comparable to those obtained in the western North Pacific, best correlation being noticed in the eastern North Pacific. However, each region has peculiarities, so conclusions drawn for one region often do not hold for another.

In the equatorial Pacific for example, the amplitude of inter-annual variations of *P* is of the order of 20 mm/month. ECMWF exhibits variations, which are three times those of the other data sets. Therefore, the good agreement noticed in the western North Pacific between the two reanalysis products and the CMAP satellite product does not hold for this region, which is characterised by a good agreement in phase and amplitude (often within 5 mm/month) between the NWP products and the MSU product (correlation coefficient above 0.80).

The northern North Pacific and the *western South Pacific* are regions where the correlation coefficients obtained from the time series of *P* anomalies are low, especially in the western South Pacific (Table 3). For the northern North Pacific, the best agreement is found between NWP (0.85). In the western South Pacific, no significant phase agreement is noticed between any series, even between data sets having the same source (no

correlation coefficient above 0.7 for that region in Table 3). It is striking to note how the two satellite products are different. SOC and ECMWF are generally out of phase (correlation coefficient is −0.53). The best phase agreement is found between ECMWF and NCEP (correlation coefficient of 0.66). All data sets agree on the amplitude of the interannual variations, which ranges between 5 and 10 mm/month, except for ECMWF, for which anomalies are once again three times greater.

6.2.2 Atlantic Ocean

Correlation coefficients between time series anomalies are smaller in the Atlantic than in the Pacific, indicating a lesser agreement between data sets.

The western North Atlantic is a good example of the kind of agreement and disagreement that can be observed. A first glance at the low-frequency anomalies of *P* in this region suggests a rough agreement between data sets about periods of *P* excess in 1982–1983, 1985–1988 and 1991–1993, and periods of *P* deficit in 1984–1985 and 1989–1991. A closer analysis shows that the agreement between the various time series is highly variable according to the period considered. The period of negative precipitation anomalies of 1989–1991 is seen in all data sets (except MSU), which agree within a few millimetre per month. They describe a sharp decrease of precipitation in 1988, which leads to a deficit in precipitation of nearly 10 mm/month in 1989 and 1990, followed by an increase in 1991, with year 1992 showing a small excess in *P* (5 mm/month). On the contrary, differences between data sets are numerous during the 5-year period 1983–1987. ECMWF shows a strong decrease of precipitation in 1983 (from +7 to −7 mm/month). A similar decrease is seen in the other data sets, shifted by half a year in MSU and by a year in CMAP, SOC and NCEP. The period of low *P*, which follows this decrease, is also differently represented by the various data sets. It barely lasts a year in ECMWF, whose anomalies turn positive again at the end of 1984, but lasts for 2 years (1984–1985) in NCEP and SOC and almost 3 years (1984–1986) in CMAP.

Again, it was not possible to extract a typical behaviour of the low-frequency variability according to the source of the data. Indeed, the data sets that appear the most in agreement with each other over the whole 14-year period in this area are SOC and NCEP (correlation coefficient is 0.88).

In the equatorial Atlantic, the only data sets that appear coherent for the whole period are CMAP and NCEP. Both are basically in phase, and their differences mainly lie in the amplitude of the anomalies, which are greater (often double) in CMAP. The correlation coefficient of the two series is 0.76. As shown in Table 3, correlations between the time series of *P* anomalies for this region are pretty low, despite a correlation of 0.64 between SOC and MSU. As it appears in Fig. 8, if the various data sets are able to agree on a few specific events of excess or deficit in precipitation, they do not do so over the whole record. ECMWF for example is catching the *P* excess of 1981–1982 and the *P* deficit of 1983 (although it clearly overestimates its amplitude), but is missing the excess in *P* of 1988, which every other data set exhibits. A striking example of disagreement between data sets from the same origin is given in 1991–1992, a period when a satellite product (MSU) and a re-analysis product (ECMWF) both suggest an excess in *P* (over 20 mm/month), whereas another satellite product (CMAP) with another re-analysis product (NCEP) show a deficit (of 15 to 20 mm/month).

The eastern South Atlantic, at the eastern side of a mid-latitude ocean basin, is characterised by a strong atmospheric subsidence and low precipitation (25 to 35 mm/month in annual mean depending on the data set—see Fig. 5). Therefore, as shown in Fig. 8, the amplitude of the low-frequency variations (5 to 10 mm/month) can reach a significant fraction of the mean. Despite large differences in long-term trends (small and negative in the satellite products, large and positive in the other products), there is a good agreement in the phase between all data sets. Agreement between the two satellite products CMAP and MSU is remarkable in the phase (correlation is very high, 0.95) but also in amplitude (except for a 2-year period in 1984–1985). All data sets agree about the periods of precipitation deficit between 1980 and 1983, in 1987 and between 1992 and 1993. They also agree about two periods of excess precipitation between 1984 and 1986, and between 1988 and 1989. Note that NCEP merges these two periods in a single long one of 7 years of *P* excess. As for all regions, which show a reasonable agreement in the phase, significant differences (5 mm/month or more) are often found in the amplitude of the anomalies. Among all data sets, ECMWF is again the one that shows the largest anomalies.

6.2.3 Indian and Southern Oceans

In the Indian Ocean, discrepancies between data sets are large. The two satellite products CMAP and MSU are the only ones to be in agreement with each other and well-correlated over the whole period (Table 3). In the western and the eastern Indian, NCEP is comparable to the satellite products between 1980 and 1988 but is very different later on. It is different in the southern Indian, where agreement is null before 1987 and is rather good in phase but not in amplitude (too large) after that date. SOC low-frequency variability follows the satellite products in the western Indian (correlation of 0.65 with CMAP and 0.78 with MSU) but is very different from all the other data sets in the eastern Indian and the south Indian. ECMWF low-frequency anomalies do not show similarities with any other data set, with fairly small (when not negative) correlation with other data sets (Table 3), and amplitudes of 40 mm/month when the other data sets have amplitudes of 20 mm/month.

In the Southern Ocean, a good agreement is found between CMAP and NCEP (as expected at high latitudes

by construction of CMAP), but also between these data sets and ECMWF. All suggest small-amplitude, low-frequency variations (3 to 5 mm/month, although higher in ECMWF), with a period of excess precipitation between 1984 and 1987, and a longer period of deficit between 1988 and 1993. SOC is not coherent with the other data sets (see Table 3), being dominated by large changes of 10 to 20 mm/month from year to year. MSU does not have enough data at high latitudes to be compared.

7 Satellite products HOAPS and GPCP

Because the HOAPS and GPCP data sets do not cover the common 1980–1993 period, they were not included in the above comparison. Nevertheless, these data sets have a significant period in common with CMAP (see Table 2): 7 years for HOAPS (from 1992 to 1998) and 8 years for GPCP (1988 to 1995). In this section, we compare these two satellite products with the merged CMAP product over their respective common periods.

7.1 Regional budgets

The spatial patterns of precipitation of these data sets have been described and compared to all the other *P* fields in Section 3. The focus of this section is on regional budgets of the mean precipitation.

Figure 9 shows the average mean precipitation over each of the 16 ocean regions defined in Fig. 3, for GPCP and CMAP (mean for 1988 to 1995) and for HOAPS and CMAP (mean for 1992 to 1998). The 14-year mean of CMAP (1980–1993), which was compared to the other *P* estimates in the previous sections, is also reported.

The first remark is that CMAP varies very little (by just a few percent) from one period to another in all regions, with two exceptions, where changes are 10% or more. The first one is the eastern South Pacific, where CMAP shows for the period 1980–1993 a mean value of *P*, which is 51 mm/year greater than in 1988–1995. As this region is characterised by low *P*, this represents a relative increase of 19%. This is easily explained by the greater number of El Nino events included in the 1980–1993 period, these events having an impact on the precipitation budget of this region of usually low *P*. The second is the western Indian, where CMAP shows for the period 1980–1993 a mean value of *P*, which is 94 mm/year (10%) smaller than in 1992–1998. Therefore, it seems reasonable to consider that the results drawn from the previous sections, where the six data sets covering the 1980–1993 period have been compared, can be extended and used in the present comparison between CMAP, HOAPS and GPCP.

GPCP and CMAP are very comparable, and the mean *P* values they propose agree within 10% or better in most regions. The largest disagreement is found in the two regions that show *P* values of the order of 2,000 mm/year or higher.

In the eastern Indian, GPCP proposes a mean *P* value which is 15% smaller than the one proposed by CMAP for the same period. Note that in this region, CMAP values are the highest among all climatologies (see Fig. 5), and GPCP appears, with nearly 2,000 mm/year, to lie between the NWP products that are above this value and the COADS-derived products that are close to 1,800 mm/year.

In the equatorial Pacific, GPCP is smaller by 10% than CMAP. With again nearly 2,000 mm/year, it compares very well with SOC, MSU and NCEP (Fig. 5).

The only regions where GPCP significantly exceeds CMAP (by nearly 10%) are the western mid-latitude ocean

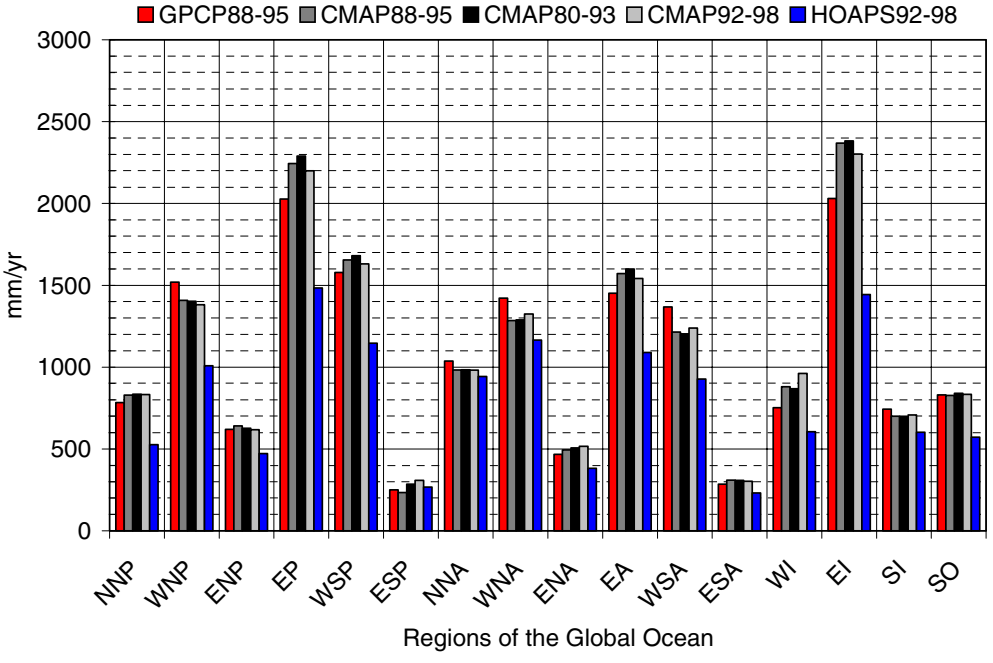

Fig. 9 Spatial average of the mean precipitation (in millimetre per year) for every ocean region defined in Fig. 3, for the CMAP, GPCP and HOAPS data sets. For the purpose of comparison, mean precipitation is calculated for the period 1988–1995 for GPCP (*red*) and CMAP (*dark grey*), for the period 1992–1998 for HOAPS (*blue*) and CMAP (*light grey*). The value obtained for CMAP averaged over the 1980–1993 is shown in *black*

basins (WNP, WNA and WSA), where air–sea interactions are greatly influenced by warm poleward western boundary currents (the Kuroshio Current in the WNP, the Gulf Stream in the WNA and the Brazil Current in the WSA). Thus, GPCP is the data set, which proposes the highest precipitation with MSU and CMAP in these regions (see also Fig. 5).

In every other region, comments made about CMAP in Section 4 hold for GPCP, the two data sets being very similar.

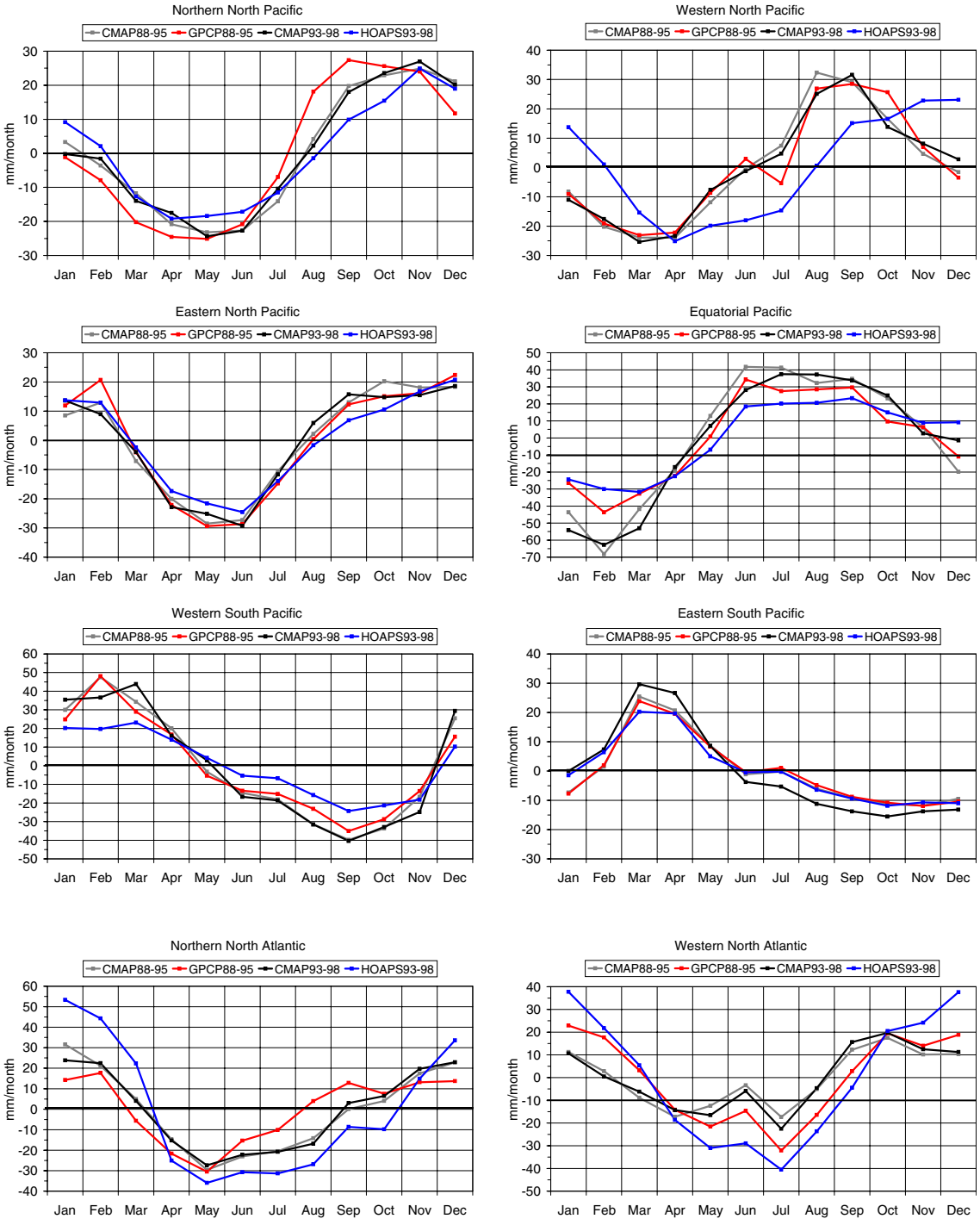

Fig. 10 Climatological seasonal cycle of precipitation (i.e. monthly mean precipitation anomalies) for the 16 ocean regions defined in Fig. 3, for the CMAP, GPCP and HOAPS data sets. Time means used to calculate this cycle (following the same method as for Fig. 6) were performed over periods common to these data sets to make direct comparisons relevant. The seasonal cycles of GPCP (*red*) and CMAP (*grey*) are relative to 1988–1995 and that of HOAPS (*blue*) and CMAP (*black*) to 1992–1998

Fig. 10 (continued)

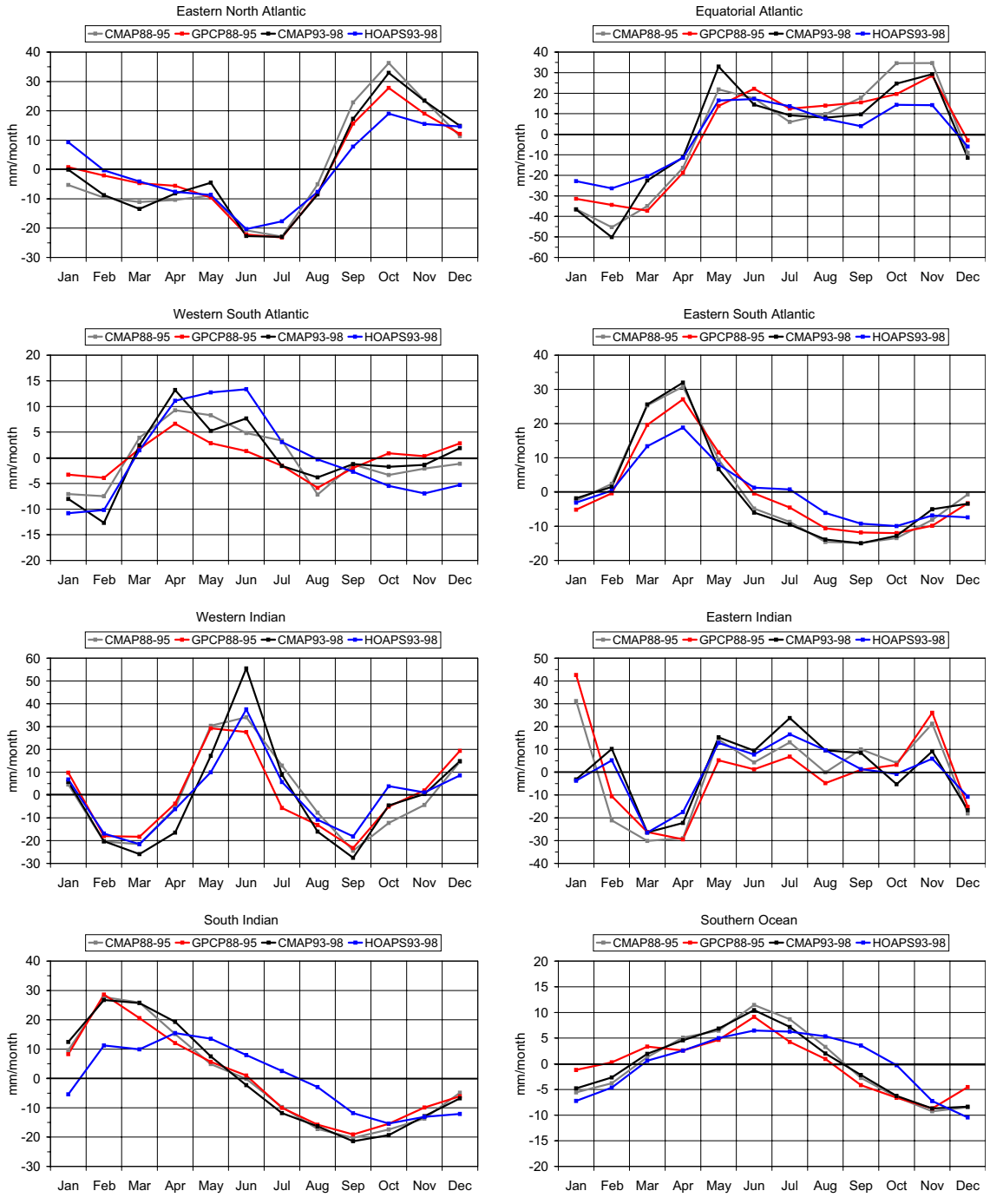

HOAPS shows precipitation values that are systematically and significantly smaller than CMAP and GPCP in every region (30% in average over all regions). Underestimation is especially large in tropical regions (by 800 mm/year in the eastern Indian, 700 mm/year in the equatorial Pacific, 500 mm/year in the equatorial Atlantic and the western South Pacific). HOAPS *P* estimate is comparable to other estimates only in the northern North Atlantic and in the region of low *P* of the eastern South Pacific and South Atlantic. This suggests a systematic bias towards low values (i.e. underestimation) in this data set.

7.2 Seasonal variability

The climatological seasonal cycle of precipitation (i.e. monthly mean precipitation anomalies) is shown in Fig. 10 for the 16 ocean regions. The seasonal cycle of GPCP has

been calculated relative to the period 1988–1995 and that of HOAPS for 1992–1998. The seasonal cycle of CMAP for these two periods is reported for comparison.

GPCP cycle follows the cycle of CMAP in almost every region. The northern North Pacific, where CMAP is largely influenced by NCEP values, is the region where HOAPS differs most (over the same period). It shows a cycle slightly shifted, extremes occurring earlier in the year. In the equatorial Pacific, the February minimum is smaller by 30 mm/month in GPCP, and a difference of nearly 10 mm/month is found in July and October. Elsewhere, both data sets agree within a few millimetre per month and always better than 5 mm/month. Considering the generally poor agreement noticed between data sets, we could qualify such agreement as very good and this is likely due to the important weight of satellite observations in both data sets.

HOAPS cycle is in phase with CMAP in most regions with a few exceptions. In the western North Pacific, the spring minimum is delayed by a month (from March to April) and so is the shift from the dry season to the wet season by 2 months (June in CMAP and August in HOAPS). In the western South Atlantic, the *P* maximum of the wet season is shifted from April to June. The southern Indian and the Southern Ocean are also regions where the phase of the seasonal cycle is different in HOAPS and CMAP. The amplitude of the seasonal cycle is generally smaller in HOAPS than in any other data set, especially in regions of high precipitation, like the equatorial Pacific (50 mm/month compared to 100 mm/month for CMAP), the western South Pacific or the equatorial Atlantic. The seasonal cycle is also smaller in HOAPS in the regions of subsidence, like the eastern South Pacific and the eastern South Atlantic (not shown). This is consistent with the systematic underestimation of precipitation already noticed for the mean.

7.3 Interannual variability

In this section, we proceed to a comparison of the low-frequency variability of the *P* estimates provided by the HOAPS and GPCP data sets. Figure 11 shows monthly mean time series of low-frequency precipitation anomalies between 1988 and 1998 for the regions defined in Fig. 3. For the period 1988–1995, CMAP and GPCP anomalies are calculated with regard to the 1988–1995 mean. For the period 1992–1998, CMAP and HOAPS anomalies are calculated with regard to the 1992–1998 mean. This explains the offset between the two sets of curve for CMAP. The filtering applied is the same as the one described in Section 6.2. Correlations between the GPCP and CMAP low-frequency time series over their respective periods of comparison are shown in Table 4. Correlation coefficients above 0.3 are above the 99% significance level. In the following, we shall consider that two series are well-correlated when the variance explained by this correlation is above 50% (i.e. coefficient above 0.7).

7.3.1 GPCP low-frequency variability

Interannual variations of the GPCP data set agree rather well with that of CMAP for the same period (1988–1995). Correlation between both series is rather high (0.82 in average for 14 of the 16 ocean regions), and only two regions show insignificant correlation (less than 0.26) (Table 4).

The western South Pacific (Fig. 11) is the region where the agreement between these two time series is the poorest, both signals appearing often out of phase (correlation of 0.11). A poor agreement was already noticed in this region between all *P* estimates in Section 6.2.1, where very small or negative correlation where found (Fig. 8, Table 3). It is clear that the determination of rainfall in this area, dominated by the SPCZ, is particularly difficult by all means.

The Southern Ocean is another region of strong discrepancies between the two data sets (correlation coefficient of 0.26). A strong disagreement was already noticed over the 1980–1993 period between the six data sets compared in Section 6 (small or negative correlation, Table 3), except for CMAP and NCEP, the first being known to be strongly constrained by the latter.

In the other ocean regions, the agreement between GPCP and CMAP low-frequency variability is rather good. Wet and dry periods occur at the same time in both series, although amplitudes may be different. Correlation is generally greater than 0.8 and is remarkably good (0.98) in the eastern South Pacific (Fig. 11, the interannual variability of *P* is characterised by a peak of high *P* in early 1992 associated with the 1991 El Nino) and the eastern South Atlantic. In the equatorial Pacific, the 1991 El Nino is characterised in both data sets by a peak of high precipitation (but with a greater amplitude in CMAP, correlation of 0.80 between both series).

When correlation is below 0.8, like in the northern North Pacific (correlation of 0.71) or the northern North Atlantic (correlation of 0.61), it is because of a disagreement about a peculiar event. In the northern North Pacific for example, the difference between the series occurs in 1993, a year given as wet in GPCP and as dry in CMAP. In the eastern Indian (no figure shown) both series show a very comparable deficit in *P* during the 1991 El Nino (correlation of 0.7). Overall, the agreement of CMAP with GPCP is significantly better than what was noticed with all the other data sets among which it has been compared to in this study.

7.3.2 HOAPS low-frequency variability

Interannual variations in HOAPS are also in very good agreement with that of CMAP for the period 1992–1998. Correlation between the two series for the 16 ocean regions is better in average than for GPCP (Table 4) as a result of a very similar representation of the various wet and dry periods (Fig. 11). However, the amplitude

of the low-frequency anomalies of P is significantly smaller in HOAPS. In the regions strongly marked by the 1997 El Nino, for example, the amplitude of the anomalies associated with this event are smaller by 10 mm/month (equatorial Pacific, eastern South Pacific) to almost 20 mm/month (eastern Indian). This is consistent with a systematic underestimation of precipitation in the HOAPS data set, already noticed on the mean budgets and the seasonal cycle. Exceptions are the northern North Pacific, where the amplitude of the wet period in 1994 is twice larger in HOAPS, and the northern North Atlantic (no figure shown), where HOAPS shows in 1993–1994 a wet period of amplitude greater than 10 mm/month whereas it is below 5 mm/month in CMAP. At these northern latitudes, the fact that NCEP, rather than satellite products, largely influences CMAP may explain this difference.

The western South Pacific is again an area where differences between HOAPS and CMAP are important, as it is between all the data sets considered in this study.

Overall, the low-frequency variability described by the satellite product HOAPS agrees very well with that of the merged product CMAP.

8 Conclusion

The freshwater input in the ocean has such an important impact on the salinity and the density flux at the ocean surface that high-quality precipitation estimates at global scale are needed to undertake almost any realistic ocean circulation studies. However, assessing precipitation over the sea remains a difficult task. This paper intends to contribute to this assessment and has carried out a comparison between several data sets, which are available for use in forcing OGCMs. Rather than focusing on a detailed comparison of every P patterns, the paper concentrates on the P budget (i.e. area average) of large areas relevant to ocean dynamics, like mid-latitude gyres or the equatorial waveguide. The objective is to document differences and similarities to provide information useful in selecting a P field as a component of the freshwater forcing of an OGCM, so we have not undertaken to explain the reasons for the discrepancies which were found. Therefore, this analysis should complement other studies that investigated precipitation over oceans in two ways. First, the comparison is made here over at least a decade between the ten major data sets estimated from all available sources, whereas most studies are limited to just a few data sets or over periods of a few months. Second, the point of view is from the ocean side, with a focus on the precipitation budget over regions relevant to the ocean circulation.

Ten data sets from several sources were gathered from: NWP models (ECMWF and NCEP); in situ data (CCR, SOC and UWM); satellite data (MSU, TOPEX and HOAPS) and composite (i.e. combination of satellite, rain gauge or model) data (GPCP and CMAP). The data sets were compared over 16 relatively large regions, representative of large-scale ocean circulation features, to diagnose biases, trends and behaviours linked to their data source. In general, the results of our analysis are not encouraging because most data sets greatly disagree in many regions. Moreover, no systematic differences between the various data sets according to their source were objectively identified on mean, or seasonal or interannual diagnostics, although agreement subjectively appears to be better between data sets of the same source.

A quantitative approach showed that P budgets over the 1980–1993 period are not homogeneously represented among the various climatologies. More precisely, mean P budgets, which represent the average of P over ocean basins and for relatively long time periods, could differ significantly (by several tens of percent in some cases). Such differences after such space–time integration are still very large because they represent several hundred of millimetre per year and would induce over a long period a drift in the salinity of an ocean gyre.

Concerning the seasonal variability of the monthly climatologies (monthly means over the common period), a better agreement was found in phase than in amplitude except in few geographical regions. Differences in amplitude reached 20 to 30% in regions of moderate P and 50 to 60% in regions of high P during the rainy season. Different behaviours, like a shift of the occurrence of the P maximum/minimum, were not found to be characteristic of a source of data; almost every data set has been found, at least in one of the 16 regions studied, to be not in agreement with the others in its description of the seasonal cycle.

Comparison of low-frequency (interannual) variability also pointed out important differences between data sets. Again, discrepancies are more important on the amplitude

Table 4 Correlation coefficients of the low frequency anomalies of precipitation between CMAP and GPCP over the period 1988–1995 (99% significance level of 0.28), and between CMAP and HOAPS over the period 1992–1998 (99% significance level of 0.30)

	GPCP-CMAP 1988–1995	HOAPS-CMAP 1992–1998
NNP	0.71	0.66
WNP	0.89	0.82
ENP	0.79	0.95
EP	0.80	0.93
WSP	0.11	0.57
ESP	0.98	0.99
NNA	0.61	0.79
WNA	0.93	0.36
ENA	0.88	0.86
EA	0.95	0.94
WSA	0.79	0.34
ESA	0.98	0.94
WI	0.91	0.97
EI	0.70	0.94
SI	0.65	0.60
SO	0.26	0.55

Significance levels are defined according to the z-Fisher transform (von Storch and Zwiers 1999)

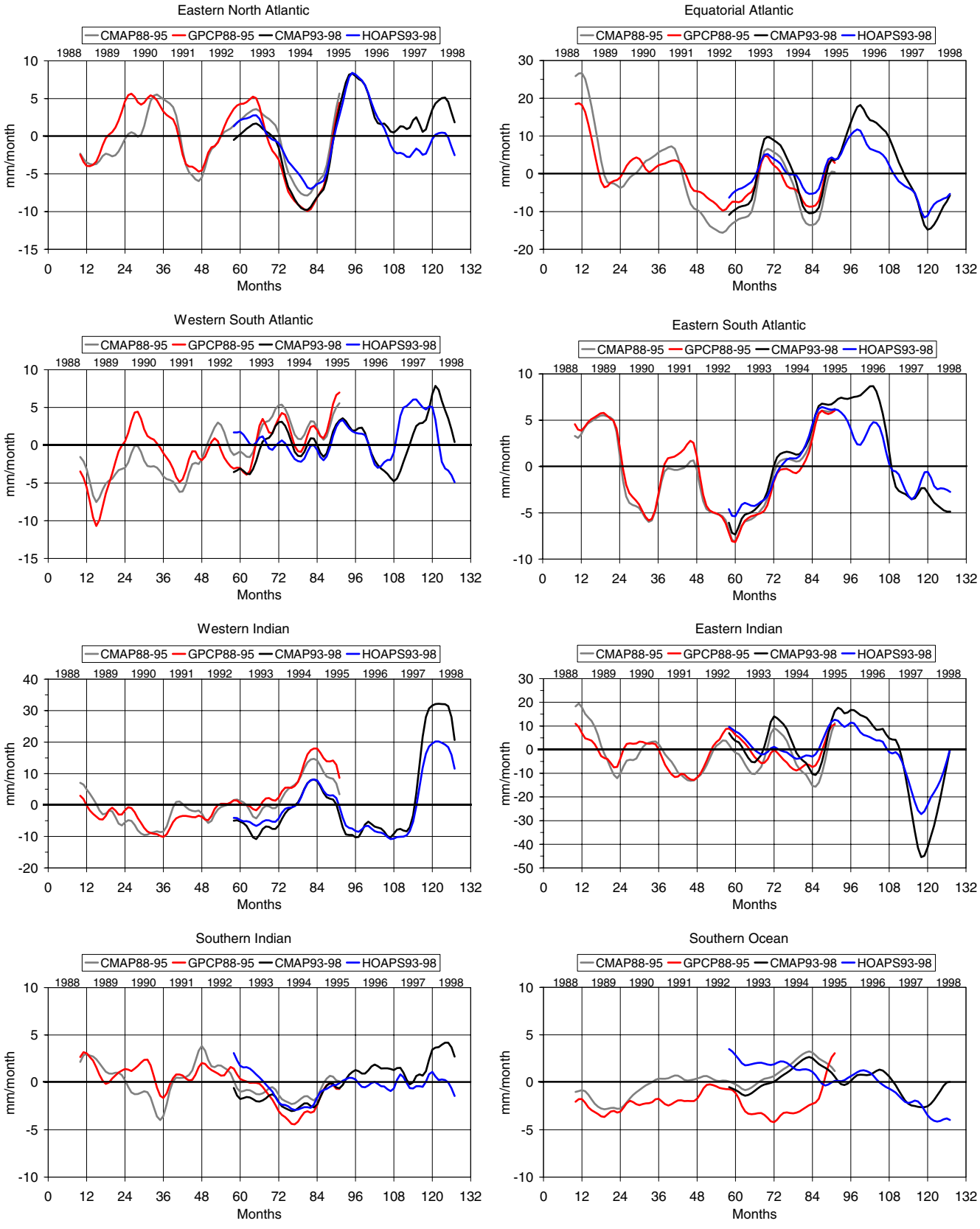

Fig. 11 Monthly mean time series of low frequency precipitation anomalies between 1988 and 1998 for the 16 ocean regions defined in Fig. 3, for the GPCP, HOAPS and CMAP data sets. For the period 1988–1995, CMAP (*grey*) and GPCP (*red*) anomalies are calculated with regard to the 1988–1995 mean. For the period 1992–1998, CMAP (*black*) and HOAPS (*blue*) anomalies are calculated with regard to the 1992–1998 mean. This explains the offset between the two sets of curve

Fig. 11 (continued)

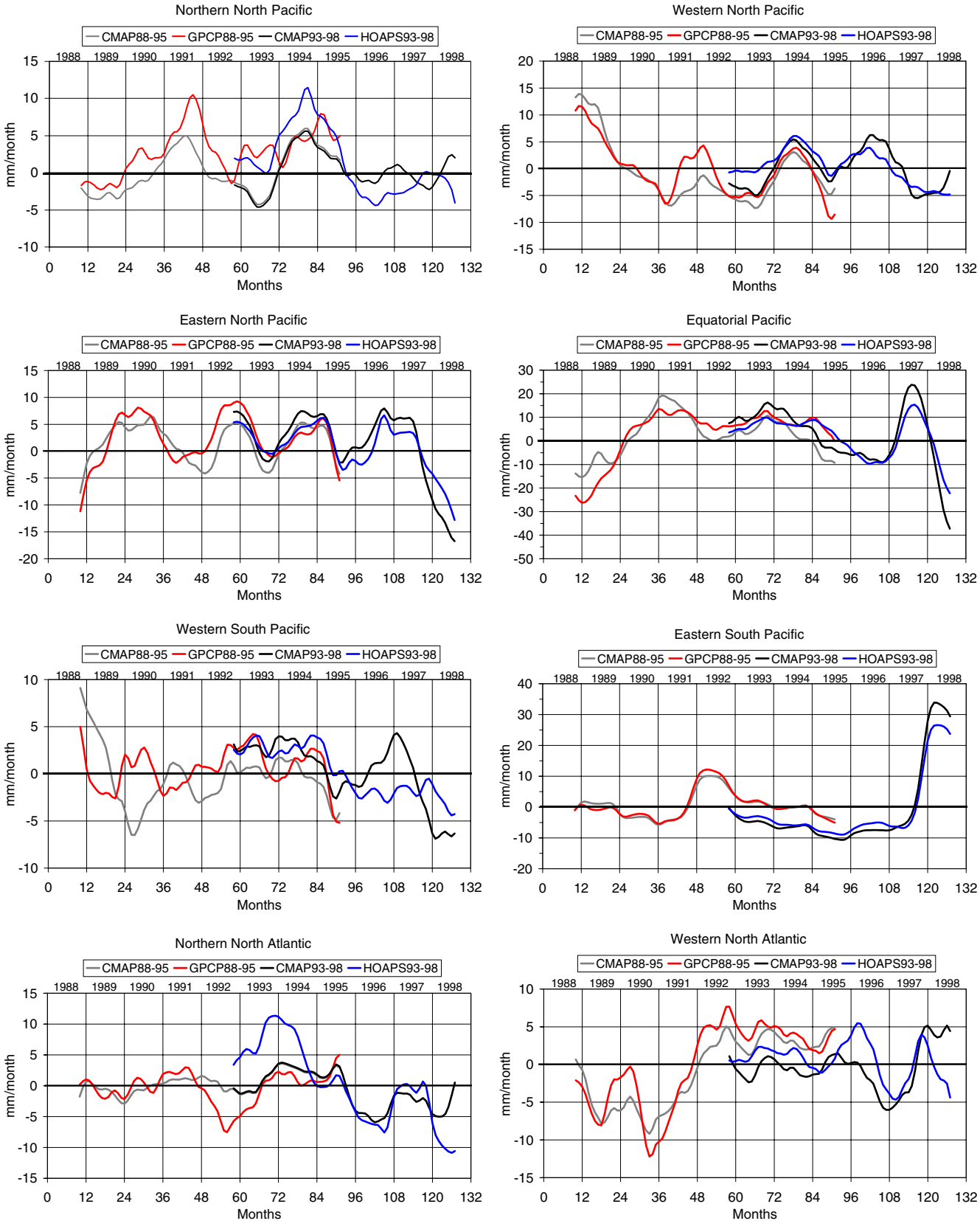

of the variations than on the phase, which generally shows a reasonable agreement. However, we could not find two data sets that agree over the whole period and for every region. Agreement rarely occurs for more than 3 years before an event occurs for which data sets disagree. Nevertheless, some consistent behaviour (for example related to El Nino events) was observed to be common to all data sets. It was also encouraging to find that HOAPS, CMAP and GPCP have a quite comparable interannual variability over their respective common periods, over most (but not all) ocean regions. Again, it was not possible to objectively discriminate the behaviour of the data sets with respect to their source. In general, the Indian Ocean and the Southern Ocean are regions where any consistency between data sets is hard to find, even between data sets of the same source.

It also happened that a specific data set has a behaviour in high disagreement with all the others. It is the case of MSU, which has a very peculiar seasonal cycle, and it is likely biased towards high (low) *P* in the first (second) part of the year in several ocean regions. We noticed that several geographical patterns, well-defined in most data sets, were not represented in in situ (COADS-derived) data sets. This is probably due to a problem in the method of interpolation or a drastic lack of observations. Concerning NWP re-analyses, NCEP shows, in general, a seasonal cycle of small amplitude. On the contrary, ECMWF produces the highest *P* values almost everywhere (and especially in the ITCZ and SPCZ), and has, by far, the largest interannual variations. Several general comments about satellite data are worthy of mention. Compared to the other data sets, they show less *P* in regions of low *P* like the eastern part of the subtropical gyres. However, they may be more correct there, in particular MSU, which is insensitive to non-precipitating cirrus clouds. Also, TOPEX and HOAPS, but to a lesser degree, show lower *P* than others in regions of high *P*. MSU does not follow, because it shows reasonably high values in regions of high *P*. An interesting point is that satellites may capture fine patterns such as the occurrence of the split of the ITCZ in March 1993 or the cut of the SPCZ, which are not present in COADS and not well-reproduced by NWP models, although they assimilate satellite data. Moreover, HOAPS data allows capturing additional *P* patterns due to its highest resolution compared to other data sets.

Composite data (GPCP and CMAP), which combine observations from several satellite and from rain gauges or NWP models, may represent the best recent data set available, despite a possible mean bias in regions of high *P* (CMAP clearly has the highest *P* in western tropics and in the equatorial band). However, these data sets never appear to be really "off" when compared to other data sets over the selected ocean regions, and they appear as the most coherent data sets in terms of seasonal and interannual variability over the period they cover, although this is only quantified by the large correlation coefficient (above 0.8) found between the low-frequency time series. For these reasons, and also because it covers a remarkably long period (20 years), the CMAP product would be our present choice to drive an OGCM. It is also used by Large and Yeager (2004) for the definition of the freshwater component of the diurnal to decadal global forcing for ocean and sea ice models they designed for Coordinated Ocean Reference Experiments.

The agreement noticed between GPCP, CMAP and HOAPS is also quite encouraging, as it suggests that some convergence is occurring despite supposed differences in data source and processing. Nevertheless, satellites do not cover the global ocean and there are still uncertainties linked to empirical algorithms.

Thus, progress in knowledge needs to be continued. Long time series are needed and then reanalysis efforts have to be periodically repeated at NWP. The *P* fields from the most recent NCEP2 and ERA40 re-analyses should be soon included in a similar evaluation study; methods to combine satellite, in situ and model data still have to be developed or improved.

Acknowledgements Authors are supported by CNRS (Centre National de la Recherche Scientifique), MESR (Ministère de l'Enseignement Supérieur et de la Recherche) and RAS (Russian Academy of Science). This work is a contribution to the Clipper project, which got support from INSU (Institut National des Sciences de l'Univers), Ifremer, CNES (Centre National d'Etude Spatiale), SHOM (Service Hydrographique de la Marine), and Météo-France. ECMWF analyses were made available by the AVISO vent-flux database in Toulouse. Finally, we would like to thank colleagues who kindly made their data sets available from the Web.

References

Adler RF, Kidd C, Petty G, Morissey M, Goodman HM (2001) Intercomparison of global precipitation products: the third precipitation intercomparison project (PIP-3). Bull Am Meteorol Soc 82(7):1377–1396

Ballabrera-Poy J, Murtugudde R, Busalacchi AJ (2002) On the potential impact of sea surface salinity observations on ENSO predictions. J Geophys Res 107(c12) 8007. DOI 10.1029/2001JC000834

Barnier B (1998) Forcing the ocean. In: Chassignet and Verron (eds) Ocean modeling and parameterization, vol 516. Kluwer, Netherlands, pp 45–80

Bauer P, Schluessel P (1993) Rainfall, total water, ice water, and water vapour over sea from polarised microwave simulations and special sensor microwave/imager data. J Geophys Res 98:20737–20759. (http://www.hoaps.zmaw.de)

Baumgartner A, Reichel E (eds) (1975) The world water balance. Elsevier, New York, p 179

Béranger K, Siefridt L, Barnier B, Garnier E, Roquet H (1999) Evaluation of operational ECMWF surface freshwater fluxes over oceans during 1991–97. J Mar Syst 22:13–36

Carmillet V, Brankart J-M, Brasseur P, Drange H, Evensen G, Verron J (2001) A singular evolutive extended Kalman filter to assimilate ocean colour data in a coupled physical–biochemical model of the North Atlantic Ocean. Ocean Model 3:167–192

Chen G, Chapron B, Tournadre J, Katsaros K, Vandemark D (1997) Global oceanic precipitation: A joint view by TOPEX and the TOPEX microwave radiometer. J Geophys Res 102:10457–10471

Da Silva A, White G (1996) Intercomparison of surface marines fluxes from the GEOS-1/DAS and NCEP/NCAR reanalyses. In: WCRP workshop on air–sea flux fields for forcing ocean models and validating CGMS, ECMWF, Reading, UK, 24–27 October 1995 (WMO/TD-N. 762)

Da Silva A, Young C, Levitus S (1994) Atlas of surface marine data 1994. In: Anomalies of fresh water fluxes, NOAA Atlas NESDIS 9, vol 4. U.S. Department of Commerce, NOAA, NESDIS. (http://www.nodc.noaa.gov)

Delcroix T, Henin C, Porte V, Arkin P (1996) Precipitation and sea surface salinity in the tropical Pacific Ocean. Deep-Sea Res Part 1 43(C7):1123–1141

Dorman CE, Bourke RH (1978) A temperature correction for Tucker's ocean rainfall estimates. Q J R Meteorol Soc 104:765–773

Erbert EE, Manton MJ, Arkin PA, Allam RJ, Holpin GE, Gruber A (1996) Results from the GPCP algorithm intercomparison program. Bull Am Meteorol Soc 77(12):2275–2887

Font J, Lagerloef G, LeVine D, Camps A, Zanife OZ (2004) The determination of surface salinity with the European SMOS space mission. IEEE T Geosci Remote 42(10):2196–2205

Ferry N, Reverdin G (2004) Sea surface salinity interannual variability in the western tropical Atlantic: an ocean general circulation model study. J Geophys Res 109(C05026). DOI 10.1029/2003JC002122

Garnier E, Barnier B, Siefridt L, Béranger K (2000) Investigating the 15 years air–sea flux climatology from the ECMWF re-analysis project as a surface boundary condition for ocean models. Int J Climatol 20(14):1653–1673

Gibson JK, Kallberg P, Uppala S, Hernandez A, Nomura A, Serrano E (1997) ECMWF re-analysis project report series, ECMWF Report

Glecker PJ, Weare BC (1997) Uncertainties in global surface heat flux climatologies derived from ship observations. J Clim 10:2764–2781

Grassl H, Jost V, Kumar R, Schulz J, Bauer P, Schluessel P (2000) The Hamburg ocean–atmosphere parameters and fluxes from satellite data (HOAPS): a climatological atlas of satellite-derived air–sea-interaction parameters over the oceans Report No. 312, ISSN 0937-1060. Max Planck Institute for Meteorology, Hamburg

Gruber A, Su X, Kanamitsu M, Schemm J (1999) The comparison of two merged rain gauge satellite precipitation datasets. Bull Am Meteorol Soc 81(11):2631–2644

Huffman GJ, Adler RF, Arkin P, Chang A, Ferraro R, Gruber A, Janowiak J, McNab A, Rudolf B, Schneider U (1997) The global precipitation climatology project (GPCP) combined precipitation data set. Bull Am Meteorol Soc 78(1):5–20

Josey SA, Kent EC, Taylor PK (1999) New insights into the ocean heat budget closure problem from analysis of the SOC air sea flux climatologies. J Clim 12:2856–2880. (http://www.soc.soton.ac.uk/JRD/MET/fluxclimatology.html)

Kalnay E, Kanamistu M, Kistler R, Collins W, Deaven D, Gandin L, Iredell M, Saha S, White G, Woolen J, Zhu Y, Cheliah M, Ebisuzaki W, Higgins W, Janowiak J, Mo CK, Ropelewski C, Leetma A, Reynolds R, Jenne R (1996) The NCEP/NCAR reanalysis project. Bull Am Meteorol Soc 77:437–471. (http://www.cisl.ucar.edu/)

Kidds C (2001) Satellite rainfall climatology: a review. Int J Climatol 21(9):1041–1066

Killworth PD, Smeed DA, Nurser AJG (2000) The effects on ocean models of relaxation toward observations at the surface. J Phys Oceanogr 30(1):160–174

Large W, Yeager S (2004) Diurnal to decadal global forcing for ocean and sea ice models: the data sets and flux climatologies. NCAR technical note: NCAR/TN-460+STR. CGD Division of the National Center for Atmospheric Research, Boulder, Colorado

Large WG, Danabasoglu G, Doney SC (1997) Sensitivity to surface forcing and boundary layer mixing in a global ocean model: annual mean climatology. J Phys Oceanogr 27:2418–2447

Legates D, Willmott C (1990) Mean seasonal and spatial variability in gauge-corrected global precipitation. Int J Climatol 10:111–127

Marchesiello P, McWilliams JC, Shchepetkin A (2003) Equilibrium structure and dynamics of the California Current System. J Phys Oceanogr 33:753–783

Quartly GD, Srokosz MA, Guymer TH (1999) Global precipitation statistics from dual-frequency TOPEX altimetry. J Geophys Res 104:31489–31516. (anonymous ftp://ftp.soc.soton.ac.uk, cd pub/TOPEX_GPS)

Rudolf B, Hauschild H, Ruth W, Schneider U (1996) Comparison of rain gauge analysis, satellite-based precipitation estimates, and forecast model results. Ad Space Res 18:53–62

Schmitt RW (1995) The ocean component of the global water cycle. (US national report to International Union of Geodesy and Geophysics 1991–94). Rev Geophys 33(Supplement, Pt. 2): 1395–1409

Siefridt L, Barnier B, Béranger K, Roquet H (1999) Evaluation of ECMWF surface heat fluxes as a thermal ocean forcing in relation to model parameterisation changes during the period 1986 to 1995. J Mar Syst 19:113–135

Smith RD, Maltrud ME, Bryan FO, Hecht MW (2000) Numerical simulation of the North Atlantic Ocean at 1/10°. J Phys Oceanogr 30:1532–1561

Speer K, Tziperman E (1992) Rates of water mass formation in the North Atlantic Ocean. J Phys Oceanogr 22:93–104

Spencer RW (1993) Global oceanic precipitation from the MSU during 1979–91 and comparisons to other climatologies. J Clim 6:1301–1326. (http://ingrid.ldeo.columbia.edu/SOURCES/.NASA/.msu)

Tiedtke M (1993) Representation of clouds in large-scale models. Mon Weather Rev 121:3040–3061

Tréguier AM, Boebel O, Barnier B, Madec G (2003) Agulhas eddy fluxes in a 1/6° Atlantic model. Deep-Sea Res Part 2 50:251–280

Tucker GB (1961) Precipitation over the North Atlantic Ocean. Quart J Roy Meteor Soc 87:147–158

von Storch H, Zwiers FW (1999) Statistical analysis in climate research. Cambridge Univ. Press, Cambridge, UK, pp 503

WCRP-115 (2001) World Climate Research Programme/Scientific Committee on Oceanic Research (WCRP/SCOR) Workshop on Intercomparison and validation of ocean–atmosphere flux fields, Bolger Center, Potomac, MD, USA, 21–24 May 2001. In: White G (ed) WMO-TD-N° 1083

White GH (1995) An intercomparison of precipitation and surface fluxes from operational NWP analysis/forecast systems, Report N°22, WMO/TD-N723

Willebrand J, Barnier B, Claus BN, Dieterich C, Killworth PD, Le Provost C, Yanli Jia J-M, Molines J-M, New AL (2001) Circulation characteristics in three eddy-permitting models of the North Atlantic. Prog Oceanogr 8(2–3):123–161

Woodruff SD, Slutz RJ, Jenne RL, Steurer PM (1987) A comprehensive ocean atmosphere data set. Bull Am Meteorol Soc 68:1239–1250

Xie P, Arkin PA (1997) Global precipitation: a 17-year monthly analysis based on gauge observations, satellite estimates, and numerical model outputs. Bull Am Meteorol Soc 78(11):2539–2558. (anonymous ftp://ftp.ncep.noaa.gov, cd pub/precip/cmap/monthly)

TECHNICAL ANNEX 1

A Climatology of runoff for the global ocean-ice model ORCA025

Technical note

August 2006

A climatology of runoff for the global ocean-ice model ORCA025

Romain Bourdallé-Badie* and Anne Marie Treguier †

Mercator-Ocean reference : MOO-RP-425-365-MER
august 2006

1 Introduction

This note documents the runoff forcing for the DRAKKAR version of ORCA025 as well as the new (2006) version of the MERCATOR ORCA025 "POG" prototype. It is based on the report written by R. Bourdallé-Badie (2005) which describes the global 1/4° version as well as the global 1/12° version. The basic assumption (usual in global ocean models) is that the runoff enters the ocean at the surface, as rain.

2 Input data

The runoffs data file comes from the Dai and Trenberth study[1]. It is documented in a publication (Dai and Trenberth, 2002, hereafter DT02). The spatial resolution of this file is $1^\circ \times 1^\circ$ with monthly data. This data are available on the web : http ://www.cgd.ucar.edu/cas/catalog/dai/

In the past (in the case of the CLIPPER model for example, Treguier et al, 2001), runoff inputs in ocean models were based on UNESCO data for the major rivers. The 50 to 100 largest rivers contribute only about half the total runoff ; to reach a reasonable total of about 1.2 Sv it is necessary to take into account the contribution of small (and often ungauged) rivers, that we call here the "coastal runoff". As an example, a first runoff file was calculated by Edmée Durand (2003) at MERCATOR based on 67 rivers plus the Antarctic coastal runoff. The total runoff in this file was 0.65 Sv, which is not enough. The Dai and Trenberth dataset has the advantage to provide monthly values of runoff that take into account both the major rivers the coastal runoff. A similar dataset is provided by Large and Yeager (2004) as part of the CORE forcing but it does not include an annual cycle and the repartition of coastal runoff is more arbitrary (less well localized).

One drawback of the Dai and Trenberth dataset is that the reference to specific rivers is lost. There are 3556 grid points different from zero in that file (DT02 have considered 921 rivers plus the coastal runoff), and the total (excluding the Antarctic runoff) is 1.25 Sv. We have found that this file was not adequate to specify the discharge of large rivers like the Amazon, or rivers that have narrow mouths like the Ob. In those cases, nothing is better than positioning directly each river mouth on the model grid

*MERCATOR-OCEANS, Toulouse, France

†Laboratoire de Physique des océans, CNRS-IFREMER-UBO, Plouzané, France

[1]New Estimate of Continental Discharge and Oceanic Freshwater Transport ; Dai & Trenberth ; Feb 2003 ; AMS symposium on Observing and Understanding the Variability of Water in Weather and Climate

and spreading the runoff onto an adequate number of grid points. The method we describe here uses the DT02 dataset as a basis but a special treatment is performed for the major rivers.

Note that the Dai and Trenberth dataset does not include the Antarctic coastal runoff due to the discharge of continental ice. We prescribe the value of Jacobs et al (1992), 2613 kg/year, or 0.0829 Sv. (units transformation : 1 Sv = $10^6 m^3.s^{-1} = 10^9$ kg.m^2.s^{-1} ; 1 kg.m^2.s^{-1}= $3600x24x365x10^{-12}$ km^3/year).

3 Identification of major rivers

We have ordered the annual mean runoff values in the DT02 dataset, and the first 99 values have been selected to be applied as "major rivers" (Table 1 at the end of this report). This makes sense because we want be able to spread large runoff values on many grid points : a 1/4° grid does not resolve the turbulence that disperses the river outflows in the real ocean. A few problems arise :

- Some runoffs are not referenced the table of the 200 greater rivers of DT02. These runoffs are indicated in Table 1 with a "XXX" in place of the DT02 river number, and a river name has been chosen from an Atlas[2].
- Some data from the Dai and Trenberth file fall in the land or away from the coast. The Jacui (50) and the Chidwin (87) have been left in land and have no impact on the global runoff discharge in the resulting files. The runoff 90 was in the sea and has been replaced like the "Huang" river in the mask file.
- Some runoff data can be just a branch of another river. In these cases, according to DT02 we take as the final value the sum of the main river and its tributaries :
  Amazon(1) = Amazon(1) + Tapajos(12) + Xingu(19)
  Tocantins(11) = Tocantins(11) + Para(21)
  St Laurence(16) = St Laurence(16) + Ottawa(92) + Saguenay(99)

The spread of each river over a few grid points has been constructed manually on the ORCA025 grid with the software developed by Edmée Durand (IDL graphic software). All rivers are given a large extension, even in the land, so that the rivermask is to a large extent independent of the coast line and can be used for higher resolution ORCA grid (like the global 1/12° MERCATOR model).

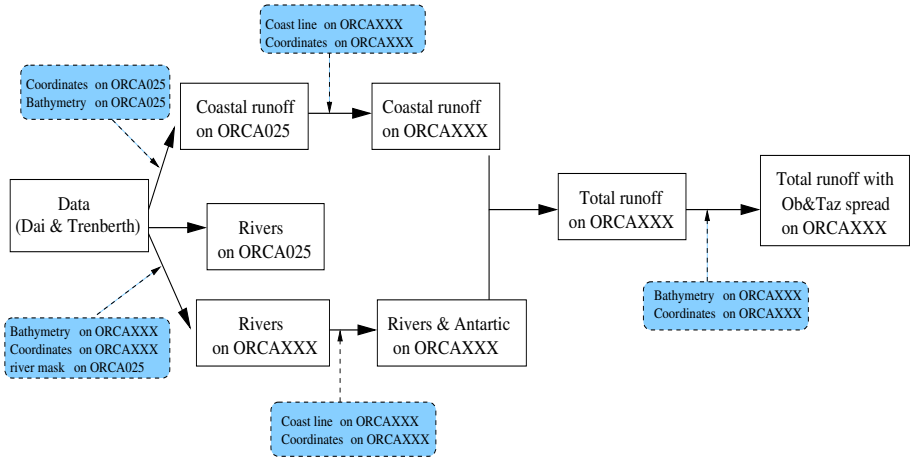

FIG. 1 – The steps to construct the runoff file. The input files are in blue

[2]The new internationnal Atlas 1982 ; Rand McNally & Compagny

4 Construction process

Several routines have been developed for the construction of the new runoff file. At each step an output file in NetCDF form is saved. The runoffs file can be created for any ORCA grid global configuration (ORCAXXX). The input file are : bathymetry, coordinates on the target grid (here ORCA025), and the river mask file on the ORCA025 grid. We use the coordinates_ORCA_R025_lombok+ombai.nc file, with modified scale factors in some Indonesian straits. The choice of the bathymetry file (ORCA025_combined_etopo_gebco_coast_corrected_oct05_G44.nc, to be precise) is not important because the coastline has not been modified often DRAKKAR or MERCATOR (this is not true of the deep bathymetry, which is not used here). The different steps are described below and on the figure 1 :

1. *compute_coast2.f90* : routine which allows the user to create a "mask file" that will be used to distribute the coastal runoff on the model grid. The first ocean point along the coast is saved in the present case (there is an option wich allows the creation of a mask with the 3 first points, *nbcoastpt* parameter). With another option the user can suppress the very little islands, where no significant amount of coastal runoff is expected. The minimum number of point for an island can be specified (*sizeisl_min* parameter).
   Input file : Bathymetry on ORCAXXX grid
   Output file : coastal mask on ORCAXXX grid
2. *compute_river.f90 :* this routine computes the N major rivers (*nbriver* parameter) from the Dai & Trenberth data base and creates two output files on the ORCA025 grid :
   One with the N major rivers placed at the nearest point of the global ORCA025 grid. For the next steps this runoff will be called "major river runoff".
   One with all the other runoff placed at the nearest point of the global ORCA025 grid. For the next steps this runoff will be called "coastal runoff".
   Input file : Bathymetry on ORCA025 grid ; Coordinates on ORCA025 ; Dai& Trenberth data file
   Output file : N major runoff on ORCA025 grid ; Other runoff on ORCA025 grid
3. *compute_costalrunoff.f90 :* the aim of this routine is to spread the coastal runoff along the coast. Each coastal runoff point of the Dai and Trenberth data base is spread over all coastal points within a $1^\circ \times 1^\circ$ box. If no coastal point of ORCA025 is found in a the box, the search is widened to a $2^\circ \times 2^\circ$ box. Even in that case, more than 200 points are found to be too far from any model coastline. Because they represent less than 0.1 Sv they are left out. Input file : Coast mask on ORCAXXX grid ; Coordinates on ORCA025 ; coastal runoff on ORCA025 grid
   Output file : Coastal runoff spread along the coast on ORCAXXX grid
4. *Construction of the river mask.* This is the only manual step of the process. A program with IDL graphic software has been developed by Edmée Durand (2003) that allows the user to attribute a number to some grid points near a river mouth, based on a high resolution map of the coastline. These numbers correspond to the numbers of the major rivers in table 1.
   Input file : surface mask on ORCA025 grid
   Output file : river mask on ORCA025 grid
5. *apply_river_ORCAgrid.f90.* With this routine, the user applies the N major rivers on the model grid with the river mask constructed manually. The process takes into account the area of the grid cells to preserve the total water input of each river (in Sv).
   Input file : Bathymetry on ORCAXXX grid ; Coordinates on ORCAXXX ; Dai& Trenberth data file, mask river on ORCA025 grid
   Output file : N major rivers on ORCAXXX grid

6. *compute_antartic.f90.* This routine adds the Antractic coastal runoff based on Jacobs et al (1992), with a pseudo annual cycle applied (fig 2, parameter *coefmois*). This value can be spread on 1 or 3 points, depending of the coast mask chosen (here 3 points). Input file : N major rivers on ORCAXXX grid ; Coordinates on ORCAXXX ; mask coast on ORCAXXX grid
   Output file : N major rivers and Antartic coastal runoffs on ORCAXXX grid
7. *compute_totalrunoff.f90 :* This routine simply adds the N major rivers and the coastal runoff.
   Input file : N major rivers on ORCAXXX grid ; Coastal runoff on ORCAXXX grid ;
   Output file : Total runoff on ORCAXXX grid
8. *compute_obtaz.f90 :* This routine allows to spread further the runoff in the Ob river estuary. It computes the total (rivers+coastal) runoff in the Ob area and spreads it in all the bay. This is to limit the risk of numerical instabilities during the month of june. We assume that those instabilities arise from the fact that the estuary is long and narrow, so that the 1/4° model is not able to generate strong enough currents to carry out the freshwater. This estuary should probably have been closed off in the 1/4° model.
   Input file : Bathymetry on ORCAXXX grid ; Coordinates on ORCAXXX ; Total runoff on ORCAXXX grid
   Output file : Total runoff (with Ob and Taz spread) on ORCAXXX grid
9. *verif_runofftot.f90 :* a simple programme to print the total annual value of the runoff file.
   Input file : Bathymetry on ORCAXXX ; Coordinates on ORCAXXX ; Total runoff on ORCAXXX grid
   Output file : None

Note that the runoff data is positive in the netcdf file but counted negative in the NEMO code.

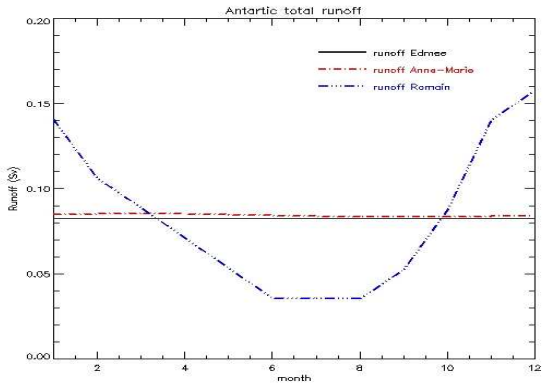

FIG. 2 – Monthly antartic discharge, in blue. The black and red lines are from previous runoff files (where the Antarctic coastal runoff did not have a seasonal cycle).

5 Results

The global annual discharge is 1.31 Sv, larger than the DT02 dataset, mainly due to the addition of the Antarctic coastal runoff. The latitudinal repartition is shown in fig 3. 84 runoff values in the data file have not been taken into account in the in the coastal runoff part : runoff located on a small island

(smaller than 20 grid points) and runoff located more than 3 degrees away from the coast. The global annual discharge of these rejected runoffs is 1.5 $1O^{-2}$ Sv

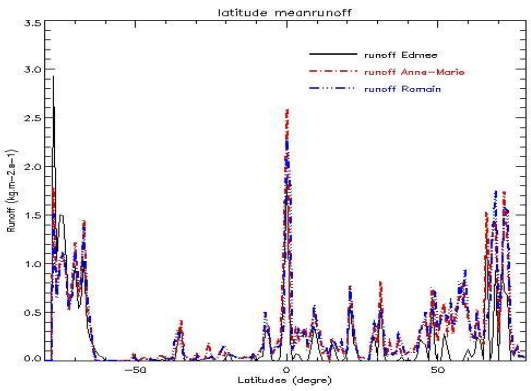

FIG. 3 – Zonal mean of the annual runoff (in blue). It is compared with a previous version (red) used for run ORCA025-G42, and to the runoff of Edmee Durand (2003), in black.

Regional maps are shown in Fig. 4. In the Amazon region (upper left), the Amazon and the Tocantins have a larger extension relative to previous runoff files (motivated by an unsufficient spreading of low salinity water in early ORCA025 experiments). Rivers near 50°W-5°N are represented with greater extension (Oyapock, Corentyne). The Alabama river (88°W-29°N) is represented. In the North of Russia (upper right), the Ob and the Taz have been spread over all the estuary. The Yenissei (110°E-74°N) is much more diffused as well. On the East coast of the North America (lower left), the St Laurence river has been spread out and more rivers appear in the north of Canada : George, Arnaud, Naskaupi. The south Asian region (lower right) shows similar features.

6 References

Bourdalle-Badie, Romain, 2005 : Note for the new runoffs file (ORCA025 and ORCA12). MERCATOR-OCEANS internal report.

Dai A., and K.E. Trenberth, 2002 : Estimates of freshwater discharge from continents : latitudinal and seasonal variations. Journal of hydrometeorology, 3, 660-687.

Durand, Edmee, 2003 : Elaboration du fichier de runoffs pour ORCA025. MERCATOR-OCEANS internal report.

Jacobs et al. 1992 : J. Glaciol. 38 (130) 375-387.

Large, W., and S. Yeager, 2004 : Diurnal to decadal global forcing for ocean and sea-ice models : the datasets and flux climatologies. NCAR technical note : NCAR/TN-460+STR, CGD division of the National Center for Atmospheric Research. Available on the GFDL CORE website.

Treguier, A.M, B. Barnier, A. P. de Miranda, J.M. Molines, N. Grima, M. Imbard, G. Madec, C Messager, T Reynaud, S Michel (2001) An eddy permitting model of the Atlantic Circulation : evaluating open boundary conditions. *J. Geophys. Res.*, 106, 22115-22129.

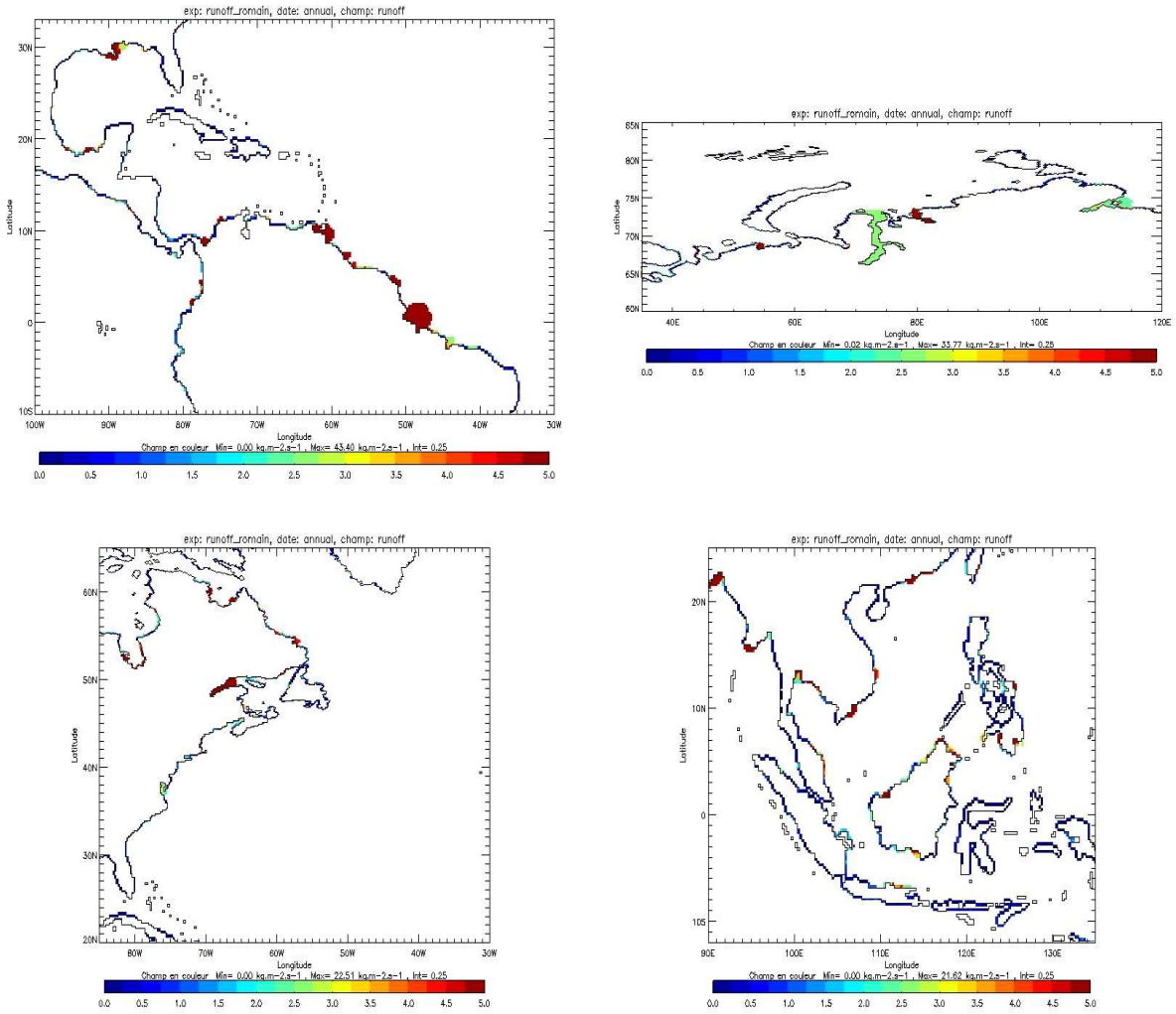

FIG. 4 – Annual runoff in four regions : Amazon, North Russia, North-East America, south Asia.

Table 1 (following pages) : list of the 99 major rivers.

river numer	Dai & Trenbeth number	River name	Annual volume (km3.yr-1)	lon D&T	lat D&T	i for ORCA025	j for ORCA025
1	1	amazon	6674.3129882812500	-51.00	0.00	946	499
2	2	congo	1306.5723876953130	13.00	-5.00	1202	479
3	3	orinoco	1126.1466064453130	-61.00	10.00	906	539
1	1	amazon	6674.3129882812500	-51.00	0.00	946	499
2	2	congo	1306.5723876953130	13.00	-5.00	1202	479
3	3	orinoco	1126.1466064453130	-61.00	10.00	906	539
4	4	changjiang	951.0073242187500	121.00	33.00	194	641
5	5	brahmaputra	624.4034423828125	90.00	25.00	70	602
6	6	mississipi	610.1058959960938	-91.00	31.00	786	630
7	7	yenissey	599.2224121093750	84.00	71.00	216	985
8	8	parana	567.9719848632813	-57.00	-34.00	922	354
9	9	lena	530.6795043945313	127.00	73.00	294	906
10	10	mekong	522.1766357421875	106.00	13.00	134	551
11	11	tocantins	517.8544921875000	-49.00	-1.00	954	495
12	12	tapajos	416.1152648925781	-55.00	-2.00	930	491
13	13	ob	413.2666320800781	70.00	67.00	1267	1007
14	14	ganges	401.1645507812500	89.00	25.00	66	602
15	15	irrawaddy	390.6878662109375	96.00	18.00	94	572
16	16	st lawrence	362.5499572753906	-67.00	49.00	886	731
17	17	amur	359.3233032226563	141.00	52.00	281	748
18	20	xijiang	357.762291015625	114.00	23.00	166	594
19	18	xingu	306.2500305175781	-52.00	-2.00	942	491
20	19	mackenzie	289.6512756347656	-134.00	69.00	551	906
21	XXX	para	268.4865112304688	-50.00	-2.00	950	491
22	36	zambeze1	266.6909790039063	36.00	-19.00	1294	422
23	21	columbia	255.1826171875000	-123.00	47.00	656	726
24	22	magdalena	235.2661895751953	-74.00	11.00	854	543
25	23	uruguay	227.9460449218750	-58.00	-33.00	918	359
26	24	yukon	215.1253509521484	-164.00	63.00	479	817
27	25	atrato	203.9931640625000	-77.00	7.00	842	527
28	26	danube	202.2315063476563	29.00	46.00	1262	724
29	28	ogooué	201.2275695800781	10.00	0.00	1190	499
30	27	niger	195.7747802734375	7.00	5.00	1178	519
31	29	essequibo	165.5147094726563	-58.00	7.00	918	527
32	XXX	bukuan	162.6399841308594	124.00	7.00	206	527
33	30	fraser	146.0812988281250	-122.00	49.00	660	742
34	31	pechora	140.2949676513672	54.00	68.00	1245	952
35	33	khatanga	128.5770568847656	107.00	74.00	265	942
36	32	nelson	126.1325759887695	-92.00	58.00	794	830
37	48	mahanadi	123.4809188842773	87.00	21.00	58	585
38	34	sepik	122.5293045043945	144.00	-3.00	286	487
39	36	zambeze2	119.6366806030273	36.00	-18.00	1294	426
40	35	kolyma	117.4317474365234	161.00	69.00	367	852
41	XXX	barka	115.8996505737305	38.00	18.00	1302	572
42	XXX	ulut	115.1665878295898	125.00	12.00	210	547
43	39	sanaga	112.9029922485352	11.00	4.00	1194	515
44	43	usumacinta	110.9588088989258	-92.00	19.00	782	576
45	XXX	nyong	106.8598785400391	10.00	4.00	1190	515
46	41	rajang	102.6780242919922	112.00	3.00	158	511
47	80	oyapock	101.2432785034180	-51.00	4.00	946	515
48	44	maroni	101.0052337646484	-54.00	6.00	934	523
49	134	senegal	99.8810424804688	-16.00	19.00	1086	576
50	XXX	turiacu	98.4281387329102	-45.00	-2.00	970	491

river numer	Dai & Trenbeth number	River name	Annual volume (km3.yr-1)	lon D&T	lat D&T	i for ORCA025	j for ORCA025
51	40	godavari	96.6239852905273	82.00	17.00	38	568
52	174	Grande de San	94.5379867553711	-106.00	23.00	726	594
53	XXX	davao	92.9742279052734	125.00	7.00	210	527
54	42	sao fransisco	91.9746551513672	-36.00	-10.00	1006	459
55	38	indus	88.5257339477539	69.00	25.00	1426	602
56	51	san juan	85.9970092773438	-77.00	5.00	842	519
57	61	taz	83.4067001342773	79.00	68.00	187	996
58	46	purari	77.9644470214844	145.00	-7.00	290	471
59	45	rhine	77.4084854125977	6.00	53.00	1166	755
60	57	tigris	76.9235153198242	47.00	32.00	1338	636
61	XXX	arnaud	72.5932998657227	-68.00	59.00	894	805
62	XXX	uda	72.5395431518555	135.00	55.00	262	773
63	50	jacui	71.7191543579102	-51.00	-29.00	946	378
64	49	sacramento	69.1390914916992	-122.00	38.00	662	667
65	92	chao praya	69.0412216186523	100.00	12.00	110	547
66	XXX	ba	69.0412216186523	109.00	12.00	146	547
67	XXX	gambia	68.2213363647461	-16.00	14.00	1086	556
68	63	courantyne	66.2140274047852	-57.00	6.00	922	523
69	77	susitna	66.1370086669922	-150.00	62.00	529	823
70	82	rufiji	66.1315231323242	40.00	-11.00	1310	455
71	XXX	sesayap	64.9734344482422	118.00	3.00	182	511
72	87	skeena	64.9120254516602	-130.00	55.00	621	789
73	150	cross	63.6736831665039	8.00	8.00	1182	531
74	189	orange	62.7484817504883	17.00	-29.00	1218	378
75	XXX	naskaupi	62.7029953002930	-60.00	53.00	916	754
76	62	po	61.8996849060059	12.00	46.00	1195	713
77	67	alabama	60.3524131774902	-88.00	31.00	798	630
78	XXX	mamberamo	59.7507133483887	138.00	-2.00	262	491
79	102	esmeraldas	59.1020812988281	-78.00	2.00	838	507
80	81	george	59.0025749206543	-68.00	58.00	892	797
81	XXX	digul	58.8638496398926	139.00	-7.00	266	471
82	XXX	cacipore	58.7281494140625	-52.00	4.00	942	515
83	131	nyanga	58.4193611145020	9.00	-2.00	1186	491
84	164	narva	57.6874122619629	29.00	60.00	1232	836
85	53	kuskokwim	57.0187950134277	-162.00	61.00	489	805
86	54	albany	56.8876037597656	-81.00	53.00	833	769
87	60	chidwin	56.6758766174316	96.00	22.00	94	589
88	129	kinabatangan	56.4265480041504	118.00	6.00	182	523
89	74	susquehanna	56.4206466674805	-76.00	40.00	847	677
90	XXX	huang	56.3485527038574	121.00	35.00	194	651
91	64	indigirka	55.8909683227539	150.00	72.00	342	878
92	59	ottawa	55.2164001464844	-74.00	46.00	856	713
93	58	krishna	54.8718070983887	81.00	17.00	34	568
94	177	juba	54.7996520996094	48.00	4.00	1342	515
95	83	nile	54.5960731506348	10.00	34.00	1190	645
96	88	garonne	53.8341102600098	5.00	44.00	1168	699
97	XXX	barito	53.6225967407227	115.00	-3.00	170	487
98	199	fortescu	53.2418670654297	116.00	-21.00	174	413
99	XXX	saguenay	52.4743309020996	-70.00	49.00	874	732

TECHNICAL ANNEX 2

Definition of the global 1/2° experiment with
CORE interannual forcing
ORCA05-G50

Technical note

November 2006

Definition of the global 1/2° experiment with CORE interannual forcing, ORCA05-G50

J.M. Molines, B. Barnier, T. Penduff, L. Brodeau [*], A.M. Treguier, S. Theetten [†], Gurvan Madec [‡]

LEGI report November 2006
reference: LEGI-DRA-1-11-2006

1 Introduction

Running ocean/ice models forced by a prescribed atmosphere is a difficult problem, because the ocean-atmopshere system is inherently coupled. This has been a topic for discussion within the Working Group for Ocean Model development, co-chaired by C. Böning and S. Griffies. This group is sponsored by CLIVAR and WCRP: annual reports are found on the CLIVAR web site. Over the years, the discussions have led to the endorsement of a forcing dataset and a modelling strategy called CORE (Coordinated Ocean Reference Experiments). This strategy is described on documents available on the GFDL CORE website, as well as in an article in the FLUXNEWS WCRP newsletter (Griffies et al, 2007). The CORE forcing dataset itself has been put together by Large and Yeager and is fully documented in a report (Large and Yeager, 2004).

The ORCA05-G50 experiment described here uses the global 1/2° ORCA05 ice-ocean model based on the NEMO code. The experiment follows the CORE forcing strategy. It covers years 1958 to 2004 after 9 years of spin-up using a repeated 1958 year forcing. Our parameterizations differs from other ORCA05 experiments performed at Kiel (Biastoch et al) because we implement the global 1/2° model in an eddy permitting mode. This may seem surprising at such a low resolution: it is less so when we look back 15 years. The first so-called "eddy resolving" semi-global model of Semtner and Chervin (1992) had a grid size of 0.4° at the equator, barely less than ORCA05. The Fine Resolution Antarctic Model FRAM (see for example Stevens and Killworth, 1992) had the same resolution as ORCA05 (722 grid points in the zonal direction). The present document describes the experiment set-up. It is a technical report: users that are not familiar with the NEMO modelling system (*w*ww.lodyc.jussieu.fr/NEMO) should refer to the model documentation. The code is based on version NEMO 1.09.

[*]Laboratoire des Ecoulements Geophysiques et Industriels, CNRS UMR 5519, Grenoble, France
[†]Laboratoire de Physique des oceans, CNRS-Ifremer-UBO, Brest, France
[‡]LOCEAN, Paris,France

Key	Description
key_orca_r05_l46	Configuration name (l46 refers to the 46 layer version)
key_dynspg_flt	Filtered free surface
key_zdftke	TKE vertical mixing scheme
key_dtatem	Use temperature data for initial conditions
key_dtasal	Use salinity data for initial conditions
key_flx_core	Use CORE forcing routines and NCAR bulk formulae
key_traldf_c2d	2D lateral diffusion for tracers (depends on dx)
key_dynldf_c2d	2D lateral diffusion for dynamics (depends on dx^3)
key_ldfslp	Need to calculate isopycnal slope
key_passivetrc	Passive tracers
key_cfc	One cfc (code James Orr)
key_c14bomb	C14 bomb (code James Orr)
key_partial_steps	Partial steps topography
key_trabbl_dif	diffusive bottom boundary layer parameterization
key_dimgout	dimg format for outputs
key_mpp_mpi	multiprocessor MPI run
key_ice_lim	Ice model
key_lim_fdd	Ice model interaction with the ocean.
key_vectopt_loop	optimization of loop for vector conputers
key_vectopt_memory	recalculates less arrays each step, more memory usage

Table 1: CPP keys for ORCA05-G50 run

2 Basic settings

The list of CPP keys used for this run is found in table 1.

2.1 Horizontal grid

The horizontal grid was defined as a generic 'ORCA' type mesh with 3 poles, using a f-point pivot for the north fold condition. The horizontal grid resolution is 1/2 deg at the equator, leading to horizontal dimensions of 722×511. The minima of the the scale factors (ocean points) are 12.6 km (zonal direction) and 9.4 km (meridional direction). The maximum is 55.6 km at the equator.

2.2 Vertical grid

There are 46 levels on the vertical, with grid spacing ranging from 6 m near the surface to 250 m at 5750 m. The maximum depth allowed in the model is 6000 m. to reach that depth with partial cells, the deepest cell can have a thickness as large as 500 m in the deep basins. The details of the vertical levels as well as the vertical metrics are given in annex A.

2.3 Bathymetry

The bathymetry is calculated from ETOPO2. Note that for the DRAKKAR 1/4° model we have used the GEBCO bathymetry on the ocean continental shelves, mainly because we had found problems off the African coast and in the Indonesian throughflow region. We are not sure those problems are significant at lower model resolutions, so no effort has been made to improve the 0RCA05 bathymetry using GEBCO. The basic file ETOPO2 is the 2-minute bathymetry file of NGDC, combination of Smith and Sandwell satellite-based bathymetry (8.2 version), IBCAO (in the Arctic region) and other data in the Antarctic region. The MERCATOR project team has applied additional corrections near the Antarctic (Remy et al, 2003). The interpolation onto the model grid has been conducted by taking all the original grid points falling into an ORCA05 grid box, and taking the median of those points. This procedure produces a smoothing of the sub-grid scale topography. Contrary to higher resolution configurations, no smoothing is applied here because we feared that this would tend to close narrow passages. To get rid of unwanted "one-grid-point" ponds or seamounts, we fill the ponds defined as one grid point lower than all surrounding communicating grid points (four directions). 14842 points are affected. Then we lower the "spikes" (one grid point higher than all eight surrounding points). This treatment modifies 7212 points.

The experiment is run using the partial cell representation of the topography (key_partial_steps). The following values are used to calculate the partial cell layer thicknesses (in namelist `namdom`: `e3zps_min = 25.` and `e3zps_rat = 0.2`.

Hand editions have been made, but some of them did not end up as intended. For details of those corrections, please contact the DRAKKAR team.

2.4 Initial conditions

The initial conditions for temperature and salinity were derived from the Levitus 98 data set for the mean and low latitudes. For high latitudes PHC climatology was used instead. For the Mediteranean Sea, **medatlas** climatology was used. The initial condition for sea ice is a constant thickness of 3 meters in the Arctic and 1 m in the Antarctic.

3 Forcings

3.1 Runoffs

A new runoff file has been calculated using the Dai and Trenberth dataset (Dai and Trenberth, 2002) by Romain Bourdalle-Badie at Mercator:
runoff_coast1pt_ant1pt_obtaz_1m_ORCA05.nc. It is a monthly climatology and includes 99 major rivers and coastal runoffs. The method is the same as for the global 1/4° model, documented in a report on the DRAKKAR web site (Bourdalle-Badie and Treguier, 2006). We use the namelist variable `nrunoff=2`. In that case, a special treatment is applied in runoff regions, where the array *upsrnfh* is non zero. This array is read in the runoff file (netcdf variable *socoefr*). It has a value of zero where there is no runoff and 0.5 at runoff points. Since we do not use the centered scheme, there is no need to revert

to upstream near runoffs (the TVD advection scheme is used everywhere). In our case the special treatment consists in an enhanced vertical diffusion at the interface of layers 1 and 2 applied in step.F90 (Drakkar configuration manager version):

```
avt  (:,:,2) = avt  (:,:,2) + 1.e-3 * upsrnfh(:,:)
```

The vertical mixing is then set to 500 below the top level at runoff points.

3.2 Atmospheric forcing files

Forcing files are from the CORE dataset (Large and Yeager, 2004) available on the GFDL CORE website. at 2m and atmospheric pressure.

The input files are the following:

- **Air temperature and specific humidity :** 6-hourly values at 10 m height from CORE (based on NCEP).
- **Solar and infra-red downwelling radiation :** Daily values from satellites (ISCCP, Zhang et al. 2004). The corrected version of this product available into the CORE dataset is used. (`qsw_CORE.nc` and `qlw_CORE.nc` for short-wave=solar and long-wave=infra-red).
- **Precipitation (total precipitation and snow) :** Monthly fields from CORE based on satellite measurements (is there a correction???)

The turbulent fluxes, outgoing radiation and albedo are calculated using the formulae proposed with the CORE dataset (Large and Yeager, 2004).

3.3 Interpolation

The forcing fields are preprocessed and interpolated using the int2df interpolation package (Brodeau 2004), available at :
http://laurent.brodeau.free.fr/f90/interpol/int2df-v0.3.tar.gz
The algorithm used follows Akima, 1974 : "A method of bivariate interpolation and smooth surface fitting based on local procedures". Prior to the interpolation, the GAP procedure implemented into int2df is used to extrapolate sea values onto an extended land mask, this prevents some coastal land values from influencing the interpolation process. Another important feature of the interpolation process is the rotation of the wind vector onto distorted regions of the target grid (northward 40°N for ORCA grids).

3.4 Forcing parameters

The forcing routine and the ice model are called only once every three hours, e.g. every 5 time steps (`nfice=5` and `nfbulk=5`) in the namelist namdom. There is relaxation to sea surface salinity (monthly climatology of Levitus/PHC). The coefficient (m/day) is set in the new namelist:

```
&namsbc
   cdmp = 0.1666666667
```

This value is chosen by consistency with the "strong relaxation" cases in the CORE papers by Griffies *et al.*, 2006. It amounts to a decay time of 60 days for 10 m of water depth. There is no SSS restoring under the ice cover. We also add extra restoring for the Red Sea. (oce_sbc_dmp routine).

3.5 Miscellaneous

We use the standard NEMO scheme for penetrative solar radiation, based on clear water only. It does not take into account data of water colour.

Note that there is no representation of the diurnal cycle in this experiment: this would require a vertical resolution of 1 m in the upper layers (Bernie and Madec, personal communication).

3.6 Sea surface height adjustment

We do not use any SSH adjustment. We set `ln_fwb = .false.` in the namelist. No attempt is made to ensure that the correction term (erp) by relaxation to observed SSS had a zero integral over the global ocean (suppression of the adjustments using "aplus" and "aminus" in routine `ocesbc.F90`). As other experiments with CORE forcings we find an increase of the global SSH (1.9 m).

4 Ice model

The ice parameters are the following. Note that the turning angle for the oceanic stress, the rheology parameter pstar and the eddy diffusivity for sea ice ahi0 differ from the ORCA025 1/4° model. The ice thickness for lateral accretion hicrit is larger than in ORCA025.

```
&namicerun
   ln_limdyn    = .true.
   acrit   = 1.0e-06 , 1.0e-06
   hsndif  = 0.0
   hicdif  = 0.0
/
&namiceini
   ln_lim_ini = .false.
   ttest = 2.0
   hninn = 0.5
   hginn = 3.0
   alinn = 0.05
   hnins = 0.1
   hgins = 1.0
   alins = 0.1
/
&namicedyn
```

```
   epsd   = 1.0e-20
   alpha  = 0.5
   dm     = 0.6e+03
   nbiter = 1
   nbitdr = 100
   om     = 0.5
   resl   = 5.0e-05
   cw     = 5.0e-03
   angvg  = -5.0
   pstar  = 1.5e+04
   c_rhg  = 20.0
   etamn  = 0.0e+07
   creepl = 2.0e-08
   ecc    = 2.0
   ahi0   = 350.e0
/
&namicetrp
   bound  = 0.
/
&namicethd
   hmelt   = -0.15
   hiccrit = 0.9 , 0.6
   hicmin  = 0.2
   hiclim  = 0.05
   amax    = 0.999
   swiqst  = 1.
   sbeta   = 1.
   parlat  = 0.0
   hakspl  = 0.5
   hibspl  = 0.5
   exld    = 2.0
   hakdif  = 1.0
   thth    = 0.2
   hnzst   = 0.1
   parsub  = 1.0
   alphs   = 1.0
/
```

5 Parametrizations

All runs are performed with the free surface, constant volume formulation (`key_dynspg_flt` defined).

5.1 Advection schemes:

We use TVD for tracers (`ln_traadv_tvd = .true.`). We use the new momentum advection scheme suitable for partial step topography (`ln_dynvor_een = .true.`).

5.2 Lateral mixing:

-tracer : a laplacian isopycnal diffusion is used with `aht0= 2000m`^{2}`/s` at the equator. The coefficient decreases polewards proportionally to the grid size. Associated keys are key_traldf_c2d and key_ldfslp.

-dynamics : A biharmonic horizontal viscosity is used with `ahm0=` $-8.5\ 10^{11}$ `m`^{4}`/s`^{2} . The viscosity depends on the grid size with δx^3.

5.3 Bottom boundary layer:

A diffusive bottom boundary layer is activated using `key_trabbl_dif` with `atrbbl` =6000 $m^2.s^{-1}$. We do not activate the advective BBL scheme (`key_trabbl_adv`) because we do not think it would make much difference at that resolution.

5.4 Vertical mixing:

There is no double-diffusive mixing.

-tke: TKE is used to compute the vertical mixing. We use the new version of the TKE routine recently proposed by Gurvan MADEC with the following namelist parameters

```
!-----------------------------------------------------------------------
!       namtke   turbulent eddy kinetic dependent vertical diffusion
!                ( #ifdef "key_zdftke" )
!-----------------------------------------------------------------------
!  ln_rstke flag to restart with tke from a run without tke (default F)
!  ediff    coef. to compute vertical eddy coef. (avt=ediff*mxl*sqrt(e) )
!  ediss    coef. of the Kolmogoroff dissipation
!  ebb      coef. of the surface input of tke
!  efave    coef. to applied to the tke diffusion ( avtke=efave*avm )
!  emin     minimum value of tke (m^2/s^2)
!  emin0    surface minimum value of tke (m^2/s^2)
!  nitke    number of restart iterative loops
!  ri_c     critic richardson number
!  nmxl     flag on mixing length used
!           = 0 bounded by the distance to surface and bottom
!           = 1 bounded by the local vertical scale factor
!           = 2 first vertical derivative of mixing length bounded by 1
!  npdl     flag on prandtl number
!           = 0 no vertical prandtl number (avt=avm)
!           = 1 prandtl number function of richarson number (avt=pdl*avm)
!           = 2 same as = 1 but a shapiro filter is applied on pdl
!  nave     =  horizontal averaged (=1/2) or not (=0) of avt  (default =1)
!  navb     = 0 cst background avt0, avm0 / =1 profile used on avtb
!  ln_lsfc  computation surface value of buoyancy lenght scale as function of wind stress
!  lmin     buoyancy lenght scale minimum value if ln_lsfc = F
!  n_etau   test param. to add tke induced by wind
!            = 0 no add tke induced by wind
!            = 1 add tke induced by wind
```

```
!            = 2 add tke induced by wind only at the base of the mixed layer
!  fr_emin  fraction of TKE surface value which penetrates inside the thermocline
!  ln_lc    flag to take into account  Langmuir circulation
!  c_lc     coef to compute verticla velocity of LC
&namtke
   ln_rstke = .false.
   ediff =       0.1
   ediss =       0.7
   ebb   =       60.
   efave =        1.
   emin  =     1.e-6
   emin0 =     1.e-4
   nitke =        50
   nmxl  =         3
   npdl  =         1
   navb   =        0
   nave   =        1
   ln_lsfc =  .true.
   lmin    =    0.4
   n_etau =       1
   nhtau  =       3
   fr_emin =     0.05
   ln_lc =   .true.
   c_lc  =    0.15
```

The key modification made to tke is `fr_emin`, the proportion of energy allowed to enter into the stratified ocean below the mixed layer. This is meant to represent mixing by unresolved turbulence due to surface waves and swell. It is supposed to improve the depth of summer mixed layers that were too shallow in experiment G42. The parameter nhtau is changed from ORCA025-G50 (it used to be 1). It sets the scheme for the penetration of this energy. The depth is hardwired in the routine. It used to be 40m with a decrease to 5m at the equator. With `nhtau=3`, the depth is allowed to be different in different hemispheres, but finally after testing we set it to 30m in both hemispheres. We want to avoid unrealistic mixing under the ice. For this reason, the Langmuir cells contribution is removed under the ice, and the background coefficient is reduced (see next paragraph).

-background and convection: The enhanced vertical diffusion is used when convection is diagnosed. The corresponding namelist block is :

```
!-----------------------------------------------------------------------
!       namzdf   vertical physics
!-----------------------------------------------------------------------
!  ln_zdfevd  enhanced vertical diffusion         (default T)
!  ln_zdfnpc  Non-Penetrative Convection          (default T)
!  avm0       vertical eddy viscosity for the dynamic (m2/s)
!  avt0       vertical eddy diffusivity for tracers (m2/s)
!  avevd      vertical coefficient for enhanced diffusion scheme (m2/s)
!  nevdm      = 0  apply enhanced mixing on tracer only
!             = 1  apply enhanced mixing on both tracer and momentum
!  ln_zdfexp   vertical physics: (=T)  time splitting (T)     (Default=F)
```

```
!                                (=F)  euler backward (F)
!  n_zdfexp   number of sub-timestep for time splitting scheme
&namzdf
   ln_zdfevd = .true.
   ln_zdfnpc = .false.
   avm0     = 1.e-4
   avt0     = 1.e-5
   avevd    =   10.
   nevdm    =     1
   ln_zdfexp =  .false.
   n_zdfexp =      3
/
```

In the previous version of TKE there was an enhancement of the background by a factor of 10 in the top layer (and 5 and 2.5 in the second and third) in order to avoid too shallow mixed layers in summer. This is suppressed in the new version of TKE. The background coefficient is divided by a factor of 10 under the ice.

5.5 Bottom friction and lateral boundary condition

The namelist is the following. We use a spatially variable coefficient: the bottom friction coefficient is multiplied by `bfrien=50` in Torres Strait: this is to reduce the flow through this strait, that is observed to be small.

```
!-----------------------------------------------------------------------
!       nambfr   bottom friction
!-----------------------------------------------------------------------
!  nbotfr  type of bottom friction
!                  nbotfr = 0 , no slip
!                  nbotfr = 1 , linear friction
!                  nbotfr = 2 , nonlinear friction
!                  nbotfr = 3 , free slip
!  bfri1   bottom drag coefficient (linear case)
!  bfri2   bottom drag coefficient (non linear case)
!  bfeb2   bottom turbulent kinetic energy  (m^2/s^2)
!  ln_bfr2d:  flag for 2d coef enhancement read in file
!  bfrien:  enhancement coefficient (integer > 1)
&nambfr
   nbotfr =       2
   bfri1  =   4.e-4
   bfri2  =   1.e-3
   bfrien = 50
   ln_bfr2d = .TRUE.
   bfeb2  =  2.5e-3
/
```

The lateral boundary condition is free slip (shlat=0 in namelist). Contrary to other global configurations like ORCA2 and ORCA025, there is no local modification of the lateral friction in some straits.

6 miscellaneous:

-timestep : The time steps is set to 2160 s (40 steps/day).

-hpg implicit : The semi-implicit scheme is applied to allow a larger time step (a factor of two on the cfl criterion linked with internal wave propagation).

-asselin : the asselin coefficient is taken to 0.1

7 Simulation strategy

The present run starts in 1949 with a nine year spin-up using year 1958, periodized and repeated 9 times(fictitious years numbered 1949 to 1957). The experiment proceeds with interannual CORE forcing for years 1958 to 2004.

8 Transient tracers

The bomb C14 and CFCs forcings are provided by Zouhair Lachktar and James Orr. The tracers use the same parameterizations as the physics (isopycnal mixing) and the TVD advection scheme.

The transients tracers begin after one year of dynamical spin-up in order to avoid the initial geostrophic adjustment of the dynamics (calendar year and model year 1950).

9 Model outputs

9.1 Archived fields

Files are stored every 5 days (nwrite = 300 steps). 3D variables are U, V, T, S, W, K_z. K_z is a time-average of the total vertical mixing including convection events (suitable for off-line tracer calculations). Two dimensional fields are taux and tauy (in U and V files) and in the "grid T" files:

sossheig Sea surface height (in meters)

somxl010 Mixed layer depth (in m) based on a σ_0 difference of 0.01 with the surface

sohefldo Net Downward Heat Flux (in W.m^{-2})

soshfldo Short wave downward radiative flux (in W.m^{-2})

sowaflup Net upward water flux in kg.m^2.s^{-1} (forcing of the sea surface height)

sowafldp Surface water flux damping in kg.m^2.s^{-1}

iowaflup Ice-ocean water flux in kg.m^2.s^{-1}

sowaflcd Concentration-dilution water flux (the product of this flux with surface salinity is the forcing term in the salinity equation)

solhflup Latent heat flux (in W.m^{-2})

solwfldo Long wave downward radiative flux (in W.m^{-2})

sosbhfup Sensible heat flux (in W.m^{-2})

9.2 Storage strategy

Although we have thought about storage in 16 bits, for now the netcdf variables are floats with 32 bits. For best performances, the output are written by each processor in direct acces files. Those files are recombined immediately after the experiment (see Molines (2004) [9] for more details). The output files stored on gaya at IDRIS are 5 days averages. They are netcdf files very similar to classical OPA netcdf output, excepted for a few differences:

- one file for each 5-day average
- definition of time_counter: The time_counter gives the number of seconds since the begining of the run.
- naming convention for the files: There are 5 types of files; 4 corresponds to the different grid points: gridT, gridU, gridV and gridW; a fifth type of file corresponds to the ice model output. File names are almost self explanatory: (*e.g.* ORCA05-G50_y0010m10d03_gridT.nc or ORCA05-G50_y0010m10d03_icemod.nc). The time indicated in the name of the file corresponds to the date at the **end** of the period used to time-average the data.
- archiving the results: The results are archived on rcli002@gaya:ORCA05/. Data are organized in many directories. Raw results from the run are stored under ORCA05-*CASE*-S (one sub-directory per year then). Mean values computed from the raw results are stored in ORCA05-*CASE*-MEAN. There are monthly means, quarterly means and annual means (one sub-directory per year). Interannual means are also computed. The implementation of this directory tree for archiving the results, is part of the strategy used in DRAKKAR to share different configurations between groups of users (see Molines *et al.*(2004) [10]).

Note that the special value on land is zero. This is properly referenced in the header of each file (and causes problems with older versions of the "ncra" software).

10 Numerics

10.1 Domain decomposition

ORCA05 runs on a massively parallel computer, using a domain decomposition technique. The message passing between processors is explicitly done using the MPI library (option

"isend").

References

[1] Barnier, B., G. Madec, T. Penduff, J.M. Molines, A.M. Treguier, J. Le Sommer, A. Beckmann, A. Biastoch, C. Böning, J. Dengg, C. Derval, E. Durand, S. Gulev, E. Remy, C. Talandier, S. Theetten, M. Maltrud, J. McClean, B. De Cuevas 2006: Impact of partial steps and momentum advection schemes in a global ocean circulation model at eddy permitting resolution. Ocean Dynamics, DOI: 10.1007/s10236-006-0082-1.

[2] Bourdallé-Badie R., and A.M. Treguier, 2006: A climatology of runoff for the global ocean-ice model ORCA025. MERCATOR report MOO-RP-425-366-MER.

[3] Brodeau, L, 2004: A comparison between two interpolation tools. Drakkar report, available at www.ifremer.fr/lpo/drakkar

[4] Dai A., and K.E. Trenberth, 2002: Estimates of freshwater discharge from continents: latitudinal and seasonal variations. Journal of hydrometeorology, 3, 660-687.

[5] Fichefet, T. and M.A. Morales Maqueda, 1997: Sensitivity of a global sea ice model to the treatment of ice thermodynamics and dynamics, J. Geophys. Res., 102, 12609-12646

[6] Griffies, S., C. Böning and A.M. Treguier, 2007: Large Design Considerations for Coordinated Ocean-Ice Reference Experiments. Flux News, Newsletter of the WCRP Working Group on Surface Fluxes, january 2007. *h*ttp://www.sail.msk.ru/newsletter/index.htm.

[7] Large, W., and S. Yeager, 2004: Diurnal to decadal global forcing for ocean and sea-ice models: the datasets and flux climatologies. NCAR technical note: NCAR/TN-460+STR, CGD division of the National Center for Atmospheric Research. Available on the GFDL CORE web site.

[8] Tartinville B.: Description of the CLIO model version 3.0, found on the LODYC/OPA web site

[9] Molines, J.M., 2004 : Drakkar I/O strategy and implementation for MPP runs with NEMO-OPA9. Drakkar technical report, Grenoble, 13pp.

[10] Molines, J.M., A.M. Treguier and S. Theetten, 2004: Drakkar Config Manager: How to manage and share various model configurations, based on NEMO-OPA9. Drakkar technical report, Grenoble, 14pp.

[11] Semtner, A. J. Jr., R. M. Chervin, 1992: Ocean General Circulation From a Global Eddy-Resolving Model, J. Geophys. Res., 97(C4), 5493-5550, 10.1029/92JC00095.

[12] Stevens, D.P. and P.D. Killworth, 1992: The distribution of kinetic energy in the Southern Ocean: a comparison between observations and an eddy resolving general circulation model. Phil. Trans. R. Soc. Lond. B, **338**, 251-257.

A Annex A

vertical levels

```
zgr_z   : Reference vertical z-coordinates
~~~~~~~

     zsur, za0, za1 computed from
             zdzmin =  6.00000000000000000
             zhmax  =  5720.00000000000000
          Namelist namzgr : value of coefficients for vertical mesh:
             zsur =  -2143.95922194325158
             za0  =  127.451110365423233
             za1  =  123.075814004137086
             zkth =  23.5629999999999988
             zacr =  9.00000000000000000

          Reference z-coordinate depth and scale factors:
     level   gdept    gdepw     e3t      e3w
        1     3.05     0.00     6.19     6.00
        2     9.45     6.19     6.64     6.40
        3    16.36    12.83     7.19     6.90
        4    23.88    20.03     7.88     7.52
        5    32.18    27.92     8.74     8.29
        6    41.44    36.68     9.80     9.25
        7    51.87    46.49    11.12    10.43
        8    63.78    57.62    12.74    11.89
        9    77.48    70.38    14.73    13.69
       10    93.39    85.13    17.18    15.89
       11   112.01   102.33    20.16    18.60
       12   133.92   122.52    23.78    21.88
       13   159.82   146.33    28.14    25.86
       14   190.49   174.50    33.36    30.63
       15   226.85   207.90    39.54    36.32
       16   269.92   247.48    46.78    43.02
       17   320.80   294.31    55.16    50.83
       18   380.63   349.52    64.70    59.78
       19   450.57   414.27    75.38    69.90
       20   531.74   489.69    87.11    81.12
       21   625.09   576.84    99.72    93.32
       22   731.40   676.59   112.98   106.29
       23   851.17   789.58   126.59   119.76
       24   984.59   916.17   140.22   133.42
       25  1131.50  1056.38   153.54   146.94
       26  1291.46  1209.89   166.25   159.99
       27  1463.71  1376.10   178.10   172.29
```

28	1647.31	1554.16	188.92	183.65
29	1841.17	1743.03	198.61	193.91
30	2044.14	1941.59	207.13	203.01
31	2255.05	2148.67	214.51	210.96
32	2472.80	2363.14	220.82	217.79
33	2696.36	2583.92	226.15	223.60
34	2924.82	2810.03	230.62	228.49
35	3157.35	3040.62	234.32	232.56
36	3393.25	3274.92	237.38	235.93
37	3631.93	3512.27	239.89	238.70
38	3872.87	3752.14	241.93	240.96
39	4115.66	3994.06	243.60	242.81
40	4359.96	4237.64	244.95	244.31
41	4605.47	4482.58	246.04	245.52
42	4851.97	4728.61	246.92	246.50
43	5099.25	4975.52	247.63	247.29
44	5347.18	5223.15	248.20	247.93
45	5595.62	5471.34	248.66	248.44
46	5844.47	5720.00	249.03	248.86

TECHNICAL ANNEX 3

Definition of the interannual experiment
ORCA025-G70
1958-2004

Technical note

November 2006

Definition of the interannual experiment ORCA025-G70, 1958-2004

J.M. Molines, B. Barnier, T. Penduff, L. Brodeau [*], A.M. Treguier, S. Theetten [†], Gurvan Madec [‡]

LEGI Report, November 2006
Reference: LEGI-DRA-2-11-2006

1 Introduction

This report describes the 1/4° model configuration ORCA025-G70 used for the first long experiment with interannual forcing (47 years, from 1958 to 2004) performed by the DRAKKAR project. Experiments with ORCA025 have started in 2004/2005 with 10-year sensitivity experiments using a climatological forcing called "DRAKKAR set 1" (Talandier et al, 2003). The results of those experiments are described in Barnier et al (2006). Following those, another 10 year experiment (ORCA025-G42) was run with climatological CORE forcing (see Large and Yeager, 2004 for the definition of this forcing set). Some aspects of this experiment are documented in Dencausse (2005) and Treguier et al. (2006). In early 2006, a first interannual experiment with the CORE forcing (ORCA025-G50) was started, and stopped after 14 years (8 years spin-up and the years 1958-1965 with interannual forcing). This decision was made because of a very weak thermohaline circulation in the Atlantic (10 Sv), as well as other problems. This is why a new forcing set (DRAKKAR forcing set 3) is used for the present experiment. Note that the forcing set uses data from ERA40 for years 1958 to 2001, but ECMWF analysis for years 2002-2004, causing an adjustment of the upper ocean in 2002, especially in the tropics. This is a technical report: users that are not familiar with the NEMO modelling system (*w*ww.lodyc.jussieu.fr/NEMO) should refer to the model documentation. The code is based on version NEMO 1.09.

2 Basic settings

The list of CPP keys used for this run is found in table 1.

[*]Laboratoire des Ecoulements Geophysiques et Industriels, CNRS UMR 5519, Grenoble, France
[†]Laboratoire de Physique des oceans, CNRS-Ifremer-UBO, Brest, France
[‡]LOCEAN, Paris,France

Key	Description
key_orca_r025	Configuration name
key_dynspg_flt	Filtered free surface
key_zdftke	TKE vertical mixing scheme
key_dtatem	Use temperature data for initial conditions
key_dtasal	Use salinity data for initial conditions
key_dtasss	Use surface salinity data for relaxation
key_tradmp	special relaxation to clim T and S in the Gulf of Cadiz
key_flx_core	Use CORE forcing routines and NCAR bulk formulae
key_trabbc	Bottom boundary condition for tracers (geothermal flux)
key_traldf_c2d	2D lateral diffusion for tracers (depends on dx)
key_dynldf_c2d	2D lateral diffusion for dynamics (depends on dx^3)
key_ldfslp	Need to calculate isopycnal slope
key_passivetrc	Passive tracers
key_cfc	One cfc (code James Orr)
key_c14bomb	C14 bomb (code James Orr)
key_partial_steps	Partial steps topography
key_trabbl_dif	diffusive bottom boundary layer parameterization
key_trabbl_adv	advective bottom boundary layer parameterization
key_dimgout	dimg format for outputs
key_mpp_mpi	multiprocessor MPI run
key_ice_lim	Ice model
key_lim_fdd	Ice model interaction with the ocean.

Table 1: CPP keys for ORCA025-G70 run

2.1 Horizontal grid

The horizontal grid was defined as a generic 'ORCA' type mesh with 3 poles, using a t-point pivot for the north fold condition. The horizontal grid resolution is 1/4 deg at the equator, leading to horizontal dimensions of 1442 x 1021. The minima of the the scale factors (ocean points) are 5.6 km (zonal direction) and 3.1 km (meridional direction). The maximum is 27.8 km at the equator.

2.2 Vertical grid

There are 46 levels on the vertical, with grid spacing ranging from 6 m near the surface to 250 m at 5750 m. The maximum depth allowed in the model is 6000 m. to reach that depth with partial cells, the deepest cell can have a thickness as large as 500 m in the deep basins. The details of the vertical levels as well as the vertical metrics are given in annex A.

2.3 Bathymetry

The bathymetry is derived from two input files:

- The 2-minute bathymetry file (etopo2) of NGDC, combination of Smith and Sandwell satellite-based bathymetry (8.2 version), IBCAO (in the Arctic region) and other data in the Antarctic region. The MERCATOR project team has applied additional corrections near the Antarctic (Remy et al, 2003). This file is used for the deep ocean (below 300m) because its spatial scales are consistent over the globe.

- The GEBCO 1mn bathymetry file provided between 88S and 88N. This file is used for bathymetry on the shelf because it is found to be more accurate there (above 200m).

The interpolation onto the model grid has been conducted by taking all the original grid points falling into an ORCA025 grid box, and taking the median of those points. This procedure produces a smoothing of the sub-grid scale topography. The two bathymetries are combined with a linear ramping between 200m and 300m to transition from Gebco to Etopo2. The topography has been smoothed by two passes of a uniform shapiro filter with weight w=0.6, and hand editing has been performed in key areas. The land/sea mask has been edited by hand by the MERCATOR team.

The experiment is run using the partial cell representation of the topography (key_partial_steps). The following values are used to calculate the partial cell layer thicknesses (in namelist `namdom`: `e3zps_min = 25.` and `e3zps_rat = 0.2`.

A list of hand editions made for this run is given in Annex B. There are substantial modifications compared with the original version of 2004 found on the DRAKKAR web site. A first series of modifications was made in the Indonesian Throughflow region by Ariane Koch Larrouy who runs a limited-area model forced at the boundaries by ORCA025-G32 (Larrouy, Madec et al, in preparation). A second series was made in the

Gulf of Cadiz following the work of R. Almar and S. Theetten (2005). This work was initiated following our finding that Mediterranean waters as well as overflow waters did not sink to the right depth in ORCA025. The results of the tests, as well as the experiments of G. Hervieux (LEGI) confirmed the small influence of the existing parameterizations in the NEMO code: advective and diffusive bottom boundary layer, as well as enhanced bottom friction downstream of the straits. A "cliff" approach was attempted for the Mediterranean outflow, which is to dig a narrow channel from the Gibraltar Strait to the right depth (1200m). This was found to produce mediterranean water at the right depth but too warm and too saline. Despite these flaws we have preferred it to the previous solution (mediterranean water with more or less the right temperature and salinity but too high in the water column). However, after running the model for seven and a half year, we decided that the spurious increase of temperature and salinity at 1000 m in the Atlantic was not tolerable. A relaxation to observed T and S has been introduced only in layers 21 to 26 (637 to 1297m), in a gaussian patch of radius 80 km centered at 36°N, 7°W. The maximum relaxation coefficient was first 3 days but it was reduced to 6 days in 1969.

The cliff approach is also applied to Denmark Strait. The strait is widened and a channel is dug downstream of the deep outflow. We note that in a short experiment with NATL4, the effect of widening Denmark Strait by a factor of two did not lead to an increase of the overall transport because the velocities became smaller in the same proportion as the increase in area. The properties of the waters downstream improved somewhat, and the overturning increased by at least one Sverdrup.

2.4 Initial conditions

The initial conditions for temperature and salinity were derived from the Levitus 98 data set for the mean and low latitudes. For high latitudes PHC climatology was used instead. For the Mediteranean Sea, **medatlas** climatology was used. The initial condition for the sea ice is taken from ORCA025-G45b, a previous run with a climatological CORE forcing. This initial condition corresponds to mean January of year 10 of the G45b experiment.

3 Forcings

3.1 Runoffs

A new runoff file has been calculated using the Dai and Trenberth dataset (Dai and Trenberth, 2002) by Romain Bourdalle-Badie at Mercator:
runoff_coast1pt_ant3pt_obtaz_1m_ORCA025.nc. It includes 99 major rivers and coastal runoffs; the total annual mean input is 1.31 Sv. It is a monthly climatology. A report describing the method is found on the DRAKKAR web site (Bourdalle-Badie and Treguier, 2006). We use the namelist variable `nrunoff=2`. In that case, a special treatment is applied in runoff regions, where the array *upsrnfh* is non zero. This array is read in the runoff file (netcdf variable *socoefr*). It has a value of zero where there is no runoff and 0.5 at runoff points. Since we do not use the centered scheme, there is no need to revert

to upstream near runoffs (the TVD advection scheme is used everywhere). In our case the special treatment consists in an enhanced vertical diffusion at the interface of layers 1 and 2 applied in step.F90 (Drakkar configuration manager version):

```
avt  (:,:,2) = avt  (:,:,2) + 2.e-3 * upsrnfh(:,:)
```

The vertical mixing is then set to 10^{-3} below the top level at runoff points.

3.2 Atmospheric forcing files

The forcing dataset is called DRAKKAR forcing set 3 (DFS3), (Brodeau and Barnier 2006, document in preparation). The early ORCA025 experiments in 2004 used DRAKKAR set 1 (Talandier, 2004). We use a blend of data from various origin and different frequencies. Some come from the CORE dataset assembled by W. Large (available on the GFDL web site); others come from the ECMWF reanalysis ERA40. Note that ERA40 stops in 2002 so that *there is a discontinuity in forcing in 2002* (see last paragraph of this section). Some ERA40 variables, provided at 2 m hight, are corrected to height 10 m. For the correction, the iterative algorithm provided by Large and Yeager (2004) is applied to the following ERA40 variables : temperature at 2m, specific humidity at 2m, scalar wind at 10m and atmospheric pressure. Prior to this correction, specific humidity at 2m is computed from the dew-point at 2m and atmospheric pressure.

The input files are the following:

- **Air temperature and specific humidity :** 6 hourly values from ERA40, corrected as indicated above.
- **Solar and infra-red downwelling radiation :** Daily values from satellites (ISCCP, Zhang et al. 2004). The corrected version of this product available into the CORE dataset is used. (`qsw_CORE.nc` and `qlw_CORE.nc` for short-wave=solar and long-wave=infra-red).
- **Precipitation (total precipitation and snow) :** Monthly fields from CORE, but with correction. Southward to 20°N, the standard CORE product is used. Northward to 30°N the uncorrected CORE product (GXGXS or Serreze) is used, because we believe that the global correction applied by Large and Yeager to the "corrected" CORE dataset is unwarranted in the northern hemisphere. The two products are blended between 20°N and 30°N. Using the standard CORE product has proven to lead to highly positive global freshwater imbalance both with model simulations and fixed SST off-line tests, leading to a consequent sea level rise. It is also emphasized that the standard CORE precipitation is over-estimated on the nordic seas. Using the proposed blending is expected to solve these two issues since the GXGXS provides much less precipitation at every latitude, especially in the north. Off-line flux computation with prescribed SST showed that along the period 1979-2000 the global freshwater imbalance is +17 mm/year with the standard CORE precipitation while it is -12 mm/year with the proposed DFS3 precipitation product. A zero imbalance was not a the purpose of this correction

since, in our experience, model simulations react differently than these off-line tests.

The turbulent fluxes, outgoing radiation and albedo are calculated using the formulae proposed with the CORE dataset (Large and Yeager, 2004).

The ERA40 reanalysis stops in early 2002. The first part of the ORCA025-G70 experiment has been carried out until the end of 2001, and we have switched to a new forcing set for years 2002-2004. The CORE radiative fluxes and precipitations are available through the end of 2004. The other variables are taken from the ECMWF analysis provided through a partnership with MERCATOR-Ocean. We have verified a good continuity of the wind and air temperature between the two datasets.

On the other hand, the air humidity differs considerably between ERA40 and ECMWF in the low latitudes. The mean ECMWF specific humidity in this region (20°S 20°N) is about 0.5 g/kg lower than the former ERA40 value. It is also interesting to note that contrary to ERA40, the ECMWF humidity perfectly fits the values of the humidity provided by the CORE dataset (NCEP humidity modified following Large and Yeager, 2004). The spurious decrease of humidity in the equatorial region from 2001 to 2002 is expected to enhance the evaporation and is thus likely to create a cold surface temperature bias in our model. The fact that the simulation prior to ECMWF data integration was actually showing a warm surface bias in this region gave us reasons to believe that the ECMWF humidity was more realistic, so we have applied no correction. Examination of time series of sea surface temperature in the Pacific shows indeed an ajustment of the ocean model in 2002, towards a value in better agreement with TAO buoys.

3.3 Interpolation

The forcing fields are preprocessed and interpolated using the int2df interpolation package (Brodeau 2004), available at :
http://laurent.brodeau.free.fr/f90/interpol/int2df-v0.3.tar.gz
The algorithm used follows Akima, 1974 : "A method of bivariate interpolation and smooth surface fitting based on local procedures". Prior to the interpolation, the GAP procedure implemented into int2df is used to extrapolate sea values onto an extended land mask, this avoids some coastal land values influencing the interpolation process. Moreover, gridded data fields extracted from spectral models such as NCEP and ECMWF have the disadvantage to propagate erroneous land values onto the sea through spatial features resembling waves especially in the vicinity of coastal mountain ranges. That is why an extended land mask has been created to flag such coastal regions. These regions may be of primary importance, such as the coast of Chile where non-treated winds would hardly generate any upwelling. Another important feature of the interpolation process is the rotation of the wind vector onto distorted regions of the target grid (northward 40°N for ORCA grids).

3.4 Katabatic winds

A modification is made to the wind forcing to improve the representation of the katabatic winds around Antarctica (Mathiot and barnier, 2005). This is done by multiplying the two components of the wind stress by a coefficient read on `katamask.nc` file. This coefficient and its area of application around Antarctica has been determined by comparison over the period 1980-1989 of ERA40 with a downscaling of ERA40 on the Antarctic carried out with the regional atmospheric model MAR designed for the simulation of katabatic winds (H. Gallée, LGGE). The coefficient is constant in time, but has a geographical dependence and an extent over the ocean which fits the results of MAR. This correction of the katabatic winds has been validated by a series of simulations long of 10 years, carried out with a model of the ACC extracted from ORCA05, and driven at its open boundary by the solution of ORCA05-G42 (on going PhD Thesis of Pierre Mathiot).

3.5 Forcing parameters

The forcing routine and the ice model are called only once every two hours, e.g. 5 time steps (`nfice=5` and `nfbulk=5`) in the namelist namdom. There is relaxation to sea surface salinity (monthly climatology of Levitus/PHC). The coefficient (m/day) is set in the new namelist:

```
&namsbc
   cdmp = 0.1666666667
```

This value is chosen by consistency with the "strong relaxation" cases in the CORE papers by Griffies *et al.*, 2006. It amounts to a decay time of 60 days for 10 m of water depth. We decided to maintain SSS restoring under the ice cover with a 5-time enhanced coefficient (12 days for 10 m). We also add extra restoring for the Red Sea and Med Sea (decay in the Alboran Sea) (oce_sbc_dmp routine).

3.6 Miscellaneous

We use the standard NEMO scheme for penetrative solar radiation, based on clear water only. It does not take into account data of water colour. We use a geothermal heat flux, spatially constant, of 86.4 10^{-3}W.m^{-2}.

Note that there is no representation of the diurnal cycle in this experiment: this would require a vertical resolution of 1 m in the upper layers (Bernie and Madec, personal communication).

Finally, there is relaxation to climatological temperature and salinity in a small region in the Gulf of Cadiz (see details in the "bathymetry" section). We relax to the initial temperature and salinity of january, with no seasonal cycle, but the seasonal cycle is small in the relaxation zone (below 637 m).

3.7 Sea surface height adjustment

We do not use any SSH adjustment. We set `ln_fwb = .false.` in the namelist. No attempt is made to ensure that the correction term (erp) by relaxation to observed SSS had a zero integral over the global ocean (suppression of the adjustments using "aplus" and "aminus" in routine `ocesbc.F90`). All experiments with CORE forcings had an increase of the global SSH, and so was the case of an hybrid forcing experiment with the 1/2° global model (ORCA05-G60). To minimize this drift, precipitations have been reduced compared with previous cases (section 3.2).

4 Ice model

Modification to the standard ice parameters have been suggested at the 2006 january DRAKKAR meeting and tried in experiment ORCA025-G50, but they were found to cause problems. We revert to the same parameters as the first CORE climatological run (ORCA025-G42)

```
&namicerun
   ln_limdyn    = .true.
   acrit   = 1.0e-06 , 1.0e-06
   hsndif  = 0.0
   hicdif  = 0.0
/
&namiceini
   ln_lim_ini = .true.
   ttest = 2.0
   hninn = 0.5
   hginn = 3.0
   alinn = 0.05
   hnins = 0.1
   hgins = 1.0
   alins = 0.1
/
&namicedyn
   epsd   = 1.0e-20
   alpha  = 0.5
   dm     = 0.6e+03
   nbiter = 1
   nbitdr = 100
   om     = 0.5
   resl   = 5.0e-05
   cw     = 5.0e-03
   angvg  = 0.0
   pstar  = 1.0e+04
   c_rhg  = 20.0
   etamn  = 0.0e+07
   creepl = 2.0e-08
   ecc    = 2.0
   ahi0   = 200.e0
/
&namicetrp
```

```
   bound  = 0.
/
&namicethd
   hmelt   = -0.15
   hiccrit = 0.6 , 0.3
   hicmin  = 0.2
   hiclim  = 0.05
   amax    = 0.999
   swiqst  = 1.
   sbeta   = 1.
   parlat  = 0.0
   hakspl  = 0.5
   hibspl  = 0.5
   exld    = 2.0
   hakdif  = 1.0
   thth    = 0.2
   hnzst   = 0.1
   parsub  = 1.0
   alphs   = 1.0
/
```

5 Parametrizations

All runs are performed with the free surface, constant volume formulation (`key_dynspg_flt` defined).

5.1 Advection schemes:

We use TVD for tracers (`ln_traadv_tvd = .true.`). We use the new momentum advection scheme suitable for partial step topography (`ln_dynvor_een = .true.`).

5.2 Lateral mixing:

-tracer : a laplacian isopycnal diffusion is used with `aht0= 300`$\mathtt{m}^2\mathtt{/s}$ at the equator. The coefficient decreases polewards proportionally to the grid size. Associated keys are key_traldf_c2d and key_ldfslp.

-dynamics : A biharmonic horizontal viscosity is used with `ahm0=` $-1.5\ 10^{11}\ \mathtt{m}^4\mathtt{/s}^2$. The viscosity depends on the grid size with δx^3.

In early runs by MERCATOR, the equatorial undercurrent in the Pacific was too energetic. Because of this, an additional laplacian viscosity had been added in a narrow equatorial band (-2 °S, 2 °N) upper layers, with a value of 500 m2/s, in the DRAKKAR runs made in 2004. We have found later that the new advection scheme slows down the equatorial undercurrent. We suppress this additional viscosity.

5.3 Bottom boundary layer:

A diffusive bottom boundary layer is activated using `key_trabbl_dif` with `atrbbl` =1000 $m^2.s^{-1}$. The advective boundary layer has been tested in the North Atlantic regional configuration NATL4 with only a small effect (small compared with the improvements found in the FLAME model). We keep the advective BBL scheme all the same (`key_trabbl_adv`).

5.4 Vertical mixing:

There is no double-diffusive mixing.

-tke: TKE is used to compute the vertical mixing. We use the new version of the TKE routine recently proposed by Gurvan MADEC with the following namelist parameters

```
!-----------------------------------------------------------------------
!       namtke   turbulent eddy kinetic dependent vertical diffusion
!                ( #ifdef "key_zdftke" )
!-----------------------------------------------------------------------
!  ln_rstke flag to restart with tke from a run without tke (default F)
!  ediff    coef. to compute vertical eddy coef. (avt=ediff*mxl*sqrt(e) )
!  ediss    coef. of the Kolmogoroff dissipation
!  ebb      coef. of the surface input of tke
!  efave    coef. to applied to the tke diffusion ( avtke=efave*avm )
!  emin     minimum value of tke (m^2/s^2)
!  emin0    surface minimum value of tke (m^2/s^2)
!  nitke    number of restart iterative loops
!  ri_c     critic richardson number
!  nmxl     flag on mixing length used
!           = 0 bounded by the distance to surface and bottom
!           = 1 bounded by the local vertical scale factor
!           = 2 first vertical derivative of mixing length bounded by 1
!  npdl     flag on prandtl number
!           = 0 no vertical prandtl number (avt=avm)
!           = 1 prandtl number function of richarson number (avt=pdl*avm)
!           = 2 same as = 1 but a shapiro filter is applied on pdl
!  nave     =  horizontal averaged (=1/2) or not (=0) of avt  (default =1)
!  navb     = 0 cst background avt0, avm0 / =1 profile used on avtb
!  ln_lsfc  computation surface value of buoyancy lenght scale as function of wind stress
!  lmin     buoyancy lenght scale minimum value if ln_lsfc = F
!  n_etau   test param. to add tke induced by wind
!            = 0 no add tke induced by wind
!            = 1 add tke induced by wind
!            = 2 add tke induced by wind only at the base of the mixed layer
!  fr_emin  fraction of TKE surface value which penetrates inside the thermocline
!  ln_lc    flag to take into account  Langmuir circulation
!  c_lc     coef to compute verticla velocity of LC
&namtke
   ln_rstke = .false.
   ediff =       0.1
   ediss =       0.7
   ebb   =       60.
```

```
   efave =        1.
   emin  =     1.e-6
   emin0 =     1.e-4
   nitke =       50
   nmxl  =        3
   npdl  =        1
   navb   =       0
   nave   =       1
   ln_lsfc =  .true.
   lmin    =    0.4
   n_etau =       1
   nhtau  =       3
   fr_emin =     0.05
   ln_lc =   .true.
   c_lc  =    0.15
```

The key modification made to tke is `fr_emin`, the proportion of energy allowed to enter into the stratified ocean below the mixed layer. This is meant to represent mixing by unresolved turbulence due to surface waves and swell. It is supposed to improve the depth of summer mixed layers that were too shallow in experiment G42. The parameter nhtau is changed from ORCA025-G50 (it used to be 1). It sets the scheme for the penetration of this energy. The depth is hardwired in the routine. It used to be 40m with a decrease to 5m at the equator. With `nhtau=3`, the depth is allowed to be different in different hemispheres, but finally after testing we set it to 30m in both hemispheres. We want to avoid unrealistic mixing under the ice. For this reason, the Langmuir cells contribution is removed under the ice, and the background coefficient is reduced (see next paragraph).

-background and convection: The enhanced vertical diffusion is used when convection is diagnosed. The corresponding namelist block is :

```
!-----------------------------------------------------------------------
!       namzdf   vertical physics
!-----------------------------------------------------------------------
!  ln_zdfevd  enhanced vertical diffusion         (default T)
!  ln_zdfnpc  Non-Penetrative Convection          (default T)
!  avm0       vertical eddy viscosity for the dynamic (m2/s)
!  avt0       vertical eddy diffusivity for tracers (m2/s)
!  avevd      vertical coefficient for enhanced diffusion scheme (m2/s)
!  nevdm      = 0  apply enhanced mixing on tracer only
!             = 1  apply enhanced mixing on both tracer and momentum
!  ln_zdfexp   vertical physics: (=T)  time splitting (T)     (Default=F)
!                                (=F)  euler backward (F)
!  n_zdfexp   number of sub-timestep for time splitting scheme
&namzdf
   ln_zdfevd = .true.
   ln_zdfnpc = .false.
   avm0     = 1.e-4
   avt0     = 1.e-5
   avevd    =   10.
   nevdm    =     1
```

```
      ln_zdfexp =  .false.
      n_zdfexp =      3
   /
```

In the previous version of TKE there was an enhancement of the background by a factor of 10 in the top layer (and 5 and 2.5 in the second and third) in order to avoid too shallow mixed layers in summer. This is suppressed in the new version of TKE. The background coefficient is divided by a factor of 10 under the ice.

5.5 Bottom friction and lateral boundary condition

The namelist is the following. We use a spatially variable coefficient: the bottom friction coefficient is multiplied by `bfrien=50` in Torres Strait: this is to reduce the flow through this strait, that is observed to be small.

```
!-----------------------------------------------------------------------
!       nambfr   bottom friction
!-----------------------------------------------------------------------
!  nbotfr  type of bottom friction
!                  nbotfr = 0 , no slip
!                  nbotfr = 1 , linear friction
!                  nbotfr = 2 , nonlinear friction
!                  nbotfr = 3 , free slip
!  bfri1   bottom drag coefficient (linear case)
!  bfri2   bottom drag coefficient (non linear case)
!  bfeb2   bottom turbulent kinetic energy  (m^2/s^2)
!  ln_bfr2d:  flag for 2d coef enhancement read in file
!  bfrien:  enhancement coefficient (integer > 1)
&nambfr
   nbotfr =       2
   bfri1  =   4.e-4
   bfri2  =   1.e-3
   bfrien = 50
   ln_bfr2d = .TRUE.
   bfeb2  =  2.5e-3
/
```

The lateral boundary condition is free slip (a test with no-slip was made in 2004 and the results were not good, Thierry Penduff, publication in preparation). We modify it locally to decrease the transport at some straits. The following modifications are made in dommsk.F90:

```
IF( cp_cfg == "orca" .AND. jp_cfg == 25 ) THEN  ! ORCA R025 configuration
  !                                             !  ======================
  ii0 = 212    ;   ii1 = 212        ! East of Ombai strait
  ij0 = 464    ;   ij1 = 465   ;   fmask( mi0(ii0):mi1(ii1) , mj0(ij0):mj1(ij1), 1:jpk ) =  2.0
  IF(lwp) WRITE(numout,*)
  IF(lwp) WRITE(numout,*) '            orca_r025: fmask = 2 at the East Ombai Strait'
  ii0 = 210    ;   ii1 = 211        ! West of Ombai strait
  ij0 = 466    ;   ij1 = 466   ;   fmask( mi0(ii0):mi1(ii1) , mj0(ij0):mj1(ij1), 1:jpk ) =  2.0
  IF(lwp) WRITE(numout,*)
  IF(lwp) WRITE(numout,*) '            orca_r025: fmask = 2 at the West Ombai Strait '
```

```
  ii0 = 210    ;   ii1 = 210        ! exit of Ombai strait
  ij0 = 464    ;   ij1 = 465   ;   fmask( mi0(ii0):mi1(ii1) , mj0(ij0):mj1(ij1), 1:jpk ) =  2.0
  IF(lwp) WRITE(numout,*)
  IF(lwp) WRITE(numout,*) '            orca_r025: fmask = 2 at the exit of Ombai Strait '
  ii0 = 172    ;   ii1 = 175        ! Lombok strait
  ij0 = 463    ;   ij1 = 463   ;   fmask( mi0(ii0):mi1(ii1) , mj0(ij0):mj1(ij1), 1:jpk ) =  2.0
  IF(lwp) WRITE(numout,*)
  IF(lwp) WRITE(numout,*) '            orca_r025: fmask = 2 at the Lombok Strait'
          !
ENDIF
```

and further modifications:

```
 ! Locally modify shlat :
 IF( cp_cfg == "orca" .AND. jp_cfg == 025 ) THEN
    !                                        ! ======================
    ! Increased lateral friction in          !  ORCA_R025 configuration
    ! the vicinity of some straits           ! ======================
    !
      !! Gibraltar strait and Gulf of Cadiz
      ij0 = 652    ;   ij1 = 654
      ii0 = 1125   ;   ii1 = 1127
      zshlat=3
      DO jj = mj0(ij0),mj1(ij1)
         DO ji = mi0(ii0), mi1(ii1)
            IF( fmask(ji,jj,jk) == 0. ) THEN
              fmask(ji,jj,jk) = zshlat * MIN( 1., MAX( zwf(ji+1,jj), zwf(ji,jj+1),   &
                  &                                    zwf(ji-1,jj), zwf(ji,jj-1)  )  )
            ENDIF
         END DO
      END DO
    !
  ENDIF
```

6 miscellaneous:

-timestep : The time steps is set to 1440 s (60 steps/day).

-hpg implicit : The semi-implicit scheme is applied to allow a larger time step (a factor of two on the cfl criterion linked with internal wave propagation).

-asselin : the asselin coefficient is taken to 0.1

7 Simulation strategy

The present run starts in 1958 (first year of ERA40 and CORE), directly with the inter-annual varying forcing. We prefer to avoid a long spin up with either climatological or repeated year (the 8 years spin up using year 1958 in ORCA025-G50 was not conclusive).

8 Transient tracers

The bomb C14 and CFCs forcings are provided by Zouhair Lachktar and James Orr. The tracers use the same parameterizations as the physics (isopycnal mixing) and the TVD advection scheme.

The transients tracers are supposed to start with zero initial conditions near year 1950. To overcome the problem of the missing years we use as initial conditions the tracer distribution of the year 1959 of ORCA025-G50. This should not be a big problem since the tracer concentrations remain quite small in the 50s. Tracers begin after one year of dynamical run in order to avoid the initial geostrophic adjustment of the dynamics.

9 Model outputs

9.1 Archived fields

Files are stored every 5 days (nwrite = 300 steps). 3D variables are U, V, T, S, W, K_z. K_z is a time-average of the total vertical mixing including convection events (suitable for off-line tracer calculations). Two dimensional fields are taux and tauy (in U and V files) and in the "grid T" files:

sossheig Sea surface height (in meters)

somxl010 Mixed layer depth (in m) based on a σ_0 difference of 0.01 with the surface

soheflds Net Downward Heat Flux (in W.m^{-2})

soshflds Short wave downward radiative flux (in W.m^{-2})

sowaflup Net upward water flux in kg.m^2.s^{-1} (forcing of the sea surface height)

sowafldp Surface water flux damping in kg.m^2.s^{-1}

iowaflup Ice-ocean water flux in kg.m^2.s^{-1}

sowaflcd Concentration-dilution water flux (the product of this flux with surface salinity is the forcing term in the salinity equation)

solhflup Latent heat flux (in W.m^{-2})

solwflds Long wave downward radiative flux (in W.m^{-2})

sosbhfup Sensible heat flux (in W.m^{-2})

9.2 Storage strategy

Although we have thought about storage in 16 bits, for now the netcdf variables are floats with 32 bits. For best performances, the output are written by each processor in direct acces files. Those files are recombined immediately after the experiment (see Molines (2004) [13] for more details). The output files stored on gaya at IDRIS are 5 days averages. They are netcdf files very similar to classical OPA netcdf output, excepted for a few differences:

- one file for each 5-day average
- definition of time_counter: The time_counter gives the number of seconds since the begining of the run.
- naming convention for the files: There are 5 types of files; 4 corresponds to the different grid points: gridT, gridU, gridV and gridW; a fifth type of file corresponds to the ice model output. File names are almost self explanatory: (*e.g.* ORCA025-G22_y0010m10d03_gridT.nc or ORCA025-G22_y0010m10d03_icemod.nc). The time indicated in the name of the file corresponds to the date at the **end** of the period used to time-average the data.
- archiving the results: The results are archived on rcli002@gaya:ORCA025/. Data are organized in many directories. Raw results from the run are stored under ORCA025-*CASE*-S (one sub-directory per year then). Mean values computed from the raw results are stored in ORCA025-*CASE*-MEAN. There are monthly means, quarterly means and annual means (one sub-directory per year). Interannual means are also computed. The implementation of this directory tree for archiving the results, is part of the strategy used in DRAKKAR to share different configurations between groups of users (see Molines *et al.*(2004) [14]).

Note that the special value on land is zero. This is properly referenced in the header of each file (and causes problems with older versions of the "ncra" software).

10 Numerics

10.1 Domain decomposition

ORCA025 runs on massively parallel computer, using a domain decomposition technique. Processors that corresponds to land are eliminated in the initialisation procedure; in the ORCA025 case, the decomposition is done on 18×12 processors, but only 186 are used. The choice of the best processor layout is done during a pre-processing phase (see details in Molines (2004) [12]). The message passing between processors is explicitly done using the MPI library (option "isend").

10.2 Performance on the IDRIS IBM HPC (zahir)

This configuration is implemented on the IDRIS IBM HPC (zahir), and run on 186 processors, using 47 nodes of 4-processor p655. The communications between the nodes is done via a 'federation' switch which gives excellent performance. The best performance is achieved using the namelist option `c_mpi_send = 'I'`, for message passing (about 30% better than mpi_bsend!). The performance has been tested with the other solver (nsolv=2) and extra halos to reduce communications: it does not bring a significant gain.

References

[1] Almar, Raphael, 2005: Etude de la sortie des eaux Mediterranéennes dans la configuration NATL4 du projet DRAKKAR. Rapport de stage de Master 1 Ocean-Atmosphere de l'université Paul Sabatier, encadrement S. Theetten.

[2] Barnier, B., G. Madec, T. Penduff, J.M. Molines, A.M. Treguier, J. Le Sommer, A. Beckmann, A. Biastoch, C. Böning, J. Dengg, C. Derval, E. Durand, S. Gulev, E. Remy, C. Talandier, S. Theetten, M. Maltrud, J. McClean, B. De Cuevas 2006: Impact of partial steps and momentum advection schemes in a global ocean circulation model at eddy permitting resolution. Ocean Dynamics, DOI: 10.1007/s10236-006-0082-1.

[3] Bourdallé-Badie R., and A.M. Treguier, 2006: A climatology of runoff for the global ocean-ice model ORCA025. MERCATOR report MOO-RP-425-366-MER.

[4] Brodeau, L, 2004: A comparison between two interpolation tools. Drakkar report, available at www.ifremer.fr/lpo/drakkar

[5] Dai A., and K.E. Trenberth, 2002: Estimates of freshwater discharge from continents: latitudinal and seasonal variations. Journal of hydrometeorology, 3, 660-687.

[6] Dencausse G., 2005: Etude de variabilité des fronts et du transport global de l'ACC dans un modèle global au 1/4°, Rapport de stage du Master 2 option OcÃ©anographie physique (Université de Bretagne Occidentale). Encadrement: S. Speich et A.M. Treguier.

[7] Fichefet, T. and M.A. Morales Maqueda, 1997: Sensitivity of a global sea ice model to the treatment of ice thermodynamics and dynamics, J. Geophys. Res., 102, 12609-12646

[8] Griffies, S.M;, and C. Böning, A. Biastoch, E. Chassignet, R. Gerdes, W. LArge, B. L. Samuels, U Schweckendiek, A.M. Treguier, M. Winton, 2006: A proposal for coordinated ocean-ice reference experiments (COREs). manuscript in preparation.

[9] Large, W., and S. Yeager, 2004: Diurnal to decadal global forcing for ocean and sea-ice models: the datasets and flux climatologies. NCAR technical note: NCAR/TN-460+STR, CGD division of the National Center for Atmospheric Research. Available on the GFDL CORE web site.

[10] Tartinville B.: Description of the CLIO model version 3.0, found on the LODYC/OPA web site

[11] Talandier, C., A.M. Treguier and B. Barnier, 2003: Preparing surface flux fields using bulk formulae for the DRAKKAR project. DRO/LPO report 03-13, Brest.

[12] Molines, J.M., 2004 : How to set up an MPP configuration with NEMO OPA9 ? Drakkar technical report, Grenoble, 8pp.

[13] Molines, J.M., 2004 : Drakkar I/O strategy and implementation for MPP runs with NEMO-OPA9. Drakkar technical report, Grenoble, 13pp.

[14] Molines, J.M., A.M. Treguier and S. Theetten, 2004: Drakkar Config Manager: How to manage and share various model configurations, based on NEMO-OPA9. Drakkar technical report, Grenoble, 14pp.

[15] Mathiot P., 2005: Interactions océan glace de mer en Antarctique. Rapport de Master 2 STUE de l'Université Joseph Fourier de Grenoble. réalisé au LEGI et au LGGE. Encadrement B. Barnier et H. Gallée. Juin 2005

A Annex A

vertical levels

```
zgr_z   : Reference vertical z-coordinates
~~~~~~~

     zsur, za0, za1 computed from
             zdzmin =  6.00000000000000000
             zhmax  =  5720.00000000000000
          Namelist namzgr : value of coefficients for vertical mesh:
             zsur =  -2143.95922194325158
             za0  =  127.451110365423233
             za1  =  123.075814004137086
             zkth =  23.5629999999999988
             zacr =  9.00000000000000000

          Reference z-coordinate depth and scale factors:
     level   gdept    gdepw     e3t      e3w
        1     3.05     0.00     6.19     6.00
        2     9.45     6.19     6.64     6.40
        3    16.36    12.83     7.19     6.90
        4    23.88    20.03     7.88     7.52
        5    32.18    27.92     8.74     8.29
        6    41.44    36.68     9.80     9.25
        7    51.87    46.49    11.12    10.43
        8    63.78    57.62    12.74    11.89
        9    77.48    70.38    14.73    13.69
       10    93.39    85.13    17.18    15.89
```

11	112.01	102.33	20.16	18.60
12	133.92	122.52	23.78	21.88
13	159.82	146.33	28.14	25.86
14	190.49	174.50	33.36	30.63
15	226.85	207.90	39.54	36.32
16	269.92	247.48	46.78	43.02
17	320.80	294.31	55.16	50.83
18	380.63	349.52	64.70	59.78
19	450.57	414.27	75.38	69.90
20	531.74	489.69	87.11	81.12
21	625.09	576.84	99.72	93.32
22	731.40	676.59	112.98	106.29
23	851.17	789.58	126.59	119.76
24	984.59	916.17	140.22	133.42
25	1131.50	1056.38	153.54	146.94
26	1291.46	1209.89	166.25	159.99
27	1463.71	1376.10	178.10	172.29
28	1647.31	1554.16	188.92	183.65
29	1841.17	1743.03	198.61	193.91
30	2044.14	1941.59	207.13	203.01
31	2255.05	2148.67	214.51	210.96
32	2472.80	2363.14	220.82	217.79
33	2696.36	2583.92	226.15	223.60
34	2924.82	2810.03	230.62	228.49
35	3157.35	3040.62	234.32	232.56
36	3393.25	3274.92	237.38	235.93
37	3631.93	3512.27	239.89	238.70
38	3872.87	3752.14	241.93	240.96
39	4115.66	3994.06	243.60	242.81
40	4359.96	4237.64	244.95	244.31
41	4605.47	4482.58	246.04	245.52
42	4851.97	4728.61	246.92	246.50
43	5099.25	4975.52	247.63	247.29
44	5347.18	5223.15	248.20	247.93
45	5595.62	5471.34	248.66	248.44
46	5844.47	5720.00	249.03	248.86

B Annex B

```
!
!  Hand modifications by Anne Marie Treguier and Thierry Penduff,
!  as well as Ariane Koch Larrouy for the Indonesian throughflow region.
!  on ORCA_R025 bathymetry for partial steps.
!
! ######################################################################
! Name of the zoomed area : Torres staits
! zoom ratio :        2
! Thierry: Put some islands in G47
bathy( 279, 460) = 0  !
```

```
bathy( 279, 458) = 0  !
bathy( 279, 456) = 0  !
!
! ######################################################################
! Name of the zoomed area : Vema fracture zone
! zoom ration :        2
! i min :      946
! i max :     1012
! j min :      507
! j max :      573

bathy( 976, 543) = 4400  ! instead of 4279
bathy( 977, 543) = 4400  ! instead of 4189
bathy( 978, 543) = 4400  ! instead of 4042
bathy( 979, 543) = 4400  ! instead of 3889
bathy( 979, 542) = 4400  ! instead of 4205
bathy( 980, 542) = 4400  ! instead of 4103
bathy( 981, 542) = 4400  ! instead of 4093
bathy( 982, 542) = 4400  ! instead of 4126
bathy( 983, 542) = 4400  ! instead of 4008
bathy( 984, 542) = 4400  ! instead of 3870
bathy( 985, 542) = 4400  ! instead of 3632
bathy( 986, 542) = 4400  ! instead of 3691
bathy( 987, 542) = 4400  ! instead of 3883
bathy( 988, 542) = 4400  ! instead of 3969
bathy( 989, 542) = 4400  ! instead of 4141
bathy( 990, 542) = 4400  ! instead of 4273
!  Thierry: new bathy G45
bathy( 992, 542) = 4482  ! instead of 4273
!!!!!!!!!!!!!!!!!!!!!!!!!!!!!!
! ######################################################################
! Name of the zoomed area : Fifteen twenty fracture zone
! zoom ration :        2
! i min :      934
! i max :     1000
! j min :      522
! j max :      588

bathy( 960, 562) = 3800  ! instead of 3782
bathy( 961, 562) = 3800  ! instead of 3630
bathy( 961, 561) = 3800  ! instead of 3597
bathy( 962, 561) = 3800  ! instead of 3542
bathy( 963, 561) = 3800  ! instead of 3560
bathy( 964, 561) = 3800  ! instead of 3636
bathy( 965, 561) = 3800  ! instead of 3703

! ######################################################################
! Name of the zoomed area : Lesser Antilles
! zoom ration :        2
```

```
! i min :      868
! i max :      934
! j min :      524
! j max :      590

bathy( 903, 547) =  200  ! instead of  670
bathy( 904, 549) =  200  ! instead of  965
bathy( 905, 550) =  200  ! instead of  799
bathy( 905, 551) =  200  ! instead of  909
bathy( 905, 553) =  200  ! instead of 1686
bathy( 906, 554) =  600  ! instead of 1089
bathy( 906, 556) =  200  ! instead of 1331
bathy( 905, 561) =  200  ! instead of 1127
bathy( 905, 563) =  200  ! instead of  636
bathy( 904, 564) =  200  ! instead of  364
bathy( 904, 566) =  400  ! instead of  673
bathy( 893, 574) =  200  ! instead of 1062
bathy( 898, 574) =  200  ! instead of  849
bathy( 898, 572) =  200  ! instead of  403
bathy( 899, 572) =  200  ! instead of  405
bathy( 899, 571) =  200  ! instead of  454
bathy( 900, 570) =  489  ! instead of  489
bathy( 900, 571) =  200  ! instead of  502
bathy( 878, 574) =  300  ! instead of  541
bathy( 881, 573) =  200  ! instead of  414

! ####################################################################
! Name of the zoomed area : Florida Straits
! zoom ration :        2
! i min :      796
! i max :      862
! j min :      560
! j max :      626

bathy( 827, 599) =  800  ! instead of  707
bathy( 828, 599) =  800  ! instead of  643
bathy( 829, 599) =  800  ! instead of  552
bathy( 829, 600) =  800  ! instead of  610
bathy( 830, 600) =  800  ! instead of  719
bathy( 831, 600) =  800  ! instead of  740
bathy( 832, 601) =  800  ! instead of  747
bathy( 832, 602) =  800  ! instead of  773
bathy( 831, 602) =  800  ! instead of  761
bathy( 832, 603) =  800  ! instead of  762
bathy( 832, 604) =  800  ! instead of  714
bathy( 832, 605) =  800  ! instead of  638
bathy( 832, 606) =  800  ! instead of  598
bathy( 832, 607) =  760  ! instead of  602
bathy( 832, 608) =  760  ! instead of  610
```

```
bathy( 832, 609) =  760  ! instead of  618
bathy( 832, 610) =  760  ! instead of  627
bathy( 832, 611) =  730  ! instead of  620
bathy( 832, 613) =  730  ! instead of  585
bathy( 832, 614) =  730  ! instead of  592
bathy( 832, 615) =  730  ! instead of  622
bathy( 832, 616) =  730  ! instead of  652
bathy( 832, 617) =  730  ! instead of  681
bathy( 832, 612) =  730  ! instead of  603
bathy( 839, 591) =  600  ! instead of  334
bathy( 840, 591) =  600  ! instead of  351
bathy( 840, 590) =  600  ! instead of  554
bathy( 838, 592) =  540  ! instead of  358
bathy( 837, 592) =  500  ! instead of  311
bathy( 836, 593) =  500  ! instead of  342
bathy( 837, 593) =  500  ! instead of  340
bathy( 835, 593) =  500  ! instead of  344
bathy( 834, 594) =  500  ! instead of  434
bathy( 834, 593) =  500  ! instead of  336
bathy( 833, 594) =  500  ! instead of  451
bathy( 833, 595) =  500  ! instead of  483
bathy( 832, 595) =  500  ! instead of  475
bathy( 831, 595) =  500  ! instead of  469
bathy( 830, 595) =  500  ! instead of  485
bathy( 838, 591) =  500  ! instead of  182

! ################################################################
! Name of the zoomed area : Gibraltar
! zoom ration :        2
! i min :     1092
! i max :     1158
! j min :      616
! j max :      682

bathy(1127, 654) =  300  ! instead of  194
bathy(1126, 654) =  280  ! instead of  144
bathy(1126, 653) =  280  ! instead of  170

!
!   Water flowing downstream of Gibraltar into the Atlantic.
!   Create an artificial deep channel based on work by Sebastien Theetten
!   and Raphael Almar (2005), revised by Thierry Penduff.
bathy(1125, 653) =  800  ! instead of  320
bathy(1124, 653) =  1100 ! instead of  415
bathy(1123, 653) =  1200 ! instead of  659
bathy(1122, 653) =  1200 ! instead of  881
bathy(1121, 653) =  1200 ! instead of  881
bathy(1120, 653) =  1200 ! instead of  881
```

```
! ####################################################################
! Name of the zoomed area : Wyville-Thompson ridge, Faroe bank channel
! zoom ration :        2
! i min :     1064
! i max :     1130
! j min :      768
! j max :      834

! Thierry
bathy(1099, 803) =  1050 !
bathy(1100, 803) =  1050 !
bathy(1101, 803) =  910  !
! Anne Marie
bathy(1108, 799) =  870  ! instead of  737
bathy(1108, 800) =  870  ! instead of  737
bathy(1108, 801) =  870  ! instead of  689
bathy(1107, 802) =  870  ! instead of  602
bathy(1107, 801) =  870  ! instead of  565
bathy(1106, 802) =  870  ! instead of  536
bathy(1105, 802) =  870  ! instead of  437
bathy(1105, 803) =  870  ! instead of  575
bathy(1104, 803) =  870  ! instead of  605
bathy(1103, 803) =  870  ! instead of  644
bathy(1102, 803) =  870  ! instead of  777
bathy(1112, 793) =  600  ! instead of  760
bathy(1111, 794) =  600  ! instead of  714
bathy(1108, 795) =  600  ! instead of  727
bathy(1107, 795) =  600  ! instead of  714
bathy(1106, 796) =  600  ! instead of  668
bathy(1113, 793) =  600  ! instead of  615
bathy(1106, 797) =  600  ! instead of  660
bathy(1110, 794) =  600  ! instead of  671
bathy(1109, 794) =  600  ! instead of  662


!!!!!!!!!!!!!!!!!!!! VERSION T.PENDUFF july 12 2006
!! Create an artificial channel to bring dense water
!! down and widen the strait.
!! Name of the zoomed area : Denmark Strait

bathy(1047,834:835) =  670  ! entrance
bathy(1046,833:835) =  670  ! entrance
bathy(1045,832:834) =  670  ! entrance
bathy(1044,831:833) =  670  ! entrance
bathy(1043,830:832) =  670  !
bathy(1042,829:831) =  670  !
bathy(1041,828:830) =  670  !
bathy(1040,828:829) =  670  !
```

```
bathy(1040,827    ) =  1950  ! first flat step (BBLadv)
bathy(1039,827:828) =  1950  !

bathy(1039,826    ) =  2158  ! second flat step (BBLdiff)
bathy(1038,826:827) =  2158  !

bathy(1038,825    ) =  2595  ! outflow channel
bathy(1037,824:826) =  2595  !
bathy(1036,824:825) =  2595  !
bathy(1035,824:825) =  2595  !
bathy(1034,824:825) =  2595  !
bathy(1033,823:825) =  2595  !
bathy(1032,822:824) =  2595  !
bathy(1031,821:823) =  2595  !
bathy(1030,820:822) =  2595  !
bathy(1029,819:821) =  2595  !
bathy(1028,818:820) =  2595  !

! ####################################################################
! Name of the zoomed area : NORTH POLE !!!!!!!!!!!!!!!!
! TPENDUFF 19 JULY 2006

bathy(1062,1019) = 0.5 * ( bathy(1061,1019) + bathy(1063,1019) )

! ####################################################################
! Name of the zoomed area : Gibbs Fracture zone
! zoom ration :        2
! i min :      982
! i max :     1048
! j min :      708
! j max :      774

bathy(1008, 742) = 3650  ! instead of 3615
bathy(1009, 742) = 3650  ! instead of 3568
bathy(1010, 742) = 3650  ! instead of 3535
bathy(1011, 742) = 3650  ! instead of 3514
bathy(1011, 741) = 3650  ! instead of 3603
bathy(1012, 741) = 3650  ! instead of 3602
bathy(1013, 741) = 3650  ! instead of 3615
bathy(1014, 741) = 3650  ! instead of 3611
bathy(1015, 741) = 3650  ! instead of 3565
bathy(1016, 741) = 3650  ! instead of 3581
bathy(1017, 741) = 3650  ! instead of 3582
bathy(1018, 741) = 3650  ! instead of 3651
bathy(1020, 741) = 3650  ! instead of 3608
bathy(1021, 741) = 3650  ! instead of 3458
bathy(1022, 741) = 3650  ! instead of 3318
bathy(1023, 740) = 3650  ! instead of 3278
bathy(1022, 740) = 3650  ! instead of 3274
```

```
bathy(1024, 740) = 3650  ! instead of 3279
bathy(1025, 740) = 3650  ! instead of 3240
bathy(1026, 740) = 3650  ! instead of 3017
bathy(1027, 740) = 3650  ! instead of 2963
bathy(1028, 740) = 3650  ! instead of 3043
bathy(1029, 740) = 3650  ! instead of 3029
bathy(1030, 740) = 3650  ! instead of 3110
bathy(1030, 739) = 3650  ! instead of 2832
bathy(1031, 739) = 3650  ! instead of 3005
bathy(1032, 739) = 3650  ! instead of 3019
bathy(1033, 739) = 3650  ! instead of 3155
bathy(1034, 739) = 3650  ! instead of 3302
bathy(1035, 739) = 3650  ! instead of 3383
bathy(1036, 739) = 3650  ! instead of 3442
bathy(1037, 739) = 3650  ! instead of 3534
bathy(1038, 739) = 3650  ! instead of 3621

! ####################################################################
! Name of the zoomed area : Oceanographer fracture Zone
! zoom ration :        2
! i min :      982
! i max :     1048
! j min :      616
! j max :      682

bathy(1001, 650) = 3000  ! instead of 2924
bathy(1002, 650) = 3000  ! instead of 2882
bathy(1003, 650) = 3000  ! instead of 2864
bathy(1004, 650) = 3000  ! instead of 2892
bathy(1006, 650) = 3000  ! instead of 2904
bathy(1007, 650) = 3000  ! instead of 2736
bathy(1007, 649) = 3000  ! instead of 2453
bathy(1008, 649) = 3000  ! instead of 2655
bathy(1009, 649) = 3000  ! instead of 2766
bathy(1010, 649) = 3000  ! instead of 2754
bathy(1010, 648) = 3000  ! instead of 2687
bathy(1011, 648) = 3000  ! instead of 2662
bathy(1012, 648) = 3000  ! instead of 2704
bathy(1013, 648) = 3000  ! instead of 2811
bathy(1014, 648) = 3000  ! instead of 2907

! ####################################################################
! Name of the zoomed area : Vema channel
! zoom ration :        2
! i min :      978
! i max :     1044
! j min :      331
! j max :      397
```

```
! ####################################################################
! Name of the zoomed area : Valvis ridge South
! zoom ration :        2
! i min :     1092
! i max :     1158
! j min :      305
! j max :      371

bathy(1119, 341) = 3500  ! instead of 3607
bathy(1123, 344) = 3500  ! instead of 3801
bathy(1126, 346) = 3500  ! instead of 3665
bathy(1141, 362) = 3500  ! instead of 3932
bathy(1142, 362) = 3500  ! instead of 3832
bathy(1143, 363) = 3500  ! instead of 3693
bathy(1141, 361) = 3500  ! instead of 3891
bathy(1140, 361) = 3500  ! instead of 3699

! ####################################################################
! Name of the zoomed area : Rio de Janeiro fracture Zone
! zoom ration :        2
! i min :     1064
! i max :     1130
! j min :      375
! j max :      441

bathy(1107, 408) = 3900  ! instead of 3714
bathy(1108, 408) = 3900  ! instead of 3805
bathy(1109, 408) = 3900  ! instead of 3882
bathy(1106, 408) = 3900  ! instead of 3593
bathy(1105, 408) = 3900  ! instead of 3533
bathy(1104, 408) = 3900  ! instead of 3561
bathy(1103, 408) = 3900  ! instead of 3570
bathy(1102, 408) = 3900  ! instead of 3539
bathy(1101, 408) = 3900  ! instead of 3399
bathy(1100, 408) = 3900  ! instead of 3282
bathy(1097, 408) = 3900  ! instead of 3529
bathy(1098, 408) = 3900  ! instead of 3404
bathy(1096, 408) = 3900  ! instead of 3722
bathy(1095, 408) = 3900  ! instead of 3815
bathy(1094, 408) = 3900  ! instead of 3777
bathy(1093, 408) = 3900  ! instead of 3871
bathy(1099, 408) = 3900  ! instead of 3336

! ####################################################################
! Name of the zoomed area : Romanche fracture zone
! zoom ration :        2
! i min :     1030
! i max :     1096
```

```
! j min :      459
! j max :      525

bathy(1057, 496) = 3700  ! instead of 3849
bathy(1058, 496) = 3700  ! instead of 3925
bathy(1059, 496) = 3700  ! instead of 3937
bathy(1060, 496) = 3700  ! instead of 3942
bathy(1061, 496) = 3700  ! instead of 4060
bathy(1062, 496) = 3700  ! instead of 4177
bathy(1063, 497) = 3700  ! instead of 3995
bathy(1064, 497) = 3700  ! instead of 4011
bathy(1065, 497) = 3700  ! instead of 4041
bathy(1066, 497) = 3700  ! instead of 4044
bathy(1067, 497) = 3700  ! instead of 4051
bathy(1068, 497) = 3700  ! instead of 4306
bathy(1069, 498) = 3700  ! instead of 4106
bathy(1070, 498) = 3700  ! instead of 4153
bathy(1070, 499) = 3700  ! instead of 3847
bathy(1071, 499) = 3700  ! instead of 3871
bathy(1072, 499) = 3700  ! instead of 3977
bathy(1073, 499) = 3700  ! instead of 4142
bathy(1074, 499) = 3700  ! instead of 4280
bathy(1075, 499) = 3700  ! instead of 4403
bathy(1076, 500) = 3700  ! instead of 4133
bathy(1077, 500) = 3700  ! instead of 3974
bathy(1078, 500) = 3700  ! instead of 3919
bathy(1079, 500) = 3700  ! instead of 3820
bathy(1082, 500) = 4200  ! instead of 4183
bathy(1083, 500) = 4200  ! instead of 4070
bathy(1084, 500) = 4200  ! instead of 3850
bathy(1085, 500) = 4200  ! instead of 3668
bathy(1086, 501) = 4200  ! instead of 3755
bathy(1087, 501) = 4200  ! instead of 3832
bathy(1088, 501) = 4200  ! instead of 3853
bathy(1089, 501) = 4200  ! instead of 3906
bathy(1090, 501) = 4200  ! instead of 4013
bathy(1086, 500) = 4200  ! instead of 3665

! ####################################################################
! Name of the zoomed area : Red Sea North
! zoom ration :        2
! i min :     1266
! i max :     1332
! j min :      558
! j max :      624

bathy(1291, 608) = 1080  ! instead of  991
bathy(1291, 610) = 1080  ! instead of  988
bathy(1308, 577) = 1080  ! instead of  974
```

```
bathy(1308, 575) = 1080  ! instead of  951

! ######################################################################
! Name of the zoomed area : Red Sea south
! zoom ration :        2
! i min :     1290
! i max :     1356
! j min :      514
! j max :      580

bathy(1319, 556) =  160  ! instead of   94
bathy(1320, 556) =  140  ! instead of   87
bathy(1320, 555) =  140  ! instead of   59
bathy(1320, 554) =  140  ! instead of   45
bathy(1321, 554) =  140  ! instead of   56
bathy(1321, 553) =  140  ! instead of   58
bathy(1322, 553) =  140  ! instead of   66
bathy(1322, 552) =  140  ! instead of   44
bathy(1323, 552) =  140  ! instead of   42
bathy(1323, 551) =  140  ! instead of   48
bathy(1323, 550) =  140  ! instead of   52
bathy(1324, 550) =  140  ! instead of   71

!!!!!!!!!!!!!! New THIERRY
!bathy(1325, 549) =  140  !
!bathy(1325, 548) =  206  !
!bathy(1325, 547) =  246  !

!bathy(1324, 549) =  172  !
!bathy(1324, 548) =  245  !
!bathy(1324, 547) =  292  !
!bathy(1324, 546) =  348  !
!bathy(1325, 546) =  400  !
!bathy(1326, 546) =  553  !

!bathy(1326, 545) =  676  !
!bathy(1327, 545) =  676  !
!bathy(1327, 546) =  676  !
!bathy(1326, 547) =  553  !



!!!!!!!!!!!!!!!!!!!! VERSION T.PENDUFF july 12 2006
!! ######################################################################
!! Name of the zoomed area : Red Sea south
bathy(1329, 547) =  790
bathy(1328, 547) =  790
bathy(1327, 547) =  790
bathy(1326, 547) =  790
```

```
bathy(1325, 547) =  790
bathy(1324, 547) =  790
bathy(1323, 547) =  790
bathy(1323, 548) =  790
bathy(1323, 549) =  790

! ######################################################################
! Name of the zoomed area : Agulhas
! zoom ration :        2
! i min :     1212
! i max :     1278
! j min :      303
! j max :      369

! ######################################################################
! Name of the zoomed area : Mozambique/Comores
! zoom ration :        2
! i min :     1292
! i max :     1358
! j min :      413
! j max :      479

bathy(1341, 448) =  200  ! instead of 1094
bathy(1342, 449) =  200  ! instead of  521
bathy(1341, 449) =  450  ! instead of 1067
bathy(1337, 449) =  200  ! instead of 2751
bathy(1336, 449) =  200  ! instead of 2196
bathy(1335, 449) = 1200  ! instead of 2371
bathy(1331, 448) =  400  ! instead of 1244
bathy(1330, 448) =  400  ! instead of 1298
bathy(1328, 449) =  400  ! instead of 2117
bathy(1327, 450) =  400  ! instead of 1827
bathy(1326, 449) =  400  ! instead of 2056

! ######################################################################
! Name of the zoomed area : Mascarene Ridge
! zoom ration :        2
! i min :     1362
! i max :     1428
! j min :      409
! j max :      475

bathy(1391, 461) =  200  ! instead of  770
bathy(1391, 462) =  200  ! instead of  606
bathy(1391, 463) =  200  ! instead of  693
bathy(1376, 476) =  200  ! instead of  753
bathy(1376, 477) =  200  ! instead of  426
bathy(1363, 477) =  200  ! instead of 1070
bathy(1363, 476) =  200  ! instead of  885
```

```
bathy(1362, 475) =  200  ! instead of 1250
bathy(1395, 450) =  280  ! instead of  508
bathy(1395, 449) =  350  ! instead of  936
bathy(1395, 448) =  600  ! instead of 1714
bathy(1394, 443) =  400  ! instead of  614
bathy(1394, 444) =  600  ! instead of  978
bathy(1393, 444) =  450  ! instead of  825
bathy(1393, 445) =  450  ! instead of 1165
bathy(1393, 446) =  500  ! instead of 1546
bathy(1394, 447) = 1100  ! instead of 1823

! ####################################################################
! Name of the zoomed area : Seychelles
! zoom ration :        2
! i min :     1346
! i max :     1412
! j min :      437
! j max :      503

bathy(1363, 478) =  800  ! instead of 1683
bathy(1363, 476) =  200  ! instead of  885
bathy(1362, 475) =  200  ! instead of 1250
bathy(1362, 474) =  400  ! instead of 1537


! ####################################################################
! Name of the zoomed area : Ninety east ridge north
! zoom ration :        2
! i min :       35
! i max :      101
! j min :      479
! j max :      545

bathy(  68, 501) = 3400  ! instead of 3507
bathy(  68, 500) = 3400  ! instead of 3571
bathy(  67, 490) = 3000  ! instead of 3537

! ####################################################################
! Name of the zoomed area : ninety east ridge middle
! zoom ration :        2
! i min :       29
! i max :       95
! j min :      425
! j max :      491

bathy(  67, 479) = 3650  ! instead of 3698
bathy(  67, 477) = 3650  ! instead of 3607
bathy(  67, 478) = 3650  ! instead of 3756
bathy(  65, 460) = 3400  ! instead of 3600
```

```
!
!
!  Hand modification by Ariane Koch-Larrouy on
!  ORCA_R025 bathymetry combined coast for
!  partial step
!
! ################################################
! Name of the zomed area : Indonesian Throughflow
! i min : 89
! i max : 290
! j min : 395
! j max : 602

! Timor passage
bathy( 202, 453) = 1300.00 ! instead of   1078.23
bathy( 202, 454) = 1300.00 ! instead of   1027.36
bathy( 203, 454) = 1300.00 ! instead of   1176.71
bathy( 204, 454) = 1300.00 ! instead of   1275.38

! Torres is not closed in ORCA025-G44
! bathy( 280, 456) = 0.00000 ! instead of   5.00000
! bathy( 279, 457) = 0.00000 ! instead of   5.00000
! bathy( 279, 458) = 0.00000 ! instead of   5.00000
! bathy( 279, 459) = 0.00000 ! instead of   5.00000
! bathy( 279, 460) = 0.00000 ! instead of   5.00000
! bathy( 279, 461) = 0.00000 ! instead of   5.00000

! land retreived between Lombok and Sape
bathy( 177, 463) = 195.000 ! instead of   0.00000
bathy( 178, 463) = 300.000 ! instead of   0.00000
bathy( 179, 463) = 400.000 ! instead of   0.00000
bathy( 180, 463) = 566.531 ! instead of   0.00000

! Sape
bathy( 187, 464) = 0.00000 ! instead of   202.594
bathy( 188, 464) = 0.00000 ! instead of   123.500
bathy( 187, 465) = 0.00000 ! instead of   104.000
bathy( 188, 465) = 0.00000 ! instead of   197.500

! Iles d'Alor
bathy( 203, 465) = 0.00000 ! instead of   241.048
bathy( 205, 465) = 0.00000 ! instead of   1010.97

! Ombai
bathy( 209, 465) = 1800.00 ! instead of   1759.98
bathy( 211, 465) = 1800.00 ! instead of   1671.20
bathy( 212, 465) = 1800.00 ! instead of   1401.44
bathy( 213, 465) = 1800.00 ! instead of   1193.37
```

```
bathy( 211, 466) = 1350.00 ! instead of   2057.59
bathy( 212, 466) = 0.00000 ! instead of   2003.67
bathy( 213, 466) = 1800.00 ! instead of   1728.50
bathy( 214, 466) = 1800.00 ! instead of   1682.30
bathy( 216, 466) = 1800.00 ! instead of   1758.57
bathy( 213, 467) = 0.00000 ! instead of   1995.10
bathy( 213, 468) = 0.00000 ! instead of   2735.98

! Molucca strait
bathy( 219, 505) = 4.00000 ! instead of   1758.61
bathy( 220, 505) = 0.00000 ! instead of   761.723
bathy( 217, 500) = 2300.00 ! instead of   2168.49
bathy( 217, 501) = 2300.00 ! instead of   2114.26
bathy( 216, 502) = 2300.00 ! instead of   2176.77
bathy( 217, 502) = 2300.00 ! instead of   2148.22
bathy( 216, 503) = 2200.00 ! instead of   2018.43
bathy( 217, 503) = 2300.00 ! instead of   2071.52
bathy( 216, 504) = 2200.00 ! instead of   1894.76
bathy( 217, 504) = 2300.00 ! instead of   1991.11
bathy( 213, 505) = 1760.00 ! instead of   1847.67
bathy( 214, 505) = 1650.00 ! instead of   1759.12
bathy( 216, 505) = 2200.00 ! instead of   1727.12
bathy( 217, 505) = 2300.00 ! instead of   1999.43
bathy( 218, 505) = 2300.00 ! instead of   2070.33
bathy( 216, 506) = 2200.00 ! instead of   1792.68
bathy( 217, 506) = 2200.00 ! instead of   2139.05
bathy( 218, 506) = 2300.00 ! instead of   2162.49
bathy( 217, 507) = 2200.00 ! instead of   2176.00
bathy( 218, 507) = 2300.00 ! instead of   2191.92
bathy( 217, 508) = 2200.00 ! instead of   2114.59
bathy( 218, 508) = 2300.00 ! instead of   2241.65
bathy( 219, 508) = 2300.00 ! instead of   2258.27
bathy( 217, 509) = 2200.00 ! instead of   2028.10
bathy( 218, 509) = 2200.00 ! instead of   2270.84

! Malacca Strait
bathy( 120, 506) = 0.00000 ! instead of   9.00000

! Sangihe Ridge
bathy( 210, 506) = 2.00000 ! instead of   295.509
bathy( 211, 507) = 1000.00 ! instead of   1368.63
bathy( 212, 508) = 2.00000 ! instead of   1442.14
bathy( 212, 510) = 2.00000 ! instead of   1160.36
bathy( 213, 514) = 50.0000 ! instead of   254.383
bathy( 213, 515) = 500.000 ! instead of   825.242
bathy( 213, 516) = 200.000 ! instead of   815.492
bathy( 213, 517) = 4.00000 ! instead of   839.386
bathy( 218, 517) = 0.00000 ! instead of   996.012
bathy( 213, 518) = 800.000 ! instead of   1035.70
```

```
bathy( 213, 519) = 1300.00 ! instead of   1526.46
bathy( 218, 519) = 0.00000 ! instead of   2027.63
bathy( 212, 520) = 4.00000 ! instead of   1947.67
bathy( 218, 520) = 0.00000 ! instead of   2984.29
bathy( 212, 521) = 0.00000 ! instead of   1521.66
bathy( 217, 521) = 0.00000 ! instead of   3147.63
bathy( 217, 522) = 0.00000 ! instead of   3276.00
bathy( 217, 523) = 0.00000 ! instead of   3154.99
bathy( 217, 524) = 0.00000 ! instead of   3272.37
bathy( 215, 525) = 0.00000 ! instead of   1061.76
bathy( 215, 526) = 0.00000 ! instead of   249.692

! Sumba
bathy( 189, 462) = 610.000 ! instead of   520.226
bathy( 190, 462) = 610.000 ! instead of   496.277
bathy( 191, 462) = 610.000 ! instead of   571.018
bathy( 190, 463) = 167.000 ! instead of   466.042

! sortie Savu
bathy( 197, 456) = 0.00000 ! instead of   770.963
bathy( 198, 456) = 0.00000 ! instead of   859.907
bathy( 199, 456) = 1041.11 ! instead of   956.650
bathy( 204, 457) = 100.000 ! instead of   299.308
bathy( 195, 458) = 1100.00 ! instead of   1023.69

! Luzon strait
bathy( 194, 575) = 200.000 ! instead of   667.179
bathy( 195, 576) = 100.000 ! instead of   239.656
bathy( 196, 577) = 0.00000 ! instead of   625.711
bathy( 196, 578) = 850.000 ! instead of   826.502
bathy( 196, 579) = 650.000 ! instead of   1396.10
bathy( 196, 580) = 1100.00 ! instead of   1909.46
bathy( 196, 581) = 850.000 ! instead of   2351.54
bathy( 196, 582) = 650.000 ! instead of   2642.53
bathy( 196, 583) = 2.00000 ! instead of   2756.72
bathy( 196, 584) = 150.000 ! instead of   2773.34
bathy( 194, 586) = 1200.00 ! instead of   1533.90

! Molucca Strait
bathy( 232, 496) = 7.00000 ! instead of   50.0000
bathy( 231, 497) = 2.00000 ! instead of   111.500
bathy( 230, 498) = 2.00000 ! instead of   313.281
bathy( 231, 498) = 2.00000 ! instead of   13.0000
bathy( 229, 499) = 147.000 ! instead of   405.520
bathy( 228, 500) = 2.00000 ! instead of   691.682
bathy( 225, 501) = 2.00000 ! instead of   289.244
bathy( 226, 501) = 300.000 ! instead of   560.011
bathy( 227, 501) = 700.000 ! instead of   730.845
```

```
! Lifamatola
bathy( 204, 492) = 3.00000 ! instead of   57.0000
bathy( 205, 492) = 4.00000 ! instead of   192.000
bathy( 206, 492) = 3.00000 ! instead of   189.000
bathy( 207, 492) = 50.0000 ! instead of   14.5000
bathy( 214, 492) = 4.00000 ! instead of   861.835
bathy( 215, 492) = 700.000 ! instead of   1153.23
bathy( 216, 492) = 1829.00 ! instead of   1525.74
bathy( 217, 492) = 1200.00 ! instead of   1851.48
bathy( 218, 492) = 200.000 ! instead of   1758.53
bathy( 219, 493) = 0.00000 ! instead of   1105.22
bathy( 203, 494) = 60.0000 ! instead of   62.0000
bathy( 220, 494) = 2.00000 ! instead of   329.407
bathy( 222, 494) = 500.000 ! instead of   373.465
bathy( 222, 495) = 500.000 ! instead of   364.917

! Island around Belitung in Java Sea
bathy( 137, 487) = 0.00000 ! instead of   7.00000
bathy( 139, 487) = 0.00000 ! instead of   16.0000
bathy( 140, 487) = 0.00000 ! instead of   1.00000
bathy( 143, 489) = 0.00000 ! instead of   27.0000

! Island isolated rattached to the coast
bathy( 134, 487) = 0.00000 ! instead of   3.00000
bathy( 135, 487) = 0.00000 ! instead of   6.00000
bathy( 133, 488) = 0.00000 ! instead of   6.00000
bathy( 134, 488) = 0.00000 ! instead of   7.50000
bathy( 133, 489) = 0.00000 ! instead of   6.00000
bathy( 130, 490) = 0.00000 ! instead of   6.00000
bathy( 131, 490) = 0.00000 ! instead of   8.00000
bathy( 132, 490) = 0.00000 ! instead of   7.00000
bathy( 133, 490) = 0.00000 ! instead of   5.00000

! Balabac Strait
bathy( 179, 530) = 15.0000 ! instead of   25.5000

! Sulu Archipelago
bathy( 188, 519) = 13.0000 ! instead of   155.383
bathy( 196, 523) = 7.00000 ! instead of   126.000
bathy( 193, 521) = 2.00000 ! instead of   17.5000

! Lombok Strait
bathy( 173, 464) = 0.00000 ! instead of   435.309
bathy( 174, 464) = 160.000 ! instead of   29.0000

! Philippine Archipelago
bathy( 213, 539) = 0.00000 ! instead of   1.00000
bathy( 213, 540) = 0.00000 ! instead of   1.00000
bathy( 213, 541) = 0.00000 ! instead of   1.00000
```

```
bathy( 213, 542) = 2.00000 ! instead of   4.00000
bathy( 207, 550) = 0.00000 ! instead of   2.00000

! Taiwan Strait
bathy( 179, 595) = 5.00000 ! instead of   16.0000
bathy( 187, 595) = 22.0000 ! instead of   35.0000
bathy( 188, 595) = 5.00000 ! instead of   22.0000

! Sunda Strait
bathy( 133, 474) = 0.00000 ! instead of   38.0000
bathy( 133, 475) = 0.00000 ! instead of   28.0000
bathy( 133, 476) = 0.00000 ! instead of   37.5000
```